Cranfield UNIVERSITY

Pilot modelling for airframe loads analysis

Mohammad Mudassir Lone

Dynamics, Simulation & Control Group
Department of Aerospace Engineering
School of Engineering

PhD THESIS

This page is intentionally left blank.

CRANFIELD UNIVERSITY

SCHOOL OF ENGINEERING

PhD THESIS

ACADEMIC YEAR 2012-13

MOHAMMAD MUDASSIR LONE

PILOT MODELLING FOR AIRFRAME LOADS ANALYSIS

SUPERVISOR: DR ALASTAIR K COOKE

JANUARY 2013

This page is intentionally left blank.

Abstract

The development of large lightweight airframes has resulted in what used to be high frequency structural dynamics entering the low frequency range associated with an aircraft's rigid body dynamics. This has led to the potential of adverse interactions between the aeroelastic effects and flight control, especially unwanted when incidents involving failures or extreme atmospheric disturbances occur. Moreover, the pilot's response in such circumstances may not be reproducible in simulators and unique to the incident. The research described in this thesis describes the development of a pilot model suitable for the investigation of the effects of aeroelasticity on manual control and the study of the resulting airframe loads. After a review of the state-of-the-art in pilot modelling an experimental approach involving desktop based pilot-in-the-loop simulation was adopted together with an optimal control based control-theoretic pilot model. The experiments allowed the investigation of manual control with a nonlinear flight control system and the derivation of parameter bounds for single-input-single-output pilot models. It was found that pilots could introduce variations of around 15 dB at the resonant frequency of the open loop pilot-vehicle-system. Sensory models suitable for the simulation of spatial disorientation effects were developed together with biomechanical models necessary to capture biodynamic feedthrough effects. A detailed derivation and method for the application of the modified optimal control pilot model, used to generate pilot control action, has also been shown in the contexts of pilot-model-in-the-loop simulations of scenarios involving an aileron failure and a gust encounter. It was found that manual control action particularly exacerbated horizontal tailplane internal loads relative to the limit loads envelope. Although comparisons with digital flight data recordings of an actual gust encounter showed a satisfactory reproduction and highlighted the adverse affects of fuselage flexibility on manual control, it also pointed towards the need for more incident data to validate such simulations.

Keywords: Pilot modelling, manual control, pilot-model-in-the-loop simulation, flight loads, aeroelastics and flight control.

This page is intentionally left blank.

Acknowledgements

I must begin by expressing my gratitude to my parents and brothers who have been very patient with me and without whose love and support I would not have been able to complete this endeavour. I must especially thank my mother and Fran for their understanding and unconditional love, and also for watering and feeding me in times of need.

I was very fortunate to have done my doctoral studies within such a supporting and intellectually stimulating research group. I am ever so grateful to Alastair Cooke for his invaluable advice, support and guidance over the last four years. I would like to thank James Whidborne for his support and for sparing the time to answer my questions. I am also grateful to Mike Cook for his guidance. Advice from Rodger Bailey and Jim Gautrey of the National Flying Laboratory Centre has also been invaluable.

I would like to acknowledge Airbus for sponsoring and supporting this research and giving me the opportunity to join the Filton aeroelastics team to gain invaluable industrial experience. I am especially grateful to Paul Kealy, Oscar Castro-Alvarez and Peggy Smith for their help and guidance. I would also like to thank Thomas Wilson, Mark Hockenhull, Alex Selyanko, Nicki Aversa, Isabelle Bloy and members of the Airbus India aerodynamics and loads team for their support in the projects I was involved in during my time at Filton.

I would like to acknowledge and thank Stuart Andrews for his work on developing the Cranfield University/Airbus AX-1 aircraft model that forms a cornerstone of this thesis. I would also like to thank past and present students of the Dynamics, Simulation and Control Group, especially Ken Lai, Peter Thomas, Pierre Daniel-Jameson and Ramey Jamil for their ideas, help and moral support, together with other members of the PhD student community at the School of Engineering, especially Solange Baena, Kashif Iqbal, Guido Monterzino and Natalia Di Matteo for their cheerfulness, creativity and fortitude. I would also like to take this opportunity to thank those who have allowed me to pursue my other academic interests, especially Neno Ruseno, Shen Yingchun and Liu Qingling for their contributions to work done in the area of pilot-induced-oscillation detection.

I would like to thank the many instructors and students from Cabair International Ltd. who kindly spared their time for discussions and participating in experiments. I am very grateful to Phil Scott, Robin Cox and Sylvain Bernon from the CAE Burgess Hill flight simulation facility who found time to discuss my research and gave me the opportunity to experience simulator based training first hand. I would also like to thank Steve Dunn (Lockheed Martin) and David Klyde (STI Inc.) whose encouragement to join the Atmospheric Flight Mechanics Technical Committee at the American Institute of Aeronautics and Astronautics gave me the opportunity to discuss my work with the wider research community.

This page is intentionally left blank.

Contents

List of Figures

List of Tables

This page is intentionally left blank.

Nomenclature

$\bar{\mathbf{A}}$	Balanced MOCM internal model state matrix
$\bar{\mathbf{B}}$	Balanced MOCM internal model input matrix
$\bar{\mathbf{C}}$	Balanced MOCM internal model output matrix
$\bar{\mathbf{D}}$	Balanced MOCM internal model feedthrough matrix
$\bar{A}$	Ratio of incremental interesting quantity rms to rms turbulence velocity
$\bar{u}$	Intended pilot input
$\bar{w}_g$	Maximum vertical gust velocity
$\hat{\mathbf{P}}$	Controllability gramian
$\hat{\mathbf{Q}}$	Observability gramian
$\hat{e}$	Inter-cue error
$\hat{e}_w$	Washed-out inter-cue error
$\hat{f}$	Sensed specific force
$\hat{F}_{[\cdot]}$	Model frequency response
$\hat{g}$	Local gravitational force vector
$\hat{P}$	Interesting quantity limit load value
$\hat{T}_{[\cdot]}$	Model transmissibility characteristics
$\hat{u}$	Delayed pilot input
$\hat{U}_\sigma$	Prescribed reference turbulence velocity
$\mathbb{F}$	Fast Fourier transform operator
$\mathbb{H}$	Matrix of Hankel singular values
$\mathbb{L}$	Likelihood function
$\mathbf{A}$	Linearised aircraft system state matrix
$\mathbf{B}$	Linearised aircraft system input matrix
$\mathbf{C}$	Linearised aircraft system output matrix
$\mathbf{D}$	Linearised aircraft system feedthrough matrix
$\mathbf{E}$	System disturbance matrix
$\mathbf{F}$	Kalman filter gain
$\mathbf{Q}$	MOCM weighting matrix for pilot perceived variables

$\mathbf{R}$	MOCM control input weighting matrix
$\mathbf{S}$	MOCM control input rate weighting matrix
$\mathbf{u}$	Aircraft model input vector
$\mathbf{V_u}$	MOCM output noise intensity matrix
$\mathbf{V_y}$	MOCM observation noise intensity matrix
$\mathbf{v}_u$	MOCM output noise disturbance
$\mathbf{v}_y$	MOCM observation noise disturbance
$\mathbf{W}$	State noise intensity matrix
$\mathbf{w}$	System disturbance vector
$\mathbf{X}$	Solution to ARE for the determination of MOCM gain
$\mathbf{x}$	Linearised aircraft system state vector
$\mathbf{y}$	Aircraft model output vector
$\mathbf{y}_{obs}$	Vector of pilot perceived variables
$\mathcal{D}$	Dissipative energy expression
$\mathcal{F}$	Flight profile alleviation factor
$\mathcal{J}_{[\cdot]}$	Cost function
$\mathcal{K}$	Kinetic energy expression
$\mathcal{Q}$	Generalised force expression
$\mathcal{V}$	Potential energy expression
a	Proprioceptive feedback lead
a_h	Acceleration of the pilot's head
A_k	Forcing function amplitude
B	Tustin's pilot introduced lead
C_z	Number of peaks observed over a time interval
e	Pilot perceived error
e_θ	Pitch attitude error
e_{rms}	rms error in manual control task
e_{th}	Error perception threshold
f	Fraction of attention allocation per observed variable
f_D	Forcing function
$F_{[\cdot]}$	Experimental frequency response data

$F_{s\phi}$	Lateral stick force
$F_{s\theta}$	Longitudinal stick force
G	Full order MOCM internal aircraft model
g	Vertical acceleration due to gravity
G_f	Pilot model feed-forward compensation
G_p	Transfer function for error compensation within precision model
G_r	Reduced order MOCM internal aircraft model
G_{nm}	Neuromuscular system transfer function
$H_{\hat{j}}$	Joint sensor feedback model transfer function
H_{att}	Attitude compensation transfer function within descriptive model
H_{ip}	Information processing transfer function within descriptive model
H_{md}	Extrafusal muscle model transfer function
H_{oto}	Otolith transfer function within descriptive model
H_{rate}	Rate compensation transfer function within descriptive model
H_{scc}	Semicircular canal transfer function
H_{sp}	Spindle feedback model transfer function
I	Pilot's torso inertia
k	Rotational stiffness of lower body and torso joint
k_0	Seat stiffness
k_1	Backrest linear stiffness
K_f	Pilot model feed-forward gain
K_p	Pilot introduced gain
$K_{\hat{j}}$	Joint sensor feedback gain
K_{ip}	Information processing gain
K_{md}	Extrafusal muscle gain
$K_{p\theta}$	Bimodal model pitch attitude gain
K_{pf}	Proprioceptive feedback gain within Hess model
K_{pq}	Bimodal model pitch rate gain
K_{sp}	Spindle feedback gain
L	Continuous turbulence length scale
L_1	Distance between aircraft centre of gravity and pilot station

L_g	Gust length
$l_{[\cdot]}$	Characteristic lengths of biomechanical torso model
m_0	Pilot's lower body mass
m_1	Pilot's torso mass
M_c	Linear output component in surge model
M_n	Nonlinear output component in surge model
M_x	Wing bending moment
N	Frequency of occurrence for loads interesting quantity
N_y	Lateral acceleration at the centre of gravity
N_z	Normal acceleration at the centre of gravity
N_{zc}	Commanded normal acceleration
N_{zp}	Normal acceleration at the pilot station
p	Aircraft roll rate
P_{1g}	Interesting quantity 1g load value
P_{sp}	Spindle feedback lag component
q	Aircraft pitch rate
q_i	Generalised coordinate
$Q_{[\cdot]}$	Output weighting for variables in MOCM cost function
r	Aircraft yaw rate
s	Laplace operator
t	Time
T_N	Extrafusal muscle lag component
T_r	Roll mode time constant
T_s	Sprial mode time constant
$T_{[\cdot]}$	Experimental transmissibility data
u	Pilot model linear control output
u_c	Commanded MOCM control output
u_f	Feed-forward component of pilot model output
u_p	Applied MOCM control output
U_σ	Limit turbulence intensity
V	Lyapunov function

v	Backrest acceleration
V_A	Manoeuvre design speed
V_B	Speed for maximum gust intensity
V_C	Structural cruise design speed
V_D	Dive speed
V_{CAS}	Calibrated airspeed
V_{EAS}	Equivalent airspeed
V_{TAS}	True airspeed
w	Aircraft vertical speed
w_g	Vertical gust velocity profile
w_p	Vertical speed at the pilot station due to fuselage flexibility
w_r	Reference gust velocity
x	Vertical displacement of lower body
x_s	Fore-aft shoulder displacement
x_w	Fore-aft wrist displacement due to biodynamic feedthrough
Y_C	Vehicle transfer function
Y_P	Pilot describing function
y_s	Lateral shoulder displacement
Y_w	Stick force due to biodynamic feedthrough
Y_{PF}	Proprioceptive feedback transfer function within Hess model
z_s	Vertical shoulder displacement
Z_{sp}	Spindle feedback lead component

Greek alphabet

α	Angle of attack
β	Aircraft sideslip angle
δ_m	Pilot model nonlinear control output
δ_x	Measured stick deflection
δ_ϕ	Lateral stick deflection
δ_θ	Longitudinal stick deflection
η	Elevator deflection angle relative to trim
η_c	Commanded elevator deflection angle

η_{GLA}	Elevator deflection due to gust load alleviation system
η_{MLA}	Elevator deflection due to manoeuvre load alleviation system
$\Gamma_{[\cdot]}$	Set of unknown pilot model parameters
$\hat{\chi}$	Kalman estimated state vector within the MOCM
$\hat{\Gamma}_{[\cdot]}$	Estimated pilot model parameter values
$\hat{\omega}$	Perceived angular rotation rate
$\hat{\sigma}$	Hankel singular value
$\hat{\varepsilon}$	Distance between incident flight conditions and flight envelope boundaries
Λ	Cost function weighting factor
λ	Rotational damping of lower body and torso joint
λ_0	Seat damping
λ_1	Backrest linear damping
λ_g	Harmonic gust wavelength
χ	State vector for MOCM internal model
$\mathbf{\Sigma}$	Estimation error covariance matrix
μ	Wing vertical displacement
ν	Pilot model remnant component
ω	Continuous turbulence frequency
ω_c	Open loop pilot-vehicle-system crossover frequency
ω_k	Forcing function frequency
ω_n	Neuromuscular natural frequency
ω_p	Phugoid mode natural frequency
ω_s	Short period pitch oscillation mode natural frequency
ω_{DR}	Dutch roll mode natural frequency
ϕ	Roll attitude (body axes system)
Φ_m	Frequency response of pilot model stick deflection
Φ_x	Frequency response of experimental stick deflection
ϕ_{t0}	Steady lateral torso inclination angle
ψ	Yaw attitude (body axes system)
ρ_y	Signal-to-noise ratio for pilot perceived variables
σ_d	Forcing function root-mean-square value

σ_u	Standard deviation of MOCM output
σ_w	rms turbulence velocity
σ_y	Standard deviation of pilot perceived variables
σ_ν	Remnant standard deviation
$\sigma_{dy/dt}$	rms of the rate of change in loads interesting quantity
σ_{task}	task dependent perception noise standard deviation
σ_{vis}	Visual perception noise standard deviation
τ	Pilot introduced time delay
τ_1	Visual perception time delay in descriptive model
τ_c	Low frequency lag in semicircular canal model
τ_d	High frequency lag in semicircular canal model
τ_e	Effective pilot-vehicle-system time delay
τ_I	Precision model high frequency lag equalisation
τ_L	Precision model high frequency lead equalisation
τ_n	Neuromuscular lag time constant
τ_w	Adaptation operator time constant
$\tau_{\hat{j}}$	Joint sensor feedback time delay
τ_a	Extrafusal muscle time delay
$\tau_{I\theta}$	Bimodal model pitch attitude lag equalisation
τ_{If}	Pilot model feed-forward lag equalisation
τ_{ILf}	Pilot model feed-forward lag equalisation
τ_{IL}	Precision model low frequency lag equalisation
τ_{ip}	Information processing delay
τ_{Iq}	Bimodal model pitch rate lag equalisation
$\tau_{L\theta}$	Bimodal model pitch attitude lead equalisation
τ_{Lf}	Pilot model feed-forward lead equalisation
τ_{LLf}	Pilot model feed-forward low frequency lead equalisation
τ_{LL}	Precision model low frequency lead equalisation
τ_{Lq}	Bimodal model pitch rate lead equalisation
τ_{sp}	Spindle feedback time delay
θ	Pitch attitude (body axes system)

θ'	Pitch attitude at the pilot station due to fuselage flexibility
θ_p	Pitch attitude at the pilot station
θ_r	Reference pitch attitude
θ_t	Torso inclination angle
θ_{FD}	Flight director pitch attitude
θ_{t0}	Steady longitudinal torso inclination angle
$\tilde{\phi}_k$	Forcing function phase
ϑ	Distance representing pitch attitude on display
ξ	Average aileron deflection angle
ξ_p	Starboard aileron deflection angle
ξ_s	Port aileron deflection angle
ξ_{AMC}	Symmetric aileron deflection due to active mode control system
ξ_{GLA}	Symmetric aileron deflection due to gust load alleviation system
ξ_{MLA}	Symmetric aileron deflection due to manoeuvre load alleviation system
ζ	Rudder deflection angle
ζ_n	Neuromuscular damping ratio
ζ_p	Phugiod mode damping
ζ_s	Short period pitch oscillation mode damping
ζ_{DR}	Dutch roll mode damping

List of Acronyms

AMC	Active mode control
ANOVA	Analysis of variance
APC	Aircraft pilot coupling
ARE	Algebraic Riccati equation
CAP	Control anticipation parameter
CAS	Calibrated airspeed
CNS	Central nervous system
CSAS	Command and stability augmentation system
CT	Continuous turbulence
DFDR	Digital flight data recorder
EAS	Equivalent airspeed
FAO	Force aileron oscillation
FBW	Fly-by-wire
FCS	Flight control system
GIF	Gravito-inertial force
GLA	Gust load alleviation
HJB	Hamilton-Jacobi-Bellman
HTP	Horizontal tailplane
IMU	Inertial measurement unit
IQ	Interesting quantity (loads)
PDF	Probability distribution function
PFD	Primary flight display
PIO	Pilot induced oscillation
PSD	Power spectral density
PVS	Pilot vehicle system
OCM	Optimal control model
LAF	Load alleviation function
LPV	Linear-parameter-varying

LQG	Linear Quadratic Gaussian controller
LTI	Linear time-invariant
MIMO	Multiple-input-multiple-output
MLA	Manoeuvre load alleviation
MLE	Maximum likelihood estimation
MOCM	Modified optimal control model
MTOW	Maximum take-off weight
OWE	Operational weight empty
ROVER	Real-time oscillation verifier
TAS	True airspeed
TFLS	Time-frequency-domain least squares
TLS	Time-domain least squares
SD	Spatial disorientation
SISO	Single-input-single-output
TAS	True airspeed
UCE	Usable Cue Environment
VAF	Variance-accounted-for
VCR	Visual cue range
VTP	Vertical tailplane
WRBM	Wing root bending moment

CHAPTER 1

Introduction

The design of civil aircraft raises interesting issues involving weight and efficiency trade-offs. The more passengers a civil aircraft carries the more efficient it becomes, but at the same time its size and weight increase. The increase in weight is compensated by a design process that relies heavily on optimisation to maximise performance and minimise structural weight. The end product is a large lightweight airframe that is characterised by reduced stiffness and damping that amplify structural flexibility effects; often referred to as aeroelastic effects. These can impact aircraft stability and control in ways that are often not fully appreciated or understood. As the aeroelastic modes encroach the upper frequency range of the rigid-body dynamics, aeroservoelastic effects appear. These are where the flight control systems (FCS) relying on feedback from the various sensors around the airframe are affected by the aeroelasticity. These sensors can no longer distinguish between aeroelastic and rigid body dynamics and this can cause unexpected behaviour. Similarly, the pilot is also unable to distinguish between these effects and rigid body dynamics and therefore, can exhibit unexpected manual control behaviour. These interactions, arising due to the structural flexibility of the airframe, between the pilot, the FCS and the aircraft's flight dynamics are not yet well understood.

Understanding the effects of aeroservoelasticity on aircraft manual control has become more important as airframes increase in size and the FCS augmenting their dynamics become more sophisticated. The FCS and low frequency aeroelastic modes can introduce significant lags into aircraft dynamics leading to degraded handling qualities that have required a change in the flight control design philosophy and a consequent change in a pilot's approach to controlling a large aircraft. Effects on manual control have also been observed on a wide variety of aircraft, for example:

- the Boeing C-17 was found susceptible to lateral aircraft-pilot-coupling (APC) due to phase lags introduced by the FCS and actuator rate limiting[1].
- coupling between the pilot and the fuselage bending mode of the Lockheed SR-71 during air-to-air refuelling led to the classification of a new category of pilot-induced-oscillations (PIO)[2].
- in the case of the Rutan Voyager, atmospheric disturbances excited a longitudinal low frequency mode that coupled symmetric wing bending with the Phugoid mode making manual control of the aircraft very difficult[2].

Such occurrences demonstrate the effects of coupling between sophisticated FCS and the aeroelastic characteristics of slender configurations on pilot's control actions.

Investigation of such scenarios requires an understanding of aircraft manual control and consequently, an understanding of the pilot-vehicle-system (PVS) as a whole. Modern civil aircraft effectively have three modes of operation:

1. Aircraft control can be achieved through complete manual control with objectives from the pilot's mind or manual control with objectives from a flight director.
2. The mode control panel which commands the various autopilots can be used. The pilot plays a more supervisory role here and his/her input is required only at particular stages of the mission.
3. The flight management computer can be programmed and based on this information, the flight director establishes control through the autopilots. The pilot then presumes a fully supervisory role for the majority of the mission.

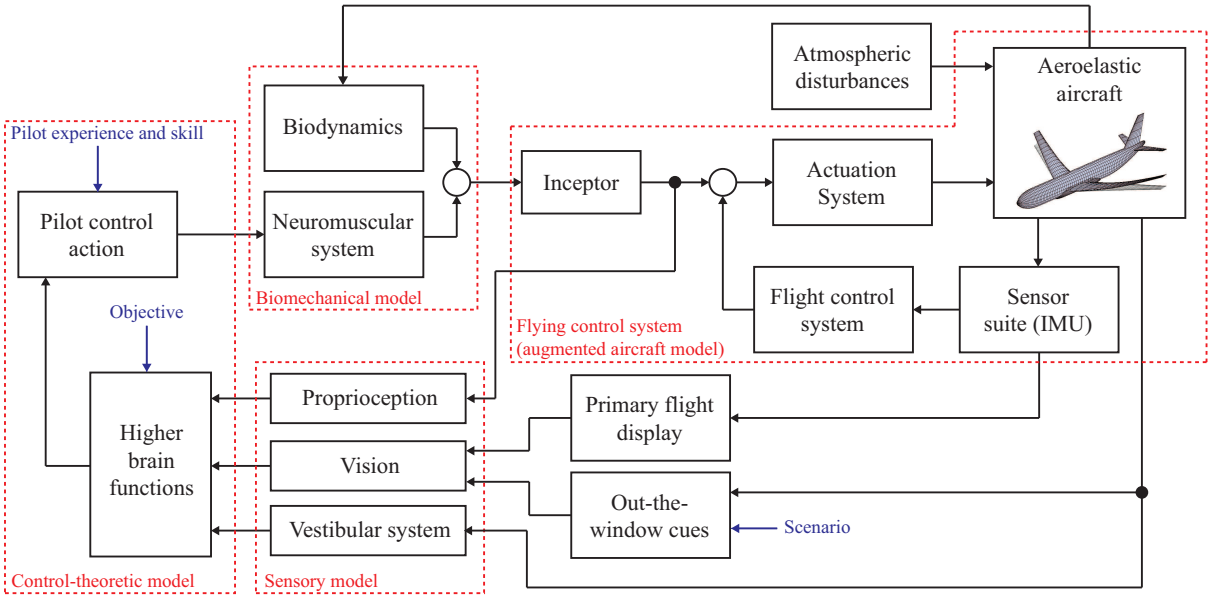

Figure 1.1: Block diagram representing the pilot-vehicle-system under manual control.

Figure 1.1 presents the key components involved in the manual control mode that are necessary to model manual control dynamics. Here, the system is driven by an *objective* that is processed by *higher brain functions* to derive a process through which it can be achieved. Pilot training plays a critical role at this stage. The resulting *pilot control action* then determines the cues and gains selected by the pilot to establish feedback control. These are typically a function of pilot *experience and skill*. The control action is executed via the forces generated by the muscles in the *neuromuscular system* and exerted on the *inceptor*. Signals from the inceptor are used by the *flight control system* as demands for flight dynamic parameters such as pitch rate or normal acceleration. These are met with the help of the *actuation system* that provides the appropriate movement of the various control surfaces on the wings and empennage or changes in engine thrust. Thus, forces and moments are generated to change the orientation of the *aeroelastic aircraft* relative to the oncoming air flow. This change is perceived by the pilot primarily through his/her *visual sensory modality* that delivers information regarding the *scenario* from *out-the-window cues* to the brain. The *primary flight display* (PFD) effectively delivers information from the *aircraft's sensor suite*. *Vestibular dynamics* play a critical role in

the perception of aircraft accelerations. The pilot also perceives the commanded inceptor input via the *proprioceptive sense*. These cues effectively close the feedback control loops. However, the pilot's position within the aircraft also means his/her body is subjected to the resulting accelerations that arise either due to his/her commands or *atmospheric disturbances*. Therefore, the neuromuscular forces acting on the inceptor are affected by a disturbance generated by the pilot's *biodynamic* response.

Supersonic transport aircraft configurations and smaller combat aircraft have attracted most of the research effort in pilot modelling and aeroservoelastics. This began during the early 1950s and 1970s when military flying and handling qualities requirements were being formulated. More recently, pilot modelling techniques are being used to improve flight simulator fidelity[3][4]. However, the design process for civil aircraft still relies on flight simulation at later stages of development simply because the process through which a pilot forms his/her opinion about an aircraft's flying and handling qualities is still not fully understood.

The complexity and versatility of the human being alongside the nature of atmospheric flight has meant that both military and civil industries have struggled to fully understand man-machine systems. Early researchers arrived at conclusions similar to that of Crowley and Skan[5]:

> "A mathematical investigation of the controlled motion is rendered almost impossible on account of the adaptability of the pilot."

In his 1973 paper on PVS analysis[5], McRuer made the following remark:

> "Actually, matters are even worse than Crowley and Skan recognised; for while much of the pilot's dynamic behaviour is governed by the aircraft dynamics, many additional factors also affect his properties."

Such remarks not only point towards the difficulties in modelling human control behaviour but also highlight the necessity of a holistic approach to pilot modelling. Flight control and handling qualities engineers, such as McRuer, provided the first techniques for PVS analysis in early 1950s. These were limited to linear single-input-single-output (SISO) models of the PVS where the pilot was performing compensatory tasks. The crossover law and simple pilot models provided great insight into human control behaviour, but were limited to the frequency domain and suitable only for small combat aircraft for which the effects of rigid-body dynamics on manual control were dominant.

It was only when the algorithmic modern control based pilot models were developed and applied to the Rockwell B-1 that aeroelastics and handling qualities could be integrated in the early design stages. However, the B-1 and other aircraft developed during the 1960s were equipped with early fly-by-wire (FBW) command and stability augmentation systems (CSAS) that had limited authority. A full authority system first appeared in late 1970s on the light weight General Dynamics F-16 fighter. Only ten years later, around the time of the first flight of the Northrop B-2, the Airbus A320 family pioneered the application of such a system for civil aviation. This has meant that the understanding of PVS dynamics, as a whole, has lagged significantly behind the advancements made in FCS design. Publications such as the National Research Council's report[6] on pilot control highlight this particular issue.

Although engineers have been exploring novel methods in which FBW FCS can be used to augment aircraft flying and handling qualities, it has resulted in pilots being subjected to ever more demanding training sessions on FCS modes and the use of cockpit automation. Although the pilot may be flying the same airframe, regarding handling qualities, each FCS

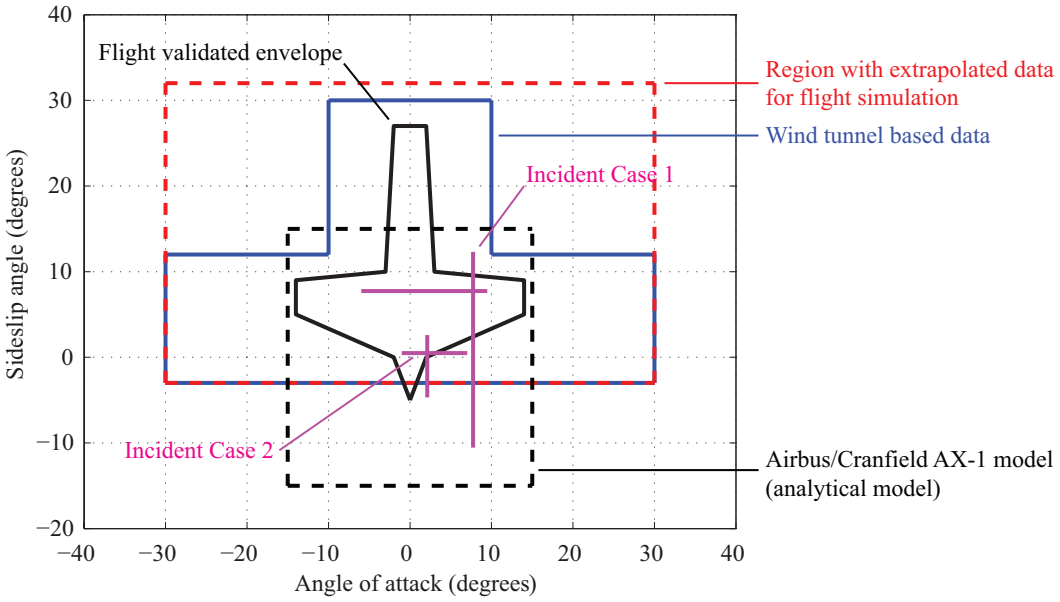

Figure 1.2: Angle of attack and sideslip envelopes for approaches to flight incident investigation.

mode effectively presents him/her with a different aircraft. Each mode exists to ensure a degree of fault tolerance, implying that the pilot must have an in-depth understanding of these modes. However, given the modern probability based requirements on fault occurrences, a pilot may never experience actually flying the aircraft in a back up mode. Consequently, the importance of flight simulator based training cannot be overlooked.

State-of-the-art training simulators for fixed-wing aircraft can reproduce pilot perceived cues during routine flying with excellent fidelity. However, in the context of flight incident or failure simulations, these devices suffer three drawbacks. These are the inability to:

1. induce levels of urgency in the crew known to exist during real incidents or failures,
2. generate sustained acceleration cues felt during these scenarios and,
3. accurately reproduce the flight dynamics undergone in such scenarios due to a limited flight dynamic database.

The manufacturers, motivated by a desire to improve safety and performance of the FCS, deal with these limitations by conducting flight test manoeuvres that are often very risky and not welcomed by test pilots.[7][8] However, as shown in Figure 1.2, the flight test validations still cover only a limited region on the incidence and sideslip envelope. In fact, a considerable region of the simulation envelope is covered by extrapolated data.

The maximum and minimum incidence and sideslip angles observed for two incidents (kindly provided by Airbus UK) are also plotted in Figure 1.2. These show the large excursions that can occur as a result of failures or atmospheric disturbances; often over a very short time span. They also highlight the critical role played by mathematical models of the aircraft (like the Cranfield University/Airbus AX-1 flight loads model[9]) that cover a more suitable flight envelope, albeit with certain limitations. As demonstrated later by the case studies in this thesis, when coupled with pilot models, these are no longer limited by the drawbacks associated with flight simulators and allow pilot-model-in-the-loop simulations of worst case scenarios. This avenue has received little attention from the research community. This is firstly due to the reliance of airframe manufacturers on flight simulation and flight testing and secondly,

due to a tendency not to trust results from simulations that use mathematical representations of manual control dynamics. The latter occurs because of the complexities involved in both the pilot modelling and the analysis of results that follows a simulation. The reader must therefore realise, that regarding the application of pilot models to recreate flight incidences, there remains a fundamental shortcoming: effectively all models are derived and parameterised from observations in controlled laboratory experiments which not only fail to reproduce the accelerations undergone but also the sense of urgency felt by the pilot. Therefore, appreciating the implications of results produced from such simulations requires an in-depth understanding of the mathematical modelling process and the worst case scenario analysis.

1.1 Aims and objectives

The aim of this project was to develop a pilot model suitable for the investigation of large aircraft flight loads. This was achieved through the following objectives:

1. Develop understanding of manual control dynamics through a series of single and multi-axis manual control experiments.
2. Develop an appropriate algorithm to generate models capable of reproducing pilot control action.
3. Develop sensory and biomechanical models suitable for the simulation of spatial disorientation and biodynamic feedthrough effects respectively.
4. Augment the Cranfield University/Airbus AX-1 model with models of the flight and active loads control systems and generate flight loads envelopes for the assessment of simulation results.
5. Conduct pilot-model-in-the-loop simulations to study the interactions between manual control and airframe flexibility effects.

Research areas like the one investigated in this thesis actually span a number of technical fields. In this case, the problem of understanding the effects of structural flexibility on manual control can be investigated through perspectives that are purely in one of the following domains: aeroservoelasticity, human factors, flight control or handling qualities. Each block within the PVS shown in Figure 1.1 is infact a technical field on its own. Consequently the scope of thesis had to be limited from the outset. Therefore, it focuses only on studying the manual control of flexible aircraft with pilot models rooted in control theory and a flexible aircraft model adopted from earlier studies[9] within the research group.

1.2 Thesis outline

The chapters within this thesis describe the development of the various building blocks of the PVS shown in Figure 1.1. Chapter 2 presents a review of pilot modelling techniques mainly focusing on the early foundational work and current developments in modelling of manual control dynamics. This is mainly qualitative simply due to the quantity of theoretical work done within this field. However, the relevant manual control theory and its mathematical basis are presented in Chapters 3 and 4. The reader's understanding of manual control modelling is developed via the discussion of a series of single-axis control experiments investigating the effects of nonlinear

FCS components in Chapter 3. This is followed by the description and validation of an optimal control based algorithm in Chapter 4 that is used to capture manual control dynamics in multiple axes. Chapter 5 moves away from the discussion of control-theoretic modelling and presents models capable of reproducing human sensory and biodynamic feedthrough effects. Chapter 6 then focuses on the flexible aircraft model used to generate flight loads and the augmenting flight and active loads control systems. Here, the reader is presented with a synopsis of current loads envelope generation processes prior to the internal loads envelopes calculated for the wing and empennage. The pilot model components are then integrated with the aircraft model in Chapter 7. Results from pilot-model-in-the-loop simulations of a soft-actuator failure and a gust encounter are presented and the severity of internal loads are assessed through comparisons with the envelopes generated in Chapter 6. Finally, the key conclusions, contributions to knowledge, areas of future work and the various ways in which the findings of this research have been disseminated are presented in Chapter 8.

CHAPTER 2

Review of pilot modelling techniques

Pilot modelling is a vast field with contributions from practically every engineering and non-engineering disciplines that consider the human being as an end customer. Aspects of this field are included either implicitly or explicitly during the design of day-to-day objects like a cup to complex machines such as the space shuttle. Modern understanding of human perception and information processing alone has advanced considerably over the last twenty years, prior to which researchers focused on mainly qualitative descriptions of possible human decision making processes. Present day scientists are taking advantage of the available computational power to identify and develop functional maps of neurons within the brain.[10][11] Yet, each miracle landing credited to skilled manual control or accident attributed to human error demonstrates the complexity of the human being and highlights our ignorance of its capabilities.[12] A detailed review of the state-of-the-art in pilot modelling merits many years of research. Therefore, the discussion presented in this chapter is limited to a thin slice of this field, which considers aspects thought to be fundamental to modelling manual control dynamics exhibited by large aircraft pilots. These are the sensory, biodynamic and control-theoretic aspects.

2.1 Sensory dynamics

A pilot perceives aircraft states through cockpit instruments and his/her physiological sensory organs. Both sources of information have their respective dynamics. The natural sensory organs have evolved to become a very sophisticated sensory suite, which in conjunction with the central nervous system (CNS), is an elaborate example of data collection and fusion. However, this system is best suited for moderate angular rotations of short durations experienced on a daily basis on the ground. Although the dynamics of the individual sensory organs are well understood, their joint role with the CNS for perception is only being investigated now. It is normally taken as granted that reality is being perceived. Whilst true for most day-to-day scenarios, the frequent low intensity and long duration rotations experienced in flight can easily result in erroneous perceptions resulting in disorientation. Spatial disorientation (SD) is defined as a situation when the pilot fails to correctly perceive position, motion or attitude of the aircraft within a fixed coordinate system provided by the surface of the Earth and its gravitational field. A human sensory model should be capable of simulating certain pilot SD.

Research in this field was initiated by Ernst Mach[1] with his investigation of the vestibular

[1]His work in supersonics actually had roots in his earlier study of the human vestibular sense and audio

system. Research in the context of aviation only began towards the end of World War 1. True progress came in the 1990's during which half of all SD research to date was conducted. SD has now been divided into three categories[13]:

- Type I: where the pilot is unaware that the perceived orientation is incorrect.
- Type II: where there is a conscious recognition of a conflict between the senses and instruments.
- Type III: where the pilot has a sense of helplessness and an inability to maintain control due to an overwhelming confusion about orientation.

It should be noted that majority of SD mishaps are of Types I and II. In such cases the pilot often refuses to believe the instruments and/or misinterprets out-the-window cues. For example, a near-fatal Type II SD occurred when the pilot of a United States Air Force (USAF) C-5 refused to believe the primary flight display just prior to entering a stall. The cause of this SD was found to be the perceived gravito-inertial force (GIF) vector (felt by the vestibular system) that falsely indicated level flight[13].

Mathematical modelling of SD requires knowledge of the mechanisms and processes involved in developing spatial orientation. At the conscious level auditory and focal visual cues are used to obtain estimates of aircraft states at any given time. Subconsciously the ambient visual, vestibular and proprioceptive inputs are processed to provide positioning, angular and linear acceleration estimates. The CNS is then responsible for the interpretation and comparison with an internal model. These models are formulated from past experience and training that in turn generate expectations concerning aircraft dynamics[14]. Such qualitative descriptions and relationships can be found in most literature concerning human perception; collectively known within the aviation community as *human factors*. On the other hand, quantitative relationships are harder to come by due to the difficulties involved in experimental design, measurement and medical ethics.

2.1.1 Visual system

The human visual system is the primary source of information required to maintain orientation in Earth-fixed space. It operates in two modes: ambient and focal. Each mode may be distinguished by considering the differences between a landscape painting and the landscape itself. The dominance of this sensory modality is reflected by the fact that even today most manufacturers rely on fixed-base simulation.

The ambient mode helps mainly in spatial orientation and relies on certain types of cues within the central and peripheral fields such as motion, linear/aerial perspective, texture and brightness gradients. It then provides a sense of self-motion, distance, slant and tilt within a three dimensional framework. Majority of the cues inducing visual SD tend to be monocular; binocular cues only contribute to perception within the first few surrounding metres. The astonishing feature of this visual mode is its capability to subconsciously process the aforementioned cues and provide a stable perception of the surroundings over a large spatial range. It does so by contributing sustained low frequency signals to the CNS that then determines spatial orientation. This is in contrast to the remaining sensory systems that provide signals of a more transient nature and relatively high frequency to help stabilise the perceived surroundings immediately after self-motion[13].

perception. It was a decade later in 1877 that he published his work on supersonic projectile motion.

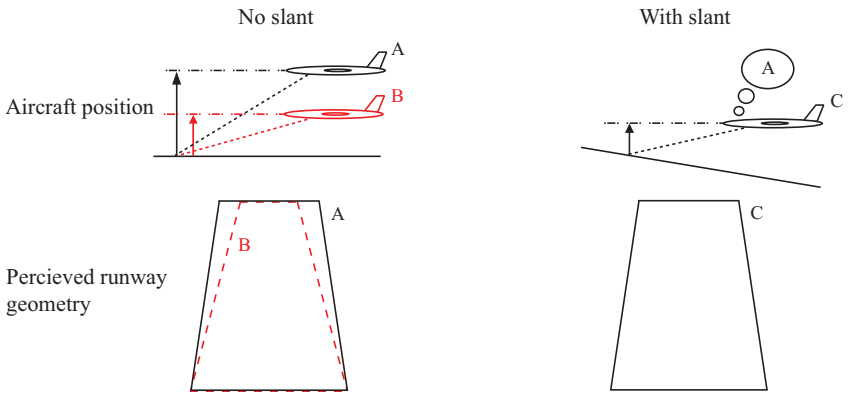

Figure 2.1: Effects of slant on pilot altitude judgement.

An area where the ambient mode has significant contribution is the perception of distance and ground slant. Correct judgement requires many of the same cues and so there exists a fundamental ambiguity in their perception leading to difficulties in estimating altitude when in flight. For example, an upsloping terrain decreases the perspective splay angle and the pilot feels as though he is flying at a higher altitude, as shown in Figure 2.1. In a degraded visual environment, observers have been found to rely on size and shape of familiar objects and memorised spatial layouts[13].

The focal mode is concerned with object identification and relies on cues (mainly binocular) within the central field of vision. It gathers highly detailed information at high spatial frequencies which is usually well represented in consciousness[14]. Instrument flight is dependant on this visual mode.

In the context of pilot modelling, the quality with which visual cues are perceived can be modelled at various levels. The simplest of these is the injection of a filtered Gaussian white noise into the control loop to account for all potential non-linear control inputs; these may arise from factors such as degradation of cue quality. The visual perception model proposed by Hess[15] (Figure 2.2) and considered by Kleinman[16] provide simple models for visual observation. The saturation limits are set to twice the variance of the zero-mean Gaussian random number generator. The variance of this random number generator implicitly determines the visual cue quality. Hess[17] relates this variance to the relationship between usable cue environment (UCE) and visual cue rating (VCR) found in military rotorcraft design standards[18] and shown in Figure 2.3 for convenience. It is selected as follows:

$$\begin{aligned} 0 < \sigma^2_{vis} < 0.1 \quad & \text{for UCE } = 1 \\ 0.1 \leq \sigma^2_{vis} < 0.2 \quad & \text{for UCE } = 2 \\ 0.2 \leq \sigma^2_{vis} < 0.3 \quad & \text{for UCE } = 3 \end{aligned} \tag{2.1.1}$$

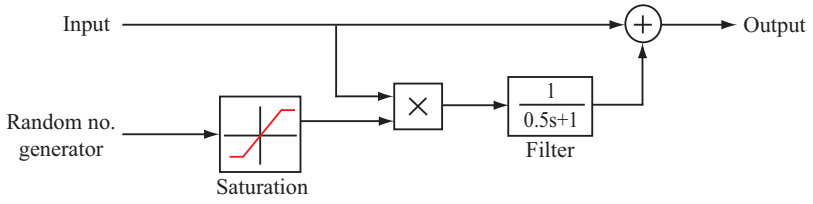

Figure 2.2: Visual cue perception model proposed by Hess.

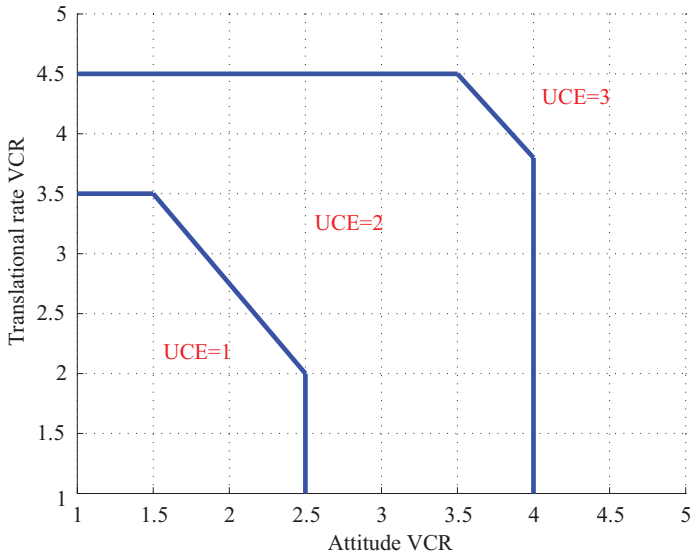

Figure 2.3: Usable Cue Environments for Visual Cue Ratings.

This has been extended to visual perception in multiple axes by introducing a task dependant variance as follows:

$$\sigma^2_{task} = \begin{cases} 0.01n & \text{for } n > 1 \\ 0 & \text{for } n = 0. \end{cases} \tag{2.1.2}$$

where n is the number of axes being controlled. This term is incorporated through the following 'f' factor which is later considered in the control-theoretic component of the pilot model:

$$f = 1 + 10(\sigma^2_{vis} + \sigma^2_{task}) \tag{2.1.3}$$

A large civil aircraft is mostly under manual control in the low to mid subsonic areas of the flight envelope; usually near an airport where the pilot tends to be fully involved in the control loop. It is also during this time that major out-the-window cues are utilised by the pilot. Therefore, the ability to model such cues is also necessary for investigating scenarios that take place during the approach, flare and takeoff. One of the earliest attempts was made by Naish[19] where the apparent runway geometry was related to observer position and velocity. Defining a so called inclination angle ($\hat{i}$) as the angle made by the runway sides with the vertical (as shown in Figure 2.4(b)) nonlinear equations governing the perceived runway shape were derived.

Considering the basic geometry as shown and annotated in Figure 2.4, the following equations may be derived for the case of a straight approach. The inclination angle may be found to vary as follows:

$$\tan\hat{i} = \frac{x+W}{H}\frac{d\hat{i}}{dt} = \frac{1}{H\sec^2\hat{i}}\left[\frac{dx}{dt} - \frac{x+W}{H}\frac{dH}{dt}\right] \tag{2.1.4}$$

As an aircraft descends during approach and flare, the runway length is perceived to elongate. Naish argues that whilst descending, the near end of the runway is perceived to be stationary whilst the far end travels backwards, giving a perception of elongation. Equation 2.1.5 governs this process.

$$\frac{\sin(\Delta_F - \Delta_N)}{\sin(\Psi - \Delta_D)} = \frac{L}{R_N} \tag{2.1.5}$$

Letting $\Delta_F - \Delta_N = \hat{a}$, the rate of elongation may be found to be as follows:

$$\frac{d\hat{a}}{dt} = \frac{\cos(\Psi - \Delta_F)\frac{d(\Psi - \Delta_N)}{dt} - \frac{1}{R_N}\sin(\Psi - \Delta_F)\frac{dR_N}{dt}}{\frac{R_N}{L}\cos\hat{a} + \cos(\Psi - \Delta_F)} \tag{2.1.6}$$

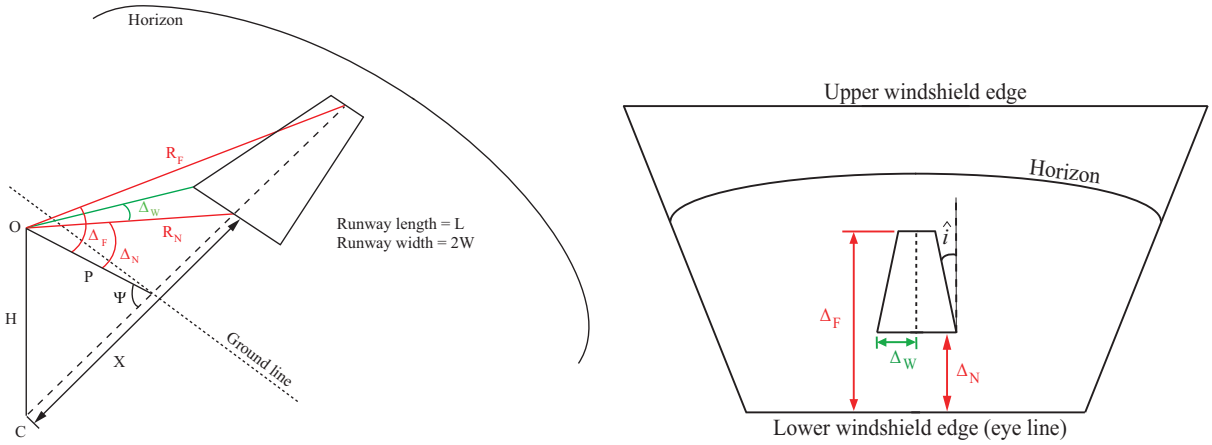

(a) External perspective of runway geometry.

(b) Cockpit view geometry with runway.

Figure 2.4: Geometric layout for human perception modelling with runway included (reproduced from Schmidt and Silk[20]).

Note the appearance of the dR_N/dt term confirming the fact that as the aircraft descends the perceived far end of the runway tends towards the horizon. Similarly, the perceived width of the runway near end varies with height. From Figure 2.4 the governing equation for this process may be found to be as follows:

$$\frac{\tan \Delta_W}{\tan \hat{i}} = \sin(\Psi - \Delta_N) \tag{2.1.7}$$

The role of flight simulation has dramatically changed since the days of Naish et al, both in terms of simulation environment quality and costs due to technical complexity. The approach presented here is useful for rapid/cheap desktop simulations. These equations can be linearised or directly implemented in a non-linear simulation environment to simulate visual cues used for judging altitude, flight path angle and speed, as found by Schmidt et al[20]. Their investigation of the cues obtained from a typical outside scene during landing showed that given a perfect internal model, the visual cues provided more information than motion cues. Furthermore, these can be included in the framework of certain control-theoretic pilot models for the analysis of handling qualities in the approach and landing flight phases.

2.1.2 Vestibular system

The vestibular system is mainly responsible for postural control and sensing body motion. It is physically housed within the inner ear and consists of the otoliths and the semicircular canals. Together these function in a similar manner to an inertial reference system. The otoliths provide a sense of tilt and specific force whilst the semicircular canals help perceive angular acceleration. Accurate estimation of their dynamic response is critical to modelling pilot perception; especially during instrument flying where the ambient visual mode has little influence. The understanding of vestibular dynamics has also played a crucial role in the development of motion based flight simulators. A detailed discussion of motion cues in flight simulation is given by Allerton[21].

Low amplitude perception of angular motion through the vestibular system is limited due to inherent thresholds that are a function of stimulus magnitude and duration. Angular accelerations lasting less than 10 seconds must satisfy Mulder's law, which states that the product of angular acceleration and its duration is approximately equal to 2.5[14]. Therefore, the weaker the acceleration, the longer it takes for it to be perceived. Data regarding lower human sensory thresholds for prolonged angular velocities and accelerations are summarised in Table 2.1.

	Angular velocity (°/s)	Angular acceleration ($°/s^2$)
Roll axis	3.2	0.50
Pitch axis	2.6	0.50
Yaw axis	1.1	0.14

Table 2.1: Typical lower vestibular system thresholds.

It is suggested that these thresholds will be slightly higher in flight due to the more stressful environment and that the pilot is likely to be preoccupied[22]. However, studies by Hosman et al[23] have concluded that since a trained pilot has expectations arising from an internal aircraft model, the threshold would in fact be lower. Nevertheless, the threshold values remain a function of pilot workload, stress and the quality of the internal model that are difficult to quantify accurately. Therefore, accurate modelling of dynamic variations in these thresholds is very difficult.

The system relies on the relative motion of a fluidic substance and sensory nerves for detecting head or whole body angular acceleration. Nerves within the canal walls are excited by the movement of a fluidic substance filling the semicircular canals called endolymph.[14] However, this sensory mechanism, relying on such relative motion, has inherent disadvantages as illustrated in the following example:

Consider a pilot rolling the aircraft to the left. A signal reflecting the roll rate is generated by the semicircular canals after an initial time constant of 3-5 ms. During prolonged angular rotation however, the perceived roll rate progressively becomes less than the actual angular velocity until a point is reached when no signal is generated by the semicircular canals. Upon recovery, the apparent sensation of rotation becomes directionally opposite and continues to persist for a while after the actual rotation has stopped in what is known as a post-turn illusion. Responding to this illusion might cause the pilot to enter a 'graveyard spiral' where the the pilot enters into a sub-threshold descending turn under a false perception of steady level flight[13]. The increased g-loading then gives rise to a false sensation of pitch and the situation may be further exacerbated by attempts to recover by first pitching upwards; this would only tighten the turn, increase the g-load and rate of descent.

The otoliths' primary role in spatial orientation is to sense the vertical, which under ideal conditions can be estimated within a threshold of around 2°. However, they are also sensitive to linear accelerations (with a lower threshold of 0.1g) and function in a similar way to mechanical accelerometers. They cannot differentiate between gravity and other linear accelerations and thus the perceived acceleration is not relative to the true vertical but relative to the GIF vector, sometimes referred to as the apparent vertical. This also means that there is no difference in the way humans sense tilt and linear acceleration. Assuming no visual cues, the human sensory suite is incapable of differentiating between the two. This ambiguity is the source of numerous SDs, which are often taken advantage of in full-motion flight simulators to induce a sense of self-motion. The means by which the brain resolves this area of conflict has been a subject of much debate but no firm theory has been proposed as yet. More recent attempts at modelling the vestibular system emanate from the field of flight simulator design and development, such as Hosman's descriptive pilot model formulation discussed in Section 4.1.

The significance of this inability to distinguish between the GIF vector and the resultant force vector is highlighted in two of the most common SDs related to the vestibular system which are described below.

The first SD may be encountered when turning an aircraft at a load positive load factor. Once steady state is achieved in a coordinated bank turn, the resultant force due to gravity and

centripetal force is aligned with the aircraft vertical, giving a sensation of wings level flight. Similarly in a flat turn, the resultant force not being aligned with the aircraft vertical gives an illusion of bank in the opposite direction, as shown in Figure 2.5.

The second SD is the false sensation of pitching during acceleration and deceleration. During an acceleration, the resultant force pushes the pilot backwards into the seat, giving a pitch up sensation. During a deceleration the opposite occurs and the pilot perceives a pitch down sensation. It has been found that a 0.1g acceleration leads to the resultant force vector being rotated by approximately 6°. This type of SD was reported in 64% of night takeoff mishaps in Australian general aviation[13].

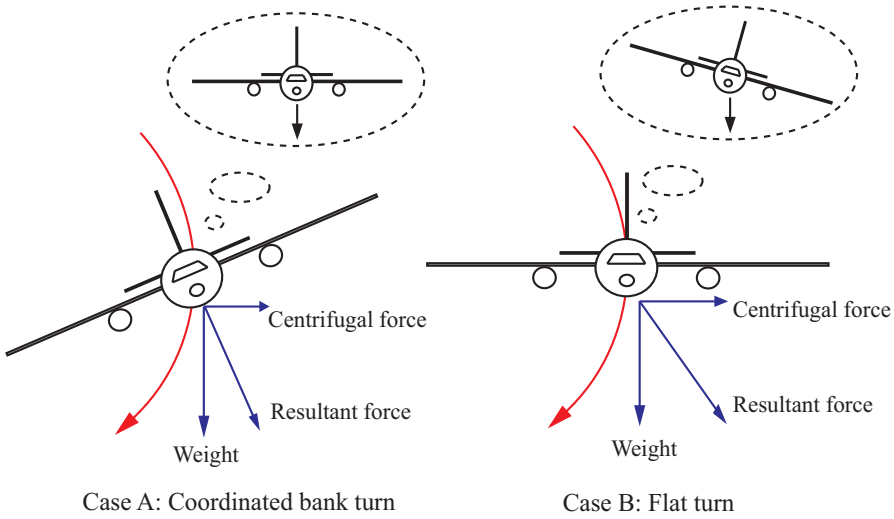

Figure 2.5: Effect of resultant force vector on bank angle perception during turns.

2.1.3 Tactile and proprioceptive systems

Tactile and proprioceptive senses are believed to be the first to develop in infants because they are required for determining the GIF vector and the development of 'anti-gravity' muscles necessary for walking. When this sense is combined with the remaining sensory systems skilled movements can be accomplished.

Proprioception or kinesthesis, is the terms used for the sensory modality due to sensors within the muscles (such as muscle spindles), which are used to determine body position, spatial limb movements and forces required for moving and maintaining joint positions against resistive loads. In aviation the role of proprioceptive and tactile sensors, together known as the somatosensory system, is to provide feedback of aircraft motion through forces or displacements felt via the control inceptors. Modern inceptors are designed to engage with this sense through pressure receptors within the skin. Present all over the human body, these receptors are primarily responsible for the *seat-of-the-pants* sensation experienced by pilots. Many early aviators wrongly believed that aircraft orientation may be deduced from this sensation. It is very important for a pilot to understand that the somatosensory system has evolved to give a sense of relative body part motion and not a sense of orientation in space. Considering the forces experienced in a flight environment this sense can lead to erroneous perceptions if relied upon for orientation.

The modelling of this system is complicated by the number of physical stimuli to which it responds. Factors such as linear and angular velocity, muscle tension and orientation relative to the GIF vector all simultaneously affect the sense's output to the CNS. The variables sensed by

the somatosensory system are also sensed by other sensory systems and usually they are not in conflict. However, when a conflict does arise it is believed that the CNS uses the combination of sensory information to develop a proprioceptive sense. Therefore, proprioception cannot be seen as a unitary sense such as vision, but has to be considered as a sense gained by combining the outputs of various sensory organs.

The structural pilot model proposed by Hess includes a transfer function representation of the proprioceptive sense which is active prior to the triggering of an APC event[24]. The model is discussed in detail in Section 4.1. Hess has actually adopted a very simple approach for modelling the affect of cues from the various senses on overall perception. For example, in Reference [17], the vestibular and proprioceptive feedback of angular rate is simply split into a 1:3 ratio. A more complex model combining the visual and vestibular senses has been proposed by Cardullo et al[25] to capture the sense of vection. This is discussed in detail in Chapter 5.

2.2 Biodynamic modelling

The excitation of aeroelastic modes often produces periodic motion in the cockpit. For aircraft with more rigid airframes this tends to be characterised by high frequency vibrations that a pilot may associate immediately with structural dynamics. However, flexible aircraft are prone to interactions between low frequency aeroelastic modes, pilot's body motion and neuromuscular dynamics. One such interaction is called *biodynamic feedthrough* where vehicle accelerations are involuntarily fed back via the pilot's body through the inceptor. In some extreme cases, it may lead to aircraft instability or excessive airframe loadings[26]. The only adequate course of action is to either ease the grip on the inceptor or completely release it (the definitive solution to any unwanted APC scenario). The modelling of this effect requires representations of the human body and neuromuscular system. Figure 2.6 is a diagram from Serafini et al[27] clearly showing the overlaps in frequency ranges between biodynamics and other aircraft dynamics. The diagram was presented in the context of rotorcraft but remains poignant and highlights the necessity to consider biomechanics during the flight control system design process.

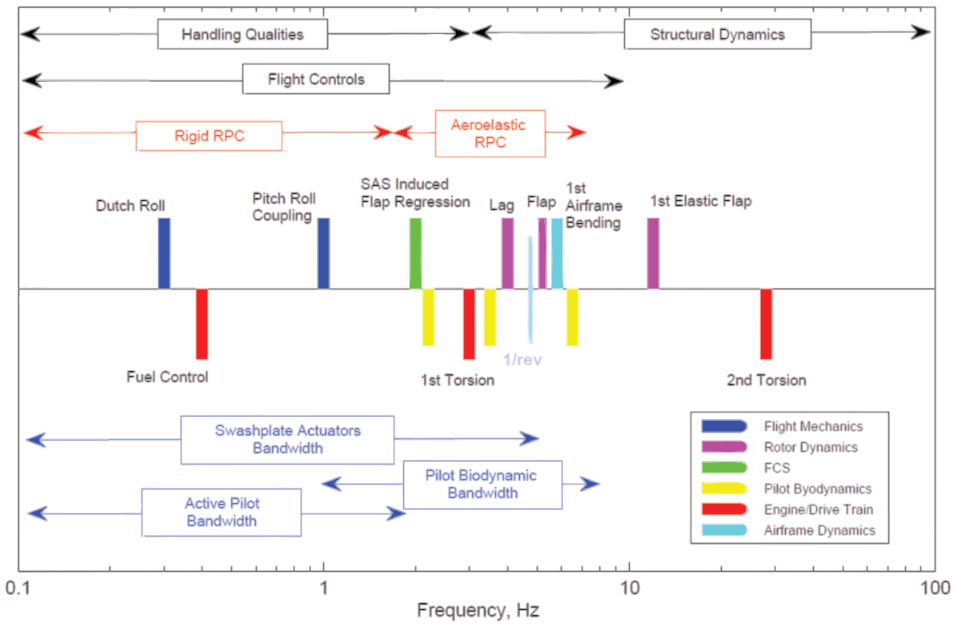

Figure 2.6: Frequency ranges of pilot and aircraft dynamics (reproduced from Serafini et al[27]).

Within the aerospace community, it is well known that manual control behaviour is significantly affected by base accelerations above 0.05g root-mean-square vertical acceleration in the region of 2 Hz to 16 Hz. The highest levels of degradation is expected to be around the body's resonant mode, which occurs between 4 Hz and 8 Hz.[28]

2.2.1 Modelling of biomechanics

Biodynamic models aim to represent the effects of human body dynamics on the pilot's desired control inputs within an accelerating (or vibrational) environment. Such a model can be implemented within a PVS as shown earlier in Figure 1.1[2]. These models may be categorised into three types: continuum, discrete and lumped-parameter models[29][30]. Each approach differs in the way the spine is modelled.

Continuum models treat the spine as a single flexible beam with properties tuned via comparison with experimental data. Griffin et al[29][31] have done considerable work in this area and have shown that finite element based models can accurately capture seven of the eight modes of motion associated with the spine's response to vertical accelerations. The approach adopted by Wood et al[32], which used beam theory to model arm dynamics also comes under this category.

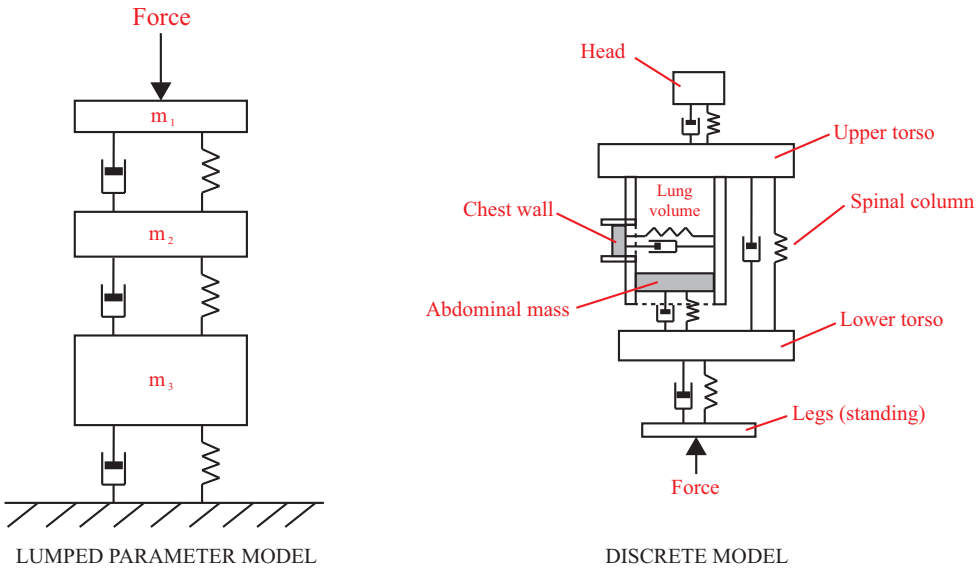

Figure 2.7: Examples of lumped parameter and discrete modelling approaches.

Discrete models on the other hand, model the spine with a series of rigid bodies interconnected via springs and dampers. The response of such a multibody system may be found by determining the differential equations governing its motion. Both continuum and discrete modelling approaches tend be descriptive and their complexity is dependant on the nature of the study. Discrete models attempt to reproduce the fact that the human body is a composite of a number of organs, each resonating at different frequencies. For example, the eyes and the abdomen resonate around 20 Hz and 5 Hz respectively[30][33]. The descriptive nature of these models can be seen in the example discrete model shown in Figure 2.7.

Lumped-parameter models attempt to capture body dynamics by developing an equivalent mass-spring-damper system, as shown in Figure 2.7. Although models of this type usually have

[2]The summation of neuromuscular and biomechanical contributions in Figure F.6 is an assumption made to simplify the modelling process. The complexity of human perception and decision making makes this relationship challenging to study.

only one or two degrees-of-freedom[34], they have been found quite useful in investigating response to vertical base excitation. However, their simplicity implies that the complete dynamics of a seated human cannot be captured. Work done by Sirouspour et al[35] has found using this approach to model the lateral dynamics especially challenging.

A key parameter in biodynamic modelling is known as whole-body transmissibility. This is the ratio of vibration at a point of interest to base vibration as a function of frequency. The transmissibility of vertical base vibrations to fore-and-aft motion of the upper body is also of particular interest here. Examples of experimental transmissibility data are presented in Chapter 5. A model aimed at the study of biodynamic feedthrough should fit the data reasonably well and capture the low frequency peaks. Accurate modelling of these features is crucial to any study investigating pilot-vehicle interaction for large aircraft.

In the late 1970s, AMRL at Wright-Patterson Air Force Base conducted a series of investigations to understand the effect of vibrational environments on pilot biodynamic response and tracking performance[36]. Unlike modelling and simulation based European work in this area, the American effort was heavily experimental and relied on human subjects placed on a large amplitude multi-degree of freedom hydraulic vibration table. Describing function data was then obtained for shoulder and elbow responses to rotational and translational vibrations in different axis. The vibration frequency range explored was 12 rad/s to 60 rad/s. It was found that vibrations causing front-back body motion, that is the motion in the longitudinal and pitching senses, produced the greatest amount of stick feedthrough. Vibrations in the vertical, roll and yaw senses had much smaller effects. The research also highlighted the roll of the inceptor dynamics in biodynamic feedthrough. Stiff sticks were found to be more affected by the vibrational environment when compared to spring sticks that provide limited proprioceptive feedback[36]. However, it should be noted that the experiments used centre sticks without elbow rests.

The AMRL research also highlighted that the upper end of manual control range cannot be ignored and aeroelastic modes at those frequencies may significantly affect aircraft handling qualities. Höhne and Koehler have highlighted the complexities in modelling the upper body as a multibody system whilst demonstrating techniques on how to model such systems. However, just like any proposed model, a biodynamic model requires validation to prove its accuracy. Guidelines and a detailed discussion concerning the validation of biodynamic models is provided by Griffin, who argues that a quality check may be conducted by considering the following features of a model: assertions, evidence, assumptions, accuracy and appropriateness.[37] Table 2.2 summarises Griffin's checklists relevant to this area.

Assertions:	Clear and adequate definition of input-output relationship.
Evidence:	Experimental data proving the input-output relationship.
Assumptions:	Definition of any assumptions made during model development. Definition of the conditions in which the model is applicable. Specification of the range of each dependent and independent variables. Accounting for inter-subject and intra-subject variability.
Accuracy:	Quantification of model output sensitivity to changes in model parameters. Specification of likely errors in model predictions.
Appropriateness:	Description of improvements over other models representing the same phenomena.

Table 2.2: Griffin's list of requirements for the validation of biodynamic models.

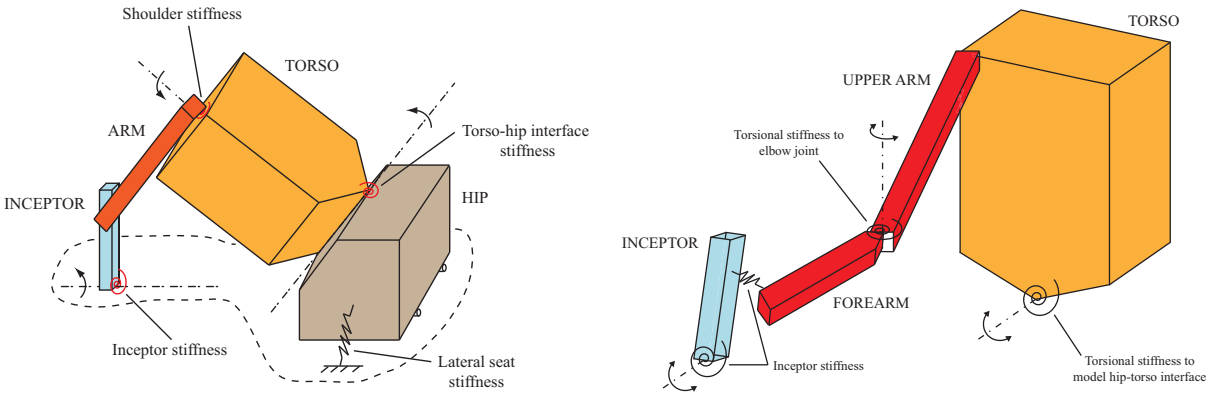

(a) Koehler's model.

(b) Höhne's improved model.

Figure 2.8: Discrete models used by Koehler and Höhne for investigating roll ratchet.

2.2.2 Biodynamics in handling qualities

Höhne[38] and Koehler[39] have investigated simplified biomechanical pilot models to study roll axis APC (also known as *roll ratcheting*) experienced during the General Dynamics F-16XL test program. Koehler's approach has the hip, torso and arm with single degrees of freedom and uses spring-damper connections to connect the multibody system together and to the aircraft. The arm-torso and hip-torso joints were rotatory joints because the studies were mainly concerned with roll axis dynamics. The model inputs were the pilot's intended control moment and accelerations at the pilot's position. Although the model was successful in reproducing the roll ratchet incident it had various shortcomings. The most significant were the unrealistic torso inclination angle and stiffness and damping coefficients for the joints.

To address the shortcomings, Höhne[40][41] re-derived the equations of motion and conducted parameter identification on the Koehler model. Figure 2.8(b) shows one of the four biomechanical models that were found equally capable of predicting roll ratcheting behaviour. Since analytical derivation of equations of motion for such a multibody system can be very lengthy, Höhne used a software package called SIMPACK® (SImulation of Multibody system PACKage) to obtain system response to various forcing functions. Use of SIMPACK® and a revised optimisation problem statement for parameter identification helped address the shortcomings of the Koehler model.

Roll ratchet was also investigated by European Aeronautic Defence and Space (EADS) company within the Eurofighter program where it was found to prohibit tracking in aggressive tasks[42]. Here, the pilot was also assumed to be a passive and linear contributor and a lumped parameter model was used to model the arm. This was found to be valid only for large accelerations and the study concluded that the damping contribution from the pilot's muscles was a function of acceleration. For small accelerations the pilot's muscles provide significant damping to overcome the consequent effects. It was also suggested that further research be done to obtain an understanding of this relationship. However, the conclusion from this study is only partly correct. Muscular damping and stiffness are both also functions of the task and its urgency: that is whether the pilot is relaxed or not. During urgent tracking tasks, the body stiffens and the grip around the inceptor tightens. The opposite is true for non-urgent compensatory tasks. More in-depth investigations done by Venrooij et al[43] have resulted in similar conclusions.

Recently, the modelling of biomechanics has been part of the research effort to suppress biodynamic feedthrough. Sirouspour et al[35] have developed robust control methods to avoid instabilities. However, a simple lumped parameter arm/joystick model was used for controller

synthesis and the moving base used for the experiments could not generate sustained accelerations or transient accelerations greater than +1.5g and -2g. Furthermore, only a single subject was tested with a force sensing joystick.[3] Gillespie et al[44][45] have also contributed to this field and published results for feedthrough due to lateral accelerations. In the proposed model-based cancellation schemes, parametric fitting of transfer function equivalent models to experimental data was found to be challenging due to difficulties in matching phase characteristics. Moreover, large inter-subject variations were found: around 15 dB and 50° in magnitude and phase at the peak resonant mode respectively.

In the light of such variations, a number of researchers have focused on accurate detection of biodynamic feedthrough using advanced signal processing methods. For example, work done at STI Inc. implements real-time wavelet-based PVS identification to identify roll ratcheting[46][47]. Earlier work done by Serafini et al[27] in Italy and Raney et al[48][26] at the National Aeronautics and Space Agency (NASA) rely on the identification of equivalent transfer functions for biodynamic modelling. These models were then used to develop mitigation schemes employing a mixture of passive and notch filters. In fact, the motivation behind work done at NASA is very relevant to this research; that is the biodynamic incidents experienced during the development of the high speed transport aircraft. These were observed during motion-based flight simulation trials in which pilots were asked to land from an offset starting point. Accelerations due to rigid body and aeroelastic modes were calculated via a model developed using Waszak's[49] approach. Biodynamic resonance occurred for two subjects following a gust encounter, which in turn excited low frequency fuselage bending modes. As the accelerations increased in magnitude, pilots tightened their grip on the side-stick and throttles to simply brace themselves, further amplifying the biodynamic coupling effect. This effect can be seen clearly in time histories shown in Figure 2.9, reproduced here for convenience. Compensations on the attitude indicators and limited structural stiffening were found to have little impact when compared to side-stick modifications. However, the observed behaviour highlights the applicability of biodynamic models to investigate involuntary coupling due to pilot physiology.

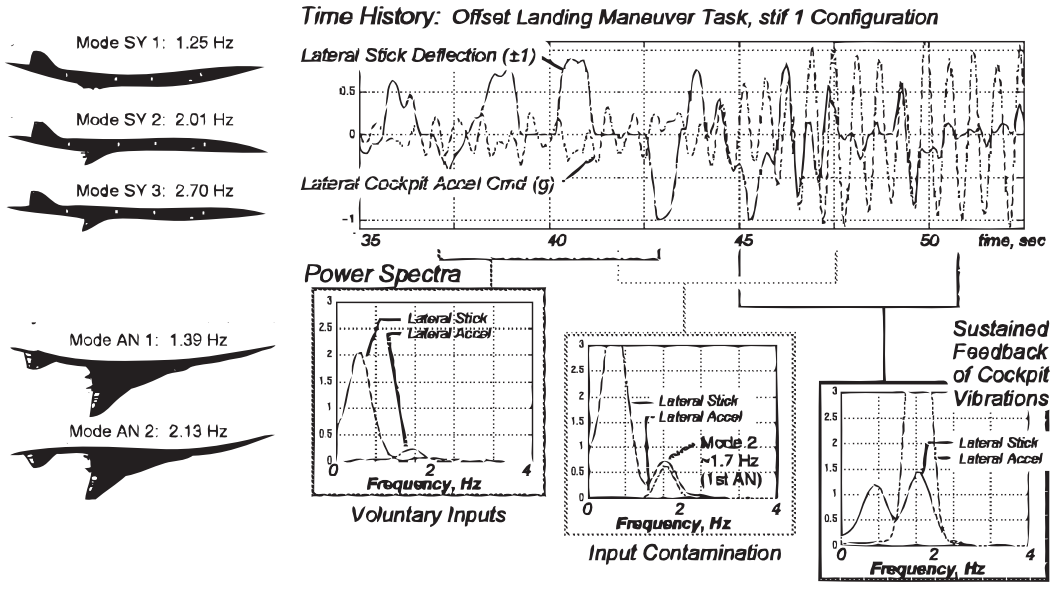

Figure 2.9: Airframe structural modes and time histories of biodynamic coupling incident (reproduced from Raney et al[48]).

The main drawback within the existing guidelines such as the British Standards[50][51] and current research in biomechanics is the assumption of linearity. However, work done by Mansfield

[3]This data has not been used in this work because all Airbus aircraft have simple passive side-sticks.

and Griffin[52] is beginning to shed light on the nonlinear response of the human body; albeit from a medical perspective. Future work in aerospace engineering can and should take advantage of advancements made in the development of virtual humans (also called avatars) used for military training simulations[53]. Such work has started to consider the nonlinear relationships in whole body transmissibility.

2.2.3 Neuromuscular system

Since the 1950s, handling qualities and flight control systems engineers have appreciated that the basic dynamics and precision of manual control are critically limited by the properties of the neuromuscular system[54][55]. Yet in most research, the neuromuscular dynamics are represented by second order transfer functions, quite similar to the treatment of aircraft control surface actuators.

The structure of the neuromuscular system is based upon the physiological operation of the human muscle. It consists of two types of muscles: extrafusal and intrafusal. Extrafusal muscles are responsible for the generation of force and make up most of the muscle. Intrafusal muscles on the other hand are scattered throughout the muscle in the form of spindles and provide the central nervous system with a degree of feedback information. They are able to detect what in physiological terms are known as 'phasic' stretch and 'tonic' length. The term phasic refers to the feedback of stimulus rate of change whilst the term tonic refers to feedback directly proportional to the stimulus. Muscle spindles are not the only source of information feedback. A significant role is also played by golgi tendons organs that are analogous to muscle spindles and detect changes in tendon tension and the forces applied by a muscle[56].

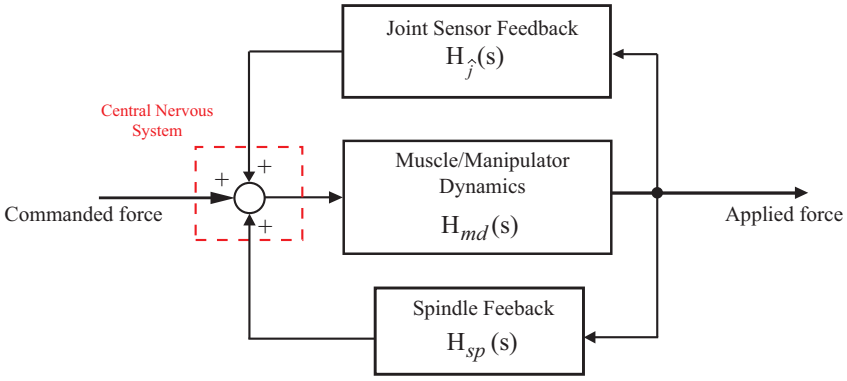

Figure 2.10: Neuromuscular model proposed by McRuer and Magdaleno.

The details of the human actuation system even for the simplest of motions are enormously complicated if individual components are considered. However, the actions of the overall system can be modelled by considering ensembles. The foundations for neuromuscular modelling in the context of pilot models was laid by McRuer and Magdaleno using this approach[57]. The form of the individual blocks in the system shown in Figure 2.10 were developed to fit data obtained from experiments involving a number of human subjects and their use of rudder pedals and hand manipulators in tracking tasks. The following transfer function was found to fit data obtained from experiments designed to isolate extrafusal muscle dynamics:

$$H_{md}(s) = \frac{-K_{md}e^{-\tau_a s}}{(1+T_N s)(1+2\zeta_a/\omega_a s + s^2/\omega_a^2)} \tag{2.2.1}$$

The spindle feedback block could be modelled using the following transfer function, which is

effectively a delayed equalisation ability.

$$H_{sp}(s) = \frac{K_{sp}(s + Z_{sp})e^{-\tau_{sp}s}}{s + P_{sp}} \tag{2.2.2}$$

The joint sensor feedback block is the ensemble that represents the golgi tendon organ feedback as well as various other modes of feedback that are difficult to isolate. It has been modelled by a simple gain and delay:

$$H_{\hat{j}}(s) = K_{\hat{j}}e^{-\tau_{\hat{j}}s} \tag{2.2.3}$$

The experiments were done using both fixed force sensing and free moving deflections sensing sticks. Data fitting procedures then determined the values of the parameters in these equations.[4] An interesting result was the differences obtained for the central processing delay: 66 ms and 82 ms for the force and deflection sensing inceptors respectively. However, McRuer and Magdaleno's study[57] only involved two subjects; making it impossible to comment on the statistical significance of the results.

Due to the simplifications, the model has lost a certain degree of realism and is incapable of replicating some important neuromuscular capabilities such as adaptability. Another loss of fidelity comes from the assumption of direct connection of muscle spindles to the central nervous system. In reality the information gathered via the spindles go through a series of motor neurons before reaching the central nervous system. Whereas, the information gathered through the golgi tendon organs arrive directly at the spinal chord through the spinal interneurons. Considering the relatively small magnitude of forces involved in the use of sidestick in FBW aircraft, modelling the ability of golgi tendon organs to provide overload protection (via the relaxation of muscles experiencing dangerous levels of tension) is also unnecessary. Furthermore, considering the scope of this work such an approach which employs simple transfer functions is adequate.[5]

2.3 Control-theoretic pilot models

The underlying principle in manual control theory was proposed by McRuer during the 1970s as the fundamental assumption of the crossover model. It stated that the human operator adjusted control action such that the PVS open loop dynamics may be described by the following transfer function:[59]

$$Y_P(s)Y_C(s) = \frac{\omega_c e^{-\tau_e s}}{s} \tag{2.3.1}$$

where Y_P, Y_C, ω_c and τ_e represent the pilot transfer function, vehicle transfer function, crossover frequency and effective time delay respectively. Equation 2.3.1 is known the *crossover law* and effectively states that the PVS behaves as an integrator around the crossover region. The crossover frequency differentiates between the regions where the open loop input to output amplitude ratio exceeds unity and the regions where it is below unity. It is also dependant on the characteristics of the controlled plant. The effective time delay is the time taken by the human body to perceive and initiate action.

Once the pilot model is placed within a closed loop system, the pilot perceived vehicle output effectively determines whether the model acts in a compensatory or pursuit mode. In compensatory mode the pilot has been found to follow error perception, whilst in a pursuit mode

[4] The state-of-the-art[31][58] relies heavily on nonlinear optimisation functions available in MATLAB for parameter identification.

[5] The fact that biodynamic feedthrough is again dependent on the task type and neuromuscular admittance must be kept in mind[43].

perception of a selected output state is dominant. The comparative study of both modes in the field of display design has found pilot performance to be superior in pursuit mode where a target is being tracked.[22]

The main challenge in pilot modelling is determining the pilot model parameter values that are all effectively task dependant. To date certain manoeuvres thought to give the greatest insight into handling qualities (e.g. pitch tracking) have been investigated with pilot models. Such investigations may be split into three stages. The first stage is the development of a pilot model structure, which is followed by the simulation of human subjects in simulators. Then pilot model parameters are estimated using the simulation data and system identification techniques. Only after this can handling qualities analysis be conducted. Investigation of different tasks requires some repetition of these stages making the whole process very time consuming and expensive.

2.3.1 Quasi-linear models

Tustin first suggested the use of servomechanism theory for the analysis of manual control in 1944[60]. He suggested the following transfer function representation for the human operator:

$$Y_P(s) = K_p e^{-\tau s}(1 + Bs) \tag{2.3.2}$$

where the operator parameters K_p, τ and B represent pilot gain, effective time delay and equalisation respectively. The term equalisation refers to the human controller's ability to adjust in order to provide good closed loop behaviour. This is characterised by the ability to[61]:

1. provide some desired relationship between the command signal and plant output.
2. provide adequate closed loop stability margins.
3. provide good disturbance rejection and suppress other unwanted inputs.
4. reduce the effects of variations and uncertainties in plant characteristics.

McRuer later developed the crossover model that led to the development of various other quasi-linear models with similar structure to that shown in Figure 2.11. The pilot describing function is intended to represent linear behaviour whilst the remnant signal, usually a filtered Gaussian white noise input, accounts for any nonlinear behaviour. The key assumption is that near the crossover frequency the pilot's linear behaviour dominates and so classical control techniques remain valid. The caveat therefore, is that the model is only accurate near the crossover frequency.

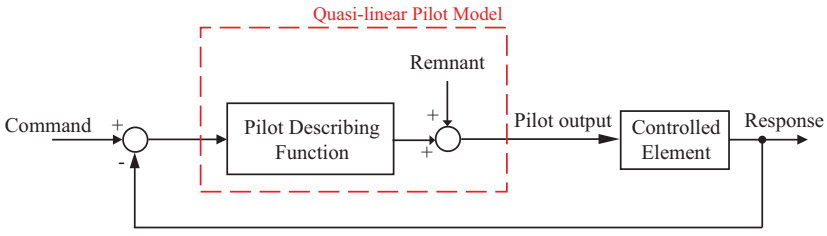

Figure 2.11: Quasi-linear pilot model.

The appeal of such models is their simplicity and the ease with which they can be applied using classical control techniques. They have been found to be most useful for the analysis of closed

loop compensatory behaviour. Equation 2.3.3 represents the quasi-linear model proposed by McRuer[22]. The pilot's gain is dependant on the task, environment and the pilot's adaptive ability. Pilot equalisation characteristics are represented by τ_L and τ_I. Pilot's physical reaction time and neuromuscular delay are represented by τ and τ_n respectively.

$$Y_P(s) = K_p \frac{\tau_L s + 1}{\tau_I s + 1} \frac{e^{-\tau s}}{\tau_n s + 1} + \text{Remnant function} \tag{2.3.3}$$

The equalisation parameters are chosen such that the open loop system behaves as an integrator around the crossover frequency (i.e. a -20 dB slope around ω_c), enforcing the crossover law. The gain is then tuned such that the closed loop characteristics approximate those of a good feedback control system, which itself is defined by engineering judgement.

At this point it is only natural to discuss the pilot model explicit in the Neal-Smith handling qualities criteria[62]. Expressed as the following transfer function:

$$Y_P(s) = K_p \frac{\tau_L s + 1}{\tau_I s + 1} e^{-\tau s} \tag{2.3.4}$$

it only lacks the remnant and neuromuscular components. It takes a simple form, but the criteria quantifies the aforementioned qualitative description of equalisation through ensuring the parameters are selected such that the following performance requirements on open-loop PVS are satisfied:

- Minimum bandwidth of 3.5 rad/s at a phase difference of 90°.
- Maximum low frequency droop of -3 dB.
- Minimum closed loop resonant peak.

A detailed discussion of the model used in the original frequency domain Neal-Smith criterion[63] and revised time domain Neal-Smith criterion[64][65] is not included here. This is because the defacto contributions of Neal and Smith have been the compilation of a handling qualities database and the successful linking of pilot compensation to handling qualities levels; not pilot model development.

The determination of the remnant function is a complicated procedure as it attempts to represent the nonlinear component of pilot behaviour. It's primary source is the pilot's ability to learn and adapt which is the source of nonlinear and non-steady behaviour. The secondary contribution comes from such things as the experimental setup and experimentally injected noise that affect pilot response to other inputs. However, careful selection of the pilot model and task can help minimise remnant effects[22].

Although the form of such a model is based upon experimental results, the main disadvantage is that they are incapable of parameter variation with respect to changes in task. The model has no ability to initiate an APC event and so for their analysis sinusoidal forcing functions of varying frequencies are used to drive the system towards instability. The phase difference between the inputs and outputs are then used to predict any APC behaviour. These models also tend to be restricted to single-input-single-output analysis. Although multiple-input-multiple-output modelling can be accomplished, it is not practiced due to the increased complexity in specifying loop closures. Due to such disadvantages, quasi-linear models although first proposed for predictive purposes, nowadays are primarily used for matching and validating experimental data. Over the years, this concept has been adapted by researchers, such as Cardullo[66] and Heffley[67], for a number of tasks where the pilot model is only piecewise linear.

2.3.2 Hosman's descriptive model

In Europe, the development of FBW aircraft motivated a renewed research effort in man-machine-interaction[68][69]. Within the United Kingdom researchers like Gibson[70] and Padfield[71] studied pilot modelling as a means towards understanding flying and handling qualities; as opposed to specifically aiming at modelling manual control action. Although researchers around the world acknowledged the complexities involved in modelling these actions, the research and engineering communities primary focus was the linear approach discussed previously. This was not only due to the ease associated with their application and interpretation, but also because these models were capable of capturing most of the observed behaviour. Therefore, it is no surprise that the state-of-the-art in pilot model identification, which is effectively represented by work done at TU Delft[72][73][74][75] and motivated by improving flight simulator cue fidelity, is based on linear (or piecewise linear) models.

The descriptive model is one such model which was the result of Hosman's research during the 1990s aimed at understanding the influence of visual and vestibular stimulation on pilot's perception and control behaviour[76]. The results have mainly been used to improve motion-based simulator realism via the optimisation of motion control algorithms. Various stimulus-response experiments were used to distinguish the contributions of individual senses towards pilot perception from the actual pilot response. The results were then applied to closed-loop control tasks assuming the human being to be a finite capacity single-channel information processor with multiple sensory inputs. This level of sensory distinction allowed for a descriptive model to be developed as shown in Figure 2.12.

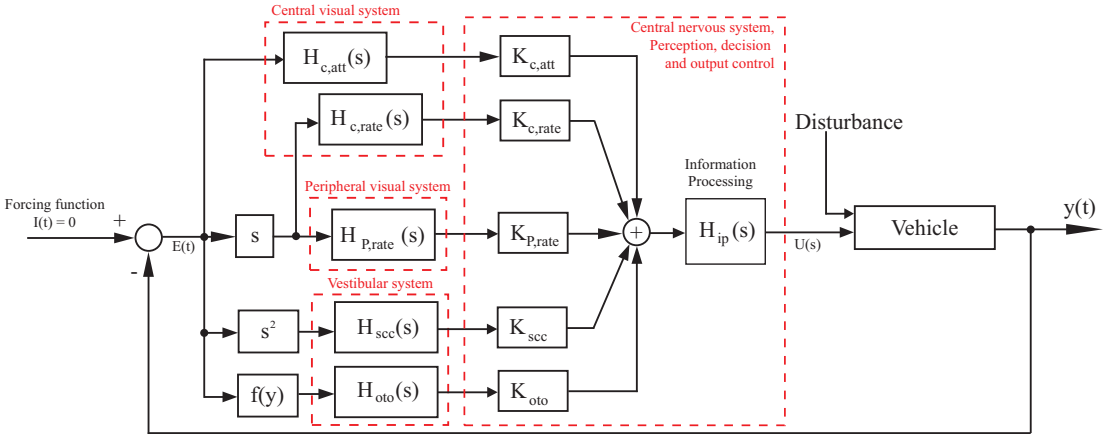

Figure 2.12: Descriptive model of the human pilot as proposed by Hosman.

Hosman relied on earlier work done on the modelling of human vision and vestibular systems to obtain transfer functions relating the error signal E(s) to the outputs of sensory systems. Therefore, the overall model was based on physiological sub-models that related aicraft states to perceived states. The visual perception of displacement was modelled by the following time delay:

$$H_{att}(s) = e^{-\tau s} \tag{2.3.5}$$

Delay associated with attitude perception is given by τ, which was found to be around 50ms. Visual perception of velocity was modelled similarly:

$$H_{rate}(s) = e^{-(\tau+\tau_1)s} \tag{2.3.6}$$

Here, the total time delay is the sum of that associated with the detection of stimulus by the eyes (τ) and that associated with information processing during perception (τ_1). This is effectively

the same time delay referred to by McRuer in the crossover model. However, an important part of Hosman's research was the distinction between contributions from central and peripheral visual perception. Hosman postulates that the peripheral sensory system is only able to sense rates and uses the same perception model of Equation 2.3.6, but with a different value of τ_1.[76] Experiments designed to relate peripheral perception and roll rate found τ_1 for peripheral visual field to be shorter ($\simeq$ 60 ms) than that for the central visual field ($\simeq$ 110 ms).

Hosman's work also confirmed that the otolith can be modelled as an accelerometer with over-damped mass-spring-damper characteristics. This may be described by a second order differential equation, represented by the following transfer function:

$$H_{oto}(s) = \frac{1 + \tau_n s}{(1 + \tau_a s)(1 + \tau_b)s} \tag{2.3.7}$$

In Figure 2.12, the function $f(y)$ preceding $H_{oto}(s)$ converts displacement input to a specific force output. For example, for bank angle, ϕ:

$$f(\phi) = \ddot{\phi} l - g\sin(\phi) \tag{2.3.8}$$

where l is the distance of the pilot's head from the rotational axis and g is gravitational acceleration.

Similar to the otolith, the semi-circular canals may be modelled as an over-damped torsion pendulum, represented by the following second order transfer function:

$$H_{scc}(s) = \frac{1 + \tau_L s}{(1 + \tau_c s)(1 + \tau_d)s} \tag{2.3.9}$$

Since Hosman's model is based on human physiology the transfer function parameters in Equations 2.3.5, 2.3.6, 2.3.7 and 2.3.9 are independent of the simulation scenario. Only the gains in the central nervous system model are scenario dependent. Hosman used the following gain delay model for information processing:

$$H_{ip}(s) = K_{ip} e^{-\tau_{ip} s} \tag{2.3.10}$$

The tactile and proprioceptive senses were assumed to be implicitly modelled within the vestibular system.

2.3.3 Optimal control models

Pilot modelling in the context of modern control was accomplished in the 1970s by Weirenga[77] and Kleinman et al[16] who developed the optimal control (pilot) model (OCM). This model assumes that a well trained and motivated human operator, behaves in an optimal manner whilst remaining subject to inherent psycho-physical limitations. These limitations are modelled as a time delay, motor noise and observation noise. Figure 2.13 presents the conceptual block diagram of the OCM.

The Kalman filter models the ability of deducing system states from perceived information and the predictor represents the pilot's compensation for his/her inherent time delay. This filter, linear predictor and the optimal gain require a model of the aircraft being controlled and so effectively represent the pilot's internal model of the aircraft dynamics. This should contain a description of aircraft behaviour expected by the pilot. Therefore, it would capture the control augmented aircraft dynamics linearised for a certain trim point and represent the pilot's psychological limitations[78]. The order of this model is a function of pilot training and

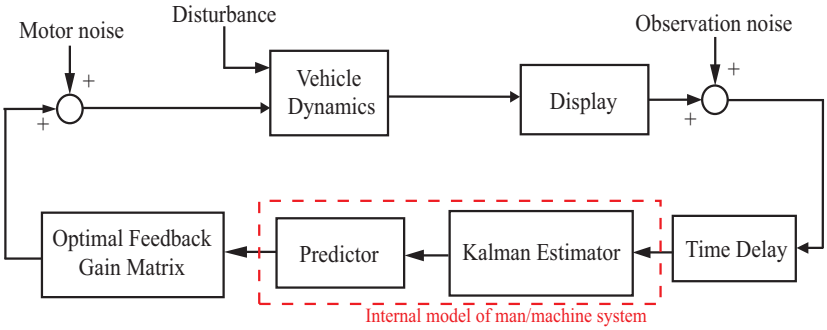

Figure 2.13: The optimal control pilot model performing a compensatory task.

experience and may include limited models of the actuation systems. This model is presented usually as a state-space system in practice, but the internal structure of this model can never be validated against the model contained within a pilot's mind. Validation may only be achieved with a black box approach where the model outputs are compared to that of real human control outputs. This problem is inherent to any attempt at modelling human control behaviour. The OCM approach therefore allows an explicit definition of pilot's internal model. This may lead to a clearer understanding of pilot perceived aircraft state mismatch due to system dynamics such as aeroelasticity.

Assuming a linear state-space representation of the internal model, the pilot's task may be defined through the appropriate choice of a cost function. The optimal pilot gains are found by solving the linear-quadratic-Gaussian (LQG) problem for the following quadratic cost function:

$$\mathcal{J}(\mathbf{u}) = E\left\{ \lim_{\eta\to\infty} \frac{1}{\eta} \int_0^{\eta} (\mathbf{y}^T\mathbf{Q}\mathbf{y} + \mathbf{u}^T\mathbf{R}\mathbf{u} + \dot{\mathbf{u}}^T\mathbf{S}\dot{\mathbf{u}})dt \right\} \tag{2.3.11}$$

where $\mathbf{Q}$ and $\mathbf{R}$ are the weightings on the outputs of the internal model and the pilot's control action respectively. The matrix $\mathbf{S}$, is a weighting on the pilot's control rate and represents a limitation on the pilot's bandwidth due to the neuromuscular system as well as the natural tendency against abrupt control actions. It cannot be over-stressed that the validity of the OCM is dependant on the accurate specification of the cost function and its weightings because these quantify the pilot's control objectives. Their selection represent the drawback of the OCM as it requires engineering judgement, experience and an iterative process. Otherwise, the algorithm certainly provides a stabilising and a robust controller representation; both qualities being characteristic of human beings in manual control.

The remnant component within the quasi-linear model is represented here by observation and motor noise. These are filtered Gaussian white noise which, in the case of observation noise may be tuned to represent levels of instrument observation accuracy and the distribution of attention levels towards different flight instruments. It has also been shown that this approach is capable of tracking more complex systems involving visual scanning between instruments and attention-sharing by assuming that observation signal to noise ratio varies directly with pilot attention towards a particular instrument[79]. The model is then completed by introducing components representing the remaining human physical limitations. These are the central processing time delay and neuromuscular dynamics. The latter requires explicit inclusion if the control rate component is ignored in the cost function of Equation 2.3.11.

The accuracy in matching experimental data using the OCM has not been significantly superior in relation to the classical control models, indicating a degree of over-parameterisation.[80] This has lead to a number of comparative studies with classical models and also various attempts to simplify the OCM algorithm. The Modified OCM (MOCM)[81] and the fixed order OCM[82]

are some results from such efforts. Both produce transfer function representations that retain the most important features for frequency domain analysis and comparison. Such studies have acted as bridges between the classical frequency domain and modern time domain approaches to the same problem. However, the complications in the simplification process far outweigh the advantages and the degree of simplification makes such models unsuitable for modern simulation purposes. Work done by Schmidt in the area of pilot-in-the-loop analysis with aeroelastic aircraft models has found the full order OCM most appropriate for capturing the full effects of aeroelasticity[83]. Over the years, OCM implementation has changed very little. The problem of over-parameterisation has been slowly addressed along with improvements to match experimental data.[84]

The OCM has mainly been applied in the analysis of time delay affects on aircraft handling qualities, such as the identification of APC prone configurations.[83] Another area of research has been the investigation of display dynamics on the overall manual control loop and in doing so obtaining relationship between display types[79] and pilot ratings.[85] The third area where the OCM has been heavily used is in the investigation of attention sharing, task interference and pilot workload. Kleinman and Baron have focused on techniques to incorporate pilot sampling behaviour based on information-theoretic ideas with the OCM.[86] This approach assumed that the pilot periodically sampled, either via the natural senses or cockpit instruments, a particular aircraft state and attempted to reconstruct it in the time-domain. Another area that has received considerable focus is the attempt to relate Cooper-Harper pilot opinion rating to the OCM cost function in single and multi-axis tasks.[87][88] Thompson and McRuer showed that the OCM cost function could be used to predict pilot opinion ratings reasonably well. The relationship was based upon the realisation that the control rate component of the cost function represents the physical and mental workload of the pilot.[80]

The $\mathcal{H}_2$ based OCM and its variants have been widely used for various purposes. On the other hand, $\mathcal{H}_\infty$ based pilot models such as that proposed by Goto et al[89] have not been so popular. Goto et al concentrate on the pilot compensation required when controlling vehicles that are statically or dynamically unstable. Comparison with experimental pilot describing functions show good agreement at high frequencies but there remains relatively significant overestimation of pilot gain at frequencies below 20 rad/s.[89] However, because such a pilot model is aimed towards the handling qualities analysis of combat aircraft with potentially unstable modes there is little reason to apply these models to large civil aircraft; especially when evaluating the flight loads experienced during typical mission profiles.

2.3.4 Nonlinear models

Around the same period in which McRuer was investigating the relationship between pilot dynamics and handling qualities, many researchers focusing specifically on manual control understood that when presented with difficult tasks human operators demonstrat highly nonlinear control behaviour. A feature of this was the bimodal amplitude distribution of inceptor deflections observed in response to tasks characterised by Gaussian forcing functions, as shown in Figure 2.14. Examples of such early research are Costello[90], who suggested the 'surge' model in 1968, and Hess[91], who published a model-based explanation of pulsive behaviour a decade later.

Hess' investigation was motivated by observations that (a) often human operators adopt control strategies resulting in discrete or pulsive inceptor motion and, (b) this behaviour was not an inherent feature of classical linear models. The study assumed that an operator, when faced with a situation where high order vehicle dynamics are combined with a demanding task, reverts to a low order controller. That is, he/she avoids the computational effort necessary for complex

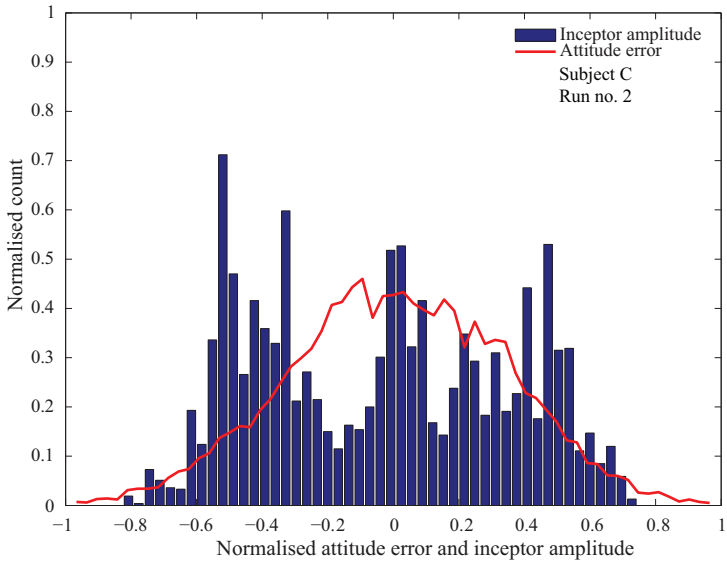

Figure 2.14: Example bimodal inceptor and error amplitude distributions.

inputs and adopts a simple nonlinear strategy relying on very few parameters. Hess further extrapolated from this assumption that pulsive control is a result of an attempt "to reduce the computational burden associated with time integration of sensory inputs"[91]. Consequently candidate models must either be based on simple nonlinear control theory (such as minimum-time optimal control also known as bang-bang control) or require only the addition of basic nonlinear elements to the classical linear model structures.

Hess then applied the above assumption to an early version of his model that was linear but maintained its emphasis on proprioceptive feedback of inceptor deflection.[91] The result was the addition of the following logic just before the operator's compensation is executed by the neuromuscular system:

$$\begin{aligned} \frac{du'}{dt} &= 0 \qquad \text{for} \qquad |\frac{du}{dt}| < \acute{v} \\ u' &= \bar{v}u \qquad \text{for} \qquad |\frac{du}{dt}| \geq \acute{v} \end{aligned} \tag{2.3.12}$$

where u and u' are the input and output variables respectively. $\acute{v}$ and $\bar{v}$ are the only parameters required to successfully reproduce pulsive behaviour. Reliance on just these two parameters clearly avoids model over-parameterisation; in turn simplifying the tuning process when attempting to match experimental data. Yet it should be noted that these parameters require tuning and are not obtained analytically. The qualitative agreement with experimental data demonstrated by Hess[91] successfully linked the assumptions associated with the model to the explanations given for pulsive behaviour in the frequency domain context established by McRuer.[6] This nonlinear element can be seen as the origin of the various switches currently found in Hess' latest model, called the structural model. It attempts to describe pilot behaviour whilst keeping with the crossover law philosophy and at the same time borrowing some ideas from the OCM, see Figure 2.15.

In the mid-1970s Smith suggested that from the standpoint of perceived aircraft handling qualities, the pilot's control of vehicle rate (for example pitch rate) in a closed loop system was of fundamental importance[92]. Smith based this theory on the belief that physiologically, a

[6]In linear frequency domain, pulsive action is attributed to the necessity for low frequency lead generation on behalf of the operator.

measure of pilot opinion rating is the rate at which nerve impulses arrive at a point within the central nervous system, where they are processed. Hess later interpreted Smith's theory within the structural model by including proprioceptive feedback and showed that this feedback signal was proportional to the plant's rate output due to the pilot's control input[24]. The dependency on pilot control input also allowed a relationship with the Cooper-Harper handling quality ratings to be developed.

With regards to APC, the model assumes that after a triggering event, the pilot regresses to a tracking behaviour where error rate is controlled with no proprioceptive feedback. Therefore, switches S1 and S2 of the model shown in Figure 2.15 are assumed to operate in unison. To simulate normal flight and flight during an APC, the model represents both the error and error rate tracking ability of the pilot. Again it should be noted that this model is incapable of generating a triggering event on its own.

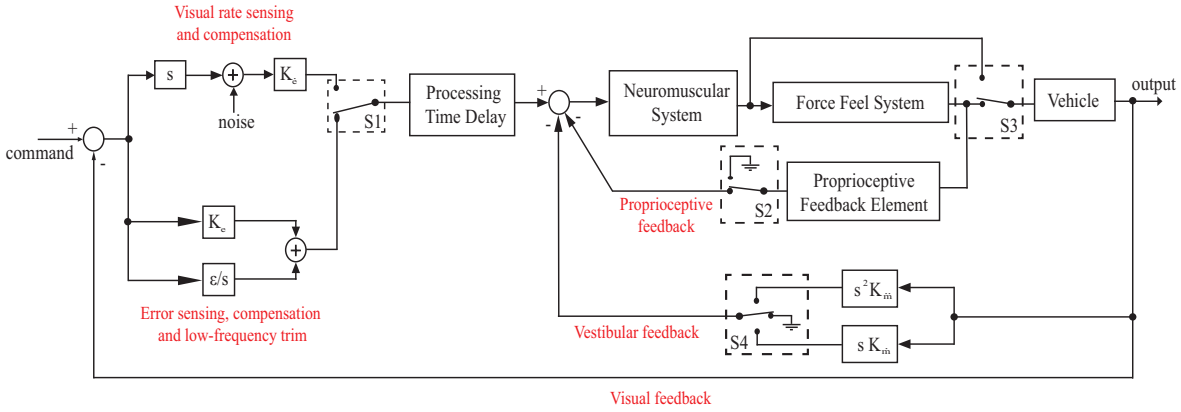

Figure 2.15: Compensatory structural model of the human pilot as proposed by Hess.

Switch S3 allows either displacement sensing or force sensing inceptors to be modelled, whilst switch S4 allows either rate or acceleration cues to be used for control.

Since only the neuromuscular and proprioceptive models need parameterisation the model remains quite simple. Hess used a second order representation of the neuromuscular block in his studies and the following representation of the proprioceptive sensory model (Y_{pf})[93]:

$$Y_{pf}(s) = \begin{cases} K_{pf}(s+a) \\ K_{pf} \\ K_{pf}/(s+a) \end{cases} \quad \text{selected such that } Y_{pf}(s) \propto sY_C(s). \tag{2.3.13}$$

The equalisation in Equation 2.3.13 represents the pilot's adaptability to changes in aircraft dynamics around the crossover frequency.[93][94] It may be interpreted as the pilot's internal representation of vehicle dynamics which in the optimal control pilot model is represented by the Kalman estimator.

The main differences from other models discussed in this report is the hypothesis that proprioceptive cues and the internal model allow the pilot to create compensatory characteristics that are appropriate for the controlled vehicle dynamics. This is quite the opposite to models that assume pilot operation based on visually sensed feedback. Hess further postulates that during an APC, the power in the proprioceptive feedback signal is the determining factor in the perception of aircraft handling qualities, but only when the crossover law is satisfied.

Overall, the approach adopted by Hess uses engineering judgement to propose a model structure that requires parameter tuning to match observed behaviour. Consequently, it lacks the

mathematical basis for parameter selection and the ease with which pilot models based on modern control deal with multi-axis tasks. However, this approach (in experienced hands) has introduced the simplicity necessary for rapid analysis of the PVS.[7]

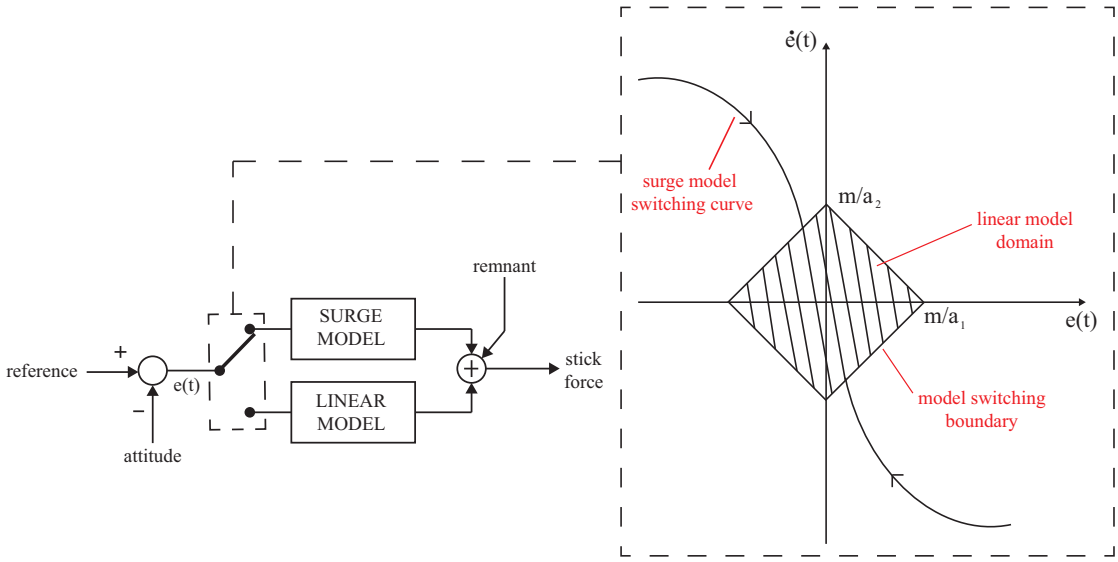

Figure 2.16: Costello's dual mode pilot model with switching logic in the phase plane.

Costello's 'surge' model was one of the early attempts at modelling the multi-modal behaviour exhibited when following discontinuous tasks. The model structure along with the switching boundary is presented in Figure 2.16. The nonlinear component's reliance on three parameters (a_1, a_2 and m) lends it some similarity to Hess' model. It is a more natural adaptation of the classical approach as it retains the quasi-linear model as one of the two modes of operation. The switching boundary is defined such that the model outputs the following:

$$u = \begin{cases} M_c & \text{if} \quad 0 \leq a_1|e(t)| + a_2|\dot{e}(t)| \leq m, \\ M_n & \text{if} \quad a_1|e(t)| + a_2|\dot{e}(t)| > m. \end{cases} \tag{2.3.14}$$

where M_c and M_n are the outputs of the linear and nonlinear models respectively. The nonlinear response is effectively the same as that of a minimum-time optimal controller. Unfortunately, the concept loses its simplicity when it comes to calculating the switching time; that is the time when the output switches from a maximum to minimum inceptor deflection or vice versa. The benefit of dealing with this complexity is the removal of unrealistic transient oscillations where stick forces are generated using linear pilot models.

Although Costello's study involved twelve subjects, the experiments were conducted in laboratory conditions, which meant that certain behaviour exhibited during flight were not observed. Work done much later by Andrisani et al[95] which analysed flight test data confirmed a number of Costello's observations but added that pilots were found to prefer particular stick amplitudes when inputting pulsive commands. Furthermore, rapid stick movements were observed before the vehicle even had a chance to respond. Andrisani's model did not aim to reproduce the observed stick movements and the model's nonlinear behaviour was only due to the quantisation of the pilot's command. It is not clear how the fixed quantisation step size was selected but variation in other pilot model parameters during pilot-model-in-the-loop simulation were found to provide insight into reasons behind the qualitative feedback from the pilots.

Andrisani's efforts, along with Hess, Innocenti et al[96][97][98] and Anderson et al[99][100], are

[7] At the time of writing, the handling qualities community is expecting a white paper to be published detailing the background and application of this the Hess model.

the only significant examples utilising nonlinear elements or control theory to model manual control dynamics.

The recent paradigm shift in nonlinear operator modelling research can be attributed to the advent of soft computing techniques, like genetic algorithms and neural networks. These take advantage of the computing power available today. Hosman's and Hess' work were brought together by Cardullo who implemented Hosman's vestibular model and a haptic sensory model within Hess' structural model and proposed a time based parameter varying model. Neural networks were used to drive the structural model parameters towards agreement with the crossover model[66]. It was also proposed that the technique may be implemented in real time for purposes such as flight safety and pilot workload assessment.

2.4 Conclusions

This chapter has presented a brief review of the aspects thought to be necessary when modelling manual control dynamics in the context of large civil aircraft. Literature covering sensory, biodynamic and control-theoretic modelling were studied. Considering the aims of this research, the following key points can be made:

- A simple time delay model of the visual system is satisfactory as long as variables representative of perceived visual cues are selected. Therefore, the focus should be accurately modelling the cues.
- Most SD cases occur due to a mismatch between sensory modalities. A satisfactory model must be able to capture at least Level I and II SDs resulting from conflicts between visual and vestibular perception.
- It can be assumed that pilot action is not a function of rate of change of acceleration, also known as jerk, but it can be a trigger to initiate closed-loop manual control.
- Although more challenging than lumped parameter models, a representative discrete model will allow insight into potential sources of biodynamic feedthrough. The main challenge in this area is the limited amount of suitable experimental data available for tuning the model parameters.
- Control-theoretic models are specific to individual experiments and rely on tuning for parameterisation. Only OCM based models minimise the necessary engineering experience required for application to multi-axis tasks and provide the capability to model attention sharing and predict handling quality ratings. However, its successful application relies on careful definition of the cost function.

This review has not covered aspects associated with decision making, such as human error modelling and information processing. The development and application of pilot models to quantify handling qualities is beyond the scope of this review and therefore, not discussed in detail. Furthermore, pilot models based on soft computing methods were not considered due to their reliance on large quantities of data which was unavailable to the author. As flight incidents tend to be rare and quite unique, the required training data for neural networked based models can only be obtained through extensive simulation trials. Finally, the processes associated with manual control experiments and parameter identifications are not discussed here because of literature available in the public domain. The reader is referred to the review by Grant et al[3], work done by Zaal et al[75] and Chapter 3 for more details.

CHAPTER 3

Nonlinear system elements and manual control

Short haul aircraft make up most of the air traffic today and the increasing demand for air transport will most likely maintain this proportion. These aircraft tend to be crewed by a relatively young pilot population who have far less experience than those flying long haul wide-body types. The sheer number of such aircraft has also meant that they encounter upset incidents more frequently[101]. At the same time, the majority of studies done in the fields of flight simulation and aircraft handling qualities have used highly trained and skilled pilots. In fact, media for pilot feedback, such as the Cooper-Harper and PIO rating scales, require well trained test pilots. Therefore, there is a need to develop an understanding of control techniques employed by young and relatively inexperienced pilots.

This study aims to investigate the control characteristics demonstrated by these pilots when faced with the activation of nonlinear FCS components such as command gearing and actuator rate-limiting. Command gearing is the most common form of nonlinearity found on modern aircraft, often used to (immediately) shape pilot commands, whilst actuator saturation and rate-limiting are inherent in all actuation systems. The reader should refer to Fielding[102] for a detailed discussion on nonlinear flight control system components. Although methods using describing functions exist for the analysis and design of control systems with such nonlinear components, changes in pilot dynamics due to these components are still not very well understood.

This chapter describes work done in two areas:

1. The setup and results of a series of manual control experiments designed to study the effects of command gearing and actuator rate limiting.
2. The modelling and parameter identification approaches used to capture pilot manual control dynamics.

3.1 Experimental design

3.1.1 Aircraft model and hardware

The experiment used to study tracking and compensatory tasks is shown in Figure 3.1. A linear-time-invariant (LTI) model representative of a large transport aircraft (discussed in Chapter

6 and 7) during climb/approach (Mach 0.68, 28500ft) was used[103]. A C* based CSAS was designed to present the subjects with representative dynamics. The FCS gains were selected via tuning such that the aircraft response lay well within the Category 1 C* boundary. Pitch attitude step and frequency responses with and without the CSAS are shown in Figure 3.2. This aircraft model was coupled with the pilot models described later in this chapter for a handling qualities analysis that included uncertainties arising from inter-subject differences. The results from this study are presented and discussed in Appendix B.

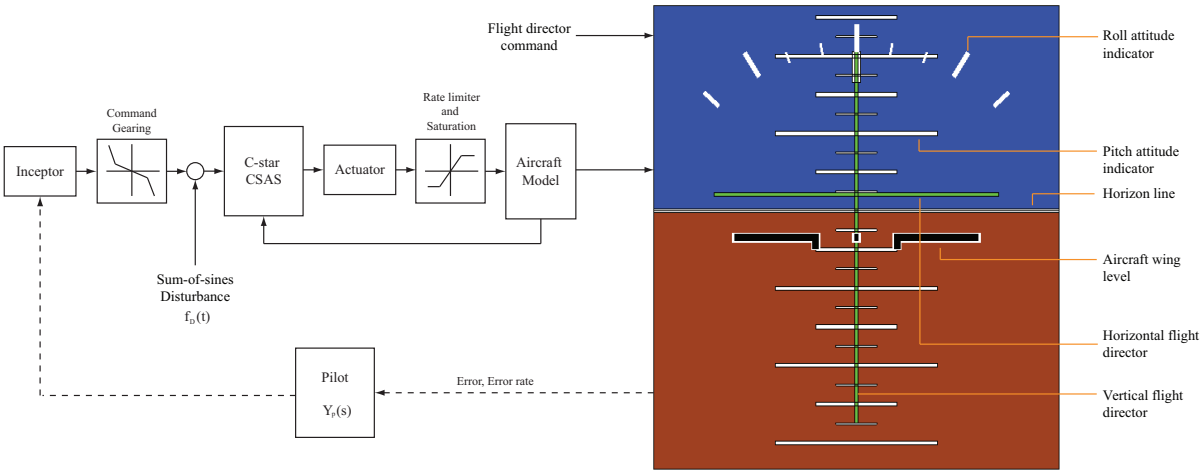

Figure 3.1: Experimental setup and display used for the experiments.

Aircraft pitch rate and attitude were presented to the pilot via a 110 mm×115 mm display shown in Figure 3.1. The attitude indicator scales were spaced such that 5° pitch attitude equalled a 10 mm separation. All tests were conducted on laptops[1] in a MATLAB/Simulink® environment with a nominal computational time delay of 13 ms. The subjects performed tasks by manipulating Microsoft Sidewinder® joysticks. The inactive nature of such an inceptor allows the relationship between pilot command and stick deflection to be kept relatively simple.

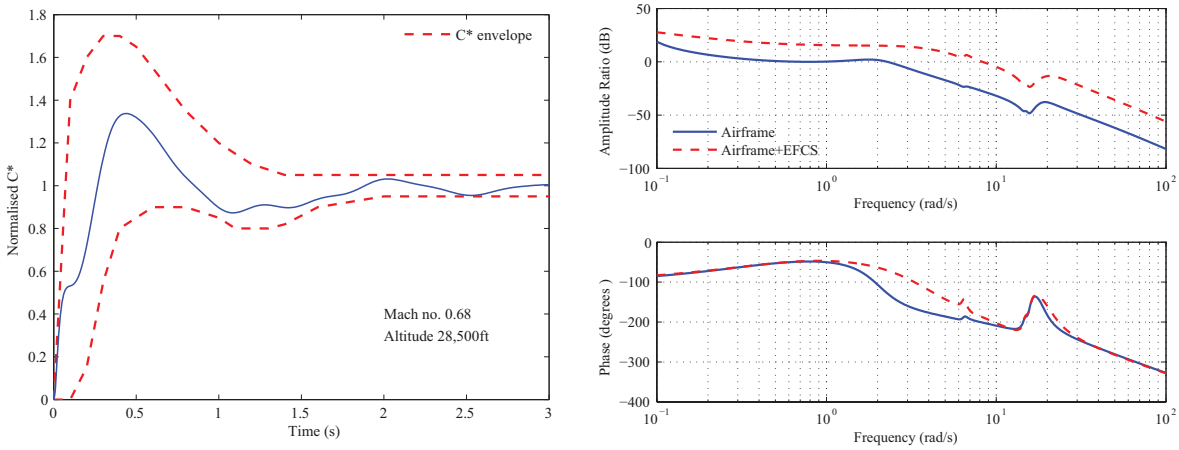

Figure 3.2: C* step and pitch attitude frequency responses.

[1]Laptop specifications: (1) IBM T-series 2.7GHz 4Gb RAM and, (2) Apple MacBook Pro 2.4GHz 4Gb RAM.

3.1.2 Procedure

The study was undertaken in two stages. The preliminary stage involved tests conducted with a mixture of young pilots and engineering students to achieve the following:

1. Develop the man-machine interface and simulation capability necessary to capture relevant dynamics.
2. Design and fine-tune tasks and analytical tools through direct testing of subjects.
3. Study the effects of training.

Tests to investigate training effects were conducted with 13 subjects of the average age and experience of 25 years and 10 flying hours respectively. The subjects were presented with a sum-of-sines compensatory task (two minutes in duration) and root-mean-square (rms) error was taken as a performance indicator. Subjects were informed of their rms error at the end of each run. Figure 3.3 shows a typical set of results and shows the symbology used on later charts. Outliers are defined as values that are two interquartile ranges away from the upper and lower quartiles.

It was found that subjects stabilised their performance between 5 to 7 runs. It was interesting to find that the least variance in rms error occurred on the second run, which demonstrated the speed of human adaptation to compensatory tasks. Within two minutes the subjects adapted to the aircraft dynamics and achieved their nominal disturbance rejection performance. However, tasks were found to require considerable amount of concentration. Therefore, fatigue became a major factor when deciding the number of training and experimental runs allowed per session for future tests. Although only a slight rise in rms error can be observed between runs 8 and 10, subjects commented that they experienced fatigue and loss of focus at this point. Upon realising the consequent increase in rms error, they refocused on the given task and improved their performance; evident by the slight decline in rms error after run number 9.[2]

The final experimental stage involved five trainee civil pilots with an average age and average experience of 24 years and 66 hours respectively. Details of individual subjects are presented in Table A.1. They performed the following 11 tasks, each of two minutes duration:

1. Five compensatory tasks for training.
2. Three compensatory tasks with varying encroachments into command gearing.
3. Three tracking tasks with increasing rate limiting.

Fatigue effects were avoided by allowing a short break after each set of tasks.

Whether these tasks were sufficiently difficult to force the pilots into using a high gain control strategy remains a matter of debate. Although more so in simulation than during actual flight tests, it is very difficult to ensure pilots maintain a consistent level of aggressiveness or introduce high gains into the PVS. Here, two subjects performed the tests alongside each other and both were informed of their and their counterpart's rms error at completion. It was hoped that this would introduce a competitive element and consequently induce the subjects to operate with higher gains. It should also be noted that the experimental setup was considerably different

[2] An analysis of variance (ANOVA) hypothesis test (that excluded results from the first run) was conducted to test the statistical significance of the increased rms error between runs 8 and 10. As an inspection of Figure 3.3 would indicate, it was found to be statistically insignificant.

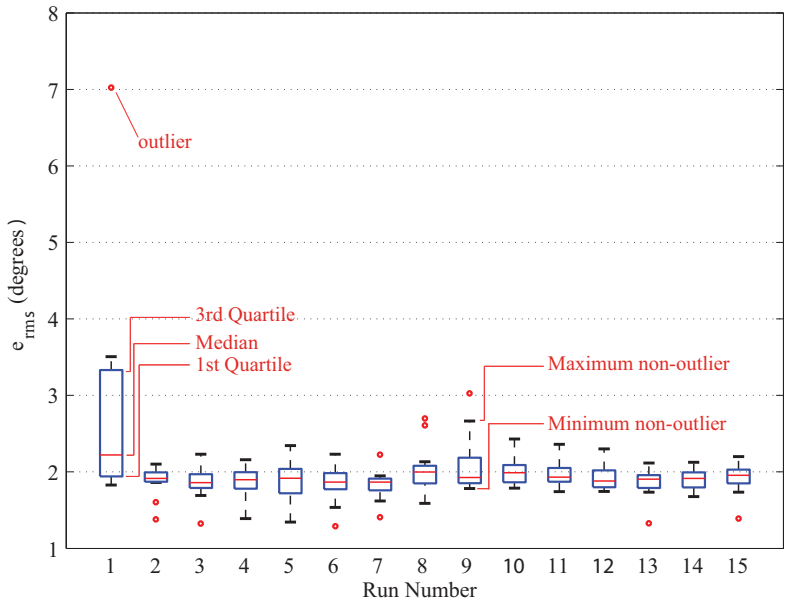

Figure 3.3: Variation of root-mean-square error with run number.

to that of manual control during normal flight. In this case, the pilots perceive and focus on only two variables at a given time and can apply control actions based on these channels alone. Minimising the number of control variables in this manner limits attention allocation and allows the subject to develop a control structure with only error and error rate as inputs and stick deflection as the sole output.

3.1.3 Experimental tasks

All experiments involved the subjects performing either compensatory (disturbance rejection) tasks or tracking tasks in the aircraft longitudinal axis. When performing compensatory tasks, the flight director was switched off and the subjects tried to align the aircraft attitude indicator with the horizon line. Disturbance was injected, as shown in Figure 3.1, in the form of the following forcing function :

$$f_D(t) = \sum_{k=1}^{15} A_k \sin(\omega_k t + \tilde{\phi}_k) \tag{3.1.1}$$

Whilst being a relatively simple task, such a forcing function effectively excites the pilot's control action at selected frequencies over the desired frequency range. The phase ($\tilde{\phi}_k$) for each sinusoid was randomised such that the subject could not perceive any internal coherence and thus adopt high level behaviour. Forcing function parameter values can be found in Table 3.1 and Figure 3.4 shows a sample time history and frequency content. To explore the effects of command gearing, the amplitudes were scaled to change forcing functions rms. This was done on a trial-and-error basis in conjunction with the development of the parameter identification schemes. Although formal guidelines relating forcing function rms to identification quality do not exist, it must be carefully selected to ensure the inceptor signal has sufficient power content for accurate identification. Furthermore, it should not be too high to force the subject to engage high brain functions, that is to adopt a strategy independent of the perceived error.

Tests conducted by Damveld et al[104] showed that phase definition did not affect subject's control behaviour. Unfortunately, due to the timing of its publication the design of forcing function for these experiments does not consider the conclusions made by Damveld et al in

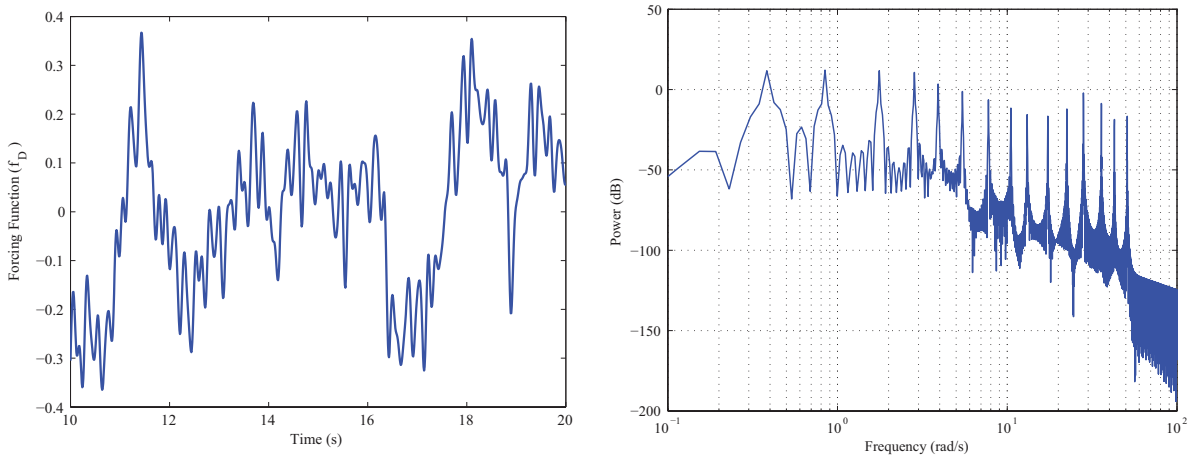

Figure 3.4: Time-domain forcing function signal and its power spectral density.

2010. Damveld's tests showed that forcing function variance should be considered along with bandwidth and power during the task design process. A detailed discussion on the design of forcing functions can be found in work done by McRuer et al[59] and Damveld et al[104].

Such a forcing function along with its corresponding pilot dynamics are well suited for the derivation of pilot's frequency response[105]. The raw time-domain data was converted to frequency-domain via the discrete fast Fourier transform. Pilot frequency response to perceived pitch attitude was then derived as follows:

$$|Y_P(s)| = \frac{|\mathbb{F}\left[\delta_x(t)\right]|}{|\mathbb{F}\left[e_\theta(t)\right]|} \tag{3.1.2}$$

$$\angle Y_P(s) = \arg\mathbb{F}\left[\delta_x(t)\right] - \arg\mathbb{F}\left[e_\theta(t)\right] \tag{3.1.3}$$

The calculation of the PVS describing function was made simpler by the LTI nature of the aircraft model. Figure 3.5 shows the definition of crossover frequency used here (defined previously by McRuer et al[59]). Being an indicator for pilot aggressiveness and open-loop stability, it is chosen as the lowest point at which the open-loop gain is unity.

The use of a sum-of-sines forcing function ensures disturbances occur at the specified frequencies and hence, the pilot's stick movements contains power mainly at these frequencies (given in Table 3.1).[3] Therefore, pilot introduced gain and phase are given by $|Y_p(j\omega_k)|$ and $\angle Y_p(j\omega_k)$ respectively. The addition of aircraft gain and phase then provides the open-loop describing function from which the crossover frequency can be obtained by interpolation.

The tracking task required the pilot to follow the pitch attitude commands provided by the flight director. This demand comprised of a series of steps and ramps as shown in Figure 3.6 and is

[3]This is of course true assuming the task has been designed to ensure the subject adopts a linear control strategy.

k	A_k (deg.)	ω_k (rad/s)	k	A_k (deg.)	ω_k (rad/s)	k	A_k (deg.)	ω_k (rad/s)
1	0.13	0.38	6	0.06	5.45	11	0.04	22.46
2	0.13	0.84	7	0.04	7.75	12	0.06	28.12
3	0.13	1.76	8	0.03	10.51	13	0.05	35.88
4	0.12	2.84	9	0.03	13.12	14	0.03	42.78
5	0.08	3.91	10	0.03	17.33	15	0.03	50.96

Table 3.1: Parameter values for sum-of-sines forcing function.

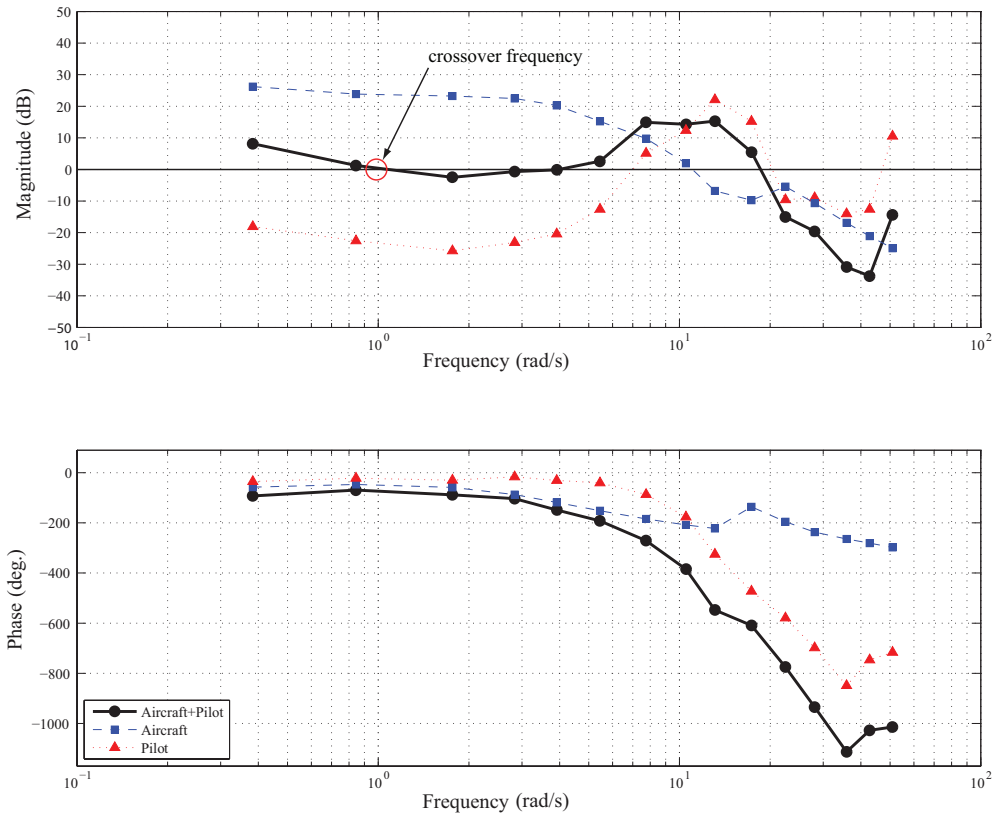

Figure 3.5: PVS describing functions (Subject E, $\sigma_d = 0.47$).

a modified version of the task used by Mitchell et al[106] in their investigation of rate-limiting effects. The forcing functions and the tracking tasks were kept relatively small in magnitude such that the LTI model remained valid. Limiting the study in this way meant that the inability to provide acceleration cues was made inconsequential.

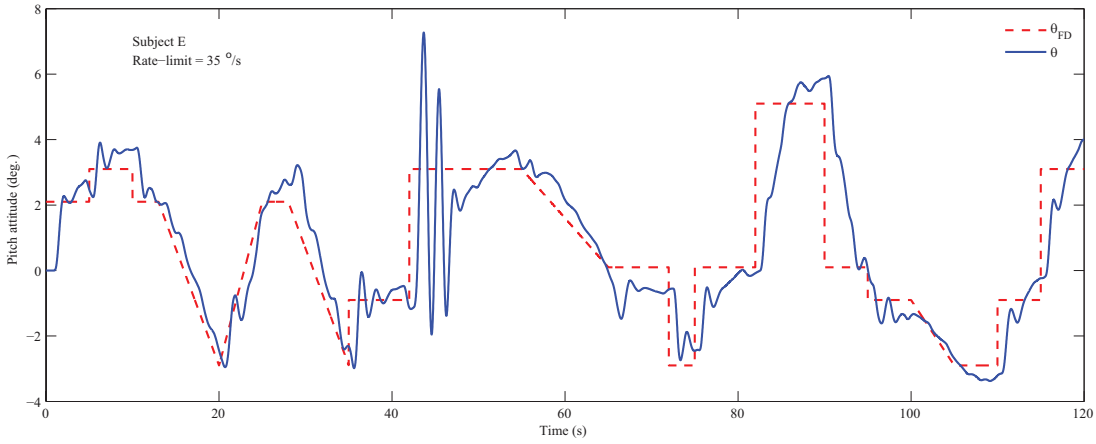

Figure 3.6: Tracking task and subject performance.

3.2 Experimental results

3.2.1 Command gearing

The effects of command gearing was investigated by presenting the subjects with a series of compensatory tasks and varying forcing function rms (σ_d). The following command gearing, similar to that used in modern civil aircraft, was used to convert the stick deflection to load factor demand:

$$\frac{N_{zc}}{\delta_x} = \begin{cases} -4, & -1.0 \leq \delta_x \leq -0.5 \\ -1, & -0.5 < \delta_x < 0.9 \\ -16, & 0.9 \leq \delta_x \leq 1.0 \end{cases} \tag{3.2.1}$$

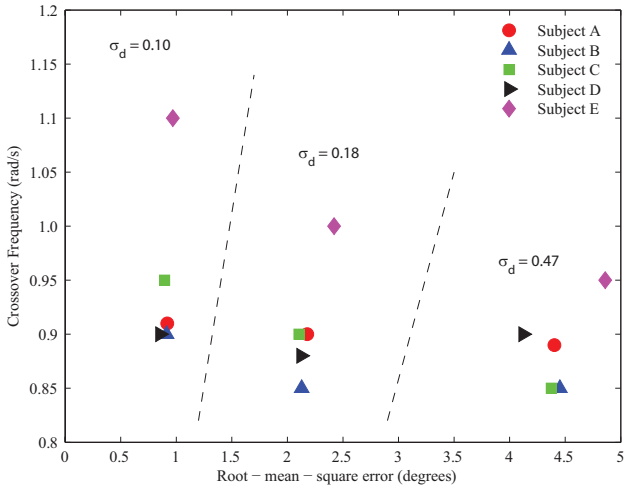

Figure 3.7: Effect of command gearing on subject performance.

The subjects' control actions were forced to span over the nonlinear region by increasing the forcing function rms. The effects are succinctly summarised in Figure 3.7. Increasing the number of incursions into the nonlinear region was found to make the task more difficult as evident by larger rms error. Most subjects maintained a crossover frequency of around 0.9 rad/s, whereas Subjects C and E resorted to different degrees of crossover regression. Adoption of greater crossover frequencies by Subject E indicates increased aggressiveness leading to degraded performance. Some insight can be gained by comparing Subject E's stick activity with that of Subject B in Figure 3.8. It shows the frequency with which the subjects encroach the nonlinear region. Subject E's aggressive control strategy leads to a cycle where every encroachment into the nonlinear region causes over-control which in turn, demands an equally aggressive recovery action. Therefore, the subject perceives high frequency oscillations in attitude and so maintains the greater crossover frequency. Thus, reinforcing the cycle. However, comments regarding crossover frequency can only be made on a relative basis. Overall, the variation is small and even though the adopted crossover frequency is dependent on aircraft dynamics, values around 0.9 rad/s indicates a lack of urgency in the pilot's control characteristics.

3.2.2 Actuator rate-limiting

Actuator rate-limiting is known to introduce phase delay and amplitude attenuation into a closed-loop system[107]. A series of tracking tasks were used to investigate their affects on manual control. Tests were conducted with 25°/s, 35°/s and 45°/s actuator rate-limits. The command gearing described earlier was retained.

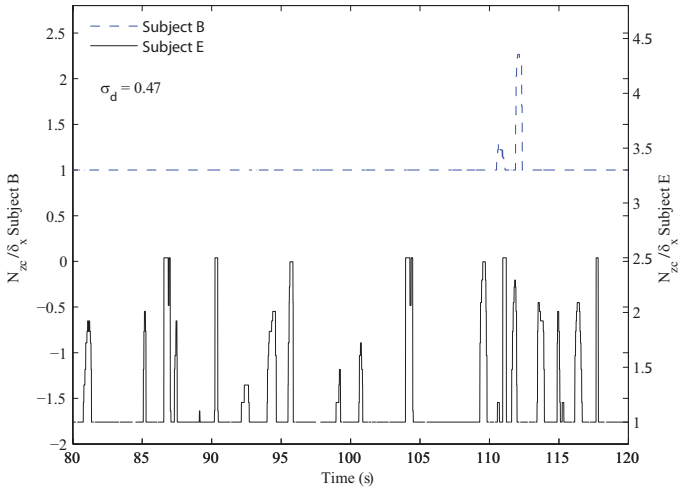

Figure 3.8: Stick activity for Subjects B and E.

Upon hitting a rate-limit, subjects were found to compensate by increasing their gain (leading to larger stick deflections) to get the desired response. However, the introduced phase delay led to larger overshoots and longer recovery times. This can be seen around 43 seconds in Subject E's data, shown in Figure 3.6. The more demanding commands occurring at 42, 82 and 115 seconds led to the triggering of nonlinear command shaping causing actuator rate-limiting. This can be seen clearly in Figure 3.9.

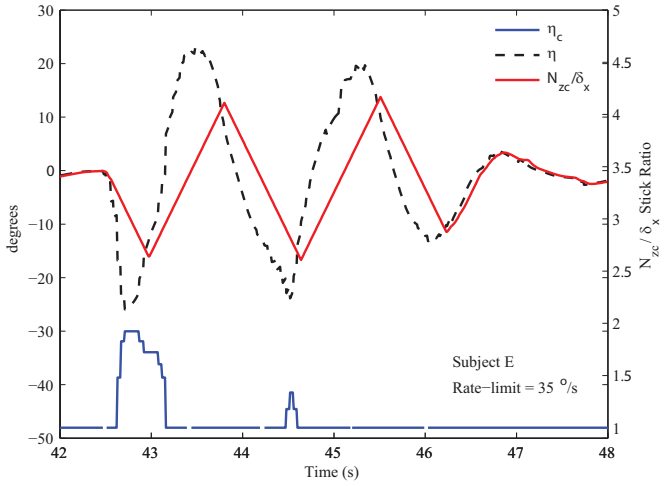

Figure 3.9: Comparison of stick activity and resulting rate-limiting.

By comparing the tracking performance at 42 seconds with that at 82 seconds, the subject can be seen to demonstrate learning and adaptability. Although this subject was found to be the most aggressive, the dynamics after the first minute is representative of the remaining subjects. They were found to apply gentle stick movements to track the flight director. Post-experiment feedback found that this characteristic was encouraged at the flight school.

Due to the older visual systems onboard the large aircraft simulators, they are used mostly in night conditions where the limited 30 Hz refresh rate has little affect on pilot visual perception. The latest systems onboard the business jet simulators are cheaper and provide high resolution imagery at 50-60 Hz, increasing the realism of daylight simulations. The only drawback is that it cannot reproduce intense bright lights as typically seen in an airport environment. The latest simulators also use electric actuation systems instead of hydraulic systems. This has significantly reduced maintenance costs and improved simulator performance.

3.3 Pilot model development

Pilot models can provide considerable insight into inter-subject variations in control characteristics. Differences in parameter values can highlight changes in subjective factors such as relative aggression and varying degrees in the understanding of vehicle dynamics. In this section, two types of classical pilot models are used: precision and bimodal. Using two models in this way allows comparison and verification of:

1. the parameter identification results,
2. recognition of outlying data points and,
3. confirmation of any hypothesis tests.

For compensatory tasks these form the complete pilot model whilst for tracking tasks a feed-forward path is added to the structure as shown in Figures 3.10 and 3.11. Reviews by Lone[108] and Grant[3] provide more detailed descriptions and comparisons of pilot models used here and in other studies.

The classical precision model proposed by McRuer[5] represents the pilot as a single transfer function relating perceived attitude error to stick deflection. This model assumes that the pilot adopts a structure with two equalisations, consisting of the typical equalisation observed during manual control to compensate for the short period oscillation mode and a low frequency equalisation for the phugoid mode:

$$G_p(s) = K_p \frac{(\tau_{\mathrm{L}} s + 1)(\tau_{\mathrm{LL}} s + 1)}{(\tau_{\mathrm{I}} s + 1)(\tau_{\mathrm{IL}} s + 1)} \tag{3.3.1}$$

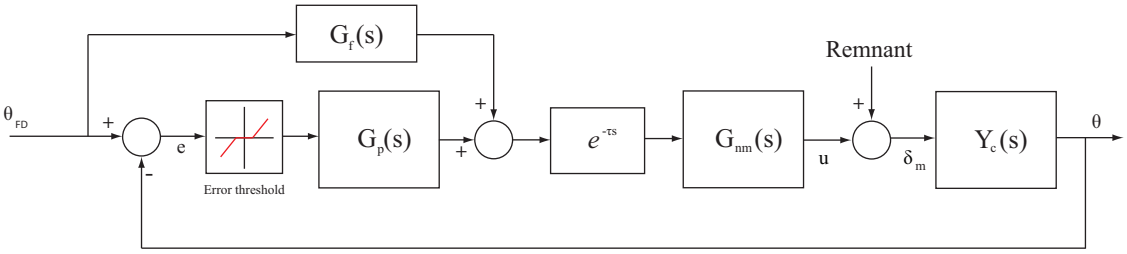

Figure 3.10: Precision pilot model structure for compensatory and tracking tasks.

The bimodal model is a simplified version of the model proposed by Hosman[3] and uses first order equalisations along both attitude error (e) and error rate ($\dot{e}$) feedback paths:[4]

$$G_p(s) = G_{\dot{e}}(s) + sG_e(s) = K_{p\theta} \frac{\tau_{\mathrm{L}\theta} s + 1}{\tau_{\mathrm{I}\theta} s + 1} + K_{pq} s \frac{\tau_{\mathrm{Lq}} s + 1}{\tau_{\mathrm{Iq}} s + 1} \tag{3.3.2}$$

Any desired control action is finally implemented through the neuromuscular system, modelled here as:

$$G_{nm}(s) = \frac{\omega_n^2}{(\tau_n s + 1)(s^2 + 2\zeta_n \omega_n s + \omega_n^2)} \tag{3.3.3}$$

[4]This simplification accounts for the lack of vestibular cues during the experiment.

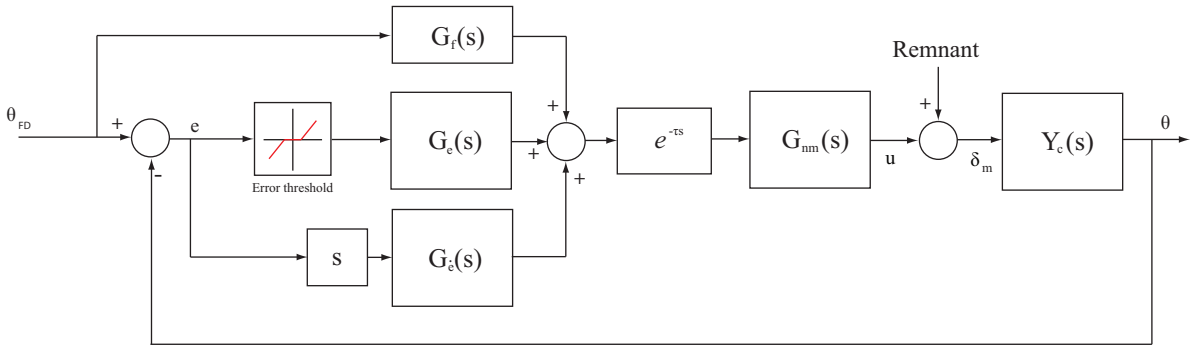

Figure 3.11: Bimodal pilot model structure for compensatory and tracking tasks.

As shown in Figure 3.10, the assumed pilot control structure consists of lead-lag compensations along the perceived error and error rate in series with a processing time delay (τ). A second order Padé approximation was used to model this delay:[5]

$$e^{-\tau s} = \frac{\bar{u}(s)}{\hat{u}(s)} \approx \frac{1 - \frac{\tau}{2}s + \frac{\tau^2}{12}s^2}{1 + \frac{\tau}{2}s + \frac{\tau^2}{12}s^2} \tag{3.3.4}$$

Since the identification codes were developed with both pilot and aircraft model parameter identification in mind, the processes require models in state-space form. The following develops the pilot models in this form. The Padé delay approximation can be expressed as follows:

$$\begin{aligned} \begin{bmatrix} \dot{x}_1 \\ \dot{x}_2 \end{bmatrix} &= \begin{bmatrix} 0 & 1 \\ -12/\tau^2 & -6/\tau \end{bmatrix} \begin{bmatrix} x_1 \\ x_2 \end{bmatrix} + \begin{bmatrix} 0 \\ 12/\tau^2 \end{bmatrix} \hat{u} \\ \bar{u} &= \begin{bmatrix} 0 & -\tau \end{bmatrix} \begin{bmatrix} x_1 \\ x_2 \end{bmatrix} + \hat{u} \end{aligned} \tag{3.3.5}$$

or

$$\begin{aligned} \dot{\mathbf{x}}_d &= \mathbf{A}_d \mathbf{x}_d + \mathbf{B}_d \hat{u} \\ \bar{u} &= \mathbf{C}_d \mathbf{x}_d + \mathbf{D}_d \hat{u} \end{aligned} \tag{3.3.6}$$

The compensations along the e and $\dot{e}$ channels take the following standard form:

$$\frac{n(s)}{d(s)} = K \frac{\tau_{\mathrm{L}} s + 1}{\tau_{\mathrm{I}} s + 1} \tag{3.3.7}$$

which may be written as:

$$\begin{aligned} \dot{x} &= \frac{1}{\tau_{\mathrm{I}}} x + \frac{K}{\tau_{\mathrm{I}}} d \\ n &= \frac{\tau_{\mathrm{L}} + \tau_{\mathrm{I}}}{\tau_{\mathrm{I}}} x + \frac{K \tau_{\mathrm{L}}}{\tau_{\mathrm{I}}} d \end{aligned} \tag{3.3.8}$$

Applying the above result to e and $\dot{e}$ channels, the parallel compensation can be written as:

$$\begin{aligned} \begin{bmatrix} \dot{\mathbf{x}}_e \\ \dot{\mathbf{x}}_{\dot{e}} \end{bmatrix} &= \begin{bmatrix} \mathbf{A}_e & 0 \\ 0 & \mathbf{A}_{\dot{e}} \end{bmatrix} \begin{bmatrix} \mathbf{x}_e \\ \mathbf{x}_{\dot{e}} \end{bmatrix} + \begin{bmatrix} \mathbf{B}_e & 0 \\ 0 & \mathbf{B}_{\dot{e}} \end{bmatrix} \begin{bmatrix} e \\ \dot{e} \end{bmatrix} \\ \hat{u} &= \begin{bmatrix} \mathbf{C}_e & \mathbf{C}_{\dot{e}} \end{bmatrix} \begin{bmatrix} \mathbf{x}_e \\ \mathbf{x}_{\dot{e}} \end{bmatrix} + \begin{bmatrix} \mathbf{D}_e & \mathbf{D}_{\dot{e}} \end{bmatrix} \begin{bmatrix} e \\ \dot{e} \end{bmatrix} \end{aligned} \tag{3.3.9}$$

[5]Recent work done by Zaal et al[4] has considered a fifth order Padé approximation for modelling the pilot model time delay. Therefore, any future developments should consider the tradeoffs involved when using higher order approximations and the resulting sparseness of system matrices.

A desired stick deflection is implemented through the neuromuscular system modelled by Equation 3.3.3, given by:

$$\begin{aligned}
\begin{bmatrix} \dot{x}_1 \\ \dot{x}_2 \\ \dot{x}_3 \end{bmatrix} &= \begin{bmatrix} 0 & 1 & 0 \\ 0 & 0 & 1 \\ -\omega_n^2/\tau_n & -\omega_n^2 - 2\zeta_n\omega_n/\tau_n & -1/\tau_n - 2\zeta_n\omega_n \end{bmatrix} \begin{bmatrix} x_1 \\ x_2 \\ x_3 \end{bmatrix} + \begin{bmatrix} 0 \\ 0 \\ \omega_n^2/\tau_n \end{bmatrix} \bar{u} \\
u &= \begin{bmatrix} 1 & 0 & 0 \end{bmatrix} \begin{bmatrix} x_1 \\ x_2 \\ x_3 \end{bmatrix}
\end{aligned} \tag{3.3.10}$$

or

$$\begin{aligned}
\dot{\mathbf{x}}_n &= \mathbf{A}_n\mathbf{x}_n + \mathbf{B}_n\bar{u} \\
u &= \mathbf{C}_n\mathbf{x}_n
\end{aligned} \tag{3.3.11}$$

Now, since the delay and neuromuscular dynamics are in series with the compensatory components, the whole system can be put in state space form along with the remnant signal as follows:

$$\begin{aligned}
\begin{bmatrix} \dot{\mathbf{x}}_e \\ \dot{\mathbf{x}}_{\dot{e}} \\ \dot{\mathbf{x}}_d \\ \dot{\mathbf{x}}_n \end{bmatrix} &= \begin{bmatrix} \mathbf{A}_e & 0 & 0 & 0 \\ 0 & \mathbf{A}_{\dot{e}} & 0 & 0 \\ \mathbf{B}_d\mathbf{C}_e & \mathbf{B}_d\mathbf{C}_{\dot{e}} & \mathbf{A}_d & 0 \\ \mathbf{B}_n\mathbf{C}_e & \mathbf{B}_n\mathbf{C}_{\dot{e}} & \mathbf{B}_n\mathbf{C}_d & \mathbf{A}_n \end{bmatrix} \begin{bmatrix} \mathbf{x}_e \\ \mathbf{x}_{\dot{e}} \\ \mathbf{x}_d \\ \mathbf{x}_n \end{bmatrix} + \begin{bmatrix} \mathbf{B}_e & 0 \\ 0 & \mathbf{B}_{\dot{e}} \\ \mathbf{B}_d\mathbf{D}_e & \mathbf{B}_d\mathbf{D}_{\dot{e}} \end{bmatrix} \begin{bmatrix} e \\ \dot{e} \end{bmatrix} \\
\delta_m &= \begin{bmatrix} 0 & 0 & 0 & \mathbf{C}_n \end{bmatrix} \begin{bmatrix} \mathbf{x}_e \\ \mathbf{x}_{\dot{e}} \\ \mathbf{x}_d \\ \mathbf{x}_n \end{bmatrix} + \text{Remnant}
\end{aligned} \tag{3.3.12}$$

This is effectively the compensatory pilot model to be used in the parameter identification process.

It was also assumed that the pilot adopted a feed-forward compensation when tracking a reference attitude (r) given by the second order transfer function:

$$G_f(s) = K_f \frac{\tau_{\text{Lf}}s + 1}{\tau_{\text{If}}s + 1} \frac{\tau_{\text{LLf}}s + 1}{\tau_{\text{ILf}}s + 1} \tag{3.3.13}$$

This assumes the subject implements a feed-forward loop with lead-lag compensation along with the same compensatory dynamics discussed earlier. Given the tracking pilot model structure shown in Figure 3.10, the linear relationship between the reference signal and stick deflection can be written as:

$$\frac{\delta_m(s)}{r(s)} = \frac{1 + G_f(s)}{1 + G_p(s)Y_c(s)} e^{-\tau s} G_{nm}(s) \tag{3.3.14}$$

It should be noted that this uses the same time delay as the compensatory loop, thus:

$$\begin{aligned}
\begin{bmatrix} \dot{x}_1 \\ \dot{x}_2 \end{bmatrix} &= \begin{bmatrix} 1/\tau_{\text{If}} & 0 \\ \frac{\tau_{\text{Lf}}+\tau_{\text{If}}}{\tau_{\text{If}}\tau_{\text{ILf}}} & 1/\tau_{\text{ILf}} \end{bmatrix} \begin{bmatrix} x_1 \\ x_2 \end{bmatrix} + \begin{bmatrix} K_f/\tau_{\text{If}} \\ K_f\tau_{\text{Lf}}/\tau_{\text{If}}\tau_{\text{ILf}} \end{bmatrix} r \\
u_f &= \begin{bmatrix} \frac{(\tau_{\text{Lf}}+\tau_{\text{If}})\tau_{\text{LLf}}}{\tau_{\text{If}}\tau_{\text{ILf}}} & \frac{\tau_{\text{LLf}}+\tau_{\text{ILf}}}{\tau_{\text{ILf}}} \end{bmatrix} \begin{bmatrix} x_1 \\ x_2 \end{bmatrix} + K_f \frac{\tau_{\text{Lf}}\tau_{\text{LLf}}}{\tau_{\text{If}}\tau_{\text{ILf}}} r
\end{aligned} \tag{3.3.15}$$

or

$$\begin{aligned}
\dot{\mathbf{x}}_f &= \mathbf{A}_f\mathbf{x}_f + \mathbf{B}_f r \\
u_f &= \mathbf{C}_f\mathbf{x}_f + \mathbf{D}_f r
\end{aligned} \tag{3.3.16}$$

Augmenting the model in Equation 3.3.12 with the above result gives the model for tracking behaviour:

$$\begin{bmatrix} \dot{\mathbf{x}}_f \\ \dot{\mathbf{x}}_e \\ \dot{\mathbf{x}}_{\dot{e}} \\ \dot{\mathbf{x}}_d \end{bmatrix} = \begin{bmatrix} \mathbf{A}_f & 0 & 0 & 0 & 0 \\ 0 & \mathbf{A}_e & 0 & 0 & 0 \\ 0 & 0 & \mathbf{A}_{\dot{e}} & 0 & 0 \\ \mathbf{B}_d\mathbf{C}_f & \mathbf{B}_d\mathbf{C}_e & \mathbf{B}_d\mathbf{C}_{\dot{e}} & \mathbf{A}_d & 0 \\ \mathbf{B}_n\mathbf{C}_f & \mathbf{B}_n\mathbf{C}_e & \mathbf{B}_n\mathbf{C}_{\dot{e}} & \mathbf{B}_n\mathbf{C}_d & \mathbf{A}_n \end{bmatrix} \begin{bmatrix} \mathbf{x}_f \\ \mathbf{x}_e \\ \mathbf{x}_{\dot{e}} \\ \mathbf{x}_d \\ \mathbf{x}_n \end{bmatrix} + \begin{bmatrix} \mathbf{B}_f & 0 & 0 \\ 0 & \mathbf{B}_e & 0 \\ 0 & 0 & \mathbf{B}_{\dot{e}} \\ \mathbf{B}_d\mathbf{D}_f & \mathbf{B}_d\mathbf{D}_e & \mathbf{B}_d\mathbf{D}_{\dot{e}} \\ \mathbf{B}_n\mathbf{D}_f & \mathbf{B}_n\mathbf{D}_e & \mathbf{B}_n\mathbf{D}_{\dot{e}} \end{bmatrix} \begin{bmatrix} r \\ e \\ \dot{e} \end{bmatrix}$$

$$\delta_m = \begin{bmatrix} 0 & 0 & 0 & 0 & \mathbf{C}_n \end{bmatrix} \begin{bmatrix} \mathbf{x}_e \\ \mathbf{x}_{\dot{e}} \\ \mathbf{x}_d \\ \mathbf{x}_n \end{bmatrix} + \text{Remnant} \tag{3.3.17}$$

This provides the state-space matrices as functions of parameters that need to be estimated. The state-space formulation for the precision model requires a similar procedure, which for brevity it is not included here.

The only nonlinear element in the pilot model is the error threshold (e_{th}); the maximum attitude errors pilots consistently chose to ignore, see Figures 3.10 and 3.11. Vectors containing the unknown parameters are therefore:

$$\Gamma_{\mathrm{B}} = \begin{bmatrix} K_{p\theta} & K_{pq} & \tau & \tau_{\mathrm{I}\theta} & \tau_{\mathrm{L}\theta} & \tau_{\mathrm{Lq}} & \tau_{\mathrm{Iq}} & e_{th} & \Gamma_{\mathrm{N}} \end{bmatrix} \tag{3.3.18}$$

$$\Gamma_{\mathrm{P}} = \begin{bmatrix} K_p & \tau & \tau_{\mathrm{I}} & \tau_{\mathrm{L}} & \tau_{\mathrm{LL}} & \tau_{\mathrm{I}} & e_{th} & \Gamma_{\mathrm{N}} \end{bmatrix} \tag{3.3.19}$$

$$\Gamma_{\mathrm{T}} = \begin{bmatrix} \Gamma_{\mathrm{B/P}} & K_f & \tau_{\mathrm{If}} & \tau_{\mathrm{ILf}} & \tau_{\mathrm{Lf}} & \tau_{\mathrm{LLf}} \end{bmatrix} \tag{3.3.20}$$

where

$$\Gamma_{\mathrm{N}} = \begin{bmatrix} \tau_n & \zeta_n & \omega_n \end{bmatrix} \tag{3.3.21}$$

3.4 Parameter identification methods

The problem of estimating pilot model parameters was approached using three methods:

1. time-domain least-squares (TLS),
2. time-frequency-domain least-squares (TFLS) and,
3. maximum likelihood estimation (MLE).

The latter two approaches were implemented mainly because of: (a) the non-convex nature of such an optimisation problem and, (b) the relatively large inter-subject variations in pilot model parameters found for the TLS method. Each method basically presents the optimiser with a different terrain to search for a minima.

The approaches based on least-squares make no assumptions about the processes or models producing the signals which are being compared. Therefore, the estimation problem for TLS and TFLS methods can be stated as follows:

$$\hat{\Gamma}_{\mathrm{TLS}} = \arg\min_{\Gamma} \left(\sum_{i=1}^{N} [\delta_x(i) - \delta_m(i)]^2 \right) \tag{3.4.1}$$

$$\hat{\Gamma}_{\mathrm{TFLS}} = \arg\min_{\Gamma} \left(\sum_{i=1}^{N} [\delta_x(i) - \delta_m(i)]^2 + \Lambda \sum_{\omega=\omega_0}^{\Omega} [\Phi_x(\omega) - \Phi_m(\omega)]^2 \right) \tag{3.4.2}$$

where Γ is a vector containing parameters that require estimation and Λ is a scalar weighting parameter (chosen to be 100). The latter is necessary to ensure a balanced match in both domains. It is clear that TLS is a single step estimation problem whereas, the TFLS method requires a parallel frequency-domain step that compares power spectral densities. The TFLS method is only made possible because the estimation is being done off-line. The signals were sampled at 100 Hz; giving a maximum Nyquist frequency of 50 Hz.

A pure frequency-domain parameter identification process was not conducted mainly due to the availability of computing power and the simplicity of the time-domain methods. Typically it is a two step method requiring the:

1. fitting of a nonparametric model (usually an autoregressive moving average model) to the pilot's frequency response and,

2. identification of LTI model parameters which provide the best fit to the nonparametric model obtained in the first step.

The advantage being that the transformation into frequency-domain helps reduce the amount of data whilst the nonparametric model helps judgements to be made regarding the structure of the parametric model. As Zaal et al[74] point out, the disadvantage is that this method requires the same number of forcing functions as the number of frequency responses to be identified; leading to subjects performing unrealistic tasks. Also the main motivation for this method, which was to minimise computational cost, is no longer an issue.

The MLE approach on the other hand, involves a clear definition of the model and noise sources along with the assumption that an observed difference between the model and the measurement adheres to a given probability density function. Although Klein et al[109] and Iliff et al[110] provide a thorough analysis and discussion on its theory and applications (for aircraft system identification), the outline of its application to pilot model parameter identification is presented here for the reader's convenience.

Given the pilot models in Equations 3.3.12 and 3.3.17, for which the remnant signal is effectively the output noise, it is assumed that the probability density function for a measured error is given by:

$$f(\nu(i)|\Gamma) = \frac{1}{\sqrt{2\pi\sigma_\nu^2}} e^{-(\delta_x(i)-\delta_m(i))^2/2\sigma_\nu^2} \tag{3.4.3}$$

where

$$\nu(i) = \delta_x(i) - \delta_m(i) \tag{3.4.4}$$

Considering all N measurements, the joint probability density function of all errors is therefore:

$$\mathbb{L}(\nu|\Gamma) = \prod_{i=1}^{N} f(\delta_x(i) - \delta_m(i)|\Gamma) \tag{3.4.5}$$

This is often referred to as the *likelihood function* and in practice its negative natural logarithm is used:

$$-\ln \mathbb{L}(\nu|\Gamma) = \frac{N}{2}\ln 2\pi + N \ln \sigma_\nu + \frac{N}{2\sigma_\nu^2}\sum_{i=1}^{N}\left[\delta_x(i) - \delta_m(i)\right]^2 \tag{3.4.6}$$

Therefore, the aim is to obtain a parameter set that maximises the probability that r is observed given the estimated parameter values $\hat{\Gamma}$. Thus, the MLE estimation problem can be stated as:

$$\begin{aligned}\hat{\Gamma}_{\text{MLE}} &= \arg\max_{\Gamma}\left(\mathbb{L}(\nu|\Gamma)\right)\\ &= \arg\min_{\Gamma}\left(-\ln\mathbb{L}(\nu|\Gamma)\right)\\ &= \arg\min_{\Gamma}\left(N\ln\sigma_\nu+\frac{N}{2\sigma_\nu^2}\sum_{i=1}^{N}\left[\delta_x(i)-\delta_m(i)\right]^2\right)\end{aligned} \tag{3.4.7}$$

Therefore, the cost functions for the TLS, TFLS and MLE approaches are as follows:

$$\mathcal{J}_{\text{TLS}} = \sum_{i=1}^{N}[\delta_x(i)-\delta_m(i)]^2 \tag{3.4.8}$$

$$\mathcal{J}_{\text{TFLS}} = \sum_{i=1}^{N}[\delta_x(i)-\delta_m(i)]^2+\Lambda\sum_{\omega=\omega_0}^{\Omega}[\Phi_x(\omega)-\Phi_m(\omega)]^2 \tag{3.4.9}$$

$$\mathcal{J}_{\text{MLE}} = N\ln\sigma_\nu+\frac{N}{2\sigma_\nu^2}\sum_{i=1}^{N}[\delta_x(i)-\delta_m(i)]^2 \tag{3.4.10}$$

These were minimised through the constrained nonlinear sequential quadratic programming optimisation tool available in MATLAB as the `fmincon` function. The search space for the optimiser was somewhat reduced by defining an upper and lower parameter bounds shown in Table 3.2. The lower bound for the lag parameters was set to zero to ensure open-loop stability. Bounds on the threshold parameter was set according to the minimum accuracy achievable through the PFD. Remaining parameter bounds were based on typical values found in literature[111][76][112]. Due to the low computing costs involved,[6] the optimiser was programmed to search for a parameter set five times from randomised initial starting points. The set corresponding to the lowest cost function value was then selected.

Parameter	Min.	Max.	Type
K_p,$K_{p\theta}$,K_{pq},K_f	$-\infty$	∞	Gain
τ_{L},τ_{LL},$\tau_{\text{L}\theta}$,τ_{Lq},τ_{Lf},τ_{LLf}	$-\infty$	∞	Lead
τ_{I},τ_{IL},$\tau_{\text{I}\theta}$,τ_{Iq},τ_{If},τ_{ILf}	0	∞	Lag
e_{th}	-2.50	2.50	Threshold
τ	0.20	0.50	Delay
τ_n	0.08	0.10	Lag
ω_n	10	20	Frequency
ζ_n	0.15	0.30	Damping ratio

Table 3.2: Pilot model parameter constraints used for the identification process.

The value of the above cost functions can be used as a quantitative measure of the individual identification quality but comparing the methods requires the definition of a parameter that may be used to normalise the cost function values (which is difficult to formulate). A metric used in more recent pilot model parameter identification studies[113][4][73][72] is the Variance-Accounted-For (VAF) which is defined as follows:

$$\text{VAF} = \left|1-\frac{\sum_{i=1}^{N}[\delta_x(i)-\delta_m(i)]^2}{\sum_{i=1}^{N}\delta_x^2(i)}\right| \tag{3.4.11}$$

[6]The batch of 55 data sets were parallel processed on a quad-core 2.50GHz computer with 8Gb of RAM in approximately 135 minutes.

It is an indication of the agreement between the measured and modelled stick movements. In this case it is a measure of the extent to which the subject behaves in a linear fashion. A VAF value of unity indicates a perfect fit. However, a more natural choice for a comparison metric is the variance of the remnant signal (σ_ν^2). A small variance would indicate a close match between the experimental data and model and vice versa. The parameter estimation methods can be compared using Figure 3.12.[7] An additional approach that used the TLS method with a fixed $\Gamma_N = [\ 0.08 \quad 0.15 \quad 10\ ]$ was implemented to observe the effects of reducing the dimensions of the search space; dubbed the Modified TLS method. These values were fixed after insignificant variations in neuromuscular dynamics were observed for the precision model (shown in Figure 3.13).

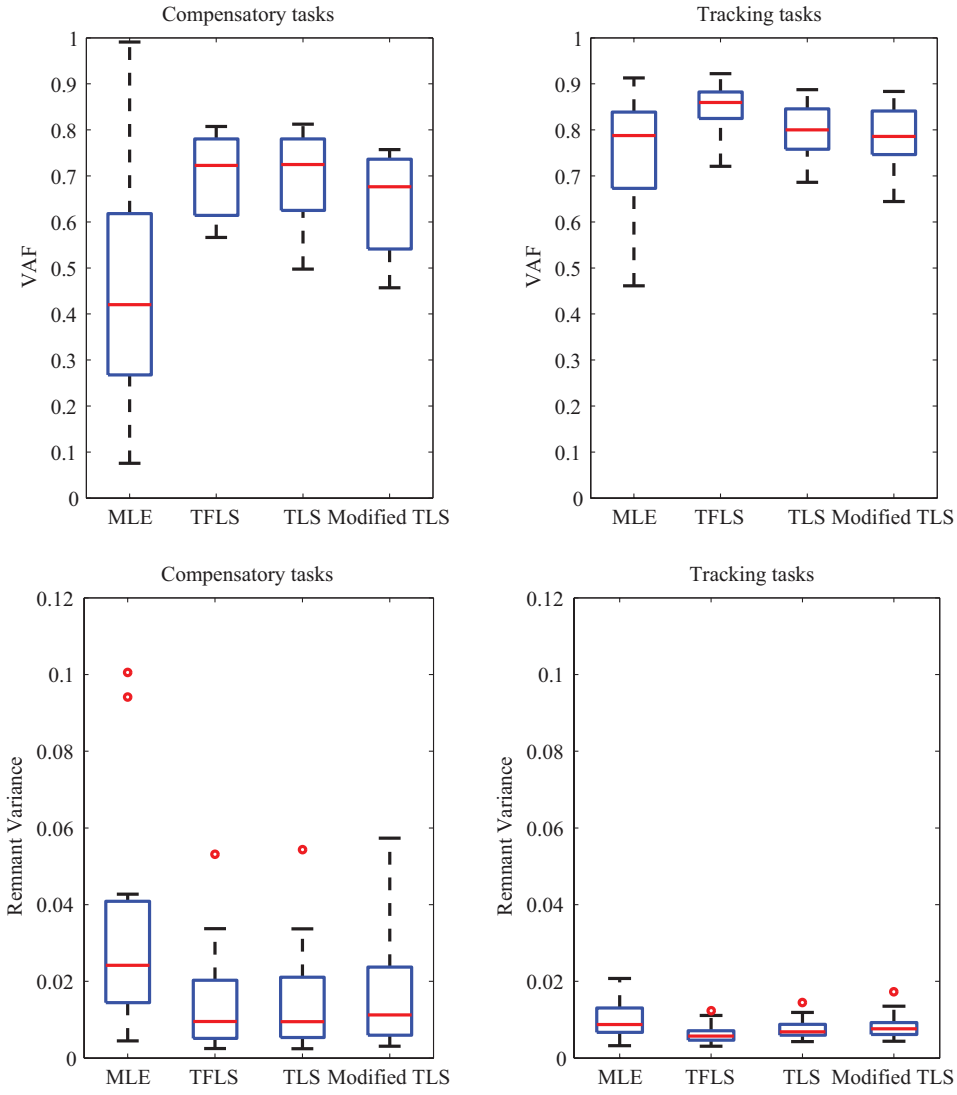

Figure 3.12: VAF and remnant variances obtained for parameter identification methods (using bimodal pilot model).

The higher VAF and low remnant variances for tracking tasks can be attributed to the feed-forward component used in the pilot models. Low variances also show that subjects adopted a mainly linear control strategy. Comparing the methods it is clear that the TFLS approach provides the best fits, which is not so surprising as it considers both frequency and time-domain data. However, the results show two surprising outcomes:

[7]Similar results were found when using the precision model to assess the parameter identification methods.

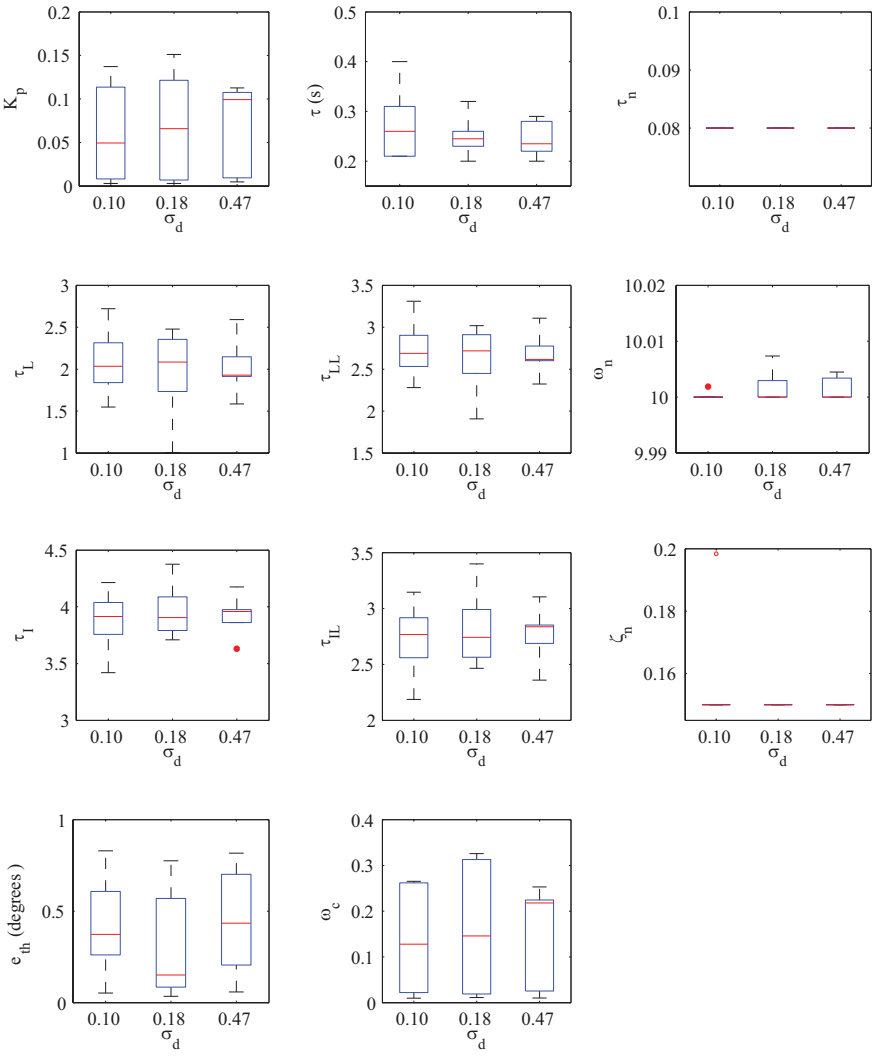

Figure 3.13: Precision model parameter values for compensatory tasks.

1. The poor performance of the MLE method; which could be due to the assumptions made for the noise process (Equation 3.4.3) and the consequent inclusion of σ_ν (as a denominator) and $\ln \sigma_\nu$ terms in the cost function. Furthermore, the process noise has been ignored and all noise sources are assumed to be output (or sensor) noise. Other methods considered here make no such assumptions.

2. The observed degradation in performance for the Modified TLS method; which implies that it is necessary to accommodate the inter-subject differences in neuromuscular dynamics. The reduction in search space dimension has in fact had an adverse effect.

Although the MLE method theoretically minimises the variance in parameter estimates for each test run, the nonlinear nature of the estimation problem does not necessarily mean the global minima is found for all tests; which is also the case for all other methods. Therefore, some estimates can be a result of the optimiser finding a local minima. A further optimisation loop which attempts to minimise the variance in parameter estimates may be closed around the current problem. However, this would exponentially increase the computational cost. Such an approach was beyond the scope of this project.

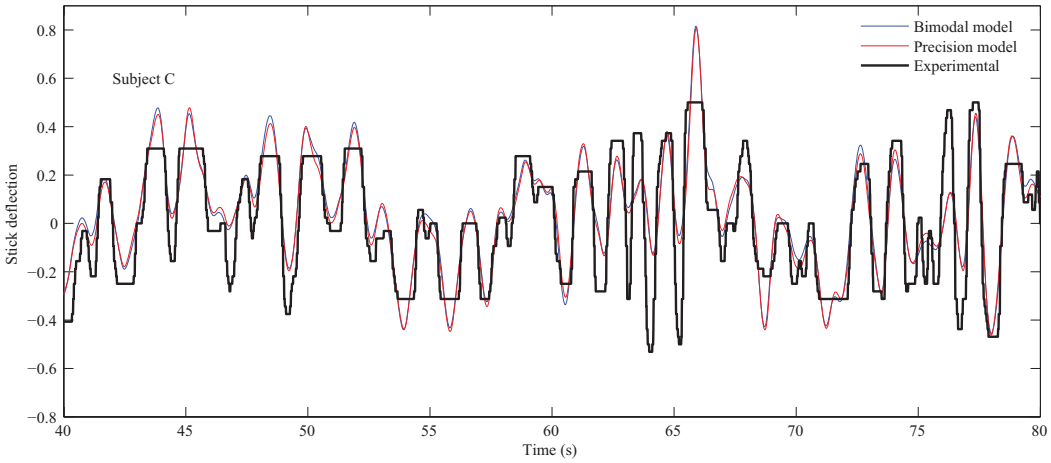

Figure 3.14: Example time-domain result from TFLS parameter identification process.

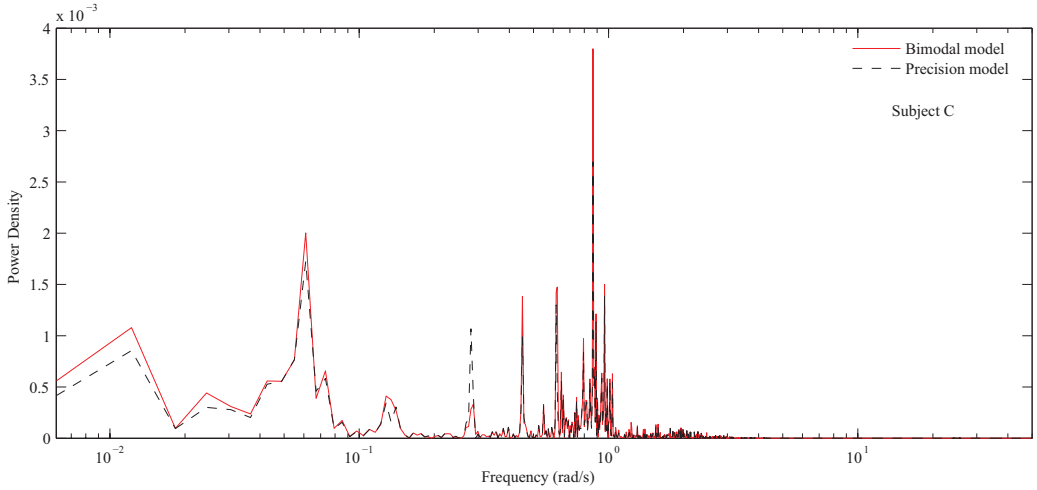

Figure 3.15: Example remnant frequency content from TFLS parameter identification process.

3.4.1 Compensatory tasks

In the light of the aforementioned findings, pilot models found through the TFLS method were used for comparison. Figures 3.14 and 3.15 show a typical time-domain and remnant frequency content for this method. The time-domain match of the models is exceptional. However, as evident in the Figure 3.15, the disagreement lies at low frequencies and around the region of the crossover frequencies determined from describing functions. This is the source of the apparent mismatch between crossover frequencies shown earlier in Figure 3.7 and those presented in Figures 3.13 and 3.17. More importantly, this sheds doubt on the assumption that subject behaviour is linear and therefore, he/she will only respond at the forcing function frequencies. Such underestimation of pilot-vehicle crossover frequencies has been observed in research conducted at NASA and other establishments (see Newell[114], Gillespie[45] and Grant[3] for examples). This has in turn provided the motivation for understanding and modelling the remnant component. An in-depth study in this area was not conducted as it was beyond the scope of this project. As shown in Figure 3.16, the remnant can be modelled as a zero-mean Gaussian noise process. However, considerable inter-subject variation exists, highlighting the difficulty in modelling pilot control behaviour (even for such simple tasks) and interpreting results from pilot-model-in-the-loop simulations.

Parameter estimates obtained from this method are shown in Figures 3.13 and 3.17. Relatively

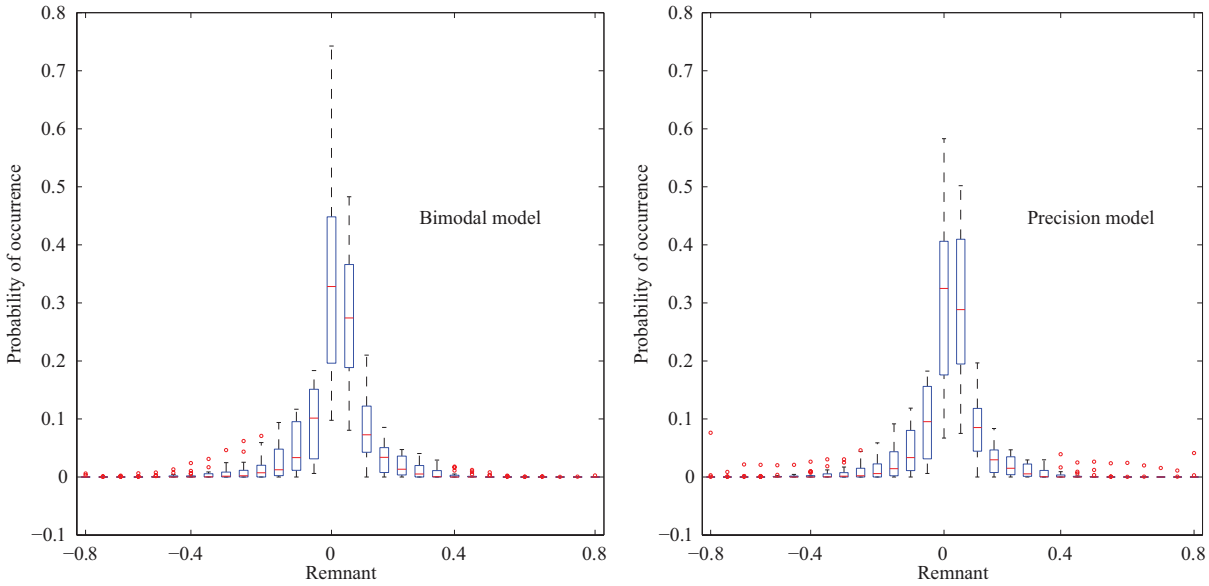

Figure 3.16: Remnant probability distribution for all compensatory tasks.

little variation was found for parameters representing the neuromuscular dynamics and time delay. Precision and bimodal model gains were found to be increasing with forcing function rms, but no significant conclusions can be made. Analysis of Variance (ANOVA) studies (see Appendix A for a summary of the statistical methodology) looking at the significance of this increase in K_p, $K_{p\theta}$ and K_{pq} gave p-values of 0.93, 0.96 and 0.79 respectively. This implies that observing such differences in the medians for the pilot population is highly likely and so no significant relationship exists between command gearing encroachment and pilot model gains. Also, changes in pilot lead-lag equalisation parameters were found to be insignificant. Consequently the rise in crossover frequency is purely due to the increase in gains. However, an interesting result is the negative lead compensation ($\tau_{L\theta}$) that some subjects exhibit; indicating that pilot introduces nonminimum phase characteristics via a right half plane zero.

The inter-subject variation in pilot model transfer functions are shown in Figure 3.18 which shows Subject B's frequency response as an example. The figure mainly highlights the variations in human linear control dynamics that:

1. must be considered during the design of a FCS and,
2. are considered in handling qualities criteria through a series of assumptions.

3.4.2 Tracking tasks

An example of the time-domain match obtained using the TFLS approach is shown in Figure 3.19. Apart from a number overshoots and undershoots, the model response follows the experimental signal relatively closely. Parameter identification results under different actuator rate-limits are shown in Figures 3.20 and 3.21. Results for the compensatory component showed no significant trends; see Appendix A for details.

ANOVA tests were conducted for each parameter and only the variations in τ_{Lf} and τ_{LLf} were found to be significant (see Table 3.3). An advantage for implementing the two pilot models becomes clear when testing the significance of the observed variation in data. It is only via comparison that results of the ANOVA tests can be verified. Furthermore, affects of omitting

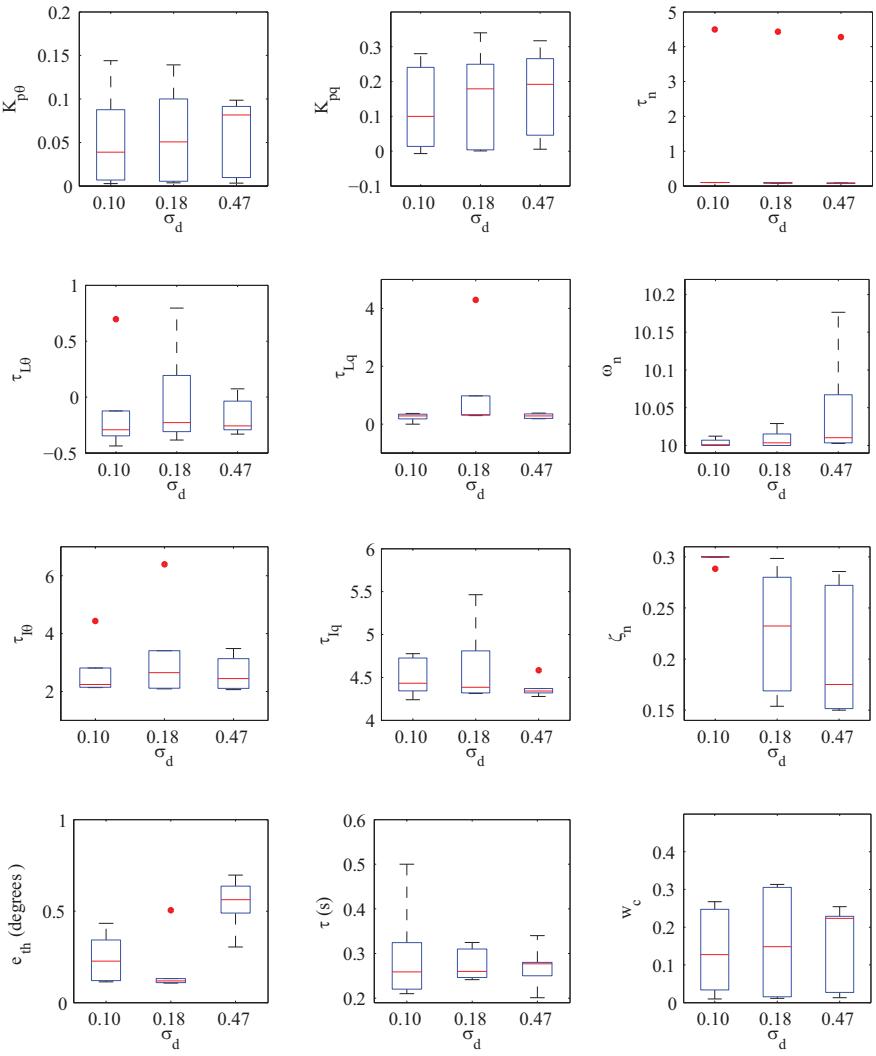

Figure 3.17: Bimodal model parameter values for compensatory tasks.

an outlier (in the precision model) on the hypothesis test results can also be observed. The drop in lead-lag equalisation values could be an effect of training. The subjects were not trained on the tracking tasks and these changes most likely reflect the modification of control characteristics in the learning process.

	K_f	τ_{Lf}	τ_{LLf}	τ_{If}	τ_{ILf}
Bimodal	0.893	0.109	0.098	0.394	0.214
Precision (with outlier)	0.921	0.121	0.023	0.665	0.393
Precision (outlier omitted)	0.897	0.541	0.550	0.346	0.650

Table 3.3: ANOVA p-values obtained for tracking component parameters.

Figure 3.22 presents the probability distribution function (PDF) for the remnant signals observed during tracking tasks. A zero-mean Gaussian noise source can also be used here for modelling this component. Inter-subject variations in this case are much lower than that for compensatory tasks. Such PDFs, shown in Figures 3.16 and 3.22, actually inform the engineer of the best and worst case remnant signal properties for use in pilot-model-in-the-loop simulation.

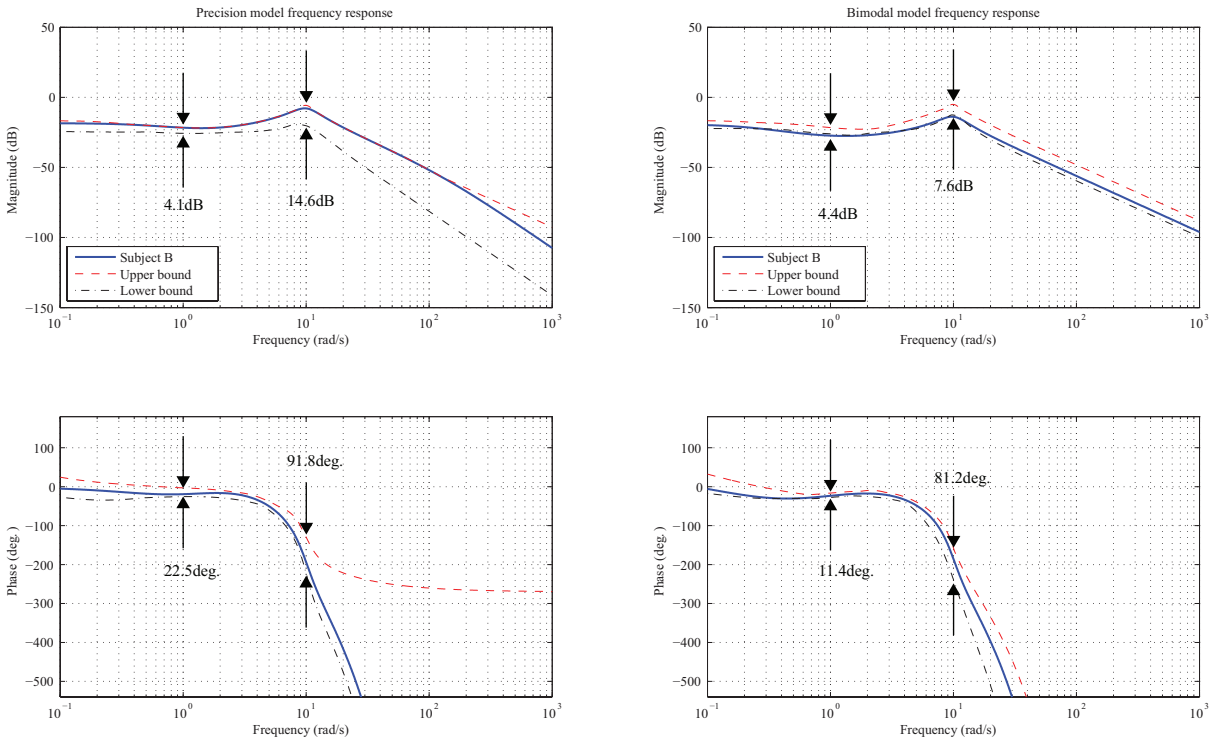

Figure 3.18: Frequency responses for compensatory pilot models.

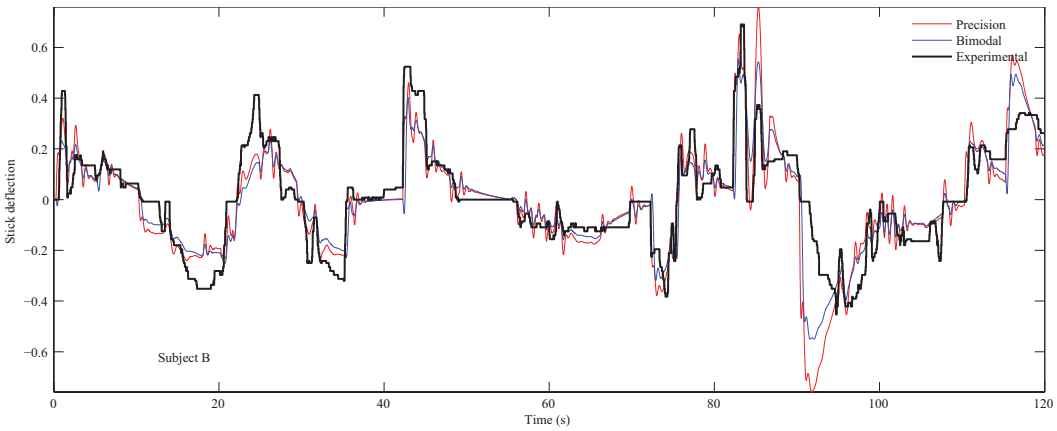

Figure 3.19: Example time domain result for TFLS process for tracking tasks.

3.5 Conclusions

The experimental method and results from a series of desktop simulation tests designed to investigate the manual control characteristics of relatively inexperienced pilots has been presented. Compensatory and tracking tasks were used to study the effects of nonlinear command gearing and actuator rate-limiting. A linear aircraft model coupled with nonlinear flight control system was used to produce realistic vehicle dynamics. Increased encroachment into the nonlinear gearing was found to make aggressive subjects resort to a high degree of crossover regression. The combined effects of rate-limiting and nonlinear command gearing was observed only for demanding tasks during which over-control was a typical feature.

The experimental data was then used for pilot model parameter identification. This was done by defining the identification process as a constrained nonlinear optimisation problem. Out of the three adopted approaches, the method which considered both frequency and time-domain

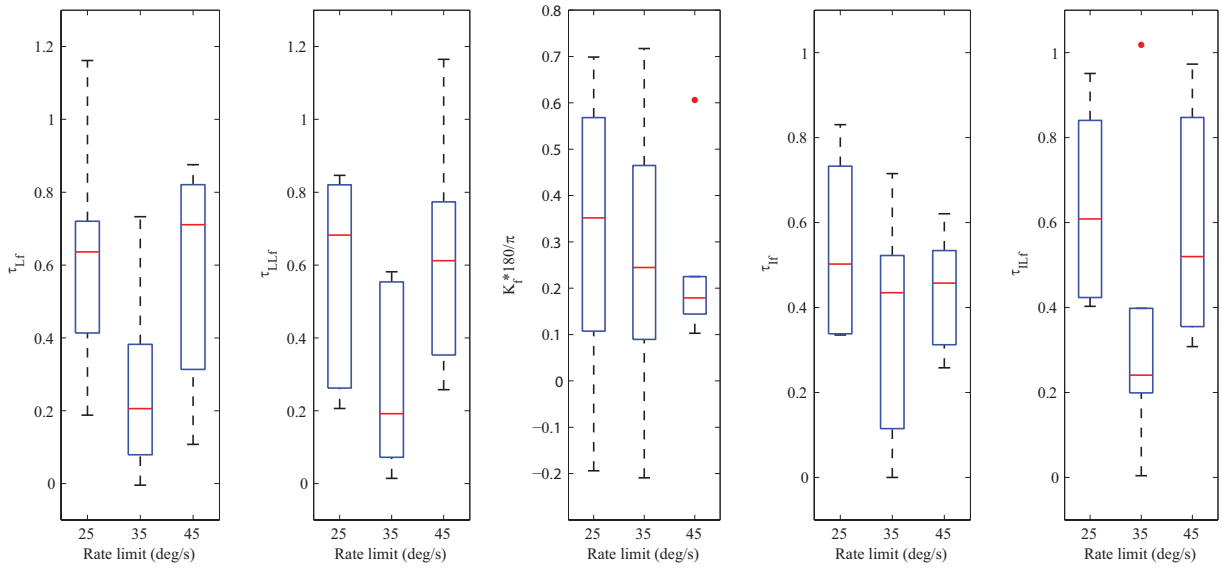

Figure 3.20: Bimodal model feed-forward parameter values for tracking tasks.

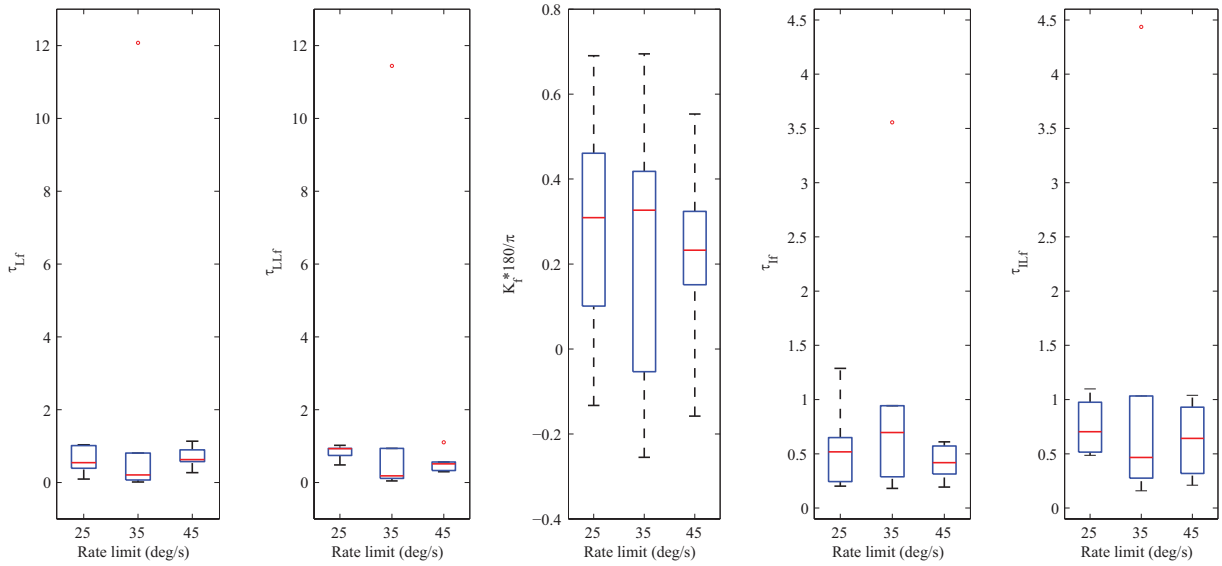

Figure 3.21: Precision model feed-forward parameter values for tracking tasks.

matching was found to provide the highest VAF and minimum remnant variance. The quality of the matching for the MLE method was found to be inconsistent.

Analysis of pilot model parameters for compensatory tasks showed that certain pilots introduced nonminimum phase characteristics. Furthermore, variations of up to 14.6 dB (at the resonant peak) were found in the pilot's linear dynamics alone. Upper and lower bounds in pilot model transfer functions were suggested. Regarding the tracking tasks, significant relationship between pilot model parameters and rate-limiting could not be observed. Inter-subject variations in the remnant PDFs for the two types of tasks only highlighted the difficulty in accurately modelling pilot dynamics. However, the PDFs provide a best and worst case models for future simulation work.

The flight control law was designed to meet the C* handling qualities criterion so that it maintained some resemblance of control laws onboard modern aircraft. Future work involving similar piloted trials that compare control laws that satisfy modern criteria such as Gibson's

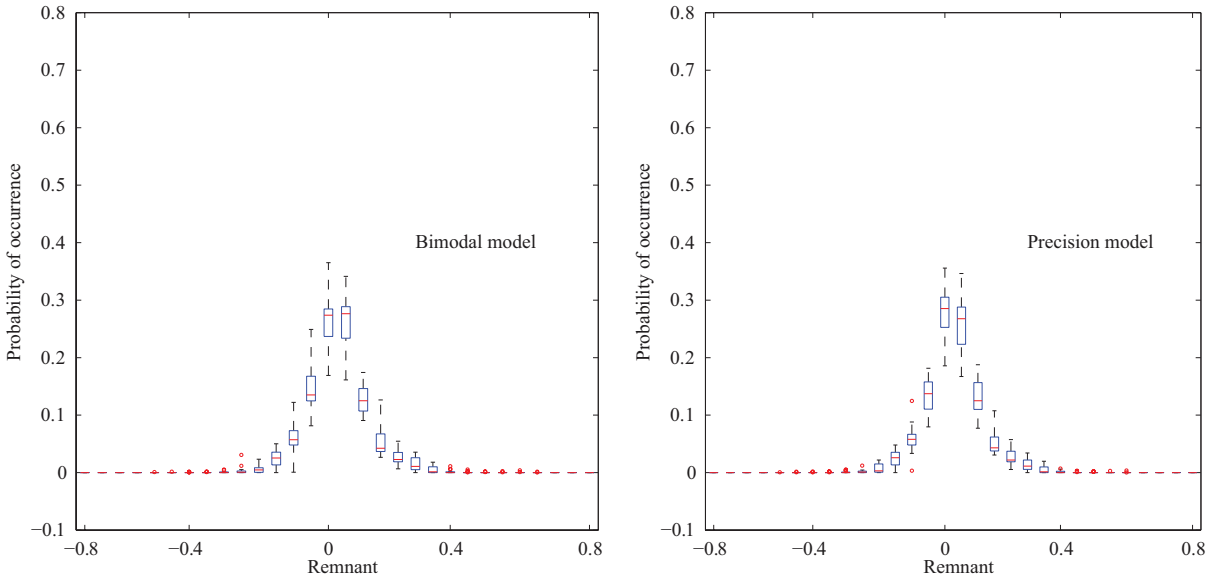

Figure 3.22: Remnant probability distributions for all tracking tasks.

dropback and time-domain Neal-Smith can provide considerable insight into the relationship between pilot model parameters and control laws.

These experiments have not only allowed a qualitative study of pilot dynamics, but also paved the way to quantify inter-subject variations in pilot equalisation. Future work should also consider expanding the experimental database by testing more subjects. A comparison with older and more experienced pilot should also be made. Another area that requires particular attention is the development of nonlinear manual control theory, even though this is a very complex research topic which can potentially have a very wide scope.

Such a study of pilot control dynamics, that focuses on relatively inexperienced pilots, highlights the necessity to review handling qualities criteria and their implementation; especially now as airlines order large numbers of short haul aircraft and the demand for pilots is rocketing.

CHAPTER 4

Control-theoretic model development

It is well known that pilots often control aircraft pitch and roll attitudes simultaneously to accomplish a desired manoeuvre. A point more relevant to this study is that pilots exhibit this strategy when conducting complex high gain tasks or when attempting to establish control during heavy turbulence. Figure 4.1 presents stick movements from the digital flight data recorder (DFDR) of a short haul aircraft during severe turbulence.[1] It is an example of the complex nature of stick movements input during gust encounters and other scenarios requiring aggressive recovery action. The pilot can be seen to prioritise longitudinal control over lateral around 84 seconds and vice versa immediately afterwards; demonstrating the well known attention allocation capability. On the other hand, multi-input-multi-output (MIMO) behaviour is clearly evident between 86 and 93 seconds. Therefore, a pilot model suitable for airframe loads analysis must be capable of reproducing such behaviour and thus, requires to be formulated within a MIMO framework. Since classical models are frequency domain SISO representations, their adaptation to a scenario such as that shown in Figure 4.1, will require time consuming sequential loop closures and considerable experience on behalf of the user. The OCM framework on the other hand, represents an elegant MIMO time domain approach, where all loop gains are calculated simultaneously. Furthermore, its algorithmic formulation minimises the time consuming tuning process required in the application of classical models.

This chapter presents the derivation of the modified optimal control model (MOCM) and its validation in frequency and time domains against experimental data. An example application of the MOCM to pitch and roll control of a large aircraft is used to demonstrate the model's MIMO capability. This is followed by a parameter variation study where the effects of key parameters on frequency response characteristics and time domain features are investigated.

4.1 The modified optimal control model

The MOCM formulation is an algorithmic approach to pilot modelling developed at NASA in the early 1990s[81]. It is based on the assumption that an experienced, well trained, highly motivated pilot will always act in an 'optimal' manner to achieve a desired goal. However, linear optimal control theory cannot be applied directly to this problem because of the necessity to capture time delay effects and remnant like components. Kleinman[115][16], Baron[116] and

[1] Stick deflections are normalised using the maximum lateral deflection.

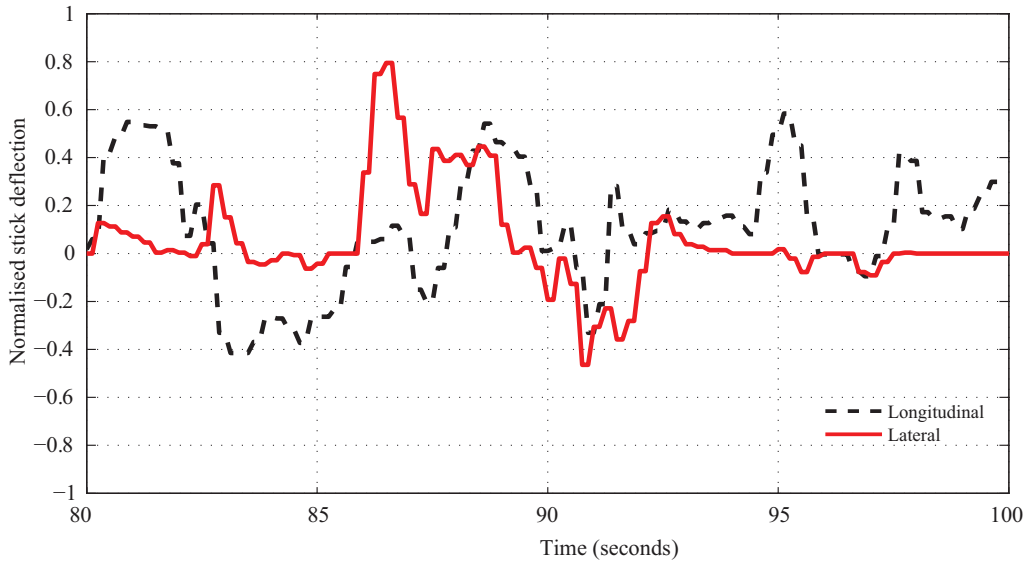

Figure 4.1: Example of pilot control actions during severe turbulence (normalised DFDR data).

Levison[79] showed in the original development of the OCM that an estimator-predictor setup addresses this issue and yields a non-anticipative optimal control input.[2] This setup allows the calculation of an optimal gain via the specification of a cost function, which is the sum of a fixed penalty due to the delays and the estimated states. For brevity, a detailed discussion of the theoretical development behind the original OCM is not presented here.

The MOCM is a variant of the OCM which allows for the direct calculation of the pilot model transfer functions. The modified algorithm is still capable of accounting for attention allocation and variations in neuromuscular lag. The layout of the MOCM is presented in Figure 4.2. The theoretical development merits presentation here not only because it is significantly different to the OCM, but also as a necessary reference for users of the code developed as part of this research. Moreover, the author feels that previous publications[117][88][118] do not present this in sufficient detail. A flow chart summarising the steps within the MOCM algorithm is presented in Figure 4.3.

4.1.1 Mathematical derivation

Any type of handling qualities analysis involving pilot models requires some form of task definition that involves a description of aircraft dynamics and usually an implicit characterisation of error compensation in the pilot perceived variable. For the latter, classical pilot models tend to use observable features on bode plots such as the droops and resonant peaks used by the Neal-Smith criteria[63]. The OCM on the other hand, uses the definition of a cost function for task characterisation and its corresponding weighting matrices to determine error compensation. The MOCM inherits this method of task definition and uses a quadratic cost function. Pilot compensation is calculated via the formulation of an LQG controller.

The first step in the algorithm is to define the pilot's internal aircraft model. This model would capture the response expected by the pilot from his/her input. The content and complexity of this model is dependant on the application and can range from a simple transfer function to a nonlinear Simulink model. In the latter case, the model is linearised and then reduced

[2] Anticipative control is where inputs are derived to be a function of estimated future states or outputs. Non-anticipative control is where an estimator is used to provide only the current states and therefore, the controller does not consist of any predictive element.

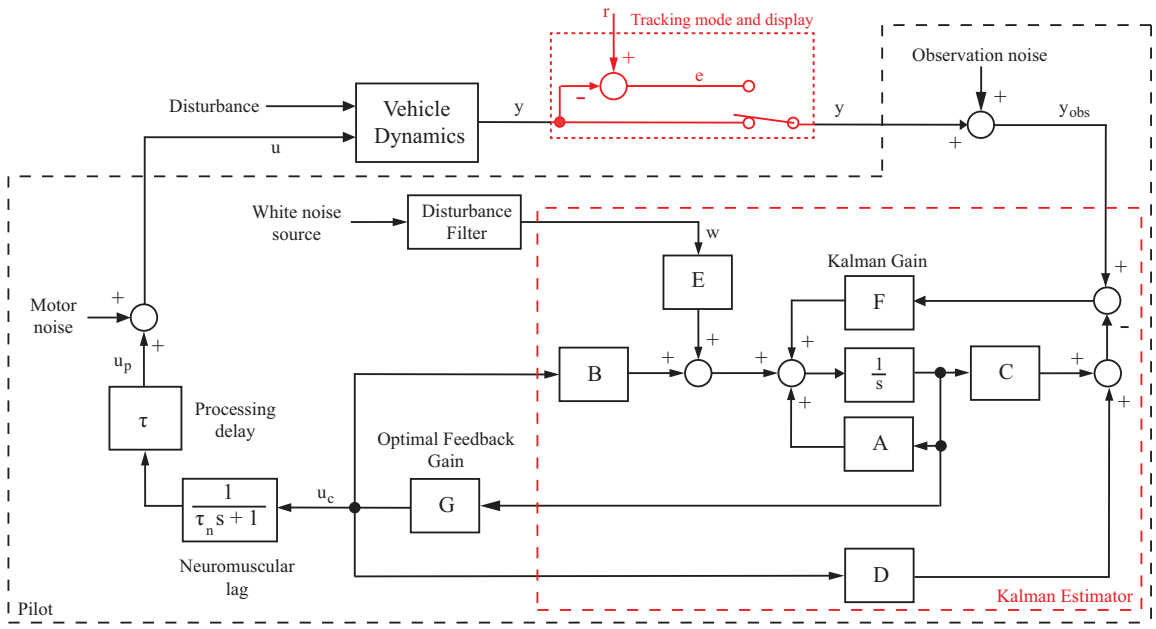

Figure 4.2: Conceptual block diagram for the modified optimal control pilot model.

via balanced truncation (see Reference [119] and Chapter 7 for example application). The theoretical development of the MOCM requires the following state space description of the internal model:

$$\begin{aligned} \dot{\mathbf{x}} &= \mathbf{A}\mathbf{x} + \mathbf{B}\mathbf{u} + \mathbf{E}\mathbf{w} \\ \mathbf{y} &= \mathbf{C}\mathbf{x} + \mathbf{D}\mathbf{u} \end{aligned} \tag{4.1.1}$$

where $\mathbf{x}(t) \in \mathbb{R}^n$, $\mathbf{y}(t) \in \mathbb{R}^r$, $\mathbf{u}(t) \in \mathbb{R}^m$ and $\mathbf{w}(t) \in \mathbb{R}^n$. The letters have their usual meaning and the state disturbance vector $\mathbf{w}(t)$ is typically modelled as a stationary zero-mean Gaussian white noise process with intensity $\mathbf{W} \geq 0$. The system is assumed to be controllable and observable.

Now, the cost function can be written as:

$$\mathcal{J} = E\left\{ \lim_{\eta\to\infty} \frac{1}{\eta} \int_0^{\eta} (\mathbf{y}^T\mathbf{Q}\mathbf{y} + \mathbf{u}^T\mathbf{R}\mathbf{u} + \dot{\mathbf{u}}^T\mathbf{S}\dot{\mathbf{u}})dt \right\} \tag{4.1.2}$$

where $\mathbf{y}(t)$ and $\mathbf{u}(t)$ are vectors of pilot's observed variables and control inputs respectively. $\mathbf{Q} \geq 0$ and $\mathbf{R} \geq 0$ are the corresponding weighting matrices. The weighting matrix $\mathbf{S} \geq 0$ represents the limitations on the pilot's bandwidth due to the neuromuscular system and also a natural tendency not to perform abrupt control actions. The importance of a correct definition of this cost function cannot be understated because it is the basis for the derivation of pilot transfer functions.

The next step is to define the pilot's effective time delay (τ) which is modelled as a second order Padé approximation:

$$\frac{u_c(s)}{u_p(s)} \approx \frac{1 - \frac{\tau}{2}s + \frac{\tau^2}{12}s^2}{1 + \frac{\tau}{2}s + \frac{\tau^2}{12}s^2} \tag{4.1.3}$$

This delay has been found to vary between 0.2 to 0.5 seconds[59]. Here, a second order approximation was chosen because it provided a good approximation to a pure delay over the frequency range of interest (0.1 rad/s to 10 rad/s). In state space form, the delay can be expressed as

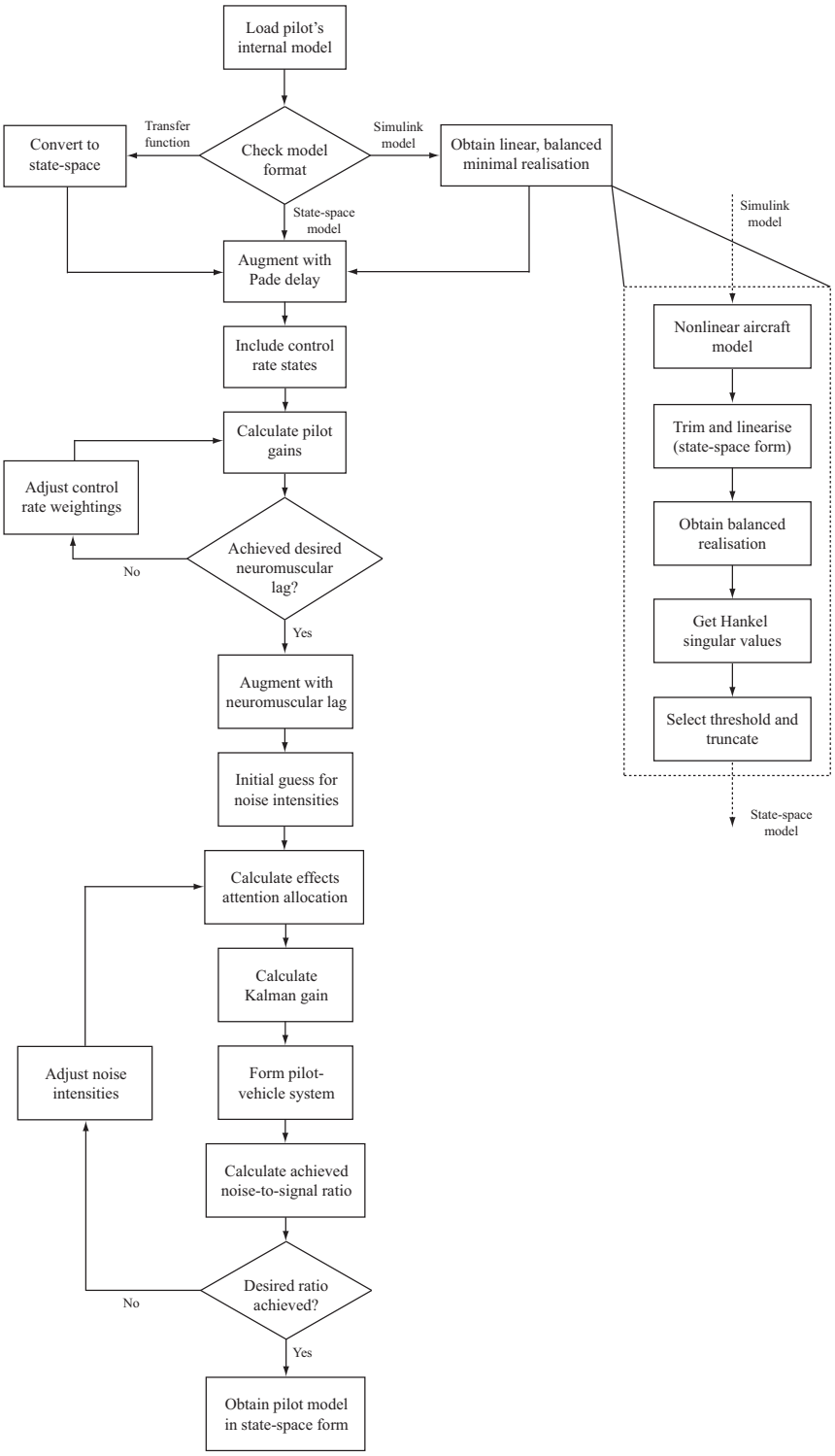

Figure 4.3: Modified optimal control model algorithm flowchart.

follows (see Equation 3.3.5 for details):

$$\begin{aligned} \dot{\mathbf{x}}_d &= \mathbf{A_d}\mathbf{x}_d + \mathbf{B_d}\mathbf{u}_p \\ \mathbf{u}_c &= \mathbf{C_d}\mathbf{x}_d + \mathbf{u}_p \end{aligned} \tag{4.1.4}$$

where $\mathbf{x}_d(t)$ is a vector of Padé delay states and $\mathbf{u}_p(t)$ is the pilot's control input before passing

through the delay. Equation 4.1.1 is augmented with this model as follows:

$$\begin{aligned}\begin{bmatrix}\dot{\mathbf{x}}\\ \dot{\mathbf{x}}_d\end{bmatrix} &= \begin{bmatrix}\mathbf{A} & \mathbf{BC_d}\\ 0 & \mathbf{A_d}\end{bmatrix}\begin{bmatrix}\mathbf{x}\\ \mathbf{x}_d\end{bmatrix} + \begin{bmatrix}\mathbf{B}\\ \mathbf{B_d}\end{bmatrix}\mathbf{u}_p + \begin{bmatrix}\mathbf{E}\\ 0\end{bmatrix}\mathbf{w}\\ \mathbf{y} &= \begin{bmatrix}\mathbf{C} & \mathbf{DC_d}\end{bmatrix}\begin{bmatrix}\mathbf{x}\\ \mathbf{x}_d\end{bmatrix} + \mathbf{Du}_p\end{aligned} \tag{4.1.5}$$

or in concise form:

$$\begin{aligned}\dot{\chi}_a &= \mathbf{A_a}\chi_a + \mathbf{B_a}\mathbf{u}_p + \mathbf{E_a}\mathbf{w}\\ \mathbf{y} &= \mathbf{C_a}\chi_a + \mathbf{Du}_p\end{aligned} \tag{4.1.6}$$

where $\chi_a = \begin{bmatrix}\mathbf{x} & \mathbf{x}_d\end{bmatrix}$.

Inclusion of the delay in this manner, at the output of the pilot model, removes the need of an OCM type predictor. Furthermore, this minimises the order of the MOCM as such delays are only required at the pilot model outputs, which are typically far fewer than the perceived variables (pilot model inputs). The generalised finite horizon quadratic cost function (Equation 4.1.2) can now be re-written as follows:

$$\begin{aligned}\mathcal{J} &= E\Bigg\{\lim_{\eta\to\infty}\frac{1}{\eta}\int_0^\eta\Big(\chi_a^T\mathbf{C_a}^T\mathbf{QC_a}\chi_a + \chi_a^T\mathbf{C_a}^T\mathbf{QDu}_p + \mathbf{u}_p^T\mathbf{D}^T\mathbf{QC_a}\chi_a\\ &+ \mathbf{u}_p^T\left(\mathbf{D}^T\mathbf{QD}+\mathbf{R}\right)\mathbf{u}_p + \dot{\mathbf{u}}_p^T\mathbf{S}\dot{\mathbf{u}}_p\Big)dt\Bigg\}\\ &= E\Bigg\{\lim_{\eta\to\infty}\frac{1}{\eta}\int_0^\eta\Bigg(\begin{bmatrix}\chi_a & \mathbf{u}_p\end{bmatrix}\begin{bmatrix}\mathbf{C_a}^T\mathbf{QC_a} & \mathbf{C_a}^T\mathbf{QD}\\ \mathbf{D}^T\mathbf{QC_a} & \mathbf{D}^T\mathbf{QD}+\mathbf{R}\end{bmatrix}\begin{bmatrix}\chi_a\\ \mathbf{u}_p\end{bmatrix} + \dot{\mathbf{u}_p}^T\mathbf{S}\dot{\mathbf{u}_p}\Bigg)dt\Bigg\}\end{aligned} \tag{4.1.7}$$

It is well known that the neuromuscular system limits the pilot's bandwidth. Such a limitation is incorporated by considering the control rate. The following formulation includes control rate and allows the application of LQG techniques to obtain an optimal control law:

$$\begin{aligned}\begin{bmatrix}\dot{\mathbf{x}}\\ \dot{\mathbf{x}}_d\\ \dot{\mathbf{u}}_p\end{bmatrix} &= \begin{bmatrix}\mathbf{A} & \mathbf{BC_d} & \mathbf{B}\\ 0 & \mathbf{A_d} & \mathbf{B_d}\\ 0 & 0 & 0\end{bmatrix}\begin{bmatrix}\mathbf{x}\\ \mathbf{x}_d\\ \mathbf{u}_p\end{bmatrix} + \begin{bmatrix}0\\ 0\\ 1\end{bmatrix}\dot{\mathbf{u}}_p + \begin{bmatrix}\mathbf{E}\\ 0\\ 0\end{bmatrix}\mathbf{w}\\ \mathbf{y}_{obs} &= \begin{bmatrix}\mathbf{C} & \mathbf{DC_d} & \mathbf{D}\end{bmatrix}\begin{bmatrix}\mathbf{x}\\ \mathbf{x}_d\\ \mathbf{u}_p\end{bmatrix} + \mathbf{v}_y\end{aligned} \tag{4.1.8}$$

or

$$\begin{aligned}\dot{\chi} &= \mathbf{A_o}\chi + \mathbf{B_o}\dot{\mathbf{u}}_p + \mathbf{E_o}\mathbf{w}\\ \mathbf{y}_{obs} &= \mathbf{C_o}\chi + \mathbf{v}_y\end{aligned} \tag{4.1.9}$$

Here, $\mathbf{y}_{obs}(t)$ is a vector of pilot perceived variables and $\mathbf{v}_y(t)$ is the observation noise, also modelled as a stationary zero-mean Gaussian white noise with intensity $\mathbf{V_y} > 0 \in \mathbb{R}^{r\times r}$.

The full state feedback optimal input can be found by considering the Hamilton-Jacobi-Bellman (HJB) equation[120]:

$$-\frac{\partial V}{\partial t} = \min_{\dot{\mathbf{u}}_p\in\dot{U}_p}\left\{\chi^T\mathbf{C_o}^T\mathbf{Q_o}\mathbf{C_o}\chi + \dot{\mathbf{u}}_p^T\dot{\mathbf{u}}_p + \frac{\partial V}{\partial\chi}\left(\mathbf{A_o}\chi + \mathbf{B_o}\dot{\mathbf{u}}_p\right)\right\} \tag{4.1.10}$$

where V is a Lyapunov function defined as follows:

$$V = \chi^T\mathbf{X}\chi \tag{4.1.11}$$

and

$$\mathbf{Q_o} = \begin{bmatrix} \mathbf{C_a}^T\mathbf{Q}\mathbf{C_a} & \mathbf{C_a}^T\mathbf{Q}\mathbf{D} \\ \mathbf{D}^T\mathbf{Q}\mathbf{C_a} & \mathbf{D}^T\mathbf{Q}\mathbf{D}+\mathbf{R} \end{bmatrix} \tag{4.1.12}$$

It follows from Equation 4.1.10 that:

$$\begin{aligned} -\frac{\partial V}{\partial t} &= \min_{\dot{\mathbf{u}}_p \in \dot{U}_p} \left\{ \chi^T \mathbf{C_o}^T \mathbf{Q_o} \mathbf{C_o} \chi + \dot{\mathbf{u}}_p^T \dot{\mathbf{u}}_p + \left(\chi^T \mathbf{X} + \mathbf{X}\chi\right)\left(\mathbf{A_o}\chi + \mathbf{B_o}\dot{\mathbf{u}}_p\right) \right\} \\ &= \min_{\dot{\mathbf{u}}_p \in \dot{U}_p} \left\{ \begin{bmatrix} \chi & \dot{\mathbf{u}}_p \end{bmatrix} \begin{bmatrix} \mathbf{C_o}^T\mathbf{Q_o}\mathbf{C_o} + \mathbf{X}\mathbf{A_o} + \mathbf{A_o}^T\mathbf{X} & \mathbf{B_o}^T\mathbf{X} \\ \mathbf{B_o}^T\mathbf{X} & \mathbf{S} \end{bmatrix} \begin{bmatrix} \chi \\ \dot{\mathbf{u}}_p \end{bmatrix} \right\} \end{aligned} \tag{4.1.13}$$

This is now in a quadratic form which can be minimised via the following lemma[121]:

Lemma 1 *Given symmetric matrices* $\mathbf{\Gamma_1}$ *and* $\mathbf{\Gamma_2} > 0$*, then*

$$\min_{x_2 \in X_2} \left\{ \begin{bmatrix} x_1 & x_2 \end{bmatrix} \begin{bmatrix} \mathbf{\Gamma_1} & \mathbf{\Delta}^T \\ \mathbf{\Delta} & \mathbf{\Gamma_2} \end{bmatrix} \begin{bmatrix} x_1 \\ x_2 \end{bmatrix} \right\} = x_1^T \left(\mathbf{\Gamma_1} - \mathbf{\Delta}^T \mathbf{\Gamma_2}^{-1} \mathbf{\Delta} \right) x_1 \tag{4.1.14}$$

with the following minimum full state feedback:

$$x_2 = -\mathbf{\Gamma_2}^{-1}\mathbf{\Delta} x_1 \tag{4.1.15}$$

Therefore, using the above equation, the optimal control law is given by the following full-state feedback relation[115]:

$$\dot{\mathbf{u}}_p = -\mathbf{S}^{-1}\mathbf{B_o}^T\mathbf{X}\hat{\chi} \tag{4.1.16}$$

where $\hat{\chi}$ is the vector of state estimates. Substituting Equation 4.1.16 into Equation 4.1.13 and using the results from the above lemma:

$$\begin{aligned} -\frac{\partial V}{\partial t} &= \min_{\dot{\mathbf{u}}_p \in \dot{U}_p} \left\{ \begin{bmatrix} \chi & \dot{\mathbf{u}}_p \end{bmatrix} \begin{bmatrix} \mathbf{C_o}^T\mathbf{Q_o}\mathbf{C_o} + \mathbf{X}\mathbf{A_o} + \mathbf{A_o}^T\mathbf{X} & \mathbf{B_o}^T\mathbf{X} \\ \mathbf{B_o}^T\mathbf{X} & \mathbf{S} \end{bmatrix} \begin{bmatrix} \chi \\ \dot{\mathbf{u}}_p \end{bmatrix} \right\} \\ &= \chi^T \left(\mathbf{C_o}^T\mathbf{Q_o}\mathbf{C_o} + \mathbf{X}\mathbf{A_o} + \mathbf{A_o}^T\mathbf{X} - \mathbf{X}\mathbf{B_o}\mathbf{S}^{-1}\mathbf{B_o}^T\mathbf{X} \right) \chi \end{aligned} \tag{4.1.17}$$

The minima can now be evaluated by equating the above to zero. Therefore, the control input which minimises the cost function specified in Equation 4.1.2 is given by Equation 4.1.16 where $\mathbf{X}$ is the solution to the following algebraic Riccati equation (ARE):

$$\mathbf{A_o}^T\mathbf{X} + \mathbf{X}\mathbf{A_o} + \mathbf{C_o}^T\mathbf{Q_o}\mathbf{C_o} - \mathbf{X}\mathbf{B_o}\mathbf{S}^{-1}\mathbf{B_o}^T\mathbf{X} = 0 \tag{4.1.18}$$

A sufficient condition for the existence of a unique solution to this ARE is that[122]:

$$\begin{bmatrix} \mathbf{Q_o} & 0 \\ 0 & \mathbf{S} \end{bmatrix} > 0 \tag{4.1.19}$$

Full state feedback plays a crucial role in the MOCM; in contrast to its role in flight control system design where it only provides an effective starting point. Classical pilot models rely on engineering intuition to identify such variables. Knowledge regarding the importance allocated by the pilot to each of his/her senses was also necessary in this process and required explicit treatment. The MOCM formulation assumes the pilot is aware of all the states within his/her internal aircraft model and reacts in an optimal manner to minimise the cost function specified in Equation 4.1.2. For example: if an inceptor model is included within the internal model, the state feedback from the inceptor represents the proprioceptive sensory loop. All the other senses are thus treated implicitly within this framework.

Now, Equation 4.1.16 can be written as follows to separate the control input component:

$$\dot{u}_p = -\left[\begin{array}{cccc} g_1 & g_2 & \cdots & g_n \end{array}\right]\left[\begin{array}{c} x \\ x_d \end{array}\right] - g_{n+1}u_p \tag{4.1.20}$$

and defining neuromuscular lag as

$$\tau_n = \frac{1}{g_{n+1}} \tag{4.1.21}$$

implies that the pilot's commanded input $u_c(t)$, that is the input signal prior to being applied by the neuromuscular system, is as follows:

$$\begin{aligned} u_c &= -\tau_n\left[\begin{array}{cccc} g_1 & g_2 & \cdots & g_n \end{array}\right]\left[\begin{array}{c} x \\ x_d \end{array}\right] && (4.1.22)\\ &= \tau_n\dot{u}_p + u_p && (4.1.23)\\ &= -\mathbf{G}\left[\begin{array}{c} x \\ x_d \end{array}\right] && (4.1.24) \end{aligned}$$

Therefore, the neuromuscular lag can be considered as the following transfer function:

$$\frac{u_c(s)}{u_p(s)} = \frac{1}{\tau_n s + 1} \tag{4.1.25}$$

However, since $1/\tau_n$ is the last element of the calculated gain, its value cannot be directly specified. Iterations with different control rate weightings eventually yield the desired neuromuscular lag. Unlike earlier versions of the MOCM where manual iterations were required, here the desired neuromuscular lag is achieved automatically through a multi-objective goal attainment optimisation algorithm (`fgoalattain`) within MATLAB. The desired τ_n value is achieved to within ± 0.001.

A stationary zero-mean Gaussian white noise signal $\mathbf{v}_u(t)$, with intensity $\mathbf{V_u} \geq 0 \in \mathbb{R}^{m\times m}$, is added to $\mathbf{u}(t)$ to model the pilot's control input noise:

$$\tau_n\dot{\mathbf{u}}_p + \mathbf{u}_p = \mathbf{u}_c + \mathbf{v}_u \tag{4.1.26}$$

It should be noted that the exclusion of $\mathbf{v}_u(t)$ from the calculation of pilot gains results in a suboptimal control law. Signals $\mathbf{v}_u(t)$ and $\mathbf{v}_y(t)$ are analogous to the remnant noise signal used in classical pilot models.

The next step is the formulation of the Kalman estimator required to generate the state estimates in Equation 4.1.16. Equations 4.1.8 and 4.1.26 are combined to formulate the equation used to obtain the Kalman gain:

$$\left[\begin{array}{c} \dot{\mathbf{x}} \\ \dot{\mathbf{x}}_d \\ \dot{\mathbf{u}}_p \end{array}\right] = \left[\begin{array}{ccc} \mathbf{A} & \mathbf{BC_d} & \mathbf{B} \\ 0 & \mathbf{A_d} & \mathbf{B_d} \\ 0 & 0 & -1/\tau_n \end{array}\right]\left[\begin{array}{c} \mathbf{x} \\ \mathbf{x}_d \\ \mathbf{u}_p \end{array}\right] + \left[\begin{array}{c} 0 \\ 0 \\ 1/\tau_n \end{array}\right]\mathbf{u}_c + \left[\begin{array}{cc} \mathbf{E} & 0 \\ 0 & 0 \\ 0 & 1/\tau_n \end{array}\right]\left[\begin{array}{c} \mathbf{w} \\ \mathbf{v}_u \end{array}\right] \tag{4.1.27}$$

or

$$\dot{\chi} = \mathbf{A_e}\chi + \mathbf{B_e}\mathbf{u}_c + \mathbf{E_e}\mathbf{w}_e \tag{4.1.28}$$

The output equation remains the same as that in Equation 4.1.8. Attention allocation effects are now calculated from an initial random guess for the variances in the observation and control variables. This provides a starting point for the process of achieving the desired observation and control noise-to-signal ratios.

State estimates are given by the following Kalman filter formulation:

$$\begin{aligned} \dot{\hat{\chi}} &= \mathbf{A_e}\hat{\chi} + \mathbf{B_e}\mathbf{u}_c + \mathbf{F}(\mathbf{y}_{obs} - \hat{\mathbf{y}}) \\ \dot{\hat{\chi}} &= (\mathbf{A_e} - \mathbf{FC_e})\hat{\chi} + \mathbf{FC_e}\chi + \mathbf{B_e}\mathbf{u}_c + \mathbf{F}\mathbf{v}_y && (4.1.29) \end{aligned}$$

where

$$\mathbf{F} = \mathbf{\Sigma C_o}^T \mathbf{V_y}^{-1} \tag{4.1.30}$$

and $\mathbf{\Sigma} > 0$ is the covariance matrix of the estimation error and the solution to the following ARE:

$$\mathbf{A_o \Sigma} + \mathbf{\Sigma A_o}^T + \mathbf{W_e} - \mathbf{\Sigma C_o}^T \mathbf{V_y}^{-1} \mathbf{C_o \Sigma} = 0 \tag{4.1.31}$$

where

$$\mathbf{W_e} = \begin{bmatrix} \mathbf{W} & 0 \\ 0 & \mathbf{V_u} \end{bmatrix} \tag{4.1.32}$$

A sufficient condition for the existence of a unique solution to this Ricatti equation is as follows[122]:

$$\begin{bmatrix} \mathbf{W_e} & 0 \\ 0 & \mathbf{V_y} \end{bmatrix} > 0 \tag{4.1.33}$$

Now, the following state-space realisation of the PVS can be derived:

$$\begin{aligned} \begin{bmatrix} \dot{\chi} \\ \dot{\hat{\chi}} \end{bmatrix} &= \begin{bmatrix} \mathbf{A_e} & -\mathbf{B_e G_1} \\ \mathbf{FC_o} & \mathbf{A_e} - \mathbf{FC_o} - \mathbf{B_e G_1} \end{bmatrix} \begin{bmatrix} \chi \\ \hat{\chi} \end{bmatrix} + \begin{bmatrix} \mathbf{E_e} & 0 \\ 0 & \mathbf{F} \end{bmatrix} \begin{bmatrix} \mathbf{w} \\ \mathbf{v}_y \end{bmatrix} \\ \begin{bmatrix} \mathbf{y}_{obs} \\ \mathbf{u} \end{bmatrix} &= \begin{bmatrix} \mathbf{C_o} & 0 \\ 0 & \begin{bmatrix} \mathbf{C_d} & 1 & 0 \end{bmatrix} \end{bmatrix} \begin{bmatrix} \chi \\ \hat{\chi} \end{bmatrix} \end{aligned} \tag{4.1.34}$$

where $\mathbf{G_1} = \begin{bmatrix} \mathbf{G} & 0 \end{bmatrix}$. A state-space realisation of the pilot's dynamics can also be derived:

$$\begin{aligned} \begin{bmatrix} \dot{\hat{\chi}} \\ \dot{\mathbf{u}}_p \\ \dot{\mathbf{x}}_d \end{bmatrix} &= \begin{bmatrix} \mathbf{A_e} - \mathbf{FC_o} - \mathbf{B_e G_1} & 0 & 0 \\ \mathbf{G_1}/\tau_n & -1/\tau_n & 0 \\ 0 & \mathbf{B_d} & \mathbf{A_d} \end{bmatrix} \begin{bmatrix} \hat{\chi} \\ \mathbf{u}_p \\ \mathbf{x}_d \end{bmatrix} + \begin{bmatrix} \mathbf{F} & \mathbf{F} & 0 \\ 0 & 0 & 1/\tau_n \\ 0 & 0 & 0 \end{bmatrix} \begin{bmatrix} \mathbf{y} \\ \mathbf{v}_y \\ \mathbf{v}_u \end{bmatrix} \\ \mathbf{u} &= \begin{bmatrix} 0 & 1 & \mathbf{C_d} \end{bmatrix} \begin{bmatrix} \hat{\chi} \\ \mathbf{u}_p \\ \mathbf{x}_d \end{bmatrix} \end{aligned} \tag{4.1.35}$$

4.1.2 Treatment of observation and control noise signals

The MOCM algorithm also inherits the OCM assumption that the stationary zero-mean Gaussian white noise signals, with appropriate intensities, added to the observed variables and the control input capture the remnant component of the pilot's input. The noise intensity matrices determine the Kalman gain (Equations 4.1.31 and 4.1.33) and therefore, significantly affect the control input generated by the pilot model. The nature of these matrices require an iterative approach towards obtaining the appropriate intensity values.

The observation noise intensity matrix is actually a function of the display type, physical environment and pilot characteristics and is quite difficult to specify numerically. However, it has been found that over a wide range of foveal viewing conditions the following relationship between vehicle output and observation noise intensity holds relatively well[16]:

$$\mathbf{V}_{\mathbf{y}i} = \frac{\pi \rho_{y_i} \sigma_{y_i}^2}{f_i \text{erfc}(T_i/\sigma_{y_i}\sqrt{2})} \qquad \text{for} \qquad i = 1, 2, ...r \tag{4.1.36}$$

where σ_{y_i} is the standard deviation associated with $y_i(t)$ and ρ_i is the average signal-to-noise ratio, found to remain roughly constant around 0.01[78]. The variable f_i represents the fraction of attention allocated towards $y_i(t)$ and satisfies:

$$\sum_{i=1}^{r} f_i = 1 \tag{4.1.37}$$

The variable T_i within the error function is aimed to represent a perceptual threshold.[3] Letting the denominator in Equation 4.1.36 equal to unity reverts the model to its original form as proposed by Kleinman et al[16].

The pilot's remnant representation is completed by an injected motor noise. The motor noise is also assumed to be a stationary zero-mean Gaussian white noise, shaped via an intensity matrix. Earlier studies[86][77][123] have found the following relationship through model matching techniques:

$$\mathbf{V}_{\mathbf{u}i} = \pi \rho_{u_i} \sigma_{u_i}^2 \qquad \text{for} \qquad i = 1, 2, ...m \tag{4.1.38}$$

where σ_{u_i} is the standard deviation associated with $u_i(t)$. ρ_{u_i} is the corresponding average signal-to-noise ratio, found to remain roughly constant at approximately 0.003[78]. It should be noted that injection of motor noise makes the pilot control input theoretically suboptimal. However, Kleinman[86] and Baron[116] argue that its inclusion does not affect the closed-loop system performance in the frequency range of interest, which is that of manual control with an upper limit of approximately 30 rad/s.

Since estimating σ_{y_i} and σ_{u_i} would require *a priori* knowledge of the pilot-vehicle system the algorithm generates a random positive initial guess for these variables and iterates with different values of noise intensities till the desired signal-to-noise ratio is achieved; each iteration requiring a recalculation of the pilot model. Unlike the OCM and earlier versions of the MOCM, the algorithm has automated this process through the use of constrained nonlinear optimisation algorithm (`fmincon`) within MATLAB. These iterations are represented by the final loop in Figure 4.3.

The novel feature of the MOCM algorithm developed here is its implementation within MATLAB so that it can be used for event simulation purposes. This has also given access to the use of modern optimisation algorithms such as `fgoalattain` and `fmincon` that automate the process and reduce the time involved in generating pilot models.

4.1.3 Treatment of tracking tasks

The conceptual block diagram in Figure 4.2 also includes components necessary for modelling tracking or reference following manual control mode, allowing the simulation of behaviour during tasks like flight director following. Although its inclusion within the framework of the MOCM algorithm is relatively simple, it relies on a clear definition of: (a) the pilot's internal model that is modified to include the reference cue signal and, (b) other perceived variables and their inclusion in the resulting cost function. It is assumed in the context of this work, that the display can provide attitude and error information only, whilst the pilot can separately deduce rate of change in these variables.

The reference and error signals are included within the internal model as follows[124]:

$$\begin{aligned} \dot{\mathbf{x}} &= \mathbf{A}\mathbf{x} + \begin{bmatrix} \mathbf{B} & 0 & \mathbf{E} \end{bmatrix} \begin{bmatrix} \mathbf{u} \\ \mathbf{r} \\ \mathbf{w} \end{bmatrix} \\ \begin{bmatrix} \mathbf{y} \\ \mathbf{y}_e \end{bmatrix} &= \begin{bmatrix} \mathbf{C} \\ -\mathbf{C} \end{bmatrix} \mathbf{x} + \begin{bmatrix} \mathbf{D} & 0 \\ -\mathbf{D} & 1 \end{bmatrix} \begin{bmatrix} \mathbf{u} \\ \mathbf{r} \end{bmatrix} \end{aligned} \tag{4.1.39}$$

[3]For the purposes of this project, perceptual limitations will be implemented explicitly within models of the human sensory system.

The resulting affect on task definition is modelled by formulating the cost function as follows:

$$\begin{aligned}\mathcal{J} &= E\left\{\lim_{\eta\to\infty}\frac{1}{\eta}\int_0^\eta (\mathbf{y}-\mathbf{r})^T\,\mathbf{Q}\,(\mathbf{y}-\mathbf{r})+\mathbf{u}^T\mathbf{R}\mathbf{u}+\dot{\mathbf{u}}^T\mathbf{S}\dot{\mathbf{u}}dt\right\}\\ &= \left\{\lim_{\eta\to\infty}\frac{1}{\eta}\int_0^\eta \chi_r^T\mathbf{Q}_\mathbf{r}\chi_r+\dot{\mathbf{u}}^T\mathbf{S}\dot{\mathbf{u}}dt\right\}\end{aligned} \tag{4.1.40}$$

where $\chi_r = [\ \mathbf{x}\quad \mathbf{u}\quad \mathbf{r}\ ]^T$ and after some algebraic manipulation, $\mathbf{Q_r} > 0 \in \mathbb{R}^{r\times r}$ can be found to be:

$$\mathbf{Q_r} = \begin{bmatrix} \mathbf{C}^T\mathbf{Q}\mathbf{C} & \mathbf{D}^T\mathbf{Q}\mathbf{C} & -\mathbf{C}^T\mathbf{Q} \\ \mathbf{C}^T\mathbf{Q}\mathbf{D} & \mathbf{D}^T\mathbf{Q}\mathbf{D}+\mathbf{R} & -\mathbf{D}^T\mathbf{Q} \\ -\mathbf{C}^T\mathbf{Q} & -\mathbf{D}^T\mathbf{Q} & \mathbf{Q} \end{bmatrix} \tag{4.1.41}$$

4.2 Model validation

4.2.1 Frequency domain validation

Kleinman's original OCM and earlier classical pilot models were validated with frequency domain data from a series of manual control experiments conducted by McRuer et al[22] at STI Inc. These involved subjects performing single manipulator based tracking tasks with different vehicle dynamics. An indicator on a display presented system error and also allowed the deduction of error rate.[4] Three types of vehicle transfer functions representing the three basic command systems were investigated in that study: position, velocity and acceleration command. Detailed description of the experimental setups can be found in work done by McRuer et al[59][61][22] and Kleinman et al[86].

Validation was done by effectively reproducing McRuer's experiment in simulation where the subject was replaced by the pilot model. The cost function was selected to model the objectives given to the subjects. Since they were told to concentrate on minimising the displayed error, the cost function did not penalise control input and no weighting was imposed on the rate of change of error. Therefore, the cost function in Equation 4.1.2 reduces to the following:

$$\mathcal{J} = E\left\{\lim_{\eta\to\infty}\frac{1}{\eta}\int_0^\eta \left(\begin{bmatrix} e & \dot{e}\end{bmatrix}\begin{bmatrix}1&0\\0&0\end{bmatrix}\begin{bmatrix}e\\\dot{e}\end{bmatrix}+S\dot{u}^2\right)dt\right\} = E\left\{\lim_{\eta\to\infty}\frac{1}{\eta}\int_0^\eta e^2+S\dot{u}^2dt\right\} \tag{4.2.1}$$

where e, $\dot{e}$ and $u(t)$ are the error, error rate and control input respectively. S is the weighting on the rate of change in control input, which is determined within the iterative process for neuromuscular lag in the algorithm. Since error and error rate are the inputs to the MOCM in this case, the following equation relates the MOCM output to these input:

$$\delta u(t) = \frac{\partial u(t)}{\partial e(t)}\delta e(t) + \frac{\partial u(t)}{\partial \dot{e}(t)}\delta\dot{e}(t) \tag{4.2.2}$$

which gives the following transfer function for the pilot model:

$$\frac{u(s)}{e(s)} = \frac{u(s)}{e(s)} + s\frac{u(s)}{\dot{e}(s)} \tag{4.2.3}$$

In this case, the above transfer function is dimensionless as error and control inputs are both measured in degrees. Generally, the units of this transfer function rely on the specific signals used during an experiment. Early manual control experiments focusing on the identification

[4] When presented with information in the form of an indicator based display (for example, a needle pointer or a horizon line), humans can directly perceive magnitude and deduce rate of change.

of operator dynamics[111][76] have taken the error to be a distance presented on a 2D display with units of centimetres or millimeters. On the other hand, handling qualities studies[83][125] have assumed the display dynamics to be negligible and assumed the error to be an aircraft attitude with units of radians or degrees. This approach is driven by a desire to predict handling qualities through pilot-model-in-the-loop simulation. Unless otherwise stated, all manual control experiments in this study adopt the latter approach. Of course, it follows that pilot-model-in-the-loop simulation, such as those done by Lone[119][126], Bruzi[127] and Shen[128], can only be conducted and interpreted if the input and output signals and their units to the pilot model are clearly defined.

MOCM Parameters	Command system		
	Acceleration	Velocity	Position
Vehicle transfer function	$1/s^2$	$1/s$	$40/(s+40)$
Pilot's inherent delay, τ	0.21	0.15	0.15
Neuromuscular lag, τ_n	0.10	0.08	0.11
Disturbance intensity, $\mathbf{W}$	0.216	8.8	10
Disturbance filter	$1/(s+2)$	$1/(s+2)$	$1/(s^2+4s+4)$
Noise-to-signal ratios (ρ_u, ρ_y) (dB)	(-50,-40)	(-50,-40)	(-50,-40)

Table 4.1: Parameter values used for the validation of MOCM algorithm.

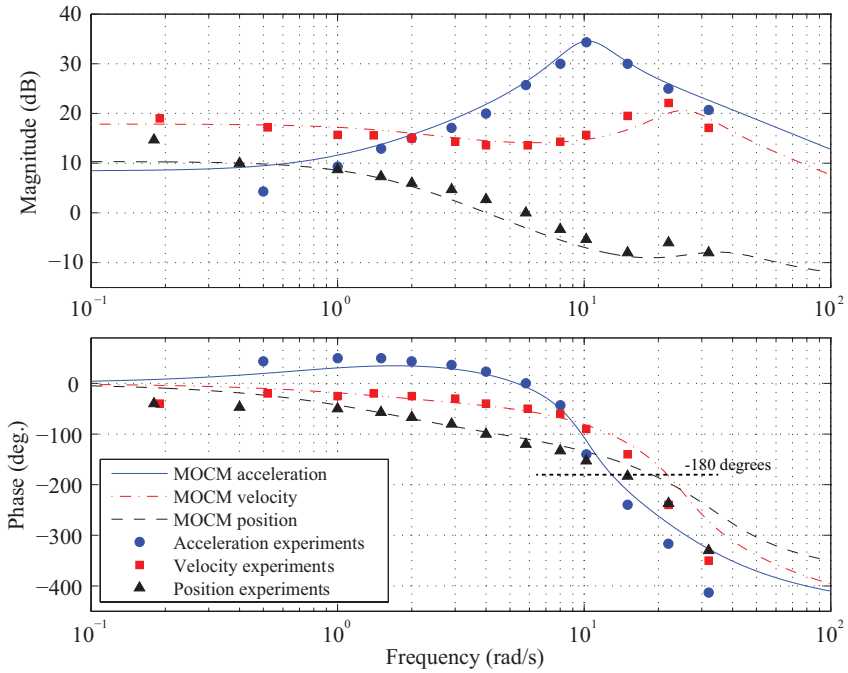

Figure 4.4: Comparison of MOCM frequency response with data from McRuer et al[61].

Table 4.1 presents the algorithm parameters used for the validation process. The performance of the MOCM model can be compared with experimental data in Figure 4.4, which presents the transfer function from perceived error to the stick deflection. The model matches the experimental data exceptionally well in the manual control frequency range (0.1 rad/s to 30 rad/s). Performance with different types of command systems can be compared by considering phase bandwidth: the frequency at which pilot model output is 180° out of phase with the input (as defined in ADS-33E-PRF[18]). This is the limiting frequency above which the pilot

completely fails to track the perceived variable. Figure 4.4 shows that the velocity and position control systems require less control effort than the acceleration command system; they do not require the pilot to provide phase lead and have almost twice the phase bandwidth.

4.2.2 Time domain validation

The MOCM's ability to reproduce manual control behaviour was assessed through a series of desktop simulations. This was mainly done due to lack of suitable data available in the public domain. Three types of tests were conducted: a disturbance rejection task to obtain compensatory behaviour, sinusoidal and discontinuous tasks to obtain tracking behaviour. The experimental setup was the same as that described in Chapter 3. The following integrator-gain transfer function was used as the plant model:

$$Y_C(s) = \frac{5}{s} \tag{4.2.4}$$

The forcing function used for the training tasks in Chapter 3 was also used for the compensatory task here. The following continuous tracking task, first presented by Neal et al[63], was used:

$$\begin{aligned} \begin{bmatrix} \dot{\theta}_r \\ \ddot{\theta}_r \end{bmatrix} &= \begin{bmatrix} 0 & 1 \\ -0.25 & -0.5 \end{bmatrix} \begin{bmatrix} \theta_r \\ \dot{\theta}_r \end{bmatrix} + \begin{bmatrix} 0 \\ 0.25 \end{bmatrix} w \\ \theta_r &= \begin{bmatrix} 1 & 0 \end{bmatrix} \begin{bmatrix} \theta_r \\ \dot{\theta}_r \end{bmatrix} \end{aligned} \tag{4.2.5}$$

where θ_r is the reference attitude and w is a zero-mean Gaussian white noise process. The time history of the reference attitude generated by this process is shown in Figure 4.6. It presents the subject with a task representative of following the flight director cue during approach in turbulence. The discontinuous tracking task can be seen in Figure 4.7. The signal had to be passed through a low pass filter with a cut-off frequency of 10 rad/s to ensure smooth movements of the flight director bar on the display. It consists of steps and a ramp in series, each with sufficient temporal separation to allow the recording of settling behaviour. This represents a more challenging task typical of flight test manoeuvres used to expose PIOs[7][129]. The subject was asked to perform each test five times for training and data from the sixth trial were used for comparison.

Figures 4.5, 4.6 and 4.7 allow the comparison of experimental data with the output of the MOCM (without the remnant components). Model parameter values used to obtain the match are presented in Table 4.2. In this case only four parameters, namely the diagonal elements of the weighting matrix, neuromuscular lag and the inherent time delay, had to be tuned to produce matches that resulted in high VAF and low remnant variances.

The MOCM code developed here was found to reproduce subject response to sinusoidal tasks reasonably well whilst maintaining Gaussian remnant distributions; implying that a better match is possible by adding Gaussian noise with the observed remnant variance to the model output. The remnant elements were omitted from the results so that the model's responses could be easily assessed without effects due to noise. Overall the model provides matches comparable to the bimodal and precision models obtained with the TFLS parameter identification method presented in Chapter 3. VAF and remnant variances are within 15% and 25% of those shown in Figure 3.12. In this case, the MOCM algorithm provides a simpler alternative because parameter identification techniques were not necessary to obtain the parameters shown in Table 4.2.

The MOCM's inability to reproduce nonlinear pulsive behaviour is highlighted by the multi-modal remnant distribution for the continuous tracking task (Figure 4.6). Inputs reflecting such

MOCM Parameters	**Compensatory**	**Tracking**	
	Disturbance rejection	Continuous	Discontinuous
Weighting matrix, **Q**	diag(7,1)	diag(2,1)	diag(10,1)
Output vector, y	(θ,q)	(e,$\dot{e}$)	(e,$\dot{e}$)
Inherent delay, τ	0.30	0.30	0.50
Neuromuscular lag, τ_n	0.08	0.03	0.09
Attention allocation, f_y	(1,1)	(1,1)	(1,1)
Disturbance intensity, **W**	8.80	8.80	8.80
Disturbance filter	$1/(s+2)$	$1/(s+2)$	$1/(s+2)$
Noise-to-signal ratios (ρ_u, ρ_y) (dB)	(-50,-40)	(-50,-40)	(-50,-40)
Comparison metrics			
Variance-Accounted-For (VAF)	0.61	0.80	0.75
Remnant variance (σ_ν^2)	0.012	0.056	0.077

Table 4.2: MOCM parameter values used for validation cases.

behaviour are especially clear in the experimental stick time history from 25 seconds onwards. The mismatch results in the two peaks around remnant values of 0.3 in the remnant distribution.

The discontinuous task was studied to compare the model's step response to the expected pulsive inputs from the subject. Due to the linear nature of the MOCM it cannot model sustained inputs such as those seen around 7 and 14 seconds. Furthermore, the model response clearly demonstrates non-minimum phase behaviour evident by the oscillations that occur immediately after the step demands in pitch attitude. The source of this behaviour is investigated in the following parameter variation study.

4.2.3 Multi-input-multi-output example

The MIMO capability of the MOCM was demonstrated through a series of dual-axis (pitch and roll) tracking tasks using a linear-parameter-varying (LPV) Boeing 747 model[119]. This model was developed by the author during this research and it is based on data provided by Heffley and Jewell[130]. For simplicity, the flight control suite was switched off so that the aircraft pitch and roll dynamics at a Mach number of 0.3 and sea level altitude were effectively represented by the following dimensionless transfer functions:

$$\frac{\theta(s)}{\eta(s)} = \frac{-0.377(s+0.44)(s+0.0801)}{(s^2+0.005791s+0.01613)(s^2+1.145s+0.8281)} \tag{4.2.6}$$

$$\frac{\phi(s)}{\xi(s)} = \frac{0.321(s^2+0.3432s+0.4225)}{(s+1.23)(s+0.0465)(s^2+0.1596s+0.5565)} \tag{4.2.7}$$

Evaluation of aircraft handling qualities in the light of requirements specified in MIL-F-8785C[131] found longitudinal dynamics to be located between Levels 1 and 2. For large aircraft, this is acceptable as the requirements are known to be conservative[132][133]. APC events were not observed in any of the formal runs.

However, as shown in Figure 4.8, informal attempts with aggressive control showed APC could be initiated with the given task, if the subject adopted a sufficiently high gain.

Here, Figure 4.8 demonstrates the complete evolution of a multi-axis APC due to aggressive roll recovery action. The pilot's stick deflections are clearly 180° out of phase with the aircraft attitude.

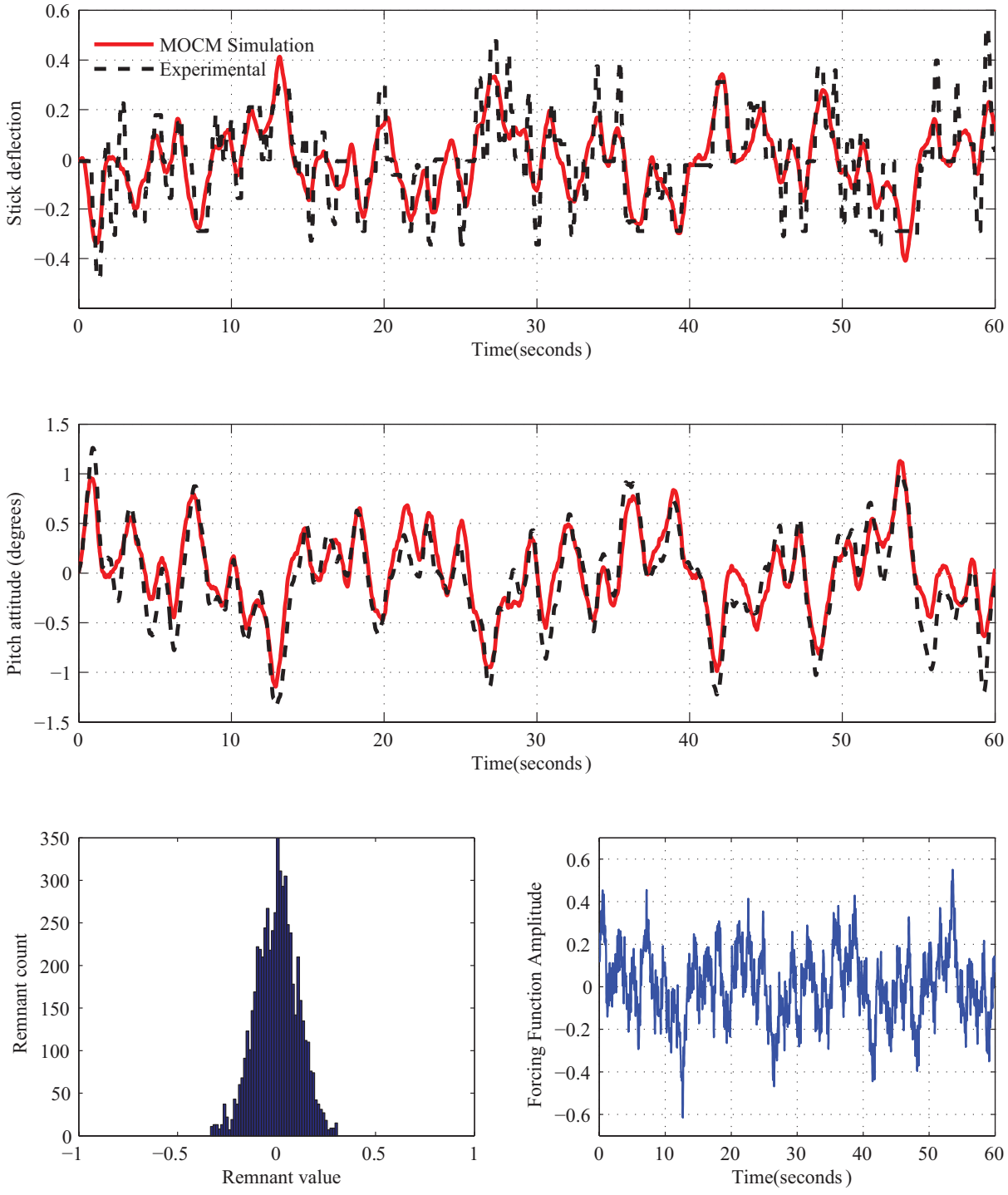

Figure 4.5: Comparison of pilot model and experimental data: Disturbance rejection task.

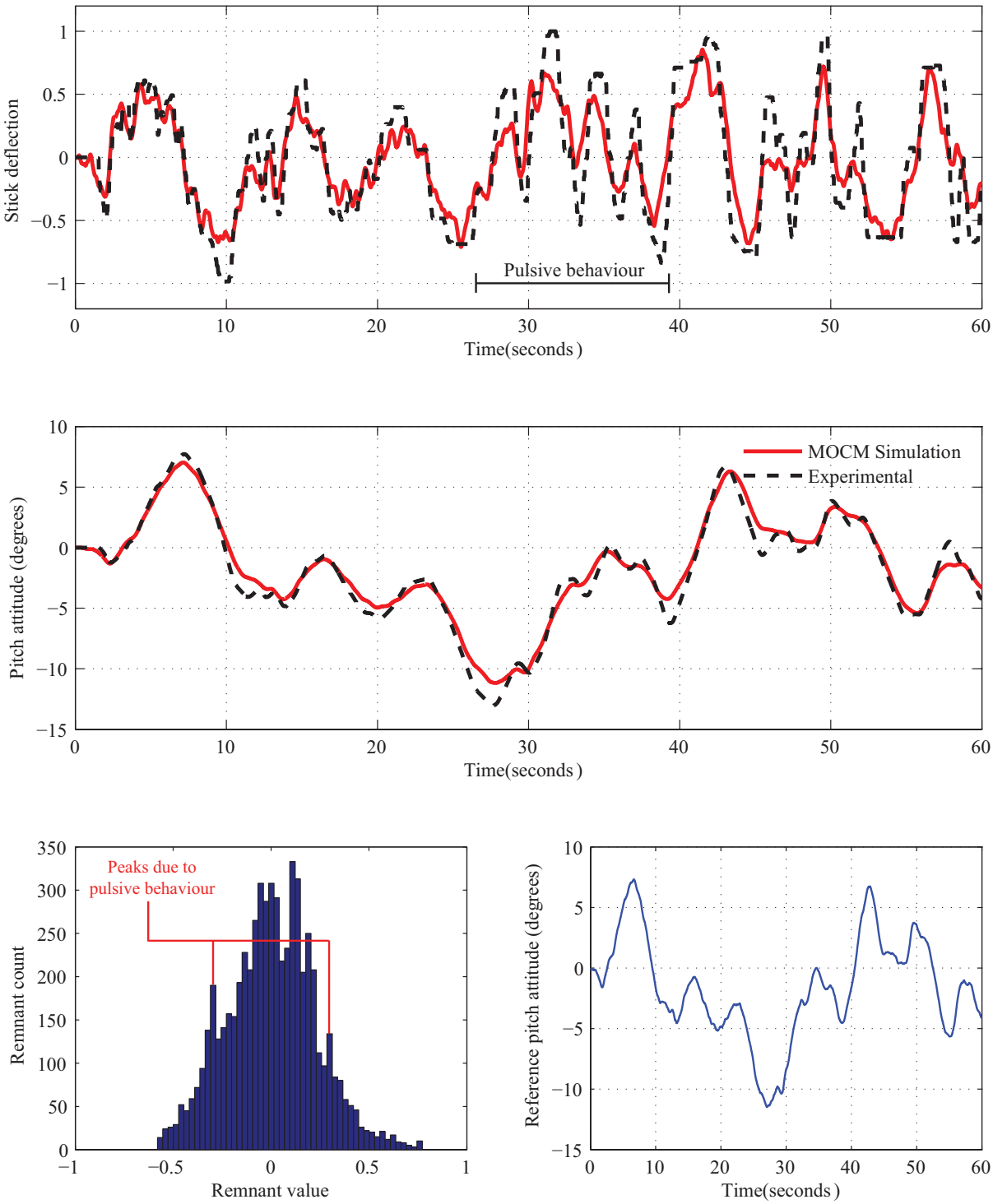

Figure 4.6: Comparison of pilot model and experimental data: Continuous tracking task.

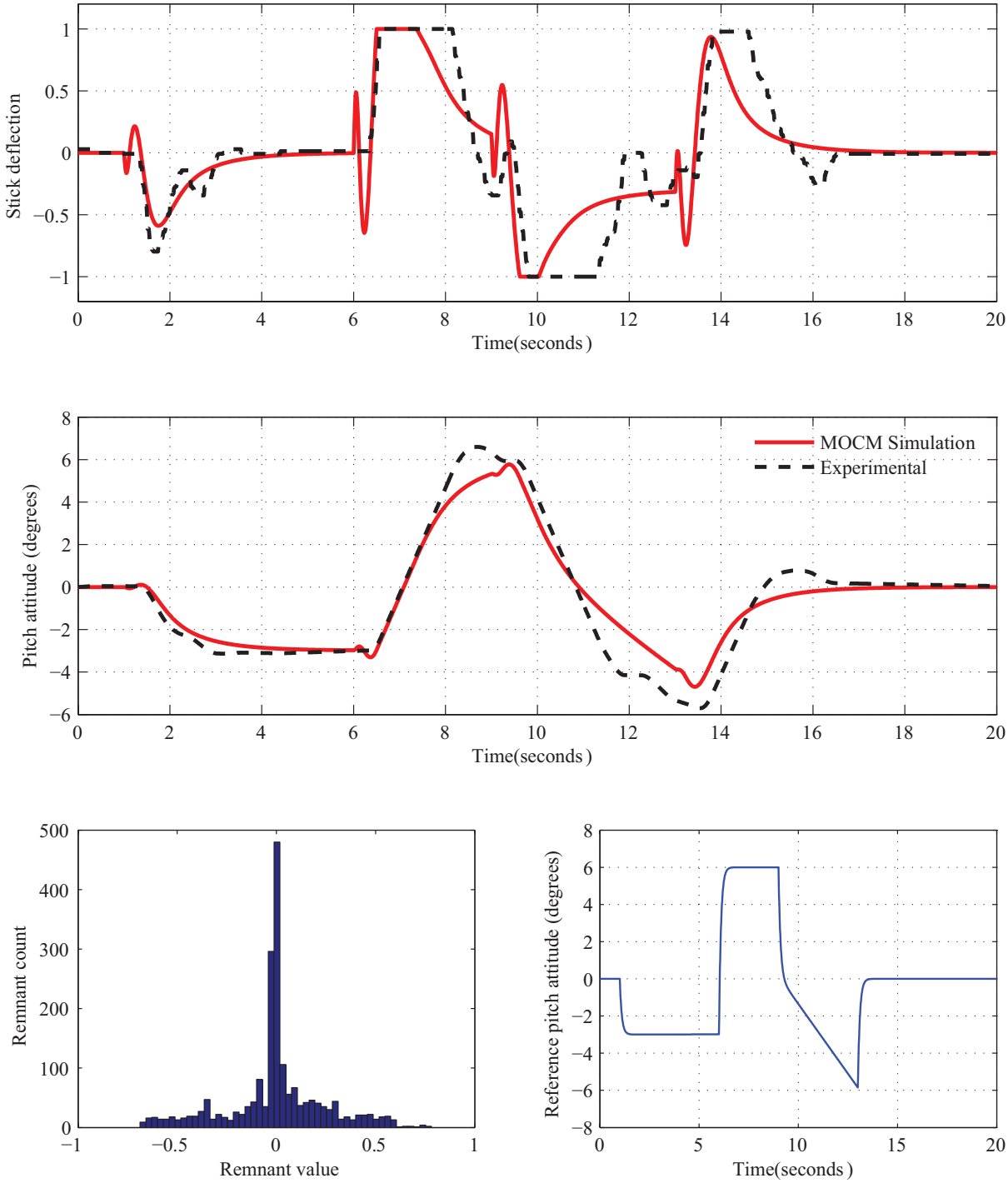

Figure 4.7: Comparison of pilot model and experimental data: Discrete tracking task.

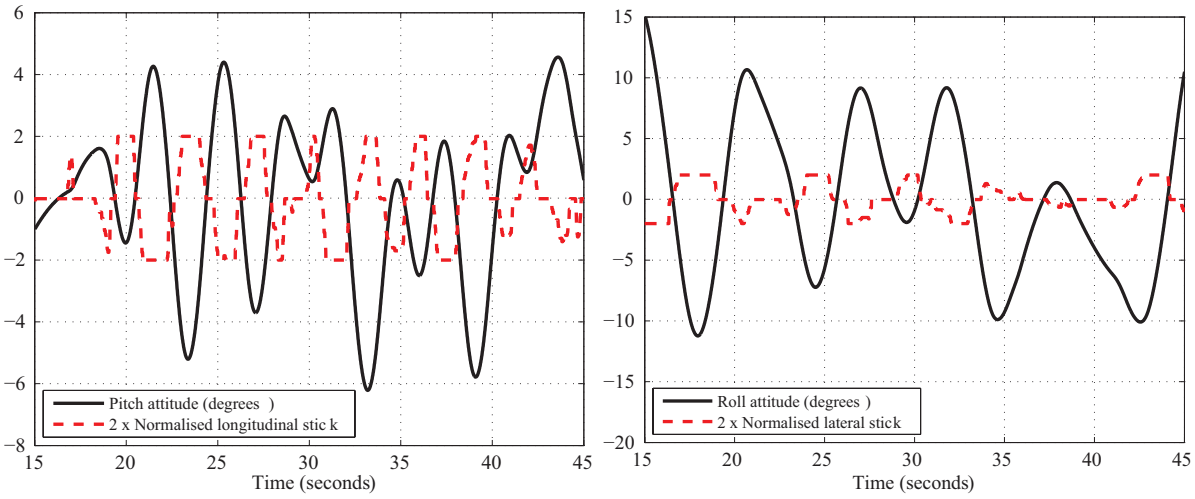

(a) Longitudinal coupling

(b) Lateral coupling

Figure 4.8: Longitudinal and lateral aircraft-pilot-coupling observed during informal an run.

Lateral dynamics were found to satisfy all Level 1 requirements except for one of the Dutch Roll criteria. The key handling qualities metrics are summarised in Table 4.3 together with MIL-F-8785C requirements for Level 1 handling qualities.

Property	Aircraft	Requirements
Short period pitch oscillation (ζ_s, ω_s)	(0.692,0.91)	$0.35 \leq \zeta_s \leq 1.30$
Phugoid mode (ζ_p, ω_p)	(0.023,0.13)	$\zeta_p > 0.04$
CAP (rads^{-2}/g)	0.157	$0.16 \leq CAP \leq 3.6$
N_{z_α} (g/rad)	5	$N_{z_\alpha} > 2.5$
Dutch roll mode $(\zeta_{\mathrm{DR}}, \omega_{\mathrm{DR}})$	(0.107,0.746)	$\omega_{\mathrm{DR}}\zeta_{\mathrm{DR}} \geq 0.10$, $\omega_{\mathrm{DR}} \geq 0.4$, $\zeta_{\mathrm{DR}} \geq 0.08$
Roll subsidence time constant (T_r)	1.23	$T_r < 1.4$
Spiral mode time constant (T_s)	0.047	Stable

Table 4.3: Handling qualities properties and Level 1 requirements (Category C, Class III).

The continuous tracking task given by Equation 4.2.5 was used to generate pitch and roll angle demands required to drive the dual cue flight director bars. However, in this case the signals were scaled to ensure $|\theta| \leq 10^\circ$ and $|\phi| \leq 10^\circ$, which in turn allows small perturbation assumptions to remain valid. Given the zero-mean nature of this task, it also leads to small changes in the LPV model's scheduling parameters (Mach number and altitude).

The experimental setup described in the previous section was also implemented here, albeit using the Thrustmaster HOTAS joystick in a sidestick configuration.[5] The subject was asked to use an elbow rest during all tests. The joystick's longitudinal axis was aligned to be parallel to the subjects forearm so that involuntary coupling in the control inputs could be avoided; that is involuntary roll demands during pitch and vice versa. The subject was a qualified flight instructor with over a 1000 flight hours in single and multi-engine propeller aircraft. A total of

[5]Coincidentally the joystick was temporarily replaced with a Logic3® joystick during the task design process. This was resulted in degraded tracking performance and more importantly, stick deflection time histories showed the subject behaving as a single channel nonlinear bang-bang controller. This was found to be due to the joystick's considerably larger deadzones, which were $\pm 5^\circ$ of the total stick deflection of $\pm 30^\circ$ along each axis. The Thrustmaster HOTAS joystick was found to have deadzones smaller than $\pm 1^\circ$ of the total $\pm 45^\circ$ deflection permitted along each axis.

ten one minute runs, including 5 training runs were conducted. Only the final five runs were used for this study.

A considerable amount of variation was found in the stick deflection time histories for all tests. Boundaries for the maximum and minimum deflections can be seen in Figure 4.9 and 4.10 together with the averaged profile. Such large variations can be attributed to the subject choosing to behave either as a single channel controller where errors along one of the axes is ignored, or as a time-varying MIMO controller where the error weighting matrix is a function of time and error magnitude. Indications of such behaviour can be found in the time histories between 15 and 30 seconds, where it seems that the subject has focused on lateral compensation and the average longitudinal stick movements are around zero. Overall, the subject's lateral stick deflections are tightly bounded and therefore, show a prioritisation of roll control in all tests.

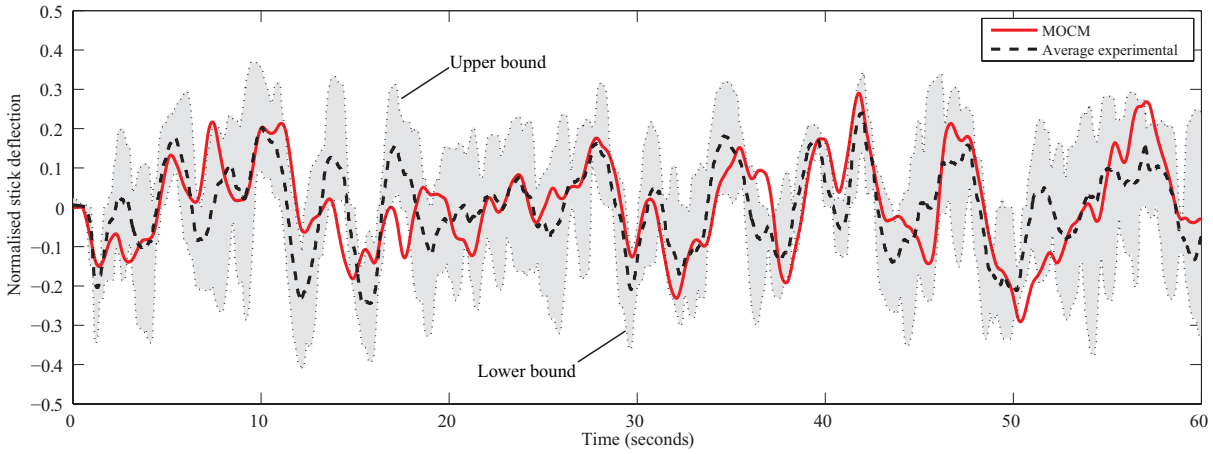

Figure 4.9: Variations in longitudinal experimental stick deflection and comparison of averaged data with MOCM output.

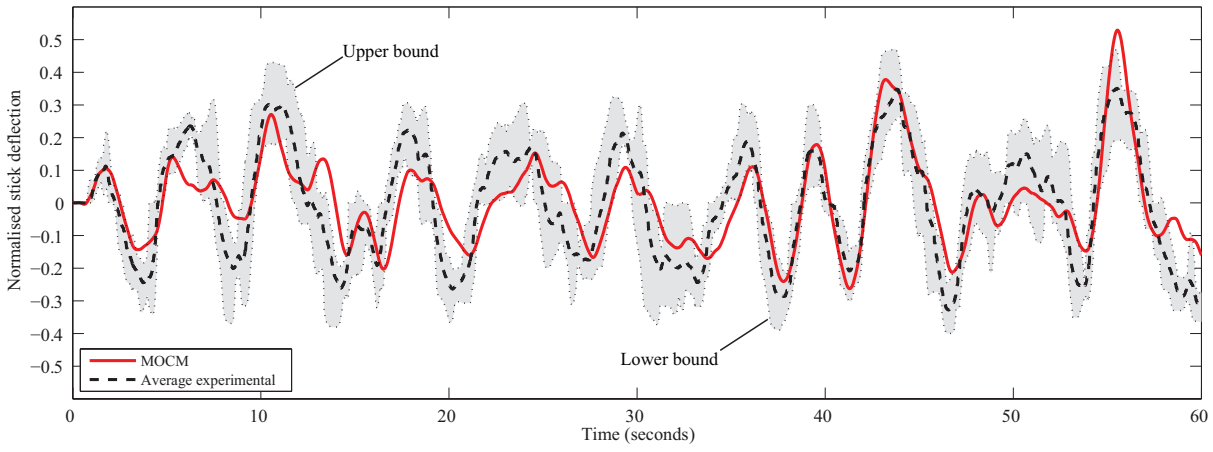

Figure 4.10: Variations in lateral experimental stick deflection and comparison of averaged data with MOCM output.

The tuned MOCM response to the same experimental task is also shown in Figures 4.9 and 4.10. Qualitatively, the response provides a reasonable match with the averaged stick deflection, although it is considerably different to observations from individual runs. This is confirmed quantitatively by the respective VAF and remnant variances presented in Table 4.4. The reader should note that a comparison with the averaged data is more relevant here because of the following reasons:

- The experiments only employed a single subject and therefore, effects of inter-subject variations are not included. These would only widen the observed bounds and thus, attempting to match individual stick profiles would not give any insight with regards to the MOCM's application for predictive purposes.
- The laboratory based experimental setup is a controlled environment in contrast to a cockpit during an incidence where pitch and roll attitudes are not the only variables affecting the pilot's stick movements. Therefore, given the aims and scope of this study, obtaining a ballpark estimate of pilot response is sufficient.

Table 4.4 also presents the MOCM parameters required to obtain the results discussed in this section. Note that the weighting matrix reflects the importance allocated by the subject to roll control. The task is therefore defined by the following cost function:

$$\mathcal{J} = E\left\{ \lim_{\eta\to\infty} \frac{1}{\eta} \int_0^{\eta} \left(\begin{bmatrix} e_\theta & e_\phi \end{bmatrix} \begin{bmatrix} Q_\theta & 0 \\ 0 & Q_\phi \end{bmatrix} \begin{bmatrix} e_\theta \\ e_\phi \end{bmatrix} + \begin{bmatrix} \dot{F}_{s\theta} & \dot{F}_{s\phi} \end{bmatrix} \mathbf{S} \begin{bmatrix} \dot{F}_{s\theta} \\ \dot{F}_{s\phi} \end{bmatrix} \right) dt \right\} \quad (4.2.8)$$

Furthermore, the necessary attention allocation has also resulted in significantly higher neuromuscular lag (reduced subject aggression) and inherent time delay.

However, a comparison with the averaged profile is more significant due to the fact that only one subject has been considered here. Keeping in mind the significant inter-subject variations shown in Chapter 3 (see Figure 3.18) for single axis tasks, even larger variations are bound to exist in this case; especially considering all other factors and cues[6] influencing pilot control input during flight in turbulence that are not modelled here. Attempting to reproduce individual stick deflection profiles is not as insightful as producing an accurate estimate of the averaged stick profile that also compensates for the inter-subject variations.

MOCM Parameter	Pitch control	Roll control
Weighting matrix element (Q_θ,Q_ϕ)	1	10
Inherent time delay, τ	0.45	0.45
Neuromuscular lag, τ_n	0.28	0.28
Attention allocation, f_y	0.5	0.5
Disturbance intensity, $\mathbf{W}$	8.8	8.8
Disturbance filter	$1/(s+2)$	$1/(s+2)$
Noise-to-signal ratios (ρ_u, ρ_y) (dB)	(-50,-40)	(-50,-40)
Comparison with averaged data		
Remnant variance	0.008	0.009
Variance-Accounted-For (%)	36.1	66.4
Comparison with Run 5		
Remnant variance	0.018	0.012
Variance-Accounted-For (%)	13.6	62.9

Table 4.4: MOCM parameters for multi-input-multi-output case.

Frequency domain stability characteristics for the open-loop PVS deduced from the Bode diagrams in Figure 4.11 are summarised in Table 4.5. It shows the subject's positive affect on phase margins; the pitch and roll transfer functions in Equations 4.2.6 and 4.2.7 have phase margins of 11.3° and 14.2° respectively. The relatively low crossover frequencies point to the fact that the subject did not exhibit high gain behaviour, which is primarily due to lack of urgency resulting from the experimental setup and the low amplitude nature of the task. The adherence of the MOCM to the crossover law is also evident by the -20 dB per decade slopes around the crossover frequencies.

[6] hdhd

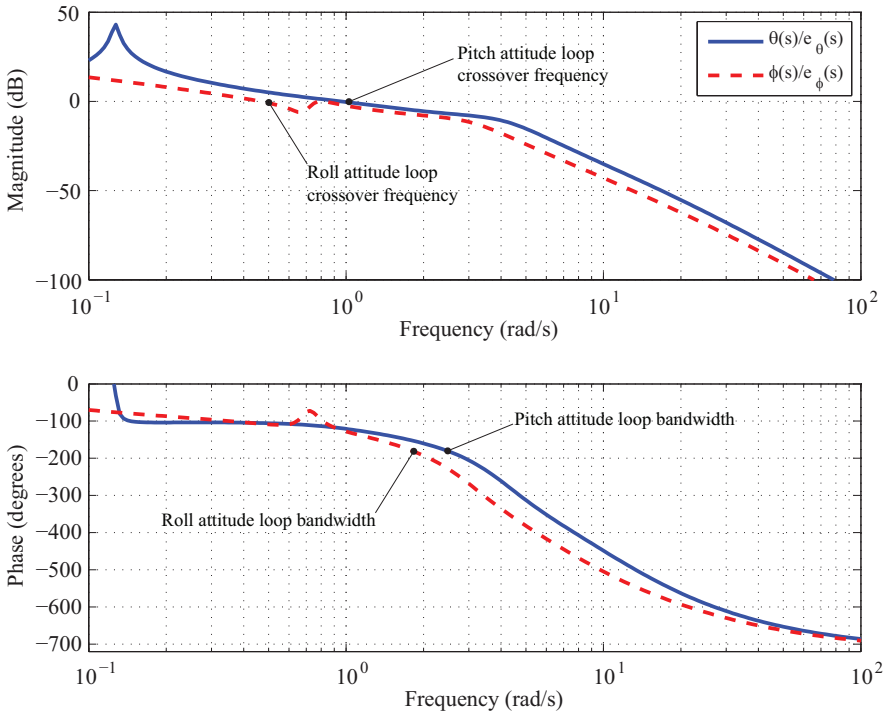

Figure 4.11: Pitch and roll attitude frequency response to elevator and aileron inputs.

Axis	Pitch	Roll
Crossover frequency (rad/s)	0.95	0.47
Bandwidth (rad/s)	2.47	1.81
Gain margin (dB)	6.77	7.30
Phase margin (degrees)	60.90	72.91

Table 4.5: Pilot-vehicle-system frequency domain stability characteristics.

4.3 Parameter variation study

A parameter variation study was done to investigate the effects of changes in MOCM parameters on frequency and time domain characteristics. The study is summarised in Table 4.6. The integrator-gain plant model given in Equation 4.2.4 was also used here. Such a study also provides an indirect means of verifying the developed code through comparisons of changes in model dynamics with those expected from actual pilots.

	Fixed parameter values					
Varying parameters	Q_e	$Q_{\dot{e}}$	τ_n	τ	f_y	Range
Weighting on error, Q_e	-	0.01	0.09	0.3	(1,1)	$10^{-2} \rightarrow 10^{4}$
Weighting on error rate, $Q_{\dot{e}}$	0.01	-	0.09	0.3	(1,1)	$10^{-2} \rightarrow 10^{4}$
Neuromuscular lag, τ_n	1.20	1.00	-	0.3	(1,1)	$0.006 \rightarrow 0.6$
Inherent time delay, τ	1.20	1.00	0.09	-	(1,1)	$10^{-2} \rightarrow 10^{0}$

Table 4.6: Summary of parameter variation study.

This study was limited to the following key MOCM parameters: the weighting matrix, neuromuscular lag and inherent time delay. Effects of their variation were studied in frequency domain by deriving the pilot model transfer function (Equation 4.2.3) and inspecting the changes in the

corresponding Bode diagrams. Furthermore, considering the transfer function in the following form provides insight into sources of the observed changes and stability characteristics:

$$\frac{u(s)}{e(s)} = K_e \frac{(s+\varrho_1)(s+\varrho_2)...(s+\varrho_{z_e})}{(s+\hat{\varrho}_1)(s+\hat{\varrho}_2)...(s+\hat{\varrho}_{p_e})} + K_{\dot{e}} \frac{s(s+\varsigma_1)(s+\varsigma_2)...(s+\varsigma_{z_{\dot{e}}})}{(s+\hat{\varsigma}_1)(s+\hat{\varsigma}_2)...(s+\hat{\varsigma}_{p_{\dot{e}}})} \tag{4.3.1}$$

where K_e, ϱ and $\hat{\varrho}$ are the gain, zeros and poles of the error feedback loop respectively. Similarly $K_{\dot{e}}$, ς and $\hat{\varsigma}$ are the gain, zeros and poles for the error rate loop respectively. z_e and $z_{\dot{e}}$ refer to the number of zeros on each feedback loop, whilst p_e and $p_{\dot{e}}$ are the number of poles. In this form, changes in gains and movements of the poles and zeros due to parameter variation can be tracked. The algorithm was found to provide an eighth order pilot model with six zeros for the first order plant model considered here.

4.3.1 Effects due to inherent time delay

The tracking performance of a human operator with a large inherent time delay is expected to be deferred and prone to large oscillatory deviations from the desired reference. Such behaviour is reflected in the frequency response by small low frequency gains, large resonant peaks and reduction in operator's phase bandwidth. These are clearly evident in Figure 4.12, which also shows a reduction in the frequency of the resonant peak. Low frequency gains are also significantly attenuated as this time delay increases.

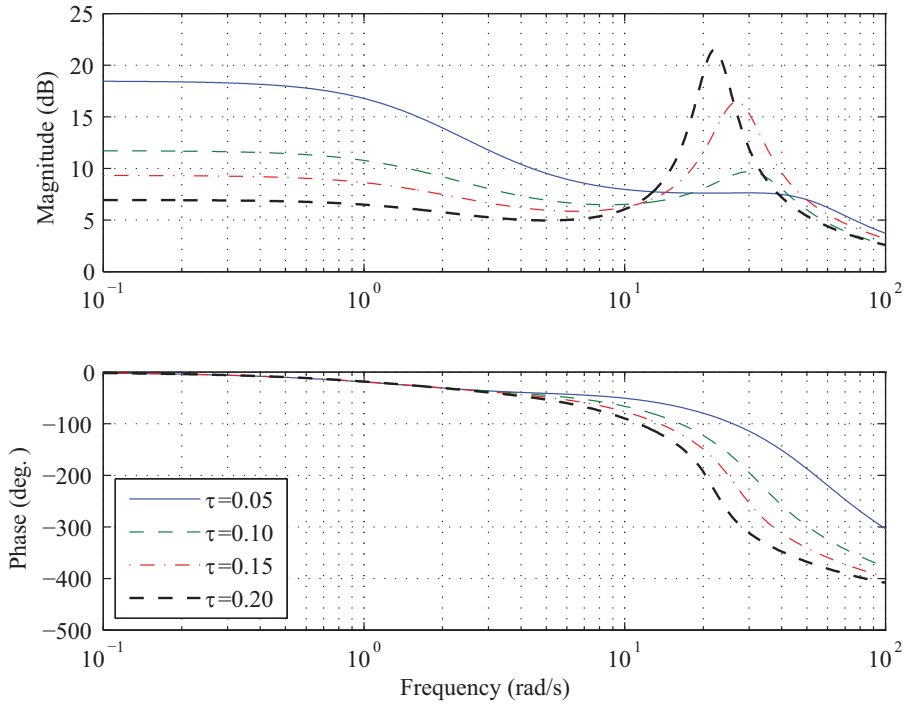

Figure 4.12: Effects of varying inherent time delay on MOCM frequency response.

Use of the simple gain-integrator plant, which only introduces a pole at the origin, also allowed the study of open-loop stability characteristics of the PVS by simply inspecting the positions of the MOCM poles. Figure 4.13 shows the movements of these poles as the time delay is varied. Only two of these poles were found to determine oscillatory characteristics and both travel towards the imaginary axis as the time delay is increased; in turn amplifying the resonant peak and introducing the destabilising effects. Movement of MOCM zeros can be found in Appendix A.

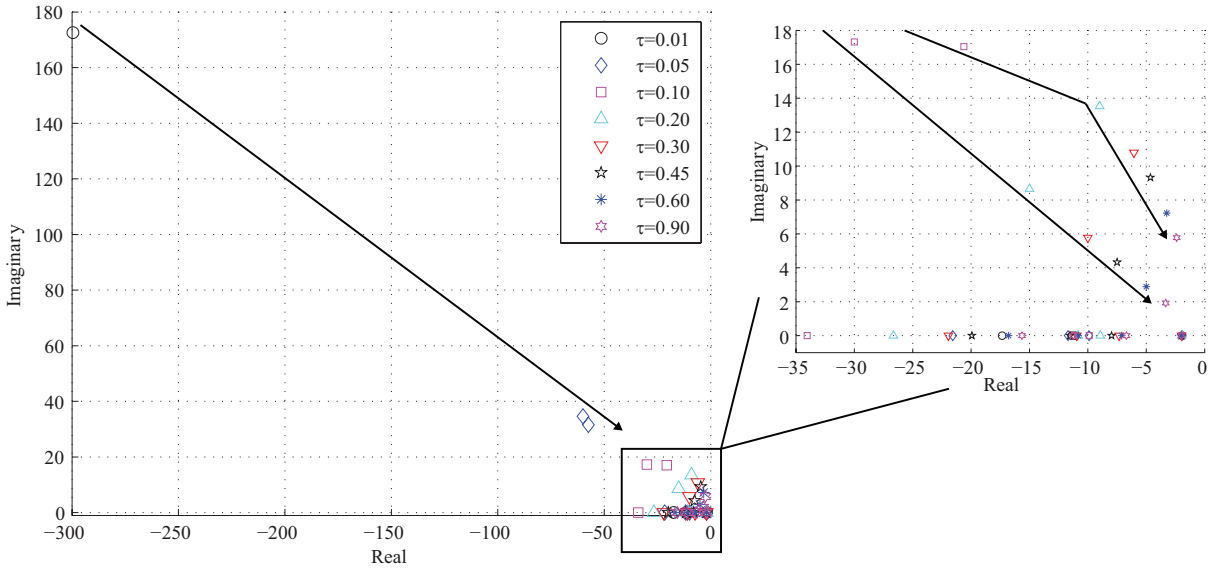

Figure 4.13: Effects of inherent time delay on MOCM poles.

Affects on time domain response can be seen in Figure 4.14(a). Increased time delay causes larger oscillations (around 1.2 seconds) whilst the reduction in gains due this delay, shown in Figure 4.14(b), cause the response to be more similar to experimental stick movements. In this case the best match is found at a realistic delay of 0.5 seconds.

Relative to other parameters the effect of time delay on loop gains was found to be small. The source of small variations in gains in Figure 4.14(b) is the accuracy bound placed on the neuromuscular lag parameter within the MOCM algorithm. Such variations are insignificant, especially relative to the inter-subject variations found in Chapter 3 and therefore, acceptable.

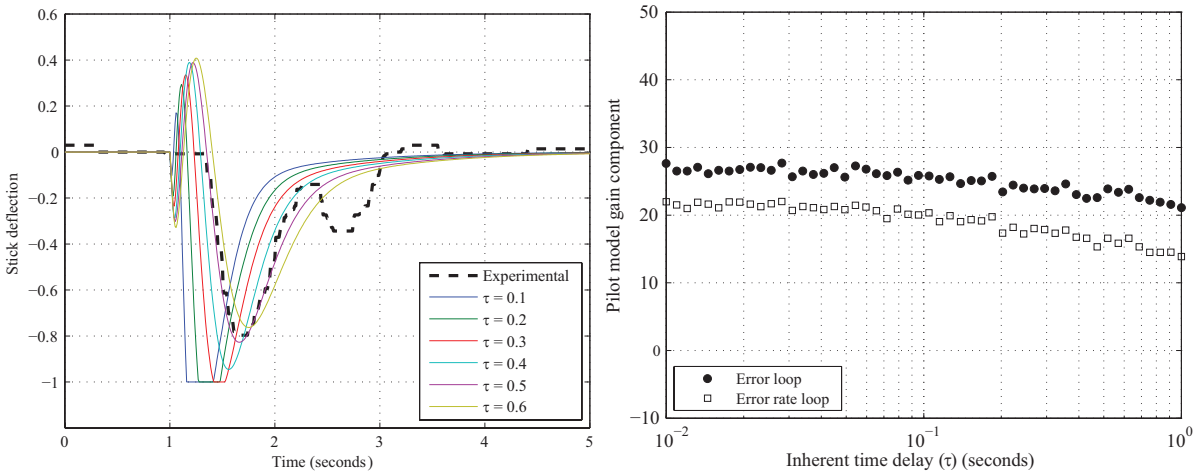

(a) (b)

Figure 4.14: Effects of inherent time delay on loop gains time domain characteristics.

4.3.2 Effects due to neuromuscular lag

The neuromuscular lag parameter is used to tune pilot model aggressiveness. Its placement immediately after the optimal gain in Figure 4.2 highlights its importance for the determination of MOCM bandwidth and gains. The inverse relationship between neuromuscular lag and

aggressiveness is clear in the Bode diagram presented in Figure 4.15 and the gain variation plot in Figure 4.16(a). From the Bode diagram it can be seen that the MOCM gain and phase bandwidths increase as the neuromuscular lag is reduced. However, the resonant peak is amplified and pushed towards higher frequencies. This implies that although the model is capable of satisfactory performance with a larger bandwidth, it will cause larger transient oscillations when operating at higher frequencies; as evident around 1.1 seconds in the time history presented in Figure 4.16(b).

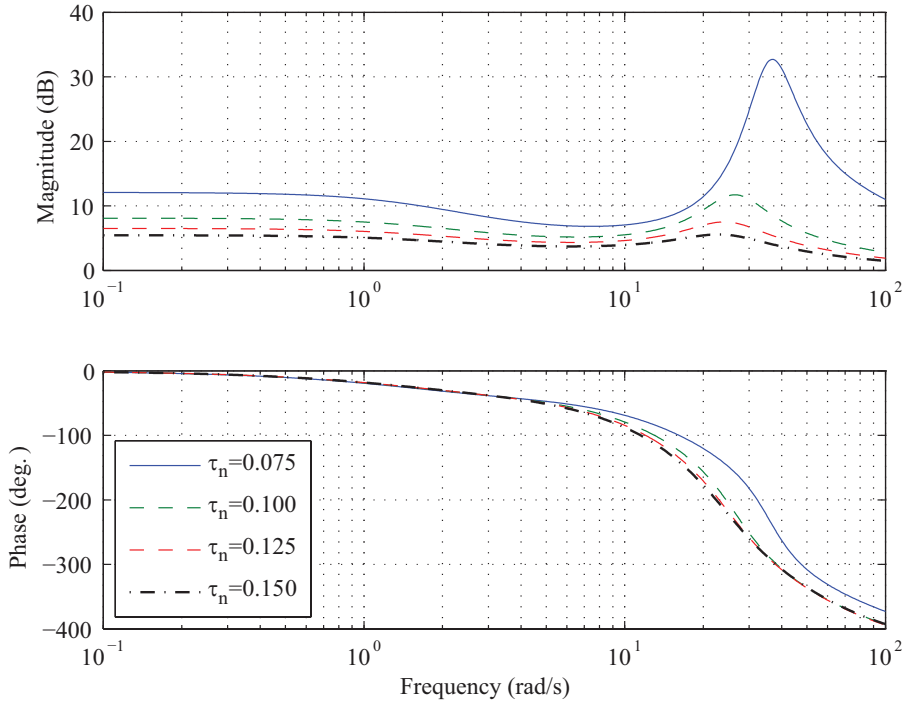

Figure 4.15: Effects of varying neuromuscular lag on MOCM frequency response.

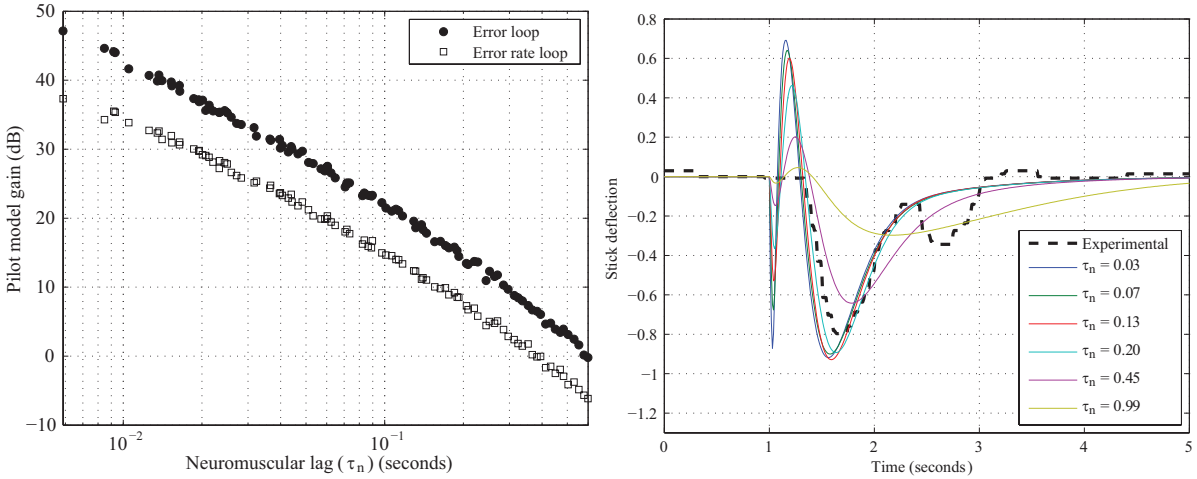

(a) (b)

Figure 4.16: Effects of neuromuscular lag on loop gains and time domain characteristics.

In comparison with other parameters, the neuromuscular lag strongly influences the magnitude of loop gains. In fact, in this case the effect can be determined through the following relationship deduced by inspecting Figure 4.16(a):

$$K_{e,\dot{e}} = \tilde{\kappa}\tau_n^{\bar{\varepsilon}} + \upsilon \tag{4.3.2}$$

where $K_{e,\dot{e}}$ represents either of the loop gains and the coefficients $\tilde{\kappa}$, $\bar{\varepsilon}$ and υ are curve fitting parameters.[7] Such a relationship may be used to obtain a rough estimate of the effect of this parameter on the MOCM frequency response.

Regarding its affect on stability, only one of the complex poles was found to be linked to this parameter. Its movements along with other real poles can be seen in Figure 4.17. Effects due to variations in neuromuscular lag on transfer function zeros can be found in Appendix A.

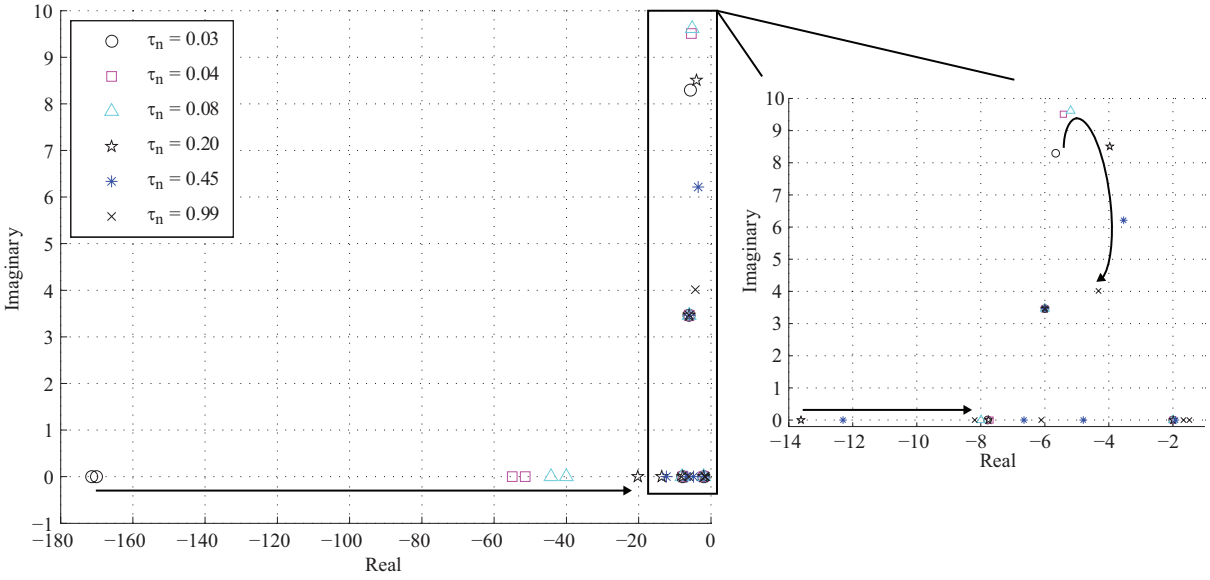

Figure 4.17: Effects of neuromuscular lag on MOCM poles.

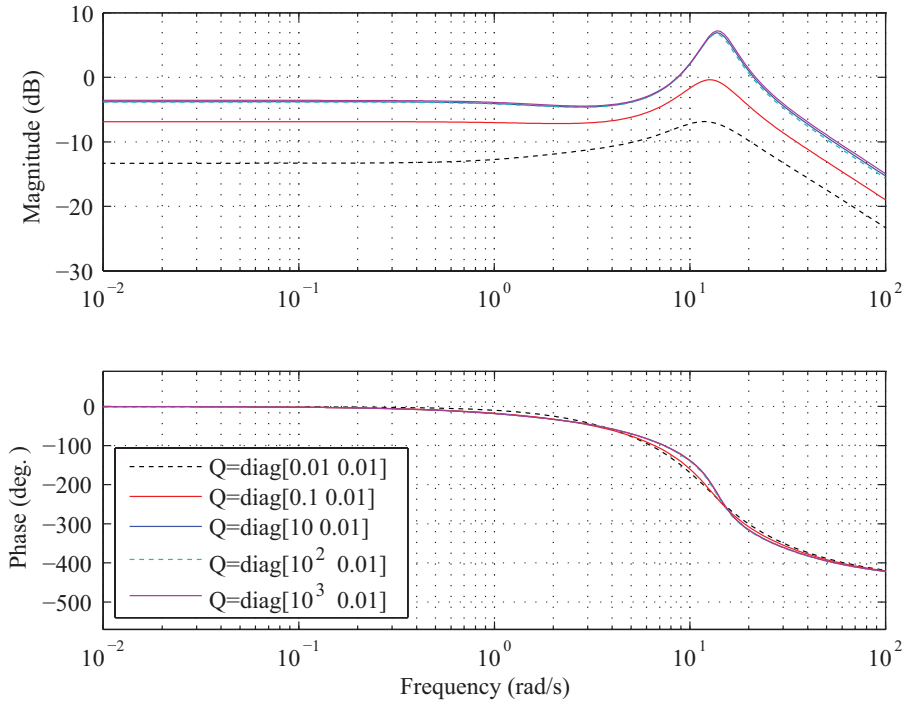

Figure 4.18: Effect of varying error weighting on MOCM frequency response.

[7] Here $(\tilde{\kappa}, \bar{\varepsilon}, \upsilon)$ were found to (-106,0.13,100) and (-91,0.16,0.78) for the error and error rate loops respectively with R^2 values greater than 99%.

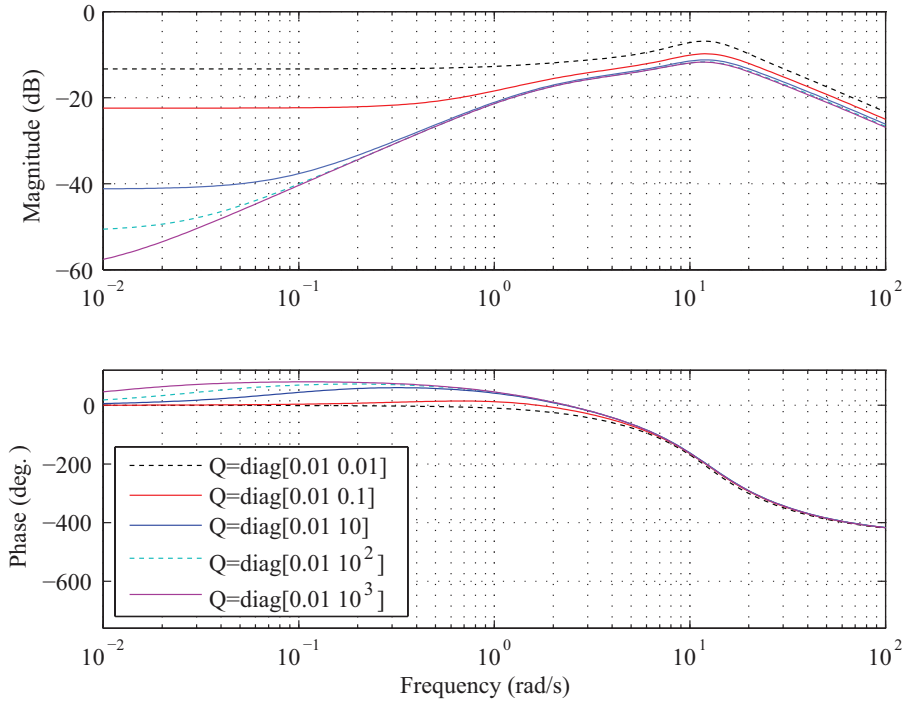

Figure 4.19: Effect of varying error rate weighting on MOCM frequency response.

4.3.3 Effects due to weighting matrix elements

As shown in Figures 4.18 and 4.19, the effects of varying the weighting matrix elements are similar to those due to variations in neuromuscular lag. These weightings effectively represent the tolerances on the observed error and error rates. In this context, the error tolerated by a particular pilot may be used as an indicator for aggressiveness. The weighting on error was found to determine the overall gain and magnitude of the resonant peak with little affect on phase bandwidth. The error rate weighting was found to determine low frequency gains and phase lead generation.

It can be seen from Figure 4.20 that these effects are primarily obtained through changes in the error loop gains. The effects of increasing error rate weighting are actually achieved via reductions in the error loop gains and ensuring the error rate loop gain remains around 15 dB.

All the above frequency domain effects are reflected in the time domain features shown in Figure 4.21. Larger transient oscillations can be seen due to increased error weighting. On the other hand, increased phase lead due to a larger error rate weighting can be seen to reduce the magnitude of these oscillations.

4.4 Conclusions

The MOCM provides a capability for control-theoretic modelling of pilot dynamics in a MIMO environment whilst allowing an explicit definition of flight dynamics expected by the pilot via an aircraft model. It was found to provide reasonable agreement with the experimental data. Significant variations were found in the experimental data from the five runs used in the MIMO case study. However, the MOCM was found to provide good agreement with the averaged stick deflection time histories. The parameter variation study focused on parameters that were found to significantly affect the MOCM dynamics during the validation process. These were the

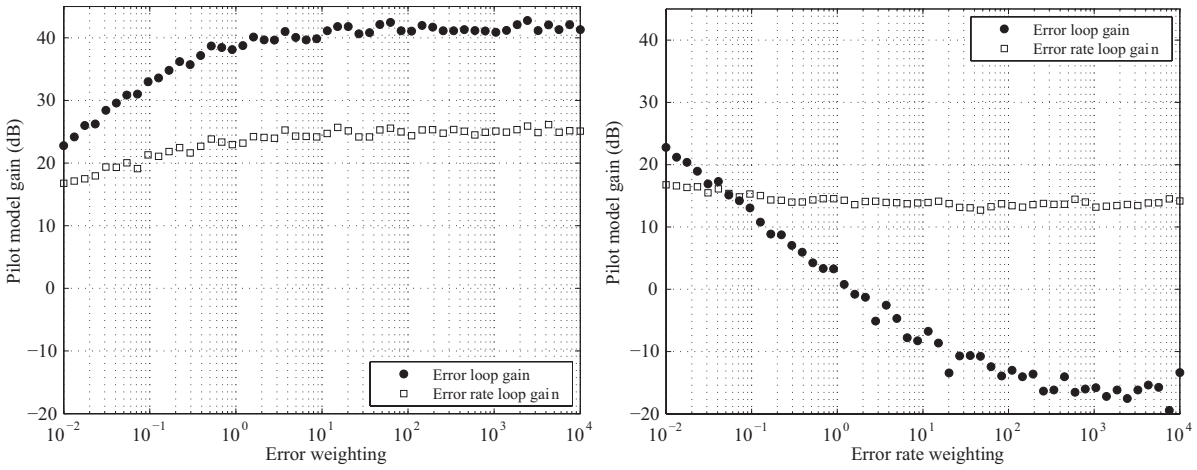

(a) (b)

Figure 4.20: Variation of loop gains with error and error rate weightings.

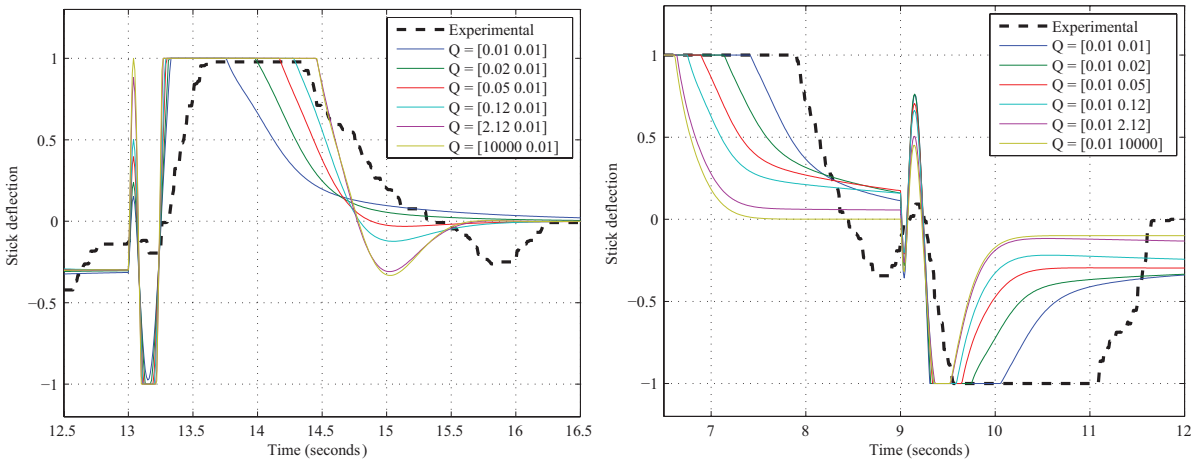

(a) (b)

Figure 4.21: Effects of error and error rate weightings on time domain characteristics.

inherent time delay, neuromuscular lag and the weighting matrix. The inherent time delay was found to have the greatest impact on phase bandwidth and the neuromuscular lag effectively determined the gains introduced into the PVS. Phase lead generation was found to be a function of the weighting on error rate feedback.

CHAPTER 5

Modelling of psychophysical limitations

Previc and Ercoline[14] state in their book (published in 2004) that statistics show up to 30% of all aircraft fatalities have been attributed to SD. Similarly in military aviation, Tsang and Vidulich[13] state that over 65% of all fixed wing pilots have experienced SD in one form or another. More significantly, fatal nighttime crashes like that of Ethiopean Airlines 409[134] and Kenya Airways 507[135], where the crew were seemingly unaware of the aircraft's bank attitude and the spiralling descent, highlight the need for modelling the vestibular and visual sensory interactions. Such a simulation capability together with the MOCM can provide rough estimates of the time taken by a crew to respond to vestibular senses and initiate recovery action. Moreover, purely from the perspective of pilot modelling, any attempt to faithfully model manual pilot control behaviour must include a sensory representation.

The excitation of fuselage bending modes together with rigid body dynamics can result in large amplitude periodic motion in the cockpit causing biodynamic feedthrough; where accelerations at the pilot station are involuntarily fed back via the pilot's body through the inceptor. Considering the effects that can potentially arise due to the coupling of biodynamics and aeroelastic mode (as shown by Raney et al[26]) a pilot model for the evaluation of flight loads should also incorporate a biomechanical model.

This chapter describes the models adopted and developed for modelling the pilot's perception of aircraft states and his/her involuntary physiological response to the forces and moments he/she is exposed to during atmospheric flight.

5.1 Modelling human perception

Pilot spatial orientation can be defined as the perceived body position relative to a reference frame. The task of maintaining spatial orientation involves conscious processing of information and subconscious fusion of cues from different sensory modalities. SD on the other hand, is a loss of the correct sense of orientation within this reference frame. As discussed in Chapter 2, factors contributing to SD range from acceleration cues during maneuvering to more complex scenarios involving pilot workload and attention allocation. Current scientific understanding of human cognition in the context of multi-sensory stimuli is still in the early stages of development. Results presented by leading neuroscientists like Ramachandran[136] and Lotto[137], only cover a small number of observed sensory interactions that are not necessarily relevant here, such as certain forms of synaesthesia, and point towards a highly complex brain function.

Most pilot modelling approaches focus on either the resulting flight dynamics of the PVS or study pilot dynamics only through monitoring inceptor inputs. Multi-sensory perception is either modelled simply through a linear summation of cues[76][22] or a weighted sum with a seemingly arbitrary selection of weightings (like that proposed by Hess[138][139]). In the majority of cases, flight dynamics under the effects of SD are either left to qualitative human factors research or flight simulator based trials. The model proposed by Telban and Cardullo[25] allow SD effects to be incorporated within the greater pilot modelling framework shown in Figure 1.1. This approach was used here for the following reasons:

- It allows the investigation of interactions between visual and vestibular cues.
- It uses Hosman's approach to model the visual, otolith and semi-circular canal dynamics and so remains relatively simple.
- It allows the sensory model to be decoupled from the control-theoretic component.

The model was parameterised to match latencies observed in medical experiments conducted in the 1970s by Berthoz et al[140] and Goldberg et al[141]. Here, it has been modified to allow the treatment of cues in both the peripheral and central visual fields. Cue quality is controlled through the signal-to-noise ratios used in the formulation of the MOCM. Figures 5.1 and 5.2 present the model structures for the perception of rotational and translational motion respectively.

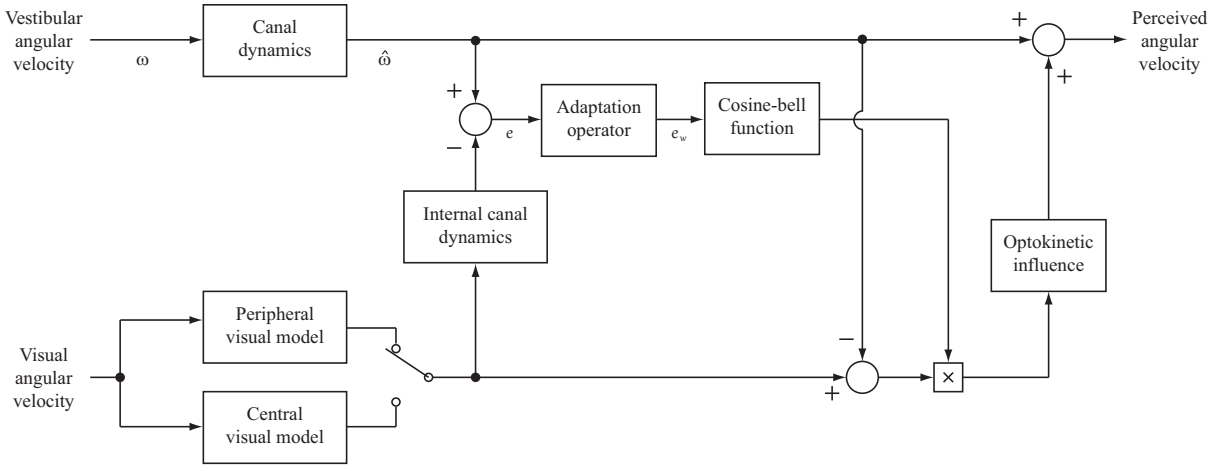

Figure 5.1: Rotational perception model.

The rotational perception model provides a means of calculating a single perceived angular velocity given the actual angular velocity input to the visual and vestibular senses; where the latter is represented by the semicircular canal dynamics. The translational perception model has a similar layout. It provides a means of obtaining the perceived velocity given the actual specific force (GIF per unit mass) and acceleration. Vestibular dynamics are represented here by the otolith organs that respond to specific force whilst the visual dynamics process velocity information; presented here in the form of integrated acceleration.

Peripheral and central visual dynamics are modelled as time delays; 90 ms and 150 ms for peripheral and central vision respectively[76]. The user can define variables that occupy the pilot's peripheral or central vision through a switch. This allows modelling of scenarios involving multi-axis tasks, where a pilot observes roll rate in the peripheral vision simultaneously with pitch rate in the central vision.

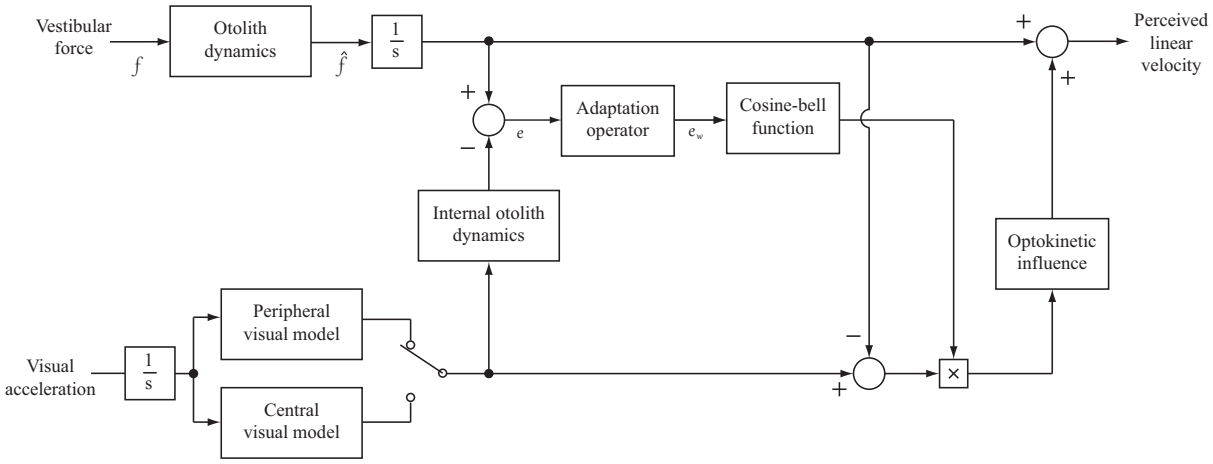

Figure 5.2: Translational perception model.

Various psychophysical experiments[76][142] have found that visually obtained perception of self-motion induces an artificial vestibular response, and to a limited degree the vice versa is also true. The primary feature of this model is its ability to capture such influenced estimates of self-motion and thus, simulate SD. The optokinetic influence components constitute a nonlinear gain and a first order low pass filter with a time constant of 1.59 seconds. The gain effectively captures the weightings given to vestibular and visual perceptions. It is computed by a modified cosine-bell function, shown in Figure 5.3, that relates it to the difference between the visual and vestibular output. The filter then models the gradual build-up of perceived self-motion. The overall perceived motion is the sum of the vestibular estimate and the optokinetic influence output. The secondary feature is the use of internal models of the semicircular canals and otoliths which, implicitly assumes that the central nervous system compares visual stimuli against its estimate of vestibular response. The models use the same cosine-bell function, optokinetic influence transfer function and visual models.

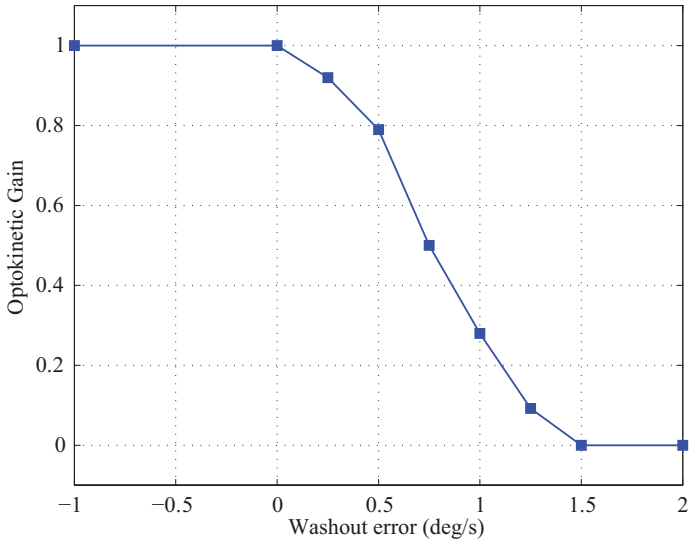

Figure 5.3: Cosine-bell function used to derive the optokinetic gain.

The vestibular model from Fernandez et al[141] and the otolith model suggested by Telban et al[142] were used here; both almost identical to those developed by Hosman[76]. The otolith organs are responsive to specific force (f) defined as follows:

$$f = \hat{g} - a_h \tag{5.1.1}$$

where $\hat{g}$ is the local gravitational force vector and a_h is the acceleration of the head with respect to a body-fixed reference frame. Therefore, the otoliths respond to both linear acceleration and tilting of the head with respect to the gravity vector. For simplicity, it is assumed that the pilot's head remains aligned with the aircraft's body axes. Transfer function relating sensed specific force ($\hat{f}$) to actual specific force is as follows:

$$\frac{\hat{f}(s)}{f(s)} = \frac{0.4(13.2s+1)}{(5.33s+1)(0.66s+1)} \tag{5.1.2}$$

The semicircular canals are the primary sensory organs for sensing rotation as they respond to angular rate motion. It has been shown that the following transfer function adequately relates perceived angular rotation rates ($\hat{\omega}$) to actual rotation rates (ω)[141]:

$$\frac{\hat{\omega}(s)}{\omega(s)} = \frac{456s^2}{(5.7s+1)(80s+1)} \tag{5.1.3}$$

The adaptation operator determines the duration for which conflict between the visual and vestibular cues are allowed. It relates the inter-cue error to the washed-out error through the following transfer function:

$$\frac{e_w(s)}{|e(s)|} = \frac{\tau_w s}{\tau_w s+1} \tag{5.1.4}$$

The time constants, τ_w for the adaptation operator within the rotational and translational perception models have been found to be eight and one seconds respectively.

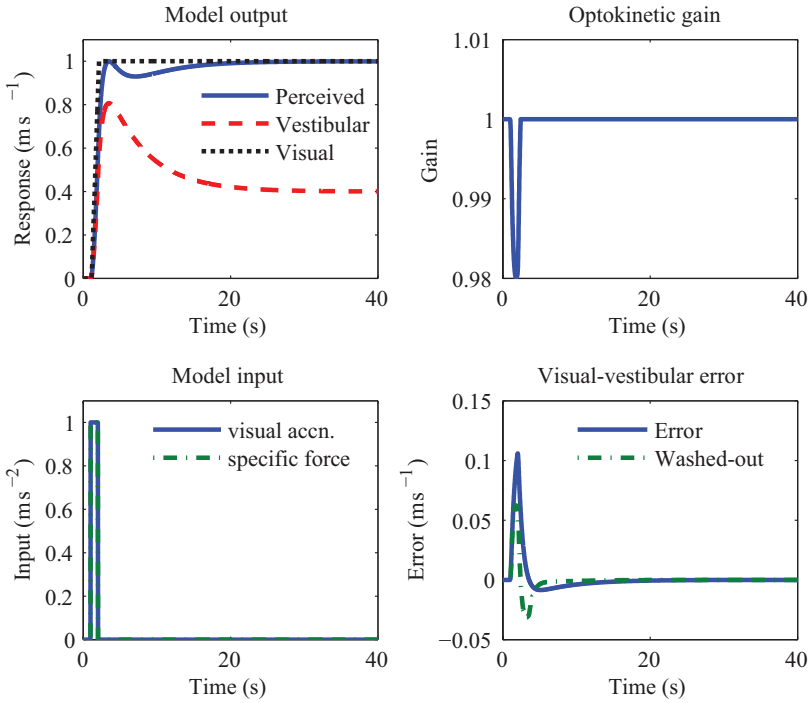

Figure 5.4: Translational model response to a visual and vestibular input of 1ms^{-2} pulse.

Dynamic response of the two perception models are shown in Figures 5.4 to 5.7. These simulation results demonstrate the model's capability to capture the fact that whilst vestibular senses have transient characteristics, induced motion through the visual channel still dominates human perception of motion.

Figure 5.4 shows the response of the translational perception model to a visual and vestibular input of 1 ms^{-2} pulse of 1 second duration; that is a change in velocity of 1 ms^{-1}. The vestibular

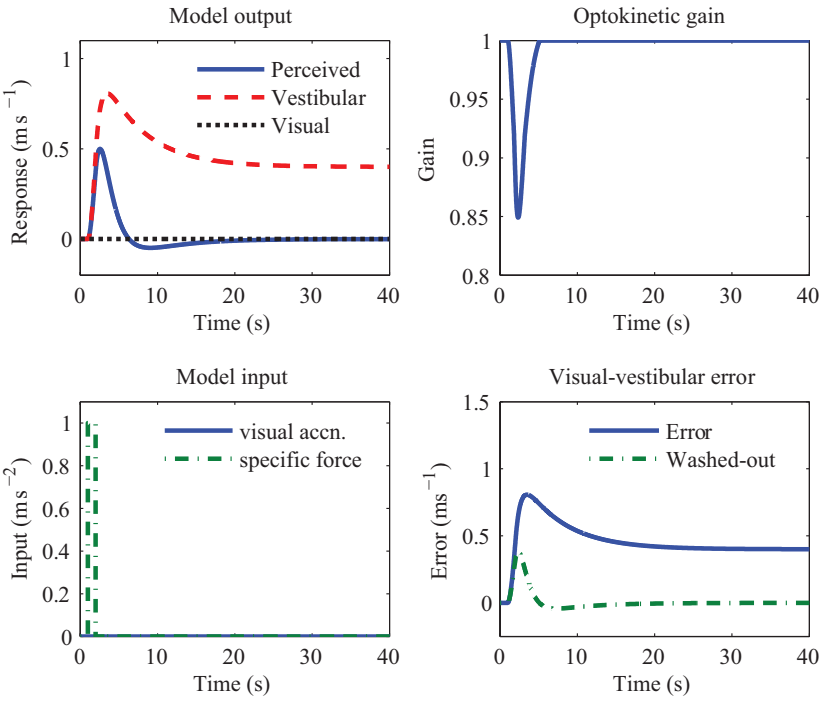

Figure 5.5: Translational model response to vestibular only input of 1ms^{-2} pulse.

response after an initial reaction decays as expected causing a brief transient in the perceived velocity. However, the steady-state velocity is accurately captured. Figure 5.5 presents a more interesting scenario. Only the vestibular sense has been given the pulse input here, whilst the visual channel has been kept blind. The resulting perceived motion consists of an initial transient peak and a steady state velocity of zero. The transient is due to the vestibular output, but it is rapidly nullified by the optokinetic influence. The larger error leads to a greater change in optokinetic influence gain resulting in the cancellation effect.

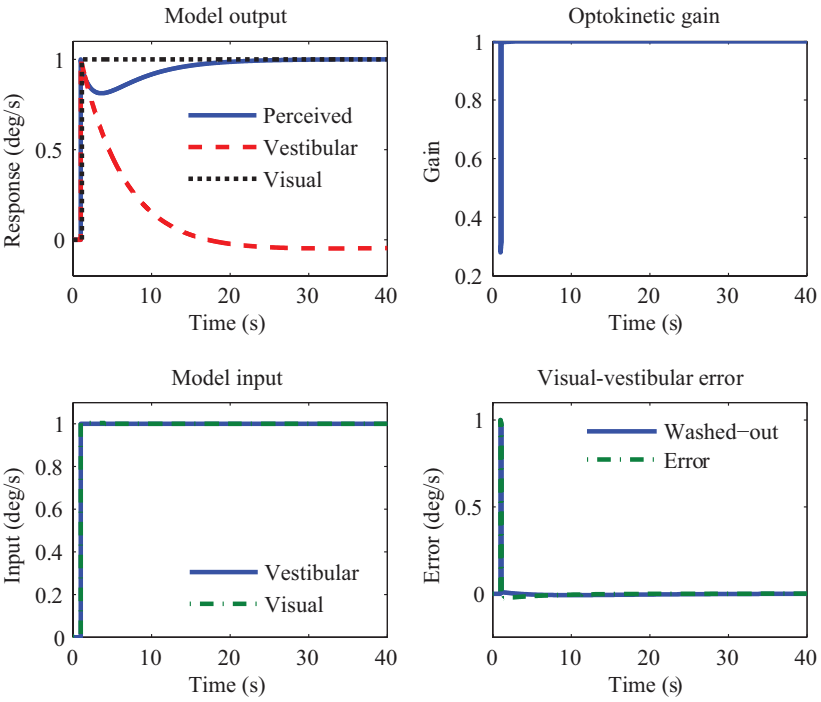

Figure 5.6: Rotational model response to vestibular and visual step input.

Figure 5.6 and 5.7 present the response of the rotational perception model. Figure 5.6 shows the response to visual and vestibular step input of 1°/s. The response is again as expected: a sharp and accurate visual response and a decaying vestibular response. Since both senses are provided with the same information, the steady state angular velocity is accurately captured.

Response to a vestibular only step input is presented in Figure 5.7. The overall perceived motion has the same features as its translational model counterpart in Figure 5.5. The initial transient is only sharper because of the faster response of the semicircular canals.

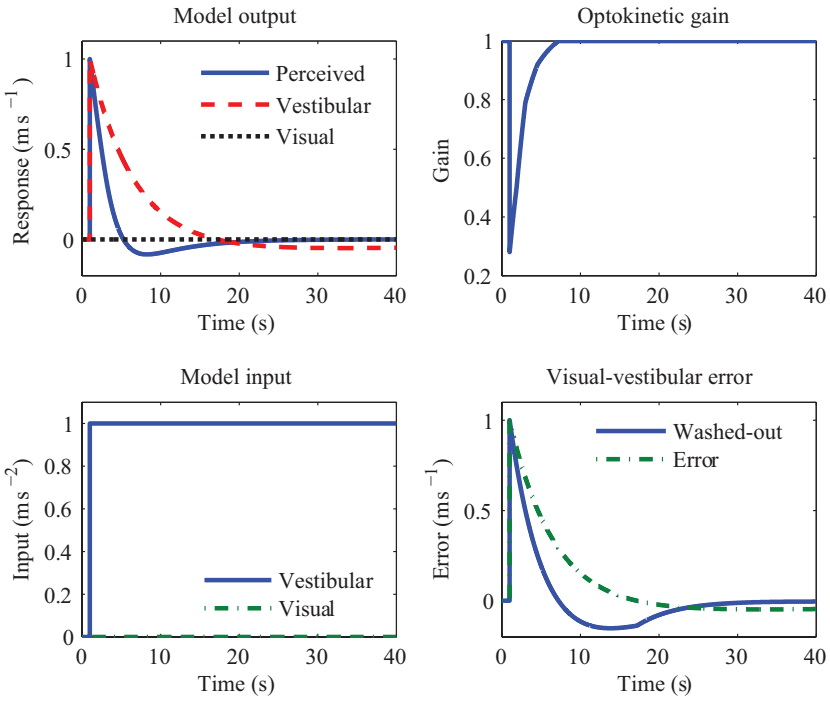

Figure 5.7: Rotational model response to a vestibular only step input.

Vestibular thresholds, presented earlier in Table 2.1 for rotational and linear motion have also been incorporated.

The development of a model capable of reproducing all SD effects is clearly beyond the scope of this research. Such an effort will most certainly require the development of numerous models because of the wide variety of SDs attributed to the human sensory organs. Here, the aim was to develop a capability to simulate effects arising due to lack of visual cues and interactions between the visual and vestibular senses in the context of large transport aircraft. Therefore, the scope has been limited to modelling SDs that initiate at relatively small aircraft attitude angles, such as *postturn illusion* and *graveyard spiral*.

5.2 Modelling human biodynamic response

The discrete modelling approach was found to be most suitable for the purposes of this project for the following reasons:

- Although simpler to develop than other models, this approach captures most low frequency features.
- Its descriptive nature allows for some insight into dynamic interactions.

- Other approaches tend to be either specialised for particular applications or too complex and computationally intensive.

Dynamics arising due to vertical accelerations, namely longitudinal dynamics, are decoupled from those resulting from lateral accelerations. It is assumed that the pilot maintains his/her grip on the inceptor at all times; a reasonable assumption given the findings presented by Raney et al[48] where the pilots tightened their grasp during biodynamic feedthrough.

5.2.1 Longitudinal model

The two dimensional planar model in Figure 5.8 shows the adopted model and key parameters. It consists of a representative torso model providing an estimate of the shoulder acceleration and a transfer function representation of the arm, which provides an estimate of wrist displacement. The arm has been modelled as a transfer function due to factors such as inceptor type and arm rest properties affecting the arm parameters; the properties of the latter being difficult to quantify. This also makes the model more versatile by allowing experimental data from different seating configurations to be used for the parameterisation process.[1]

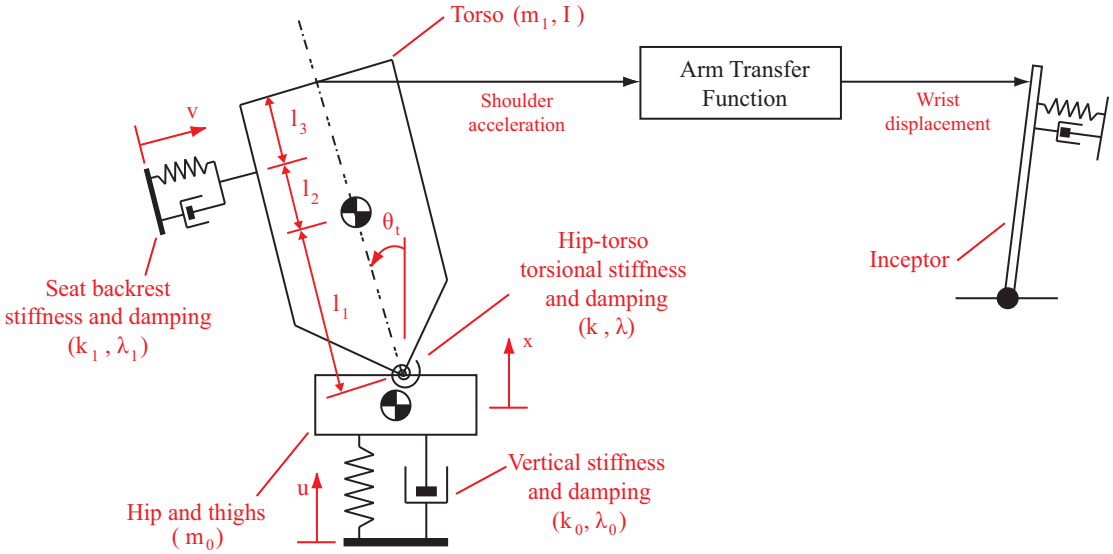

Figure 5.8: Longitudinal biomechanical model.

Equations of motion for the torso may be derived via the extended Euler-Lagrange equation:

$$\frac{d}{dt}\left(\frac{\partial \mathcal{K}}{\partial \dot{q}_i}\right) - \frac{\partial \mathcal{K}}{\partial q_i} + \frac{\partial \mathcal{V}}{\partial q_i} + \frac{\partial \mathcal{D}}{\partial \dot{q}_i} = \mathcal{Q}_i \tag{5.2.1}$$

where $\mathcal{K}, \mathcal{V}$ and $\mathcal{D}$ refer to system kinetic, potential and dissipative energy components respectively and are given by:

$$\mathcal{K} = \frac{1}{2}m_0\dot{x}^2 + \frac{1}{2}m_1\left(\dot{x}^2 + l_1^2\dot{\theta_t}^2 - 2\dot{x}\dot{\theta}_t l_1 \sin\theta_t\right) + I\dot{\theta_t}^2 \tag{5.2.2}$$

$$\mathcal{V} = \frac{1}{2}k_0(x-u)^2 + \frac{1}{2}k_0\theta_t^2 + \frac{1}{2}k_1\Big((l_1+l_2)\theta_t - v\Big)^2 \tag{5.2.3}$$

$$\mathcal{D} = \frac{1}{2}\lambda_0(\dot{x}-\dot{u})^2 + \frac{1}{2}\lambda_1\left((l_1+l_2)\dot{\theta}_t - \dot{v}\right)^2 \tag{5.2.4}$$

[1]Modelling the arm as a constrained double pendulum in three dimensions led to an over-parameterised model that would result in a challenging parameter identification task. This approach was deemed beyond the scope of this thesis.

Q_i refers to the generalised force associated with generalised coordinate q_i, in this case:

$$\begin{aligned}\sum_{i=1}^{2} \mathcal{Q}_i \delta q_i &= \mathcal{Q}_1 \delta x + \mathcal{Q}_2 \delta\theta_t \\ &= -g(m_0+m_1)\sin\theta\delta x + m_1 l_1 g\cos(\theta-\theta_t)\delta\theta_t \end{aligned} \tag{5.2.5}$$

where gravity has been treated as a pitch attitude (θ) dependant generalised force input. Substituting the above into Equation 5.2.1 yields the following two nonlinear equations of motion:

$$(m_0+m_1)\ddot{x} - m_1 l_1(\ddot{\theta}_t \sin\theta_t + \dot{\theta_t}^2\cos\theta_t) + \lambda_0(\dot{x}-\dot{u}) + k_0(x-u) + (m_0+m_1)g\sin(\theta) = 0 \tag{5.2.6}$$

$$(m_1 l_1^2 + I)\ddot{\theta}_t - m_1 l_1 \ddot{x}\sin\theta_t + \lambda_1\Big((l1+l2)\dot{\theta}_t - \dot{v}\Big) + k + k_1(l_1+l_2)^2 - k_1(l_1+l_2)v = m_1 l_1 g\cos(\theta-\theta_t) \tag{5.2.7}$$

For lateral torso equations of motion, it has been treated as a roll attitude dependant force input. The above equations fit into the following general form after linearisation about a seating posture:

$$\mathbf{M}\ddot{\varrho} + \mathbf{\Lambda}\dot{\varrho} + \mathbf{K}\varrho = \mathbf{\Lambda}_\varphi\dot{\varphi} + \mathbf{K}_\varphi\varphi \tag{5.2.8}$$

where $\mathbf{M}$, $[\mathbf{\Lambda}, \mathbf{\Lambda}_\varphi]$ and $[\mathbf{K}, \mathbf{K}_\varphi]$ are the system mass, damping and stiffness matrices respectively and

$$\varrho = \begin{bmatrix} \delta x & \delta\theta_t \end{bmatrix} \tag{5.2.9}$$

$$\varphi = \begin{bmatrix} \delta u & \delta v & \delta\theta \end{bmatrix} \tag{5.2.10}$$

These contain the generalised coordinate variables and system inputs respectively. Linearisation about a torso inclination angle (θ_{t0}) and a pitch attitude (θ_0) yield the following system matrices:

$$\mathbf{M} = \begin{bmatrix} m_0+m_1 & -m_1 l_1\sin\theta_{t0} \\ -m_1 l_1\sin\theta_{t0} & m_1 l_1^2 + I \end{bmatrix} \tag{5.2.11}$$

$$\mathbf{\Lambda} = \begin{bmatrix} \lambda_0 & 0 \\ 0 & \lambda_1(l_1+l_2)^2 \end{bmatrix} \tag{5.2.12}$$

$$\mathbf{K} = \begin{bmatrix} k_0 & 0 \\ 0 & k + k_1(l_1+l_2)^2 - m_1 l_1 g\sin(\theta_0-\theta_{t0}) \end{bmatrix} \tag{5.2.13}$$

$$\mathbf{\Lambda}_\varphi = \begin{bmatrix} \lambda_0 & 0 & 0 \\ 0 & \lambda_1(l_1+l_2) & 0 \end{bmatrix} \tag{5.2.14}$$

$$\mathbf{K}_\varphi = \begin{bmatrix} k_0 & 0 & -(m_0+m_1)g\cos\theta_0 \\ 0 & k_1(l_1+l_2) & -m_1 l_1 g\sin(\theta_0-\theta_{t0}) \end{bmatrix} \tag{5.2.15}$$

The equations can be simplified by considering relative linear and angular motion of coordinate variables together with input. Further simplifications can be made by assuming backrest accelerations to be a component of base acceleration (N_{z_p}). Therefore, letting:

$$z = x - u \tag{5.2.16}$$

$$y = (l_1+l_2)\theta_t \tag{5.2.17}$$

$$u = N_{zp} \tag{5.2.18}$$

$$v = N_{zp}\sin\theta_{t0} \tag{5.2.19}$$

and making the substitutions allows Equation 5.2.8 to be put into the following state-space form:

$$\begin{bmatrix} 0 & m_0+m_1 & 0 & -\tilde{h} \\ 0 & -m_1 l_1 \sin\theta_{t0} & 0 & \check{h} \\ 1 & 0 & 0 & 0 \\ 0 & 0 & 1 & 0 \end{bmatrix} \begin{bmatrix} \delta\dot{z} \\ \delta\ddot{z} \\ \delta\dot{y} \\ \delta\ddot{y} \end{bmatrix} = \begin{bmatrix} -k_0 & \lambda_0 & 0 & 0 \\ 0 & 0 & -\hat{h} & -\lambda_1(l_1+l_2) \\ 0 & 1 & 0 & 0 \\ 0 & 0 & 0 & 1 \end{bmatrix} \begin{bmatrix} \delta z \\ \delta\dot{z} \\ \delta y \\ \delta\dot{y} \end{bmatrix} + \begin{bmatrix} \tilde{h}\sin\theta_{t0} - m_0 - m_1 & -(m_0+m_1)g\cos\theta_0 \\ m_1 l_1 \sin\theta_{t0} - \check{h}\sin\theta_{t0} & -(m_0+m_1)g\sin\theta_0 \\ 0 & 0 \\ 0 & 0 \end{bmatrix} \begin{bmatrix} \delta N_{zp} \\ \delta\theta \end{bmatrix} \quad (5.2.20)$$

where,

$$\hat{h} = \frac{k + k_1(l_1+l_2)^2 - m_1 l_1 g \sin(\theta_0 - \theta_{t0})}{l_1+l_2} \quad (5.2.21)$$

$$\tilde{h} = \frac{m_1 l_1 \sin\theta_{t0}}{l_1+l_2} \quad (5.2.22)$$

$$\check{h} = \frac{m_1 l_1^2 + I}{l_1+l_2} \quad (5.2.23)$$

The output equation provides the expressions for horizontal ($\ddot{z}_s$) and vertical ($\ddot{x}_s$) shoulder accelerations as follows:

$$\begin{bmatrix} \delta\ddot{x}_s \\ \delta\ddot{z}_s \end{bmatrix} = \begin{bmatrix} \frac{l_1+l_2+l_3}{l_1+l_2}\cos\theta_{t0} & 0 \\ \frac{l_1+l_2+l_3}{l_1+l_2}\sin\theta_{t0} & 1 \end{bmatrix} \begin{bmatrix} \delta\ddot{y} \\ \delta\ddot{z} \end{bmatrix} + \begin{bmatrix} \frac{l_1+l_2+l_3}{2(l_1+l_2)}\sin 2\theta_{t0} \\ 1 + \frac{l_1+l_2+l_3}{2(l_1+l_2)}\sin^2\theta_{t0} \end{bmatrix} \delta N_{zp} \quad (5.2.24)$$

After the derivation of the equations of motion, model parameters were selected such that its frequency response matched experimental data. This was done by specifying the parameter identification process as a series of constrained optimisation problems that minimised a cost function. For the torso model, lack of phase data meant that only magnitude ratios could be considered:

$$\mathcal{J}_{\texttt{torso}} = \sum_{i=1}^{N} \Big(T_x(\omega_i) - \hat{T}_x(\omega_i)\Big)^2 + \sum_{i=1}^{N} \Big(T_z(\omega_i) - \hat{T}_z(\omega_i)\Big)^2 \quad (5.2.25)$$

where T_x and T_z are the experimental horizontal and vertical magnitude ratios respectively. $\hat{T}_{[\cdot]}$ is the corresponding model frequency response. ω_i represents the frequencies at which experimental data was provided. The arm model was parameterised via the following cost function that included phase information:

$$\mathcal{J}_{\texttt{arm}} = \sum_{i=1}^{N} \Big(F_m(\omega_i) - \hat{F}_m(\omega_i)\Big)^2 + \frac{\pi}{180}\sum_{i=1}^{N} \Big(F_p(\omega_i) - \hat{F}_p(\omega_i)\Big)^2 \quad (5.2.26)$$

where F_m and F_p are the experimental magnitude ratio and phase data respectively. Similar to Equation 5.2.25, $\hat{F}_{[\cdot]}$ is the corresponding model data. Parameters varied to obtain the best fit with experimental data were stiffness and damping coefficients. Mass, inertia and characteristic lengths were obtained from publications by AMRL[143] and Matsumoto et al[144] and kept fixed during this process.

Torso parameters were selected first to match data from Kitazaki[29] and AMRL. The arm models were then parameterised to fit data from Gillespie et al[44] and AMRL for the lateral and longitudinal cases respectively.

Most experiments in literature involved a subject undertaking a control task whilst seated on a vibration platform. Lack of access to such experimental equipment meant that each parameterisation stage required the recreation of the actual experiment within MATLAB®; requiring the use of the MOCM for longitudinal dynamics. It should be noted that the dependance of the parameterisation process on experimental data means that the models remain only representative of the experimental setup. The torso properties used for the model parameterisation process and the resulting stiffness and damping parameters are summarised in Table 5.1.

Parameter	Longitudinal model	Lateral model	Units
m_0, m_1	24, 34	24, 34	kg
I	5	5	kgm^2
l_1, l_2, l_3	0.3, 0.2, 0.15	0.3, 0.2, 0.15	m
θ_0, θ_{t0}	21, 90	0, 90	degrees
k, k_0, k_1	2500, 5000, 5700	287, 1009, 17452	N/m
λ, λ_0, λ_1	1900, 510, N/A	163, 41, 183	N/ms^{-1}

Table 5.1: Torso model parameters used for and obtained via the optimisation process.

Experimental results from Kitazaki and Matsumoto were found to be ideal for parameterising the torso model. Kitazaki obtained experimental data from eight subjects (and did not consider phase response) whilst Matsumoto's work focused in more detail on a single subject. Accelerometers were attached to the pelvis, abdomen, head, along the spine and the seat. The seat lacked a backrest and was positioned on a vibration platform. Once seated, subjects were exposed to vertical vibrations ranging from 3 rad/s to 220 rad/s. They were not asked to perform any type of control tasks as only upper body transmissibility was being investigated.

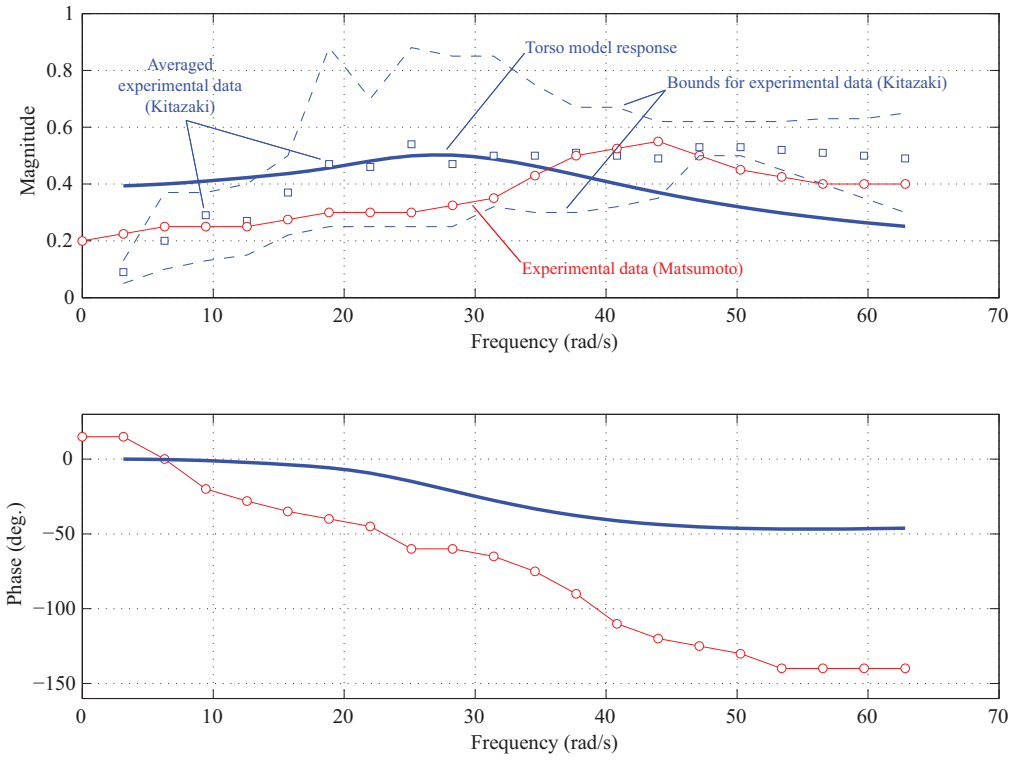

Figure 5.9: Comparison with experimental data: $\ddot{x}_s$ due to N_{z_p}.

Matsumoto's and Kitazaki's experimental data are presented together with the torso model frequency response in Figures 5.9 and 5.10. The differences between the model and experimental

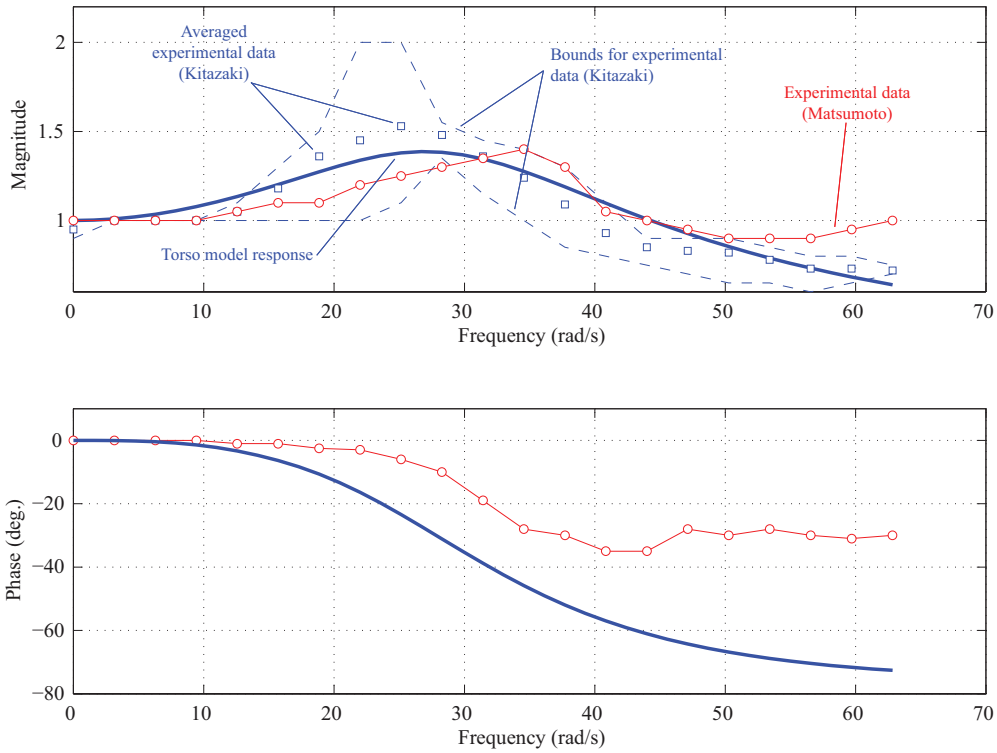

Figure 5.10: Comparison with experimental data: $\ddot{z}_s$ due to N_{z_p}.

setup causes significant disagreement in horizontal transmissibility characteristics (Figure 5.9). Higher feedthrough below 20 rad/s can be attributed to the inclusion of a backrest in the model. Lower feedthrough above 40 rad/s is mainly due to the restriction of the pelvis mass to a single degree of freedom.

It is evident from Figure 5.10 that the upper-body's vertical response to seat vibration has two resonant modes. The primary resonance peak occurs between 20 rad/s and 30 rad/s and consists of vertical and pitching motion of the pelvis and vertical motion of the legs. These result in the overall vertical translational motion of the upper body as well as the angular motion of the spine. Above 60 rad/s the body acts like a heavy damper. The secondary resonant mode exists mainly due to the rotational mode of the pelvis and is evident around 50 rad/s in Kitazaki's data. The same mode appears above 60 rad/s in Matsumoto's data, which was obtained through the same experimental setup but where all subjects were asked to adopt an erect posture. Matsumoto and Kitazaki both attribute the disagreement to subject posture. A slouched posture was found to have a damping effect and reduced the frequency of this mode. An erect posture was found to have the opposite effect as evident in Matsumoto's experimental data.

However, the model does capture the essential features of the biodynamic response, especially given the inter-subject variations. Phase characteristics differ significantly from that obtained by Matsumoto, but large inter-subject variations could also exist here. Therefore, an assessment of its accuracy requires data from a statistically significant sample size. This difference must be kept in mind when analysing simulation results concerned with pilot torso dynamics.

The arm model was parameterised using data from one of the earliest experimental studies into the effects of biodynamic feedthrough on aircraft control that was done at AMRL[143] in the 1970s. The effects of vibrations (ranging from 6 rad/s to 60 rad/s) along the vertical and lateral axes were studied. Due to the limitations of the experimental hardware available at the time, each axis was investigated separately with only two subjects; another fact to be kept in mind when interpreting the results.

The experimental setup involved a display showing pitch/roll reference and error lines that the subject controlled via a centre stick. Platform vibration and movement of the display lines were independent of each other. Forcing functions used for the control task were kept at sufficiently low frequencies to the signal used to drive the biodynamic response. Accelerometers were attached around the subject's upper body including the arms. The subjects were seated on a standard Republic F-105 ejection seat with a comfortable shoulder strap and seat belt arrangement, thereby allowing any seat-subject coupling effects to be captured. The overall setup aimed to be as close to that of a typical military aircraft operation as possible. This has been summarised in the block diagram shown in Figure 5.11.

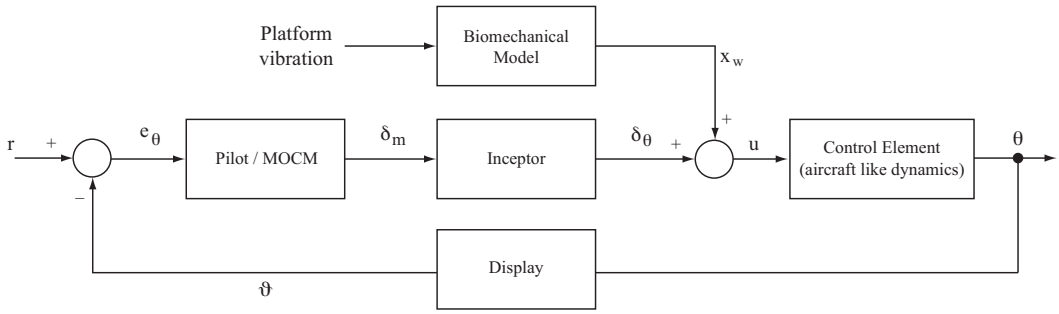

Figure 5.11: Block diagram representing the experimental setup of AMRL studies.

Effects of vertical vibration were investigated while the subject concentrated on a compensatory pitch control task. Since platform vibration was perpendicular to the required inceptor motion, the effects of direct vibration-induced control action were minimised, allowing only the biodynamic feedthrough components to appear within the response. This was not the case with lateral vibration experiments where the inertial forces due to the subject's upper body mass and the inceptor mass caused a bobweight effect.

Although the AMRL study[143] investigated three types of plant dynamics, the following was found to be the most suitable to parameterise the biodynamic model:

$$\frac{\vartheta(s)}{u(s)} = \frac{2.56(s+1.42)}{s(s^2+2(0.56)(1.71)s+1.71^2)} \frac{\text{cm}}{\text{cms}^{-2}} \tag{5.2.27}$$

where ϑ is the displayed pitch attitude and u is the input to the aircraft model. This is an approximation of the short period response of a large bomber similar to the North American XB-70. The experiments also investigated the differences between the use of a spring stick and a stiff stick. Since Airbus aircraft are equipped with a passive spring stick inceptor, only the corresponding data set was used. The following transfer function was used to represent stick dynamics:[2]

$$\frac{\delta_{\theta_t}(s)}{\delta_m(s)} = \frac{164}{s^2+2(0.3)(23)s+23^2} \frac{\text{m}}{\text{N}} \tag{5.2.28}$$

Formulation of the MOCM leaves only the arm model to be identified in the block diagram in Figure 5.11. The input parameters to the MOCM algorithm are given in Table 5.2. Simulating the subject's response using this control-theoretic model and minimising the cost function in Equation 5.2.26 resulted in the following transfer function relating stick deflection (x_w) to shoulder acceleration ($\ddot{x}_s$):

$$\frac{x_w}{\ddot{x}_s} = \frac{274.81(s-228.80)}{(s+33.33)(s+21)(s^2+2(0.23)(28.02)s+28.02^2)} \frac{\text{cm}}{\text{ms}^{-2}} \tag{5.2.29}$$

[2]The representation found for the Thrustmaster HOTAS® joystick was found to be $20.28^2/(s^2 + 2(0.22)(20.28)s + 20.28^2)$.

Weighting matrix, $\mathbf{Q}$	1
Output vector	ϑ
Inherent delay, τ	0.1
Neuromuscular lag, τ_n	0.1
Attention allocation	1
Disturbance intensity	8.8
Disturbance filter	$1/(s+2)$
Noise-to-signal ratios, (ρ_u, ρ_y) (dB)	(-50,-40)

Table 5.2: MOCM parameters used to model subject response to compensatory task.

Figure 5.12 presents the results of the frequency response of the final biomechanical model in comparison with the two subjects. It can be seen that the phase characteristics of the model matches those of the subjects exceptionally well. The magnitude response captures the main feature associated with biodynamic feedthrough, that is the high frequency resonant peak around 4 Hz. The low frequency peak is introduced by the MOCM and occurs as a result of the control task given to each subject. The slight disagreement in the frequency of the biodynamic resonance peak may be attributed to subject posture and also the model's inclusion of a backrest during torso parameterisation. An experimental study involving more subjects is required to obtain a precise estimate of the frequency at which biodynamic resonance occurs.

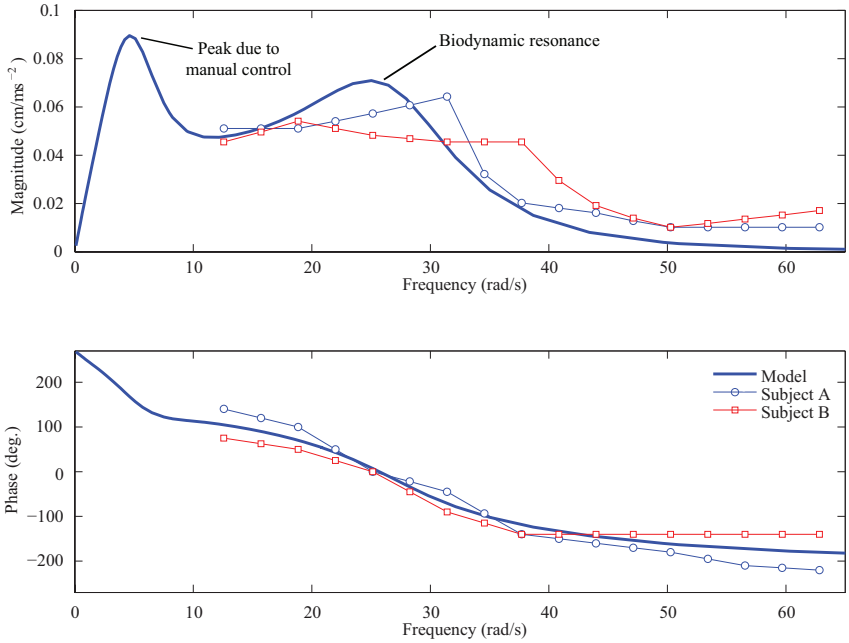

Figure 5.12: Model frequency response in comparison with AMRL subjects.

5.2.2 Lateral model

The AMRL setup to investigate lateral biodynamic effects was the same as that used to study vertical acceleration effects. Although data relating wrist motion due to lateral acceleration is available within the AMRL report, it is limited over a frequency range of 6 rad/s to 63 rad/s and also involves only two subjects. Experiments conducted by Gillespie et al[44] on the other hand, cover a frequency range of 2 rad/s to 400 rad/s and involve twelve subjects. However, it lacks data relating seat acceleration to lateral shoulder acceleration. As a result, AMRL data

was used to parameterise the lateral torso model, shown in Figure 5.13, and those from Gillespie et al was used to parameterise the arm model.

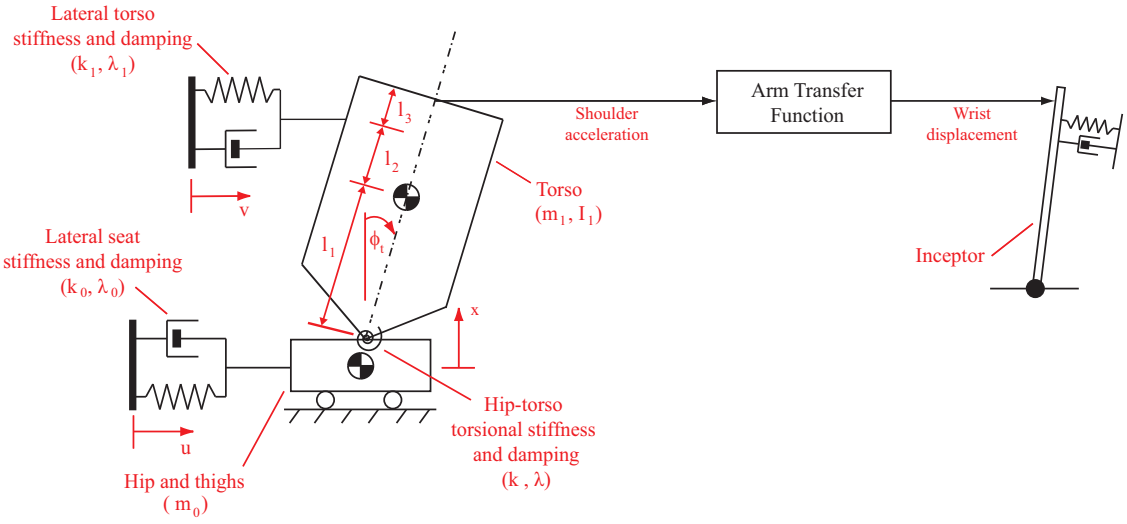

Figure 5.13: Lateral biomechanical model.

The derivation of the equations of motion is similar to the longitudinal model and presented in Appendix E. The model was parameterised using the same parameter identification process discussed earlier for the longitudinal model.

Figure 5.14 allows the lateral torso model to be compared with experimental data. Above 6 rad/s the model's magnitude response captures the resonant peak evident in the experimental data. However, it also predicts a larger low frequency resonant peak that cannot be validated. The phase response of the model is not very coherent with experimental data. However, in Reference [143] the authors doubt the reliability of the technique used to obtain phase data above 30 rad/s.

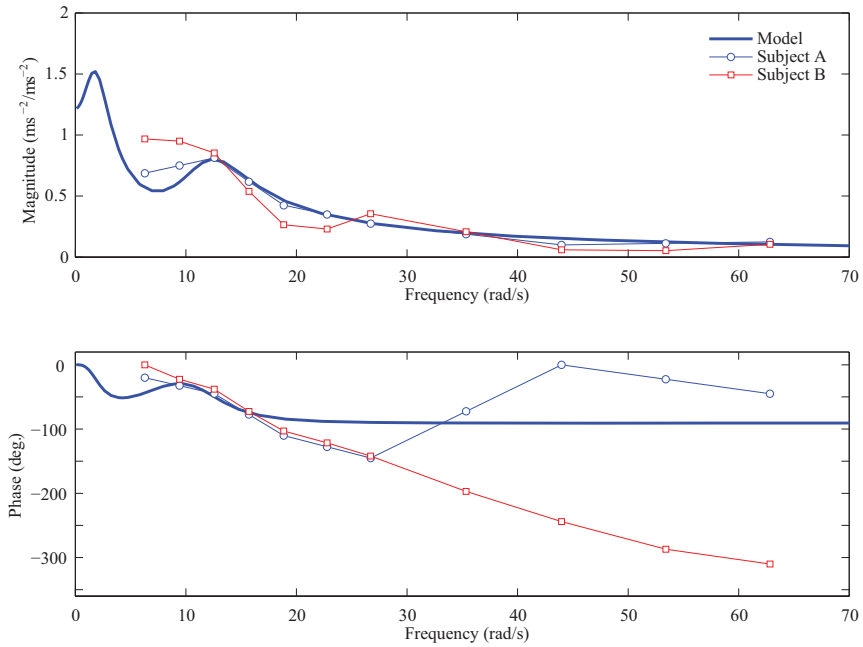

Figure 5.14: Lateral shoulder acceleration due to lateral seat acceleration.

Gillespie et al's experiments were aimed towards the development of a biodynamic feedthrough

cancellation scheme. The experimental setup and the corresponding block diagram of the PVS is presented in Figure 5.15. The use of a side-stick inceptor along with the seating arrangement brings the experimental setup close to that experienced by pilots on modern Airbus aircraft. The use of linear guides for the seating platform implied that the subjects underwent purely lateral translational but no rotational accelerations.

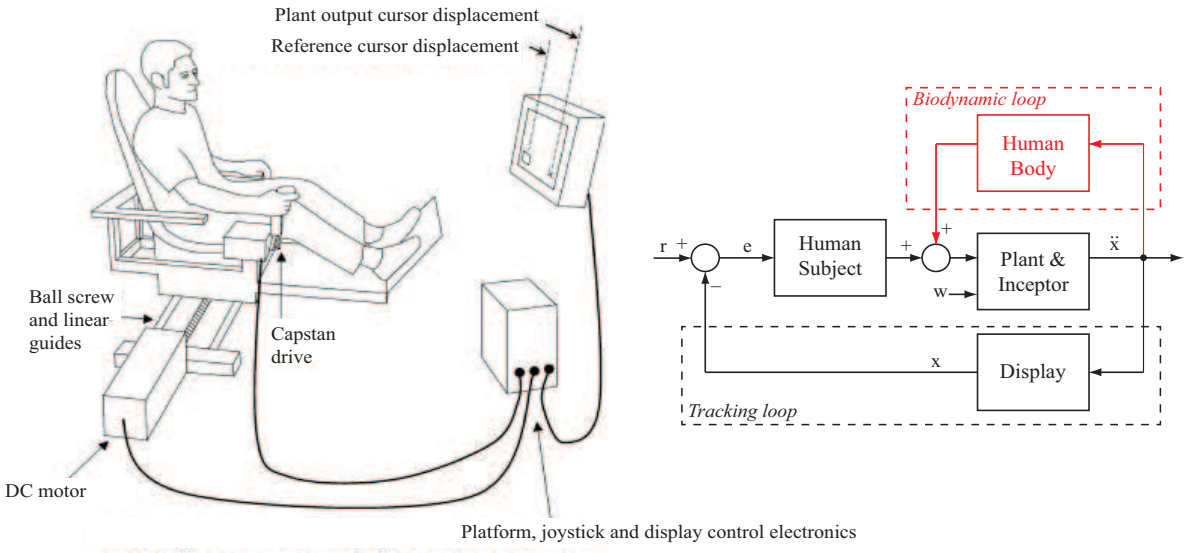

Figure 5.15: Experimental setup and corresponding block diagram of Sovenyi et al's experiments (adapted from Sovenyi and Gillespie[44]).

The key assumptions in Gillespie's approach were that stick force due to biodynamic feedthrough was independent of human volitional force and the relation between the two was linear. This implied that each component could be captured independently in separate experiments and then summed to give the overall stick force. Therefore, an MOCM representation of the subject's control input was not needed. To capture the biodynamic effects, Gillespie et al conducted experiments where the subject on a moving platform simply held on to a stiff stick with a force sensor. Biodynamic system's frequency response was obtained by making the platform position follow a filtered white noise signal. Maximum platform acceleration was 9.3 m/s^2 with a root-mean-square average of 2.3 m/s^2.

The final series of experiments conducted by Gillespie et al involved twelve subjects performing tracking tasks during which platform motion and the displayed pointer were controlled via side-stick input. Each subject also had several hours of practice on the platform prior to the experimental sessions.

The arm parameters were found by putting the lateral arm model with the parameterised torso model in series and selecting parameters that provided the best match with the experimental data. The most suitable transfer function approximate for stick force (Y_w) due to shoulder acceleration ($\ddot{y}_s$) was found to be as follows:[3]

$$\frac{Y_w}{\ddot{y}_s} = -\frac{22842(s+1.29)(s+5.54)}{(s^2+2(0.35)(6.03)s+6.03^2)(s^2+2(0.17)(84.36)s+84.36^2)}\frac{\text{N}}{\text{cms}^{-2}} \tag{5.2.30}$$

The model's response can be compared with experimental data in Figure 5.16. The model's magnitude response gives a conservative estimate of biodynamic feedthrough at frequencies

[3]Here, the lateral arm model actually outputs stick force instead of displacement because of the data provided by Gillespie et al. Multiplying Equation 5.2.30 with the inceptor dynamics (Equation 5.2.28) yields the relationship in terms of stick displacement.

below 10 rad/s; nonetheless provides a relatively accurate overall magnitude response in the region where low frequency aeroelastic modes exist. Unlike the longitudinal model that accurately matched its corresponding experimental phase data, the model's phase response is not as coherent with experimental data. The sharp drop in phase around 6 rad/s is due to the fourth order denominator of the arm transfer function.

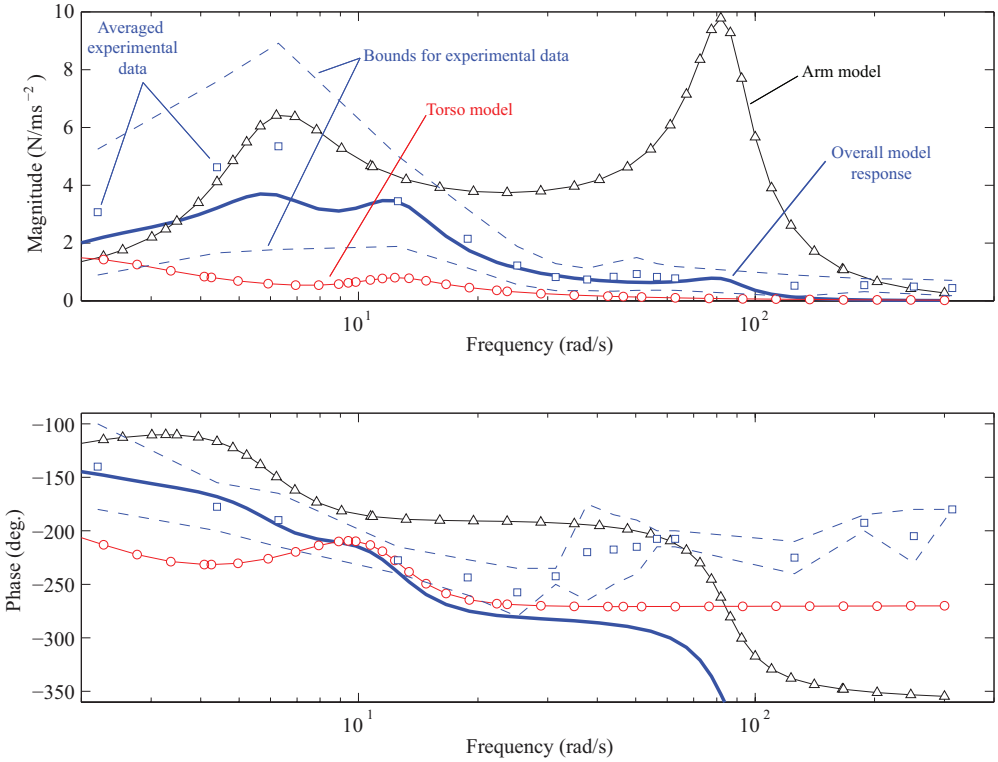

Figure 5.16: Comparison with experimental data from Sovenyi and Gillespie[44].

5.3 Conclusions

This chapter has presented models adopted and developed to capture psychophysical limitations in a pilot's perception of aircraft dynamics and his/her biodynamic response during atmospheric flight. Faithfully modelling the pilot perception requires not only models of the individual sensory channels, but also models of interactions between them. Telban's approach presented in this chapter achieves this for two of the most dominant senses affecting manual control: visual and vestibular. Unlike the proprioceptive sense that is affected by the inceptor, dynamics of these senses are kept independent of the control-theoretic component of the pilot model and vehicle dynamics.[4] The models' time-domain responses were verified against those presented by Telban and demonstrated the capability to simulate pilot perception when the visual and vestibular are in conflict with each other. The developed model provides the capability to simulate SD scenarios such as spiral divergence and postturn illusion.

The discrete biomechanical modelling approach was used to separately model the biodynamic response to longitudinal and lateral accelerations felt by the pilot. In both cases, the torso has been modelled through two dimensional planar models and coupled with a transfer function representation of the arm. Reliance on experimental data in literature necessitated the simulation of experiments in the model parameterisation process. Model frequency responses fall

[4]The proprioceptive sense has been treated implicitly within the formulation of the internal model required for the MOCM.

within the upper and lower bounds arising due to inter-subject variations, especially within the frequency range of aeroelastic modes.

This page is intentionally left blank.

CHAPTER 6

Dynamic loads envelope generation

The study of civil aircraft dynamics under the effects of atmospheric disturbance has been motivated by a number of factors, for example, crew and passenger safety and comfort. However, unsurprisingly the key driver for such analysis is the accurate prediction of airframe loads (static, dynamic and fatigue) and consequently the precise estimation of an airframe's weight distribution. Loads estimation processes are typically design loops relying on the supply of the distribution of forces and moments acting on the airframe. These are called "external" loads and are supplied by aerodynamicists for the estimation of flight loads. The resulting forces and moments arising due to shearing, bending and torsion undergone by the airframe are called "internal" loads and these are the focus of this chapter.

Methods of calculating internal loads during manoeuvres have been available for a considerable period of time. State-of-the-art research focuses on the precise calculation of the effects of atmospheric disturbances. Consequently, this chapter presents a study of gust and turbulence loads whilst treating manoeuvre loads through methods given in CS-25 that specifies a number of book case manoeuvres. The reader is directed to books by Howe[145], Wright and Cooper[146] and CS-25 appendices[147] for a detailed discussion.

This chapter begins by presenting the reader with a brief synopsis of methods used for the calculation of loads due to atmospheric disturbance. This is followed by a description of the Cranfield/Airbus AX-1[9] model together with its capabilities and limitations. The chapter concludes with the derivation and presentation of dynamic loads envelopes for the AX-1. These are later used for the assessment of pilot-model-in-the-loop simulations of flight incidents and failure scenarios.

6.1 Synopsis of dynamic gust loads concepts

Methods for the calculation of loads endured by an airframe when encountering atmospheric disturbances fall into two distinct categories: deterministic and stochastic. This separation is primarily due to the assumptions made in modelling the atmospheric disturbance itself. Deterministic methods rely on gust velocity profiles calculated via a smooth mathematical function, whereas the stochastic approach assumes turbulence profiles to be a noise process defined through its power spectral density (PSD). Note that, a distinction has been made here between the terms 'gust' and 'turbulence'. The term gust will be used in the context of deterministic methods whilst turbulence will be employed when discussing stochastic methods.

Both approaches take advantage of nonlinear time domain simulations and linear frequency domain methods and each carries roughly equal computational costs when calculating loads envelopes. The application of such methods not only require a significant modelling effort but also substantial integration of the following key components:

- structural and aerodynamic forces and moments.
- flight control laws and control surface actuation.
- active loads control systems (load alleviation functions).
- autopilot systems.
- pilot models to predict manual control actions.

Once such a simulation environment is created, correlated loads at a given instant of time or non-correlated loads for design envelope analysis can be extracted.

The processing and interpretation of the large quantity of data generated through the numerous simulations is the next challenge in the process. This requires the analysis of simulation data for the expected mass cases at critical flight envelope points (or flight profiles) and various gust lengths or turbulence intensities. A large number of simulations must be run and the data searched to highlight the most extreme loadings and load combinations, which are effectively the airframe's limit loads. Increasing these by a factor of 1.5 yields the ultimate load.

In addition to the definition of aircraft model parameters, each simulation also requires the selection of gust or turbulence model parameters according to the certification requirements. For both approaches, these parameters are a function of the following airspeed boundaries:

- V_A is referred to as the *manoeuver design speed* below which the pilot is allowed care free handling of the aircraft.
- V_B is the upper bound for flight in turbulent weather conditions often called *speed for maximum gust intensity*.
- V_C is the *structural cruise design speed* not to be exceeded deliberately.
- V_D is an airspeed boundary that provides a margin between V_C and the aircraft's upper airspeed limit; known as the *dive speed*.

Basing the limit loads calculations on these airspeeds allows the aircraft's operational use to considered and the resulting loads envelopes are consequently not overly conservative.

6.1.1 Deterministic approach

Also referred to as the 'discrete' gust method, techniques in this area have existed since the 1940s, when atmospheric disturbance was crudely modelled as a sharp-edged gust defined as follows:

$$w_g(t) = \begin{cases} 0 & \text{if } t < t_0, \\ \bar{w}_g & \text{if } t \geq t_0. \end{cases} \tag{6.1.1}$$

where w_g is the vertical gust velocity as a function of time t, and $\bar{w}_g$ is the maximum gust velocity occurring instantaneously at a time t_0. This was found to be overly conservative and

therefore, was succeeded by a ramp like representation, which in turn, was superseded by the *1-cosine* profile widely in use today. The *1-cosine* profile is defined as follows:

$$w_g(t) = \begin{cases} 0 & \text{if } t < t_0, \\ \pm\frac{\bar{w}_g}{2}\left(1 - \cos\frac{2\pi V_{\text{TAS}}}{L_g}t\right) & \text{if } t_0 \leq t \leq t_0 + \frac{L_g}{2\pi V_{\text{TAS}}}, \\ 0 & \text{if } t > t_0 + \frac{L_g}{2\pi V_{\text{TAS}}}. \end{cases} \tag{6.1.2}$$

where V_{TAS} is the aircraft's true airspeed (TAS) and L_g is the gust length. These profiles are shown in Figure 6.1 and form the basis of dynamic loads analysis.[1]

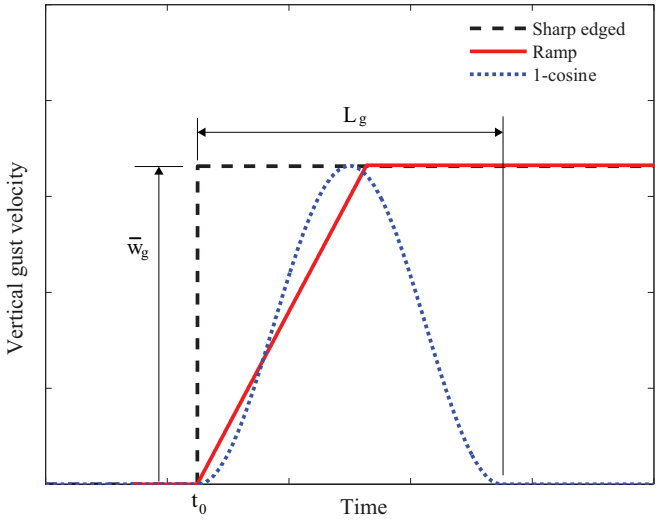

Figure 6.1: Examples of discrete gust profiles.

The first section of CS-25.341(a)(2)[148] specifically requires the use of the *1-cosine* in a loads calculation process commonly known by loads and aeroelastic engineers as the *tuned discrete gust method*. However, it does not provide any details on how such an analysis is to be carried out and only refers to it as follows:

> "A sufficient number of gust gradient distances in the range 9 m (30 feet) to 107 m (350 feet) must be investigated to find the critical response for each load quantity."

This method is intended to provide the worst case loads acting on the airframe upon a gust encounter. It requires simulations with combinations of gust lengths and maximum velocities, as shown in Figure 6.2(a), followed by a sorting process to identify the worst cases of correlated and non-correlated loads. The gust lengths (which are twice the gust gradient) are related to the peak gust velocities as follows[148]:

$$\bar{w}_g = w_r \mathcal{F}\left(\frac{L_g}{700}\right)^{1/6} \tag{6.1.3}$$

where w_r is a reference gust velocity that varies linearly with altitude. Its variation is prescribed in terms of equivalent airspeed (EAS) and can be found in CS-25[148]. $\mathcal{F} \leq 1$ is called the flight profile alleviation factor and is a function of the aircraft's weight and altitude ceiling. It is effectively a weighting to reduce the impact of particular areas of the flight envelope where the aircraft is unlikely to operate; for example, airspeeds between V_C and V_D at low altitudes. The

[1] Note that the profile defined in Equation 6.1.2 implies the effects of both positive and negative gust profiles are to be analysed.

prescribed variation proposed in Equation 6.1.3 is an attempt to model the frequency content of disturbances within the atmosphere. It associates gust velocities linearly with gust lengths and its effect in the frequency domain is shown in Figure 6.2(b). Basically each profile has an associated bandwidth frequency and aircraft modes lying beyond it are not sufficiently excited.

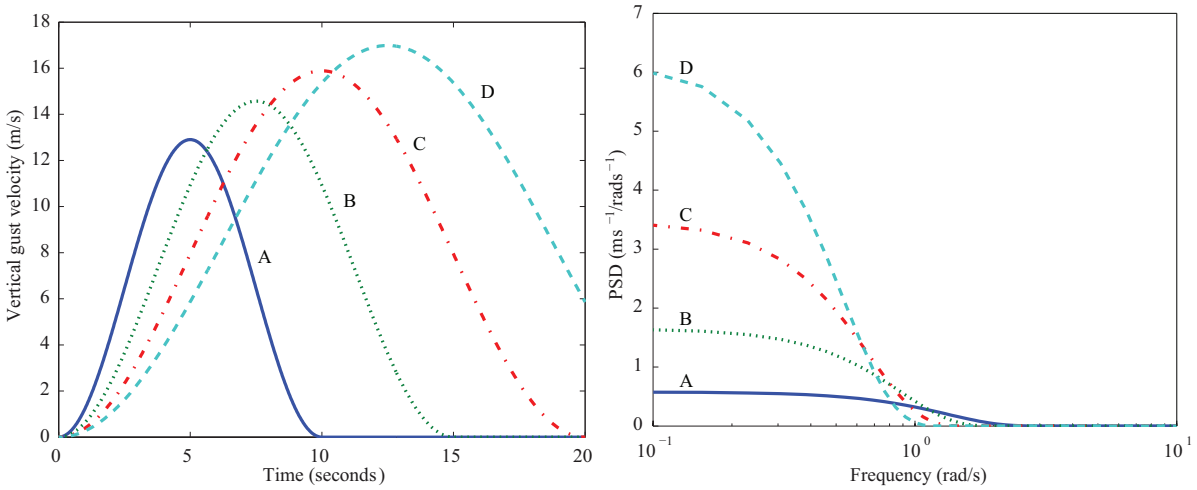

(a) (b)

Figure 6.2: *1-cosine* gust profiles and corresponding PSDs used in tuned discrete gust analysis.

Hoblit states that two fundamental drawbacks of the tuned discrete gust method exist:

1. compared to stochastic turbulence profiles the gust profiles do not resemble real turbulence and,
2. the resulting loads are highly sensitive to the chosen range of gust lengths.

The first point refers to the generalisation of the *1-cosine* profile to all atmospheric disturbances and strictly speaking, it is a valid point. However, as shown in Figure 6.3(a), gust profiles close to the *1-cosine* shape do exist and are significantly large in amplitude to justify the use of such profiles. On the other hand, other gust encounters have shown profiles like that presented in Figure 6.3(b),[2] which points to a need for a reassessment of current assumptions regarding the nature of gust and turbulence as well as the adoption of methods such as the statistical discrete-gust[149][150][151], that combine aspects of deterministic and stochastic approaches. Hoblit's second point more importantly, refers to the assumption that the prescribed gust lengths and velocities cover a sufficiently wide frequency range that includes the most significant airframe elastic modes. Consequently, it is assumed that each gust inserts enough energy to sufficiently excite the corresponding mode and yield a maximum load quantity at a given part of the airframe. Therefore, the method is not capable of capturing the combined effects of modes interacting with each other.

The method's popularity stems from its intuitive time domain nature. Considering the current trend in large aircraft design that has resulted in low frequency structural modes, a deterministic approach that covers the low frequency range is becoming more relevant.

[2]The gust profiles presented in this thesis were kindly supplied by Airbus UK and obtained through an in-house process that took advantage of a validated impulse response function database. The convolution of the relevant impulse response functions with and without control surface deflections allows the derivation of the gust profile experienced by the aircraft.

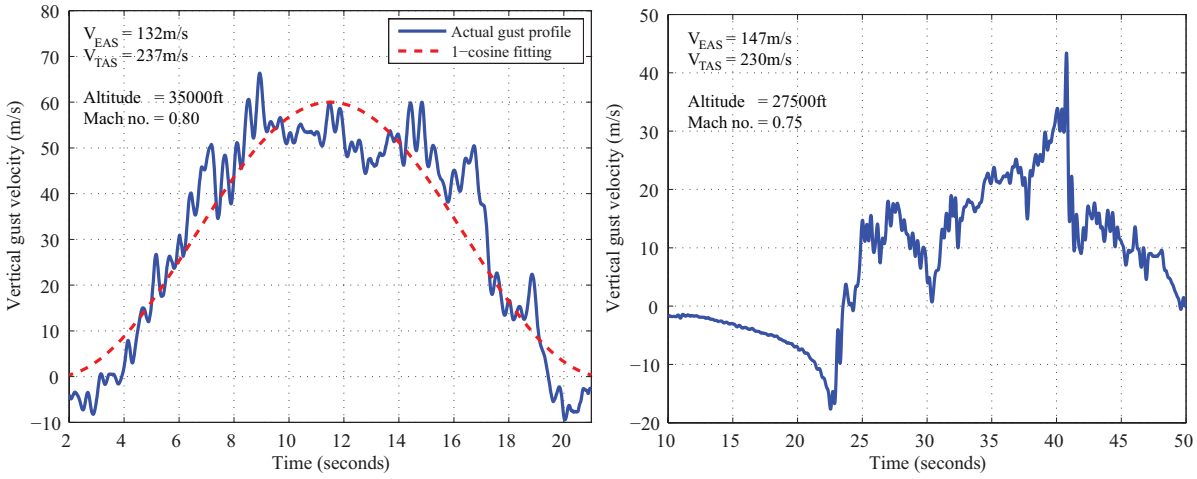

(a) Incident A

(b) Incident B

Figure 6.3: Example gust profiles.

In the frequency domain, the harmonic gust technique[146, p.315] uses the linear harmonic forced vibration method by considering a gust profile to be defined as follows:

$$w_g(t) = \bar{w}_g \sin\left(\frac{2\pi V_{\text{TAS}}}{\lambda_g} t\right) \tag{6.1.4}$$

where λ_g effectively determines the gust wavelength. However, such a study is strictly a linear analysis requiring linearised models and frequency response functions relating the load quantity of interest (IQ) to the gust input. This ignores nonlinear dynamics exhibited by the aircraft or introduced through the FCS.

6.1.2 Stochastic approach

Turbulence profiles used in this approach assumes the atmospheric disturbance to be a *homogenous isotropic stationary Gaussian* noise process[152]. The homogeneity assumption allows the profile to be independent of spatial variables. So although high altitude turbulence is known to occur in patches, it is assumed that there is no significant dependence on spatial coordinates. The term isotropic implies that the turbulence profiles along each axis are independent of each other. Finally, assuming a Gaussian noise process that is stationary also simplifies statistical analysis.

As is the case with deterministic methods, it is further assumed that the aircraft travels through a frozen disturbance field. This is based on the observation that typically an aircraft is travelling at a far higher airspeed than the velocities associated with the disturbance field. So the oncoming perturbations in angle of attack or sideslip are not affected by the aircraft itself. However, as shown in Figure 6.3, flight incidents involving disturbances up to 25% of the aircraft's true airspeed do occur.

The turbulence profile is characterised through the use of a filter with a characteristic PSD to shape the frequency content of the noise signal. The von Kármán and Dryden PSDs typically used within the aerospace industry are presented in Table 6.1. The terms ω, L and σ_w refer to frequency, turbulence scale and rms gust velocity respectively. L effectively determines the filter's cut-off frequency whilst σ_w fixes the low frequency gain.

The definition of such a filter to characterise atmospheric turbulence simplifies the analysis involved in linear frequency domain methods. A PSD for a particular IQ can now be obtained

Turbulence PSD	Longitudinal	Lateral and vertical
von Kármán	$\sigma_w^2 \frac{2L}{\pi}\left[\frac{1}{(1+1.792L^2\omega^2)^{5/6}}\right]$	$\sigma_w^2 \frac{L}{\pi}\left[\frac{1+4.781L^2\omega^2}{(1+1.792L^2\omega^2)^{11/6}}\right]$
Dryden	$\sigma_w^2 \frac{2L}{\pi}\left[\frac{1}{(1+L^2\omega^2)^2}\right]$	$\sigma_w^2 \frac{L}{\pi}\left[\frac{1+3L^2\omega^2}{(1+L^2\omega^2)^2}\right]$

Table 6.1: The von Kármán and Dryden turbulence power spectral densities.

by simply multiplying the turbulence PSD with a predetermined frequency response function for the IQ. This process relies on the validity of a linear relationship between the atmospheric disturbance and the forces and moments acting on the airframe. It requires linearised models of the FCS and load alleviation functions (LAF); which can have highly nonlinear features such as acceleration thresholds and hold functions.

The von Kármán PSD has been used for all continuous turbulence (CT) simulations in this study because:

- It represents a better fit to the observed turbulence data[153].
- Certification and regulatory bodies such as European Aviation Safety Agency (EASA) require its use in the estimation of airframe loads[148].
- Although the Dryden PSD can be transformed into a state-space form exactly[154], excellent approximations of the von Kármán PSD are available in modelling suites such as the MATLAB/Simulink Aerospace Toolbox®.

Another advantage of such a turbulence profile, other than realism, is that it subjects the aircraft to a random mix of gust lengths and speeds; allowing effects arising from the potential resonant build up of lightly damped structural modes to be captured. This approach is even more relevant considering the current industry use of damping ratios lower than 10% for their calculation of airframe loads. However, deterministic methods maintain their relevance when flexible modes are highly damped.

Design envelope analysis required by CS-25 for the determination of limit loads adopts a similar process to that of the tuned discrete gust method. Simulations must be conducted with a range of aircraft configurations and turbulence intensities. Limit loads ($\hat{P}$) are then obtained as follows:

$$\hat{P} = P_{1g} \pm U_\sigma \bar{A} \tag{6.1.5}$$

where P_{1g} is the steady 1g load and U_σ is the limit turbulence intensity (in terms of TAS) calculated as follows:

$$U_\sigma = \bar{U}_\sigma \mathcal{F} \tag{6.1.6}$$

where $\bar{U}_\sigma$ is the reference velocity prescribed in CS-25 as a piecewise linear function of altitude. It varies from 27.43m/s at sea level to 24.08m/s at 24000ft and remains constant up to 64000ft for V_B and V_C. These values are halved for V_D. $\bar{A}$ is the ratio of the incremental IQ to turbulence velocity in terms of rms, that is:

$$\bar{A} = \frac{\sigma_y}{\sigma_w} \tag{6.1.7}$$

where y and σ_y refer to the IQ and its rms respectively and σ_w is the rms value for the turbulence velocity profile. Therefore, in this analysis the product of U_σ and $\bar{A}$ represents the incremental limiting IQ value due to turbulence.

The design envelope analysis method has its advantages, disadvantages and complications that are thoroughly discussed by Hoblit[153]. It is also versatile because it can be used to study fatigue loads for a given flight profile. However, instead of searching for peak loadings CS-25 requirements focus on rms values, which in the context of this research is inappropriate; primarily due to the fact that profiles obtained from turbulence and gust encounters do not tend to be sufficiently stationary or zero mean. A calculated rms value does not reflect the presence of peaks that are bound to be higher than the rms value itself. This is addressed through a method known as *mission analysis* that takes advantage of the concept of frequency of occurrence and applies it to determine probabilistic flight loads envelopes.[153][155]

Given a long enough time history for an IQ, its associated probability density function (pdf) can be obtained. However, this does not provide information on either the chances that a maximum loading will occur nor the number of times it will occur in a given period of time. To obtain such information the time history must be processed to obtain data from which the frequency of particular peak values can be deduced; that is data from which the frequency of occurrence can be calculated. Peak counting is an approach that can be used here and it involves the division of the IQ range into a number of intervals and counting of corresponding occurrences of peaks.

The *peak-between-means* method is a peak counting technique used by the US Federal Aviation Authority (FAA) to obtain statistical data from the DFDR of operational aircraft such as the Airbus A320[156] and the Boeing 777-200ER[157]. A time history for an IQ (typically acceleration) is extracted from the DFDR and its mean value is subtracted to obtain incremental data. The maximum or minimum peaks are then identified between each zero crossing. A threshold zone is defined to ignore peaks that represent insignificant deviations from the mean or are present due to measurement noise. This threshold is usually set to ±5%, ±0.5% and ±0.25% for IQs primarily affected by vertical, sideways and fore-aft turbulence. The application of this method to a vertical acceleration time history is shown in Figure 6.4.

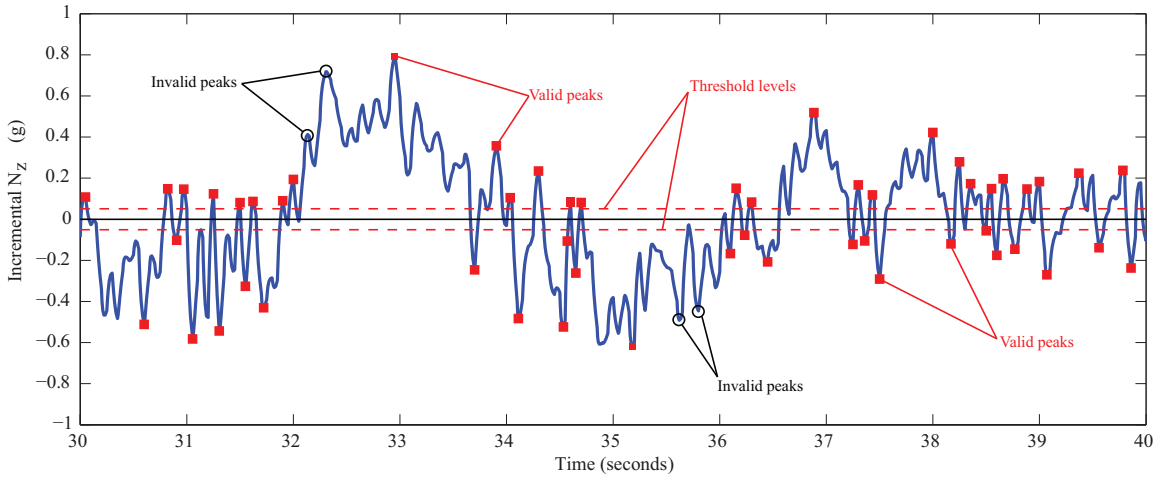

Figure 6.4: Example time history showing peak selection process.

The collected peak counts for each interval can then be summed in a descending order to obtain the number of peaks that occur above a given IQ value. In this way, the number of occurrences per unit time effectively yields the frequency of occurrence of a particular loads IQ, denoted here as $N(y)$. Assuming a Gaussian turbulence profile, this can be theoretically approximated by Rice's equation[153]:

$$N(y) = N_0 e^{-\frac{1}{2}(y/\sigma_y)^2} \tag{6.1.8}$$

where

$$N_0 = \frac{1}{2\pi}\frac{\sigma_{dy/dt}}{\sigma_y} \tag{6.1.9}$$

The idea of frequency of occurrence lays the foundation for the mission analysis criterion which allows the treatment of the complete flight profile as follows:

$$N(y) = \sum_i t_i N_0 \left[P_1 e^{\Delta y/\bar{A}b_1} + P_2 e^{\Delta y/\bar{A}b_2} \right] \tag{6.1.10}$$

where t_i is the fraction of time spent at the i^{th} flight phase and Δy is the incremental IQ. The terms P_1, P_2, b_1 and b_2 are functions of altitude and prescribed values can be found in work done by Hoblit[153][158]. A frequency of occurrence of 2×10^{-5} cycles per hour is generally accepted for the limit load value. With regards to the ultimate load, it must be demonstrated that it only occurs once in 10^8 hours or has a frequency of occurrence lower than or equal to 10^{-8} cycles per hour.[153]

The reliance of mission analysis on a predefined flight profile is its strength as well as weakness. Assuming it is defined appropriately, loads envelope for aircraft operating close to the design envelope can only be obtained via such an analysis. However, this requires simulations over the entire flight envelope and the validity of the results depend on the correct definition of the flight profile.

In contrast, the design envelope requires simulations only at critical points of the flight envelope with different aircraft configurations and mass cases. However, the use of such envelopes from a perspective that assumes guaranteed airframe structural integrity within the design envelope is incorrect. Hoblit presents the fundamental assumption of such an approach:

> "...design gust velocities are based on experience; the design gust velocities that are selected are adequate only when the new airplane, like its predecessors, operates well within its design envelope."

In fact, this is also true for deterministic methods and is the basis of one of the motivations behind the study presented in this thesis.

Both approaches are attempts to approximate the complex turbulent behaviour of the atmosphere and in doing so simplify the process of loads calculation. When used together these methods have been found to adequately capture critical load cases. Current design criteria and methods are based on operational experience with current and past aircraft and so they remain relevant as long as the design is conventional. That is, the aircraft configuration is such that each lifting surface responds to changes in respective angles of attack along a particular axis. This section has only covered aspects of aircraft loads relevant to this research project and for brevity basic ideas have only been discussed briefly. The reader is referred to textbooks by Hoblit[153], Wright and Cooper[146] and Howe[145] for a thorough treatment of the subject.

6.2 Cranfield/Airbus AX-1 model

The AX-1 flexible aircraft model was developed at Cranfield University with the help of Airbus UK. It is a numerical simulation model in a MATLAB/Simulink® environment modularised to fit within the generic aeroelastic modelling framework shown in Figure 6.5. It has been developed such that key components necessary for flight loads generation can be modified or replaced without requiring significant modifications to the overall structure. Key features required from an aircraft model for the flight loads estimation are: (1) rigid body and structural degrees of freedom, (2) steady and unsteady aerodynamics, (3) representation of aircraft mass case and, (4) FCS and autopilots. The AX-1 provides the first three of these features.

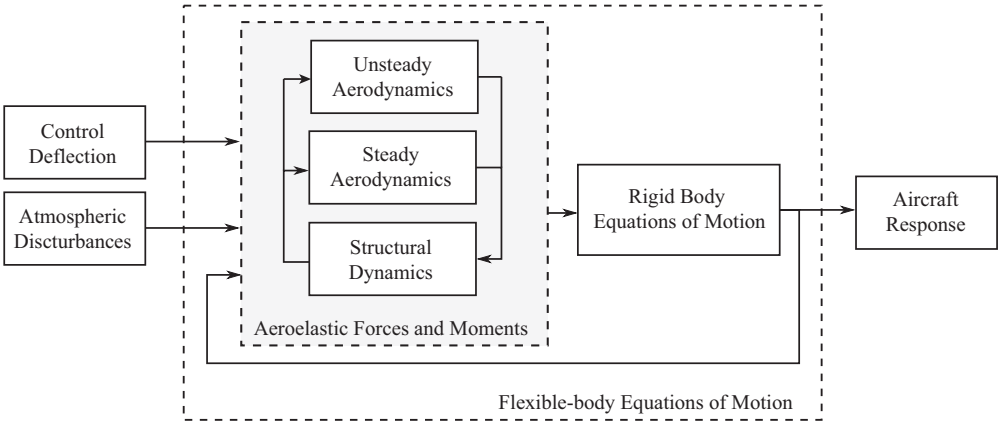

Figure 6.5: Generic aeroelastic modelling framework for flight loads (adapted and modified from Andrews[9]).

The model's geometry and performance specifications are presented in Figure 6.6. So far, the model has been used to study the effects of flexibility and LAF on handling qualities of large flexible aircraft[9][159], develop advanced simulation environments[119] and various pilot modelling studies[126][160].

6.2.1 Airframe model

The airframe has been modelled via the standard beam-element approach often adopted for reduced order flight loads modelling. The layout of the beam-element model (also referred to as 'stick' models) has been shown superimposed over the aircraft geometry in Figure 6.6. The airframe is represented by 39 beam elements each constrained by two nodes at the ends. The beam elements have individual stiffness, mass and inertia properties and their lengths are defined by the nodes. These nodes have six degrees of freedom whilst the beams are allowed to undergo deformations in bending, torsion and tension. Normalised stiffness data has been provided by Andrews[9, p.253]

Aircraft rigid body and elastic deformations are coupled using the concept of a mean-axis system[49][146, p.258]. This takes advantage of an origin that is free to move in space such that the angular and linear momenta relative to the body axis remains zero. The origin of the mean-axes system coincides with the instantaneous centre of mass and ensures that there is negligible coupling between the rigid body motion and the airframe's elastic deformation. Moreover, it is assumed that the changes in the airframe's inertia properties due to the elastic deformations are negligible. Li et al[161] have compared the use of such a mean-axes system with the approach using the fixed axis system and found this assumption to be acceptable.

Upon the definition of the airframe's configuration and mass case, eigen-analysis yields the natural frequencies and mode shapes of the airframe structure. The dynamic response of the structure is then estimated using the normal mode method where modal contributions are summed together to obtain the overall elastic deformation. Such an approach requires *a priori* knowledge of the mode shapes and frequencies, and more importantly, relies on the structural deformations being sufficiently small to ensure the validity of linear elastic theory. A detailed discussion of the limitations of such a linear structural model are highlighted by Waszak et al[162][163][49] and more recently by work done by Palacios et al[164][165]. The model was validated through the use of ground vibration test data provided by Airbus. Modal frequencies were found to be within 15% of those determined experimentally. A global damping ratio of 10% has been adopted for this study.

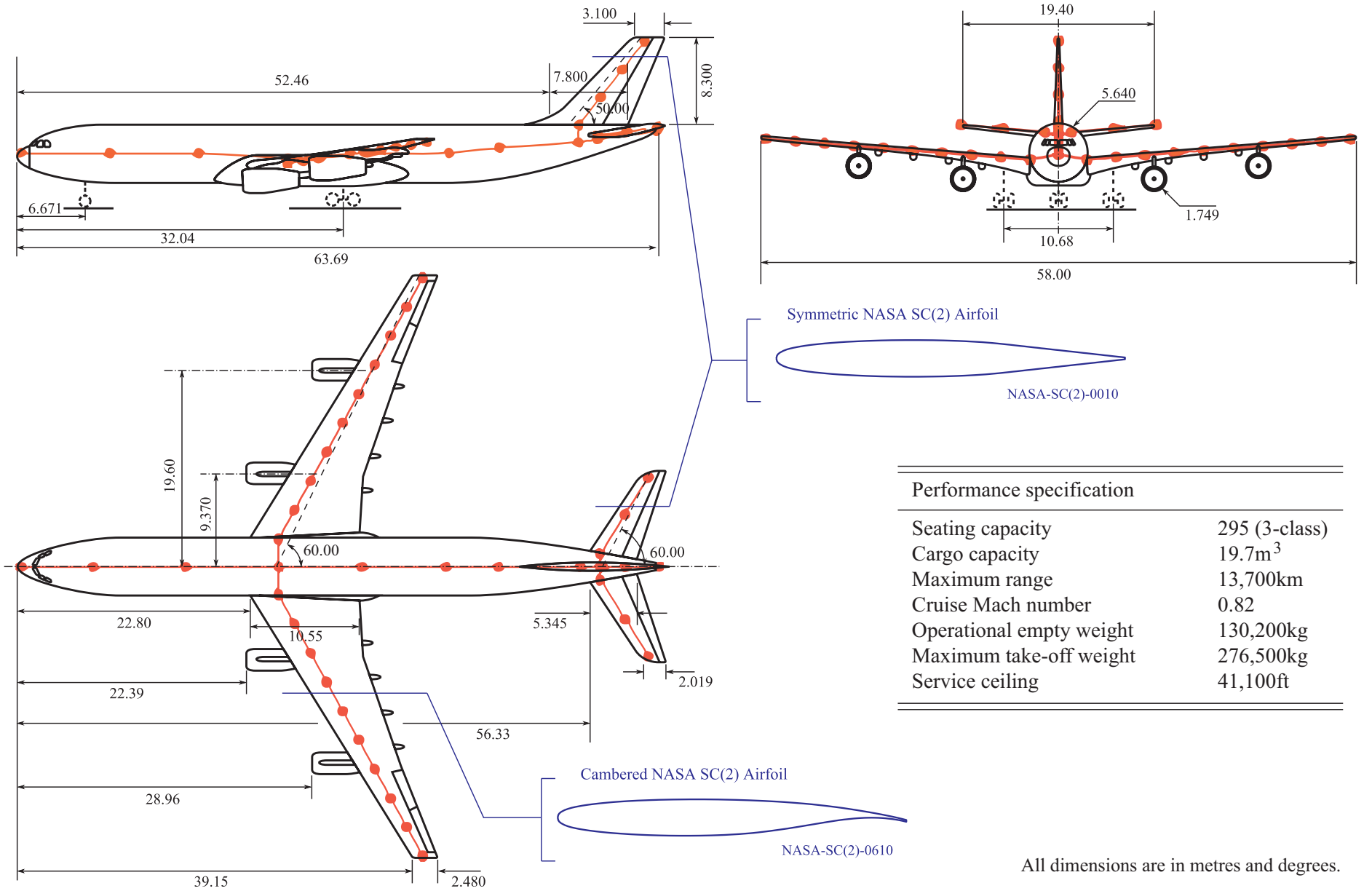

Performance specification	
Seating capacity	295 (3-class)
Cargo capacity	19.7m^3
Maximum range	13,700km
Cruise Mach number	0.82
Operational empty weight	130,200kg
Maximum take-off weight	276,500kg
Service ceiling	41,100ft

All dimensions are in metres and degrees.

Figure 6.6: Cranfield University Airbus AX-1 model: geometry, performance and beam-element representation.

The unsteady aerodynamic model combines a two-dimensional indicial model with modified three dimensional strip theory to calculate the aerodynamic forces and moments on lifting surfaces. This is based on Leishman's state-space approach that includes a Mach number term and so allows compressibility effects to be included via the Prandtl-Glauert correction.[166][9] Wagner and Kussner functions were not used due the incompressible flow assumption employed in their theoretical development. The effects of unsteady aerodynamics is then propagated by the indicial model as changes in local angle of attack for each strip. Furthermore, the effect of wing downwash on the tailplane is also modelled allowing accurate simulation of gust penetration effects as demonstrated by Andrews[9, p.60]. The relationship between steady wing aerodynamic coefficients and angle of attack are included within the model as look-up-tables containing values for zero angle of attack followed by lift-curve slope data, which is a function of Mach number and Reynolds number. The model's aerodynamic flight envelope lies between Mach 0.05 and 0.8 along with an angle of attack range of -10° to +15°.

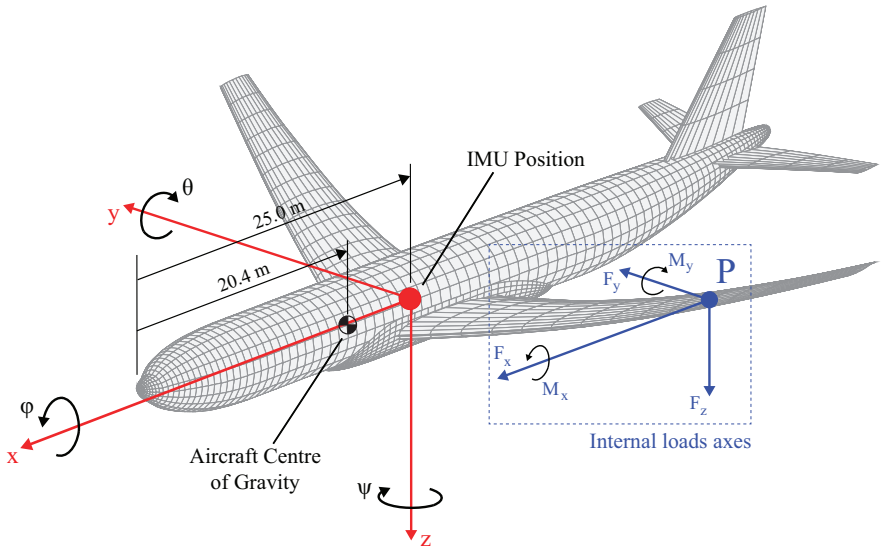

Figure 6.7: AX-1 body axes system together with internal loads axes.

Internal loads are calculated using the force summation method[146, p.369]. Compared to other methods such as the mode acceleration method[146], this is the most direct and intuitive process. Forces and moments are calculated directly from the displacements, velocities and accelerations together with mass and inertial properties at each station. These are then added to the externally applied forces to calculate the total dynamic loading. The sign convention used for the internal loads can be seen in Figure 6.7. The figure also shows the position of the aircraft centre of gravity and the position of the inertial measurement unit (IMU). The latter coincides with the aircraft body axes centre.

Together with the loss of fidelity due to the reduction of the entire airframe to a beam-element model,[3] the desire to achieve real-time simulation has led to other significant limitations. The key limitations are:

- Aerodynamics: the model's use of lift-curve slope data instead of actual lift and drag coefficients limits its validity to angles of attack where the linear relationship is valid; a maximum angle of attack of 15°.

[3]The beam-element approach reduces a finite-element model with hundreds of thousands of degrees of freedom to a model with a few hundred states. The AX-1 has a total of 906 states: 12 rigid body states, 24 for structural dynamics and 870 to capture unsteady aerodynamic effects.

- Control: lack of secondary control surfaces limits simulations to parts of the flight profile where the aircraft is in a clean configuration. Therefore, operations in the low speed corner of the flight envelope cannot be represented and the complete FCS architecture currently onboard modern aircraft can only be replicated to a limited fidelity.

- Atmospheric disturbance: the AX-1 model does not allow the definition of a two dimensional disturbance field capable of modelling spanwise variation. Turbulence or gust representations used in this study are therefore, one dimensional.

These limitations have a profound impact on the suitability of this model for simulation of flight incidents and failure cases. Incidents involving angles of attack greater than 15° cannot be simulated and failure cases during which secondary control surfaces such as spoilers are deployed cannot be studied thoroughly either.

6.2.2 Flight control system and load alleviation functions

Modern airliners are equipped with sophisticated fly-by-wire FCS that not only ensure satisfactory handling qualities but also play a crucial part in controlling airframe loads. A further suite of autopilots help in reducing the crew's workload. During the development of the AX-1, a parallel study was undertaken to develop the FCS architecture that could be easily adapted upon the completion of the airframe model. This study has been detailed by the author in Reference [167] where the development of a quasi-linear parameter varying model of a Boeing 747 is presented. This is followed by the description of the design process used to develop the inner-loop flight control laws and autopilots. A straight forward rate-command-attitude-hold controller was developed for lateral control whilst a C* control law was designed for longitudinal control. An autopilot suite allowing the primary automatic control features available to the pilot on the mode control panel, such as autothrottle and altitude hold, was also developed. The FCS and autopilot suites were coupled with the AX-1 model successfully through a process requiring relatively little gain tuning. The reader is directed to Lone et al[167] for further details. Appendix C presents the design process for structural mode filters and the final handling qualities assessment using the time-domain Gibson Dropback criterion.

Active loads control systems have become an essential part of the FCS onboard large aircraft. The aim of such a system is to minimise the internal loadings on the wings, especially at the wing root where considerable weight savings can be achieved together with improved fatigue performance. Moreover, since loadings such as shear force (and consequently bending moment) are almost entirely dependent on load factor, active loads control also contributes towards passenger comfort. The loads control system used in these studies consists of two nonlinear LAF: gust LAF (GLA) and manoeuvre LAF (MLA).

The GLA is activated when the aircraft undergoes a load factor greater than +0.1g without any sidestick deflections, that is, due to some form of atmospheric disturbance. In this case, the system deflects the ailerons to reduce outboard lift and thus minimise the impact at the wing root. The deflection is maintained for two seconds to compensate for unknown disturbances immediately upstream of the aircraft. This LAF is augmented by an active mode control (AMC) system that improves the damping of the first wing bending mode. It utilises accelerometers placed at 60% of the span to derive compensatory symmetric aileron deflections. Figure 6.8 presents the block diagram for the GLA and AMC systems and shows their placement within the FCS. It should be noted that lack of secondary control surfaces means LAF effects can significantly affect rigid body dynamics, especially in scenarios involving large control surface deflections. It should be noted that the addition of the AMC, GLA and MLA output to the

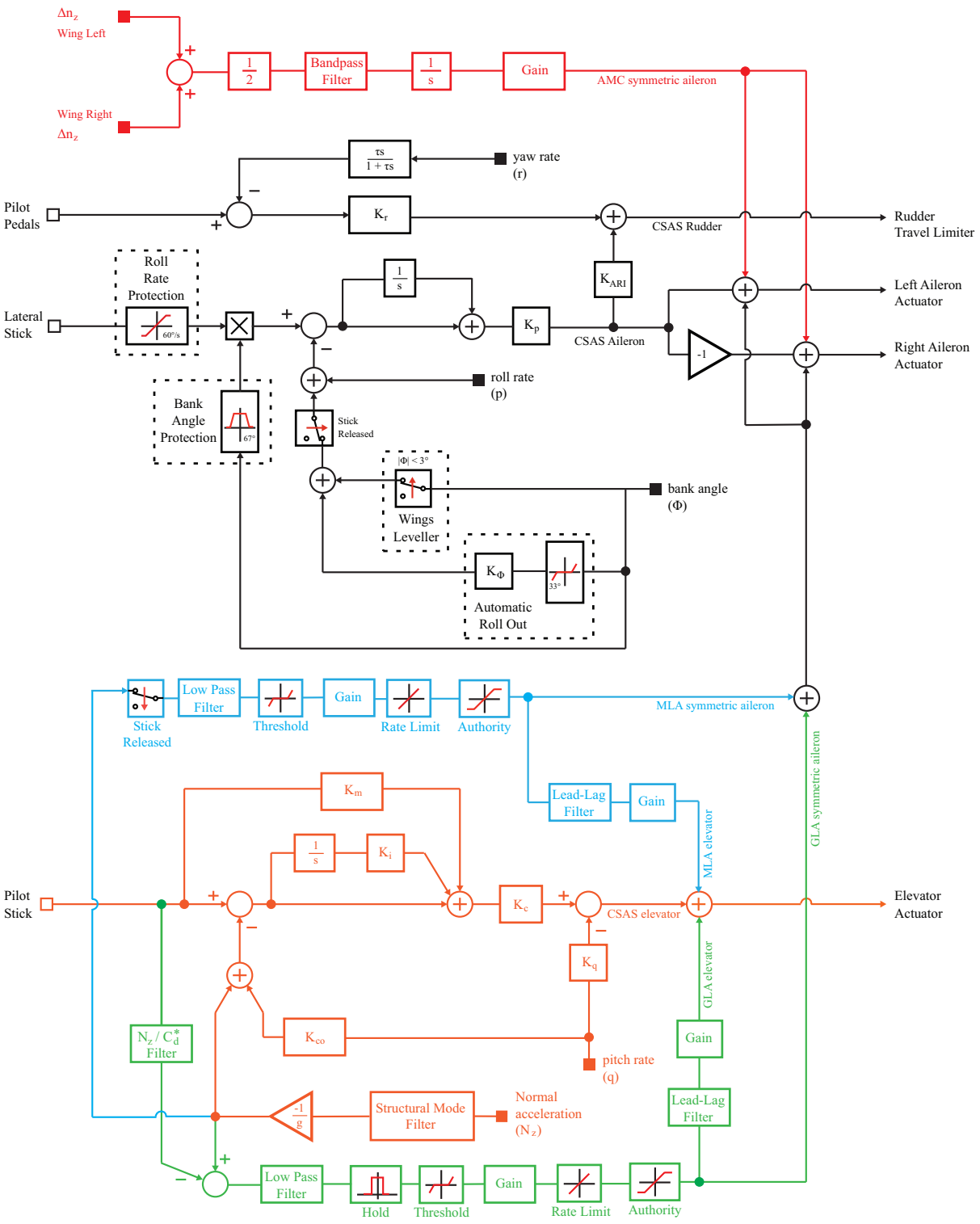

Figure 6.8: Command stability augmentation system and load alleviation function architecture.

CSAS commands is a simplifying assumption made to avoid modelling the complex control allocation system used onboard modern aircraft.

The impact of GLA on particular IQs in the time domain was briefly studied by Andrews[9, p.136]. Here, the system's frequency domain performance at flight conditions of Mach 0.58 and 25000ft with CT characteristics defined by σ_w of 6 m/s along each axis is presented in Figure 6.9 to demonstrate the positive effects. Attenuation of the responses at the airframe's modal

frequencies are clearly evident, albeit at the cost of amplified rigid body motion. Benefits with regards to fatigue are also clear.

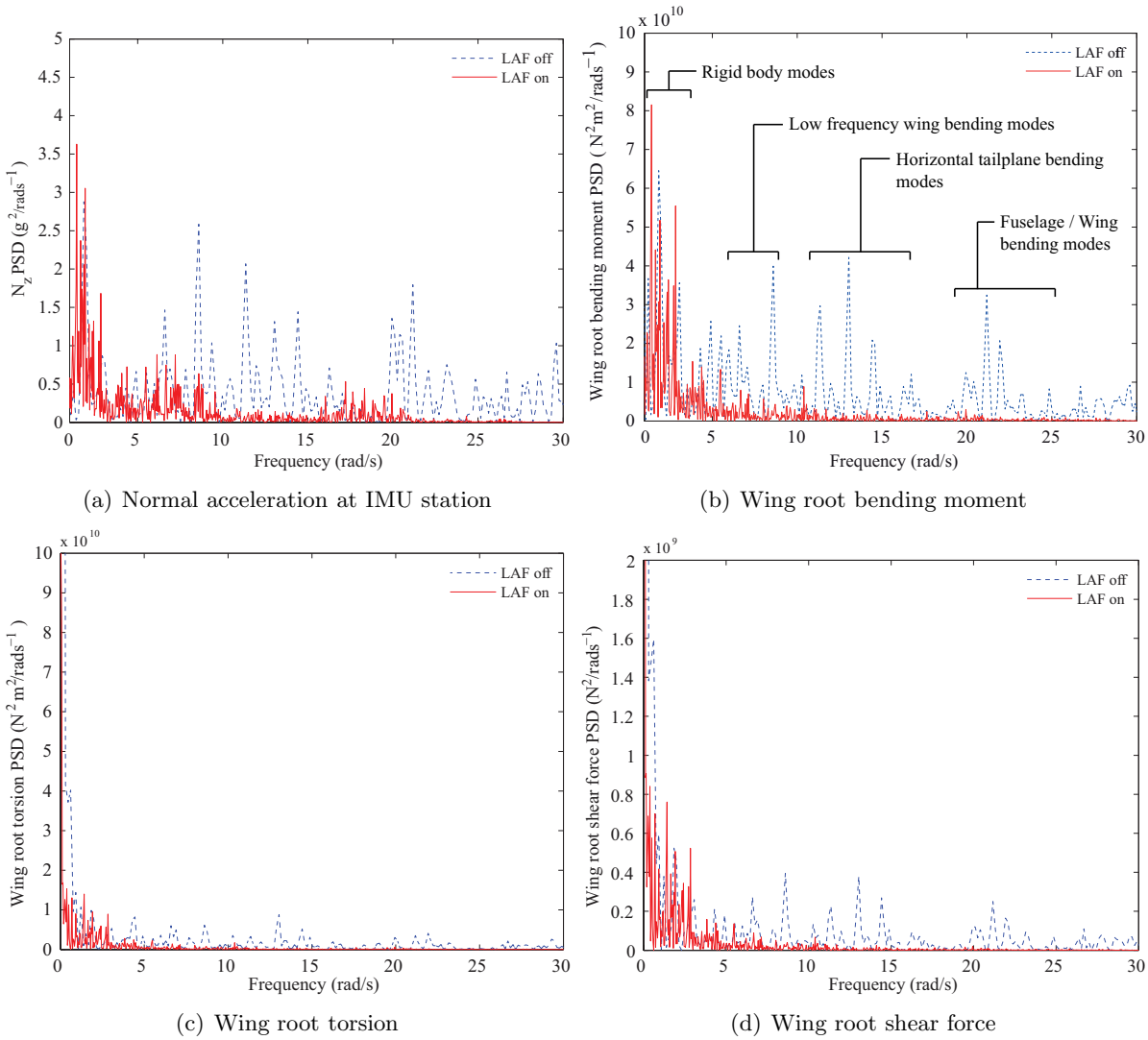

(a) Normal acceleration at IMU station

(b) Wing root bending moment

(c) Wing root torsion

(d) Wing root shear force

Figure 6.9: Frequency domain effects of LAF on key loads interesting quantities.

	Bending Moment	Shear Force	Torsion
Positive loading	5.67	26.83	63.55
Negative loading	28.50	5.56	7.69

Table 6.2: Percentage reduction in internal loads at the wing root due to LAF.

Computational tools developed for the derivation of loads envelopes were used here to highlight the impact of the GLA on limit loads envelopes during operations in CT. The design envelope analysis method discussed in Section 6.1.2 was used to obtain wing loads envelope with and without the GLA. Figure 6.10 shows the observed reductions in internal loadings. The affect on wing root bending moment (WRBM) was found to be relatively small, especially compared to results observed in industry. This is primarily because the AX-1 lacks spoilers that are typically used to dramatically offload the inboard wing sections.[4] However, as summarised in Table 6.2, significant reductions in internal loads can still be achieved without spoilers.

[4]Conventional aircraft have spanwise loading that tend to be elliptic distributions with maximum loading occurring over the inboard wing sections. Therefore, the deflection of spoilers in these areas results in a large

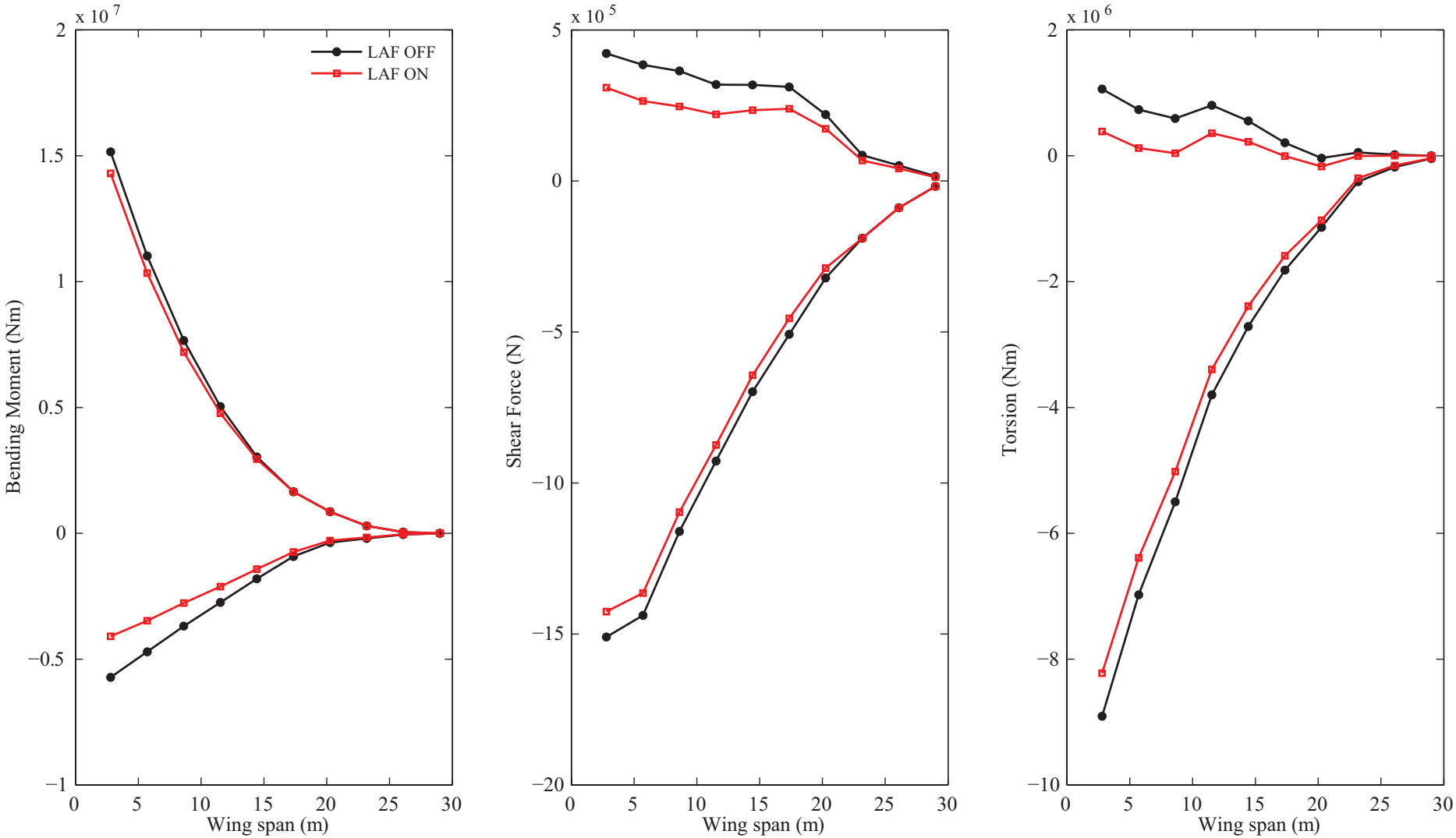

Figure 6.10: Impact of GLA system on wing internal loads envelope.

The MLA system on the other hand, is very similar to the GLA except that it is activated when the pilot demands a load factor greater than 0.1g. It also relies on symmetric aileron deflection. Its structure can be found in Figure 6.8. The GLA and MLA systems also provide elevator commands to compensate for the loss in pitching moment during operation. The reader is directed to work done by Andrews[9] for a detailed discussion on the AX-1's LAF systems.

Response of the pilot-vehicle-system under atmospheric disturbances is the focus of this study. As a result, although the MLA system was developed, it is not engaged in any simulations. The analysis of a system that contains high order models of the aircraft and the pilot, coupled with a nonlinear FCS is quite challenging on itself. Exclusion of this nonlinear MLA system helps reduce complexity and simplifies the interpretation of simulation results. Furthermore, for simplicity no FCS gain scheduling has been adopted.

6.3 Loads envelope generation

The process adopted for the derivation of loads envelopes relies on nonlinear time domain simulations at various points on the flight envelope. These points are shown in Figure 6.11 together with critical airspeed boundaries directly taken from the Airbus A340-300 flight crew operational manual[168]. These were selected to cover as much of the flight envelope as possible whilst remaining within the valid flight regime of the AX-1 model.[5]

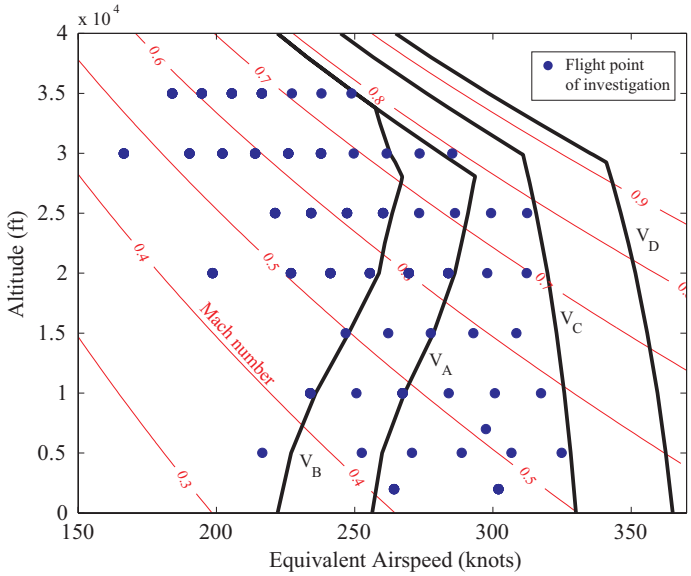

Figure 6.11: Adopted airspeed boundaries and flight points of investigation.

Only one mass case with the aircraft weighing 75.6% of the maximum take-off weight and centre of gravity as shown in Figure 6.7 was considered. A detailed breakdown of this mass case can be found in Appendix D. Overall, the loads envelope generation process is very similar to that used in industry: involving simulation of manoeuvres and CT followed by a sorting process to obtain the highest loadings on the wings and empennage.

loss of lift and thus, equal reduction in shear force. With regards to wing root bending moment WRBM, lack of a lengthy moment arm is simply balanced by the large magnitude of lift lost due to such spoiler deflection. The AX-1's lack of spoilers means that this feature cannot be exploited.

[5]The main assumption to note is that compressibility effects in the high speed regime are assumed to be sufficiently reduced by the wing and empennage sweep angles and also adequately represented by the Prandtl-Glauert correction.

The scope of this process has been limited to unchecked manoeuvres, CT analysis and mission analysis approach. The manoeuvre and CT envelopes together yield conservative and non-conservative envelopes respectively; which are then suitable for later comparison with incident simulations covered in Chapter 7. Mission analysis on the other hand, provides a probabilistic envelope. The study of load combinations was deemed to be beyond the scope of this research.

6.3.1 Manoeuver envelope generation

The manoeuver loads envelope for the wing and empennage were obtained via the simulation of the following traditional book-case unchecked maneuvers:

- Positive pitching manoeuver as specified in CS-25.331(c)(1). This involves the stick being deflected fully aft until the load factor reaches either a maximum or 2.5g at the centre of gravity. Similarly, the unchecked negative pitching manoeuver requires the achievement of either a minimum or -1.0g load factor. The stick is released immediately after the relevant load factors are achieved and loadings beyond this point are not considered. Example time histories are shown in Figure 6.12.
- Rolling manoeuvre as specified in CS25.349(a) where the aircraft is banked until the maximum allowable roll rate is achieved, which in this case is limited to 15°/s by the FCS. The aircraft is then recovered to zero bank angle. The lateral acceleration and roll rate time histories from an example case is shown in Figure 6.13(a).
- Yaw manoeuver as specified in CS25.351 where the rudder is deflected to its maximum at the fastest rate of deployment to cause an overswing in sideslip after which the rudder is returned to zero deflection.[6] Example time history can be seen in Figure 6.13(b).

In all cases the aircraft starts in a trimmed level flight condition before the manoeuver is executed. These were performed at all 53 flight points shown in Figure 6.11 to provide a conservative internal loads envelope. The envelopes can be compared in Figures 6.14 to 6.16.

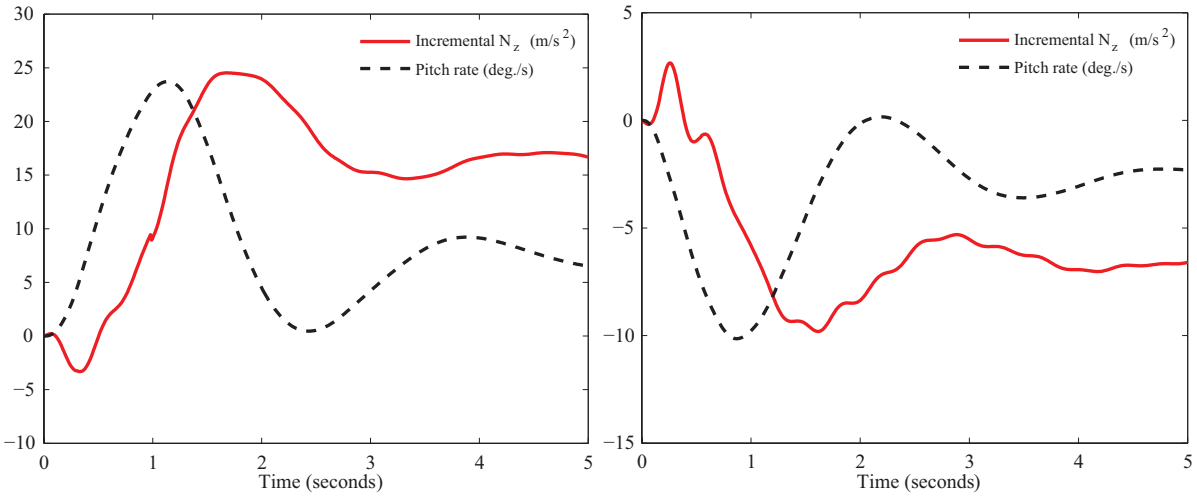

(a) 2.5g Pitch up

(b) -1g Pitch down

Figure 6.12: Example unchecked symmetric pitching manoeuvres (Mach 0.50, 15000ft)

[6]The AX-1 rudder actuator has been modelled such that the maximum rudder deflection and deployment rate are airspeed dependent.

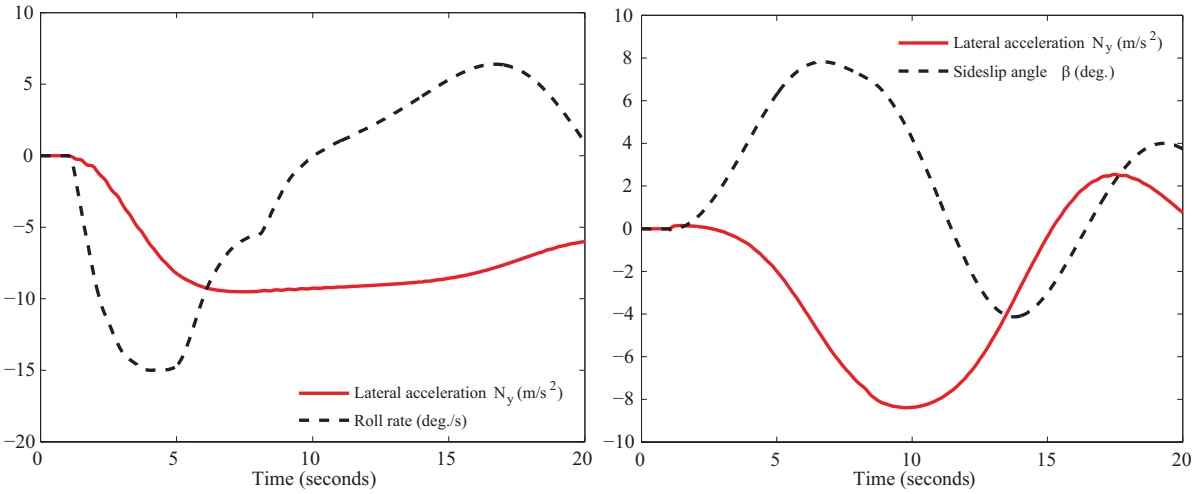

(a) Maximum roll rate

(b) Sideslip overswing

Figure 6.13: Example roll and yaw manoeuvres (Mach 0.58, 10000ft)

The results highlight the necessity for such a multi-facetted approach towards the determination of dynamic loads envelopes. Each manoeuvre can be seen to define the limit load at a particular part of the wing or empennage. The pitching manoeuvres together define the limit WRBM. The positive 2.5g load factor is critical to determine wing and horizontal tailplane (HTP) loading envelopes, whilst the maximum roll rate manoeuver effectively determines the vertical tailplane's (VTP) bending moment and shear force limit loads. The yaw manoeuver did not define any limit loads for the VTP, primarily because engine-out scenarios were not considered together with other failure cases, such as hard actuator failures or control surface free-play. The analysis of such failures via pilot-model-in-the-loop simulations are presented in Chapter 7.

6.3.2 Turbulence envelope generation

The approach used here was described in Section 6.1.2 and adheres to the methodology given in CS25.341(b). Given the nonlinear FCS components and the significant influence of unsteady aerodynamics as highlighted by Andrews[9], time history analysis is the only adequate approach that can be adopted. The turbulence profiles used are characterised by rms velocities of around 6m/s; corresponding to severe turbulence or stormy weather conditions. Figure 6.17 presents sample time histories of the atmospheric disturbances together with corresponding PSDs. These were generated using the von Kármán turbulence model given in Table 6.1 with the turbulence scale set to 2500ft. Limit loads for the wing and empennage were then obtained through the use of Equation 6.1.5 followed by a data sorting process.

The simulations were conducted with the aircraft initially in trimmed level flight with the auto-throttle and height hold autopilots engaged. Each simulation was of 5 minutes duration as suggested by Hoblit[153] to ensure sufficient data was generated to obtain statistically significant rms values together with an adequate quantity of peak count data. The aircraft model was subjected to translational turbulence in all three axes simultaneously; similar to the approach dubbed "three-dimensional gust analysis" at Lockheed-Martin[153]. An example time history with key flight dynamic parameters is been presented in Figure D.2. It can be seen that the autopilots maintain altitude and Mach number relatively accurately. The GLA system's response via the ailerons and elevators is also shown. A total of 53 five minute simulations were conducted resulting in 4 hours and 25 minutes of data recorded at a sampling frequency of 100 Hz.

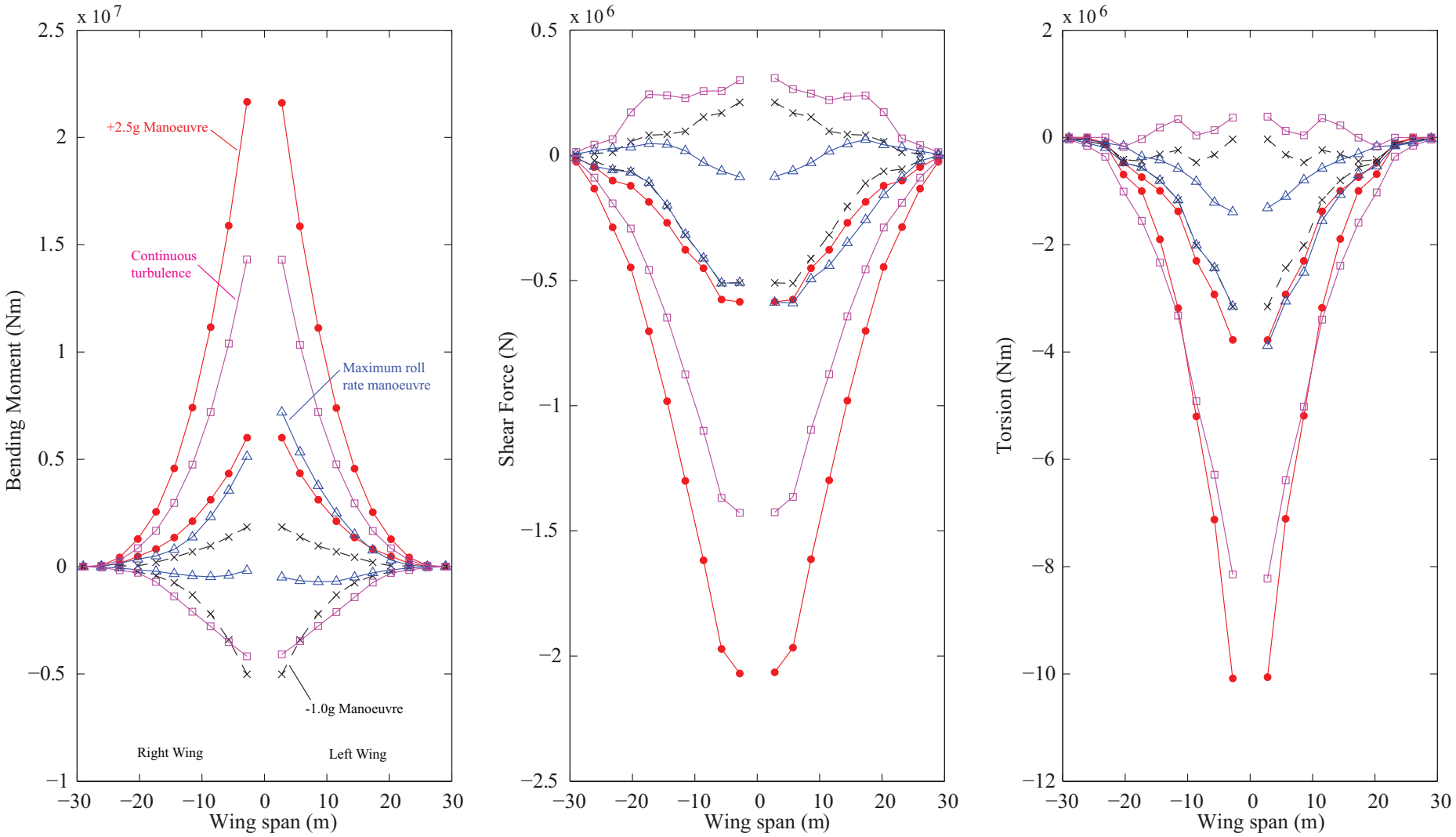

Figure 6.14: Wing internal loads envelope.

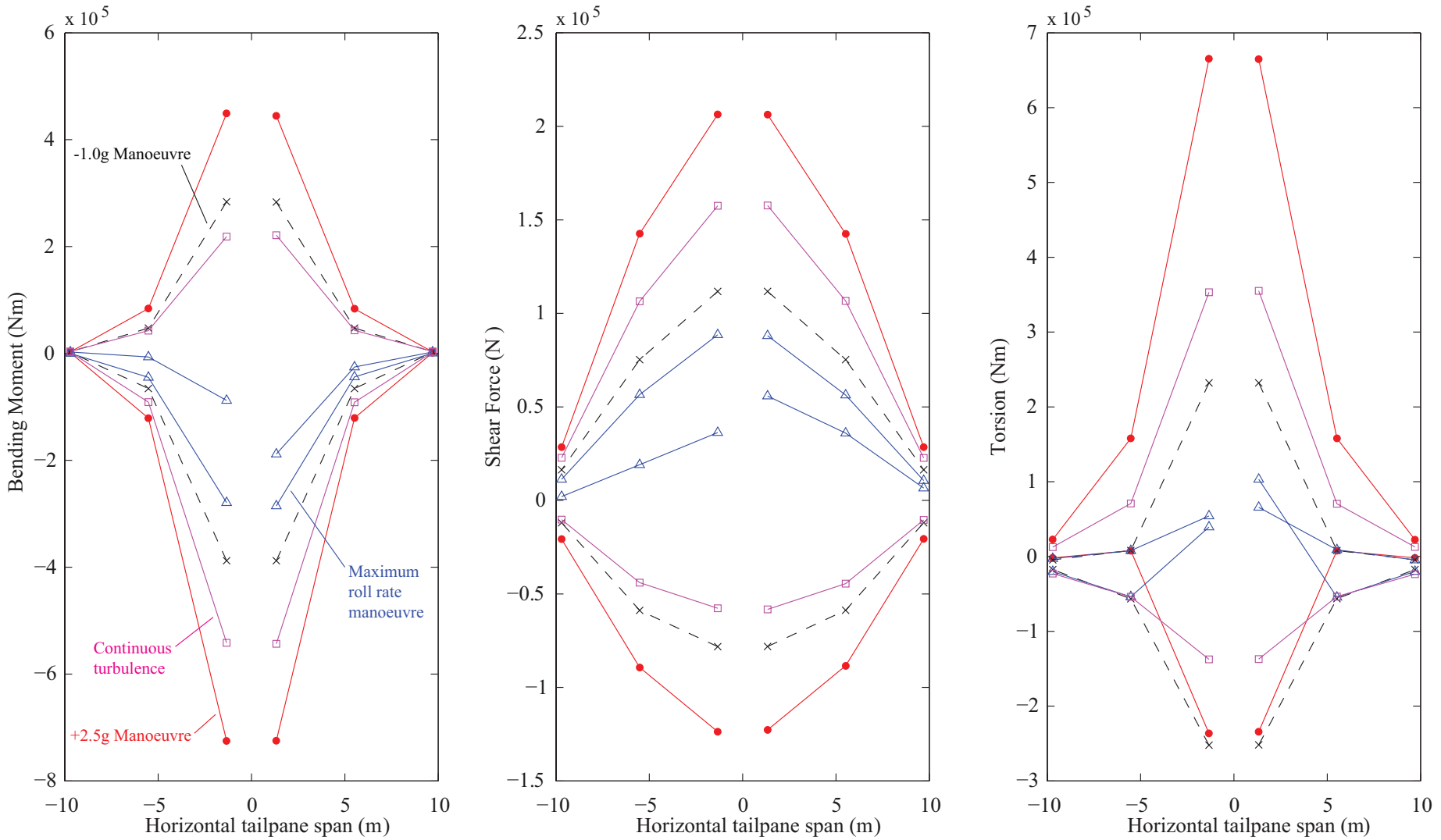

Figure 6.15: Horizontal tailplane internal loads envelope.

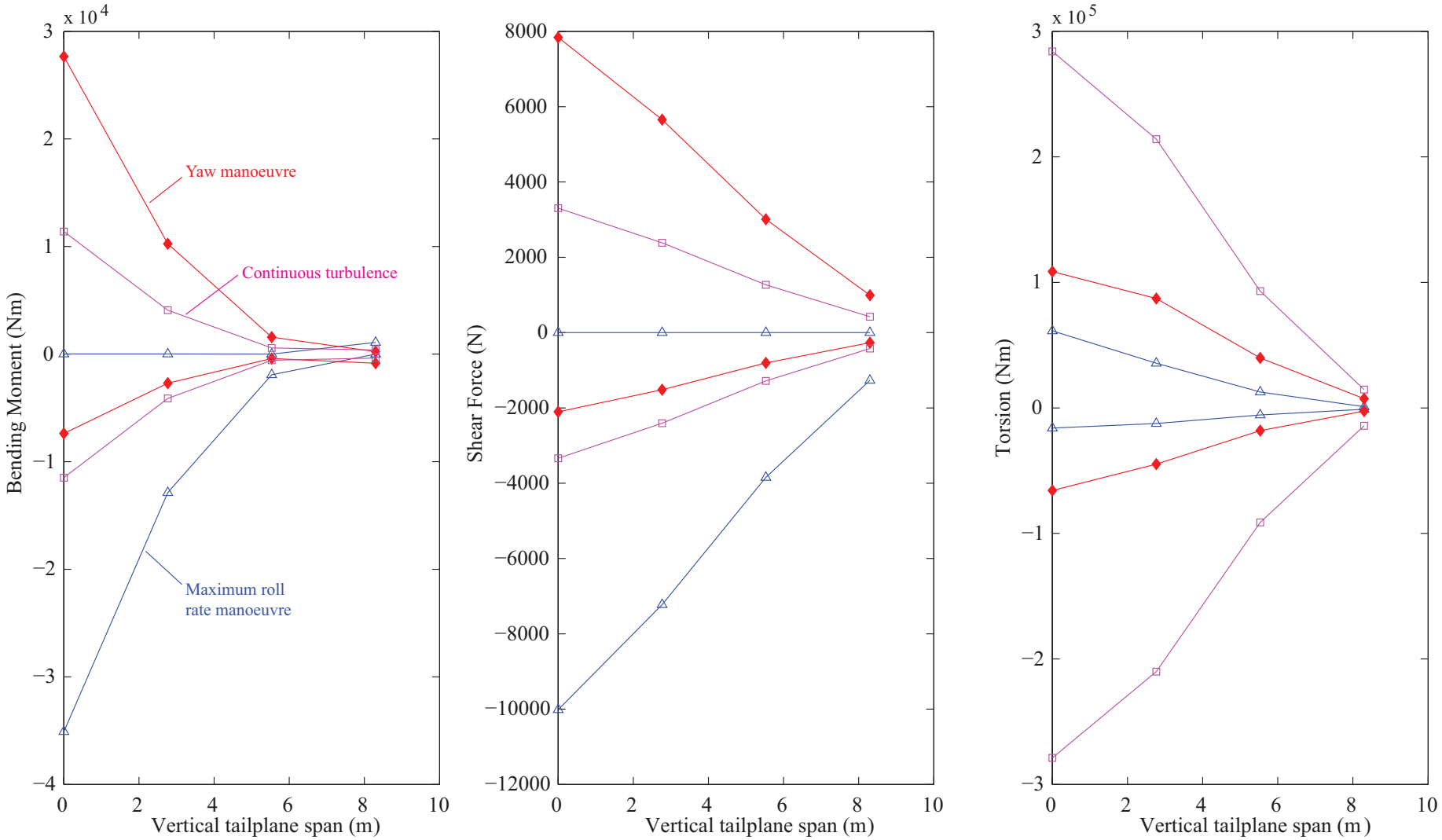

Figure 6.16: Vertical tailplane internal loads envelope.

Limit load envelopes for the wings and empennage are also presented in Figures 6.14 to 6.16. The CT envelope effectively determines the wing's mid-span bending moment and torsion envelopes whilst defining the positive shear and torsion envelopes over the entire span. In case of the VTP, it also defines the critical torsion envelope. It does not significantly impact the HTP loads envelope.

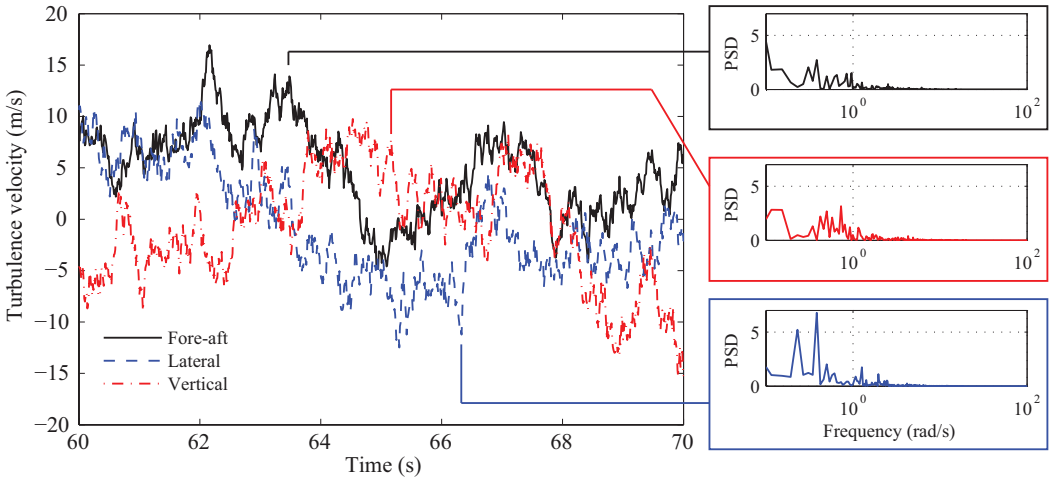

Figure 6.17: Example of continuous turbulence profile and corresponding power spectra.

The peak counting method summarised in Section 6.1.2 was adopted here to analyse load factor data from a probabilistic perspective. The pdfs shown in Figures 6.18 and 6.19 have been derived from this data and each function is defined as follows:

$$p(N_z) = \frac{C_{z_i}}{\sum_{i=1}^{N} C_{z_i}} \tag{6.3.1}$$

where C_{zi} refers to the number of peaks observed over a time interval. In this case, the pdfs represent observations from simulations conducted at all flight points and therefore, represent the probability of an acceleration peak occurring in 4 hours and 25 minutes of flight in severe turbulence.

However, this does not give information regarding either the magnitude of the highest peak or the number of times it will occur in a given period of time. To obtain such information, the peak count data can be used to derive cumulative number of occurrence curves. This involves a cumulative summation of peak counts from the highest to zero incremental acceleration along with the most negative acceleration back to zero. In effect these curves are discontinuous functions theoretically symmetric about zero incremental acceleration due to the Gaussian nature of the turbulence source. Figures 6.20 and 6.21 show these cumulative occurrence curves for accelerations observed at the IMU and pilot stations respectively. These have been normalised using the total number of positive and negative peaks observed. Therefore, the proportion of peaks expected to be above a particular acceleration can now be estimated. For example, it can be deduced from Figure 6.20 that in severe turbulence the proportion of peaks greater than 1g reduces from 5.04% to 0.8% due to the implementation of the GLA system.

Impact of the moment arm between the aircraft centre of gravity and pilot station together with the effects of fuselage structural flexibility are very clear in the overall difference between Figures 6.18 and 6.19 (and also in Figures 6.20 and 6.21). The distributions are dramatically widened and the proportion of peaks greater than 1g has risen to 25.76%. The significance of these effects are emphasised again in the time domain gust encounter simulations discussed in Chapter 7.

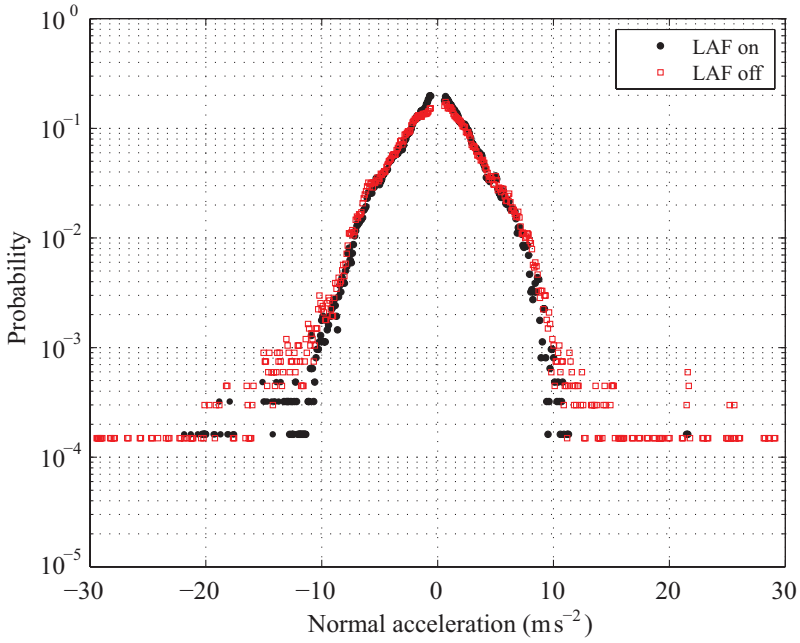

Figure 6.18: Probability density function for normal acceleration at IMU station.

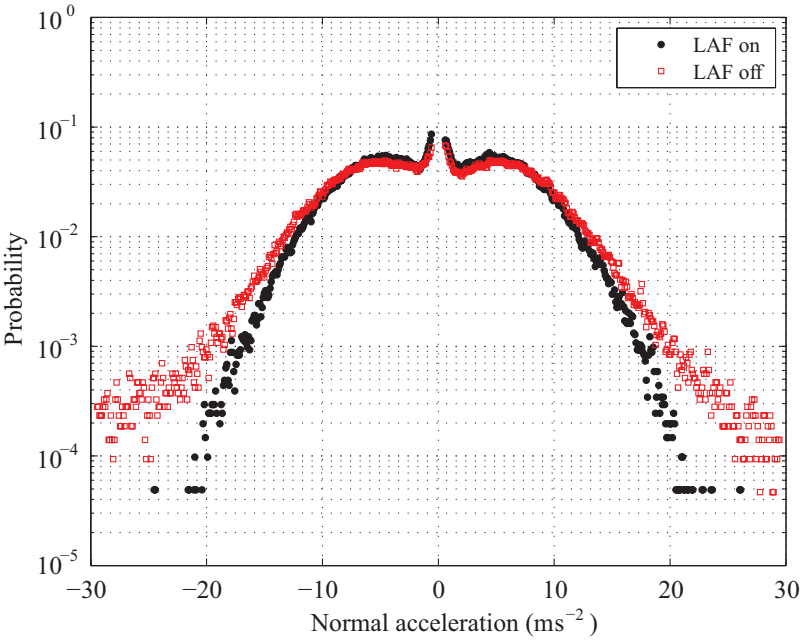

Figure 6.19: Probability density function for normal acceleration at pilot station.

Such figures allow comments to be made with regards to the likelihood of acceleration peaks experienced during an incident. It should be kept in mind that these curves represent occurrences in severe turbulence that are typically avoided and so the overall probabilities and occurrences presented here are not representative of complete aircraft operations.

6.4 Conclusions

This chapter is a considerable step away from the manual control aspects discussed previously. Therefore, it begins by presenting a brief synopsis of flight loads analysis techniques and certifi-

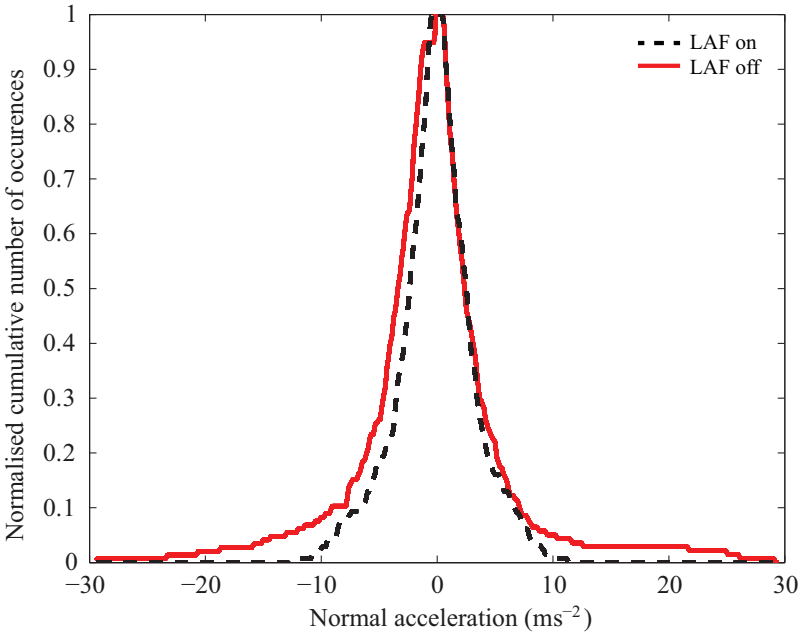

Figure 6.20: Normalised frequency of occurrence curve: IMU station.

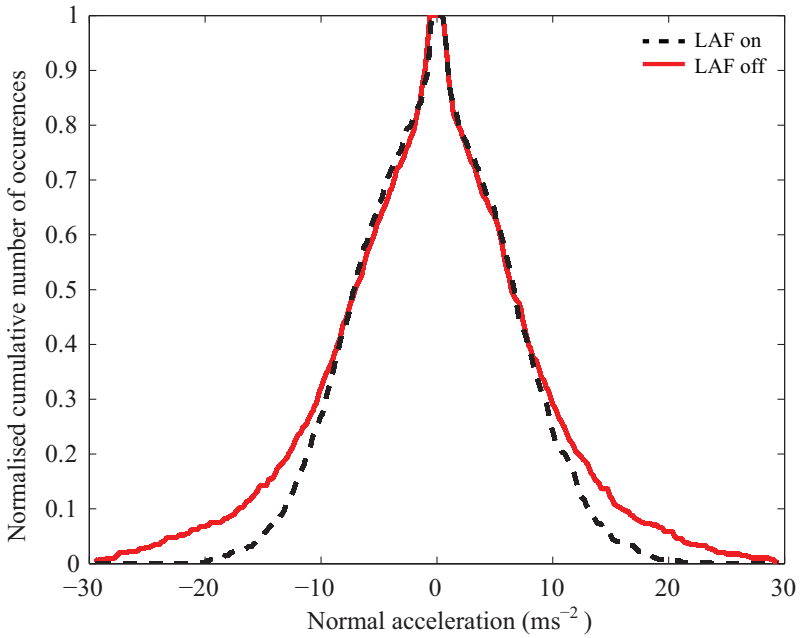

Figure 6.21: Normalised frequency of occurrence curve: Pilot station.

cation requirements. The different forms of atmospheric disturbance that separate deterministic and stochastic approaches were discussed. Three of the main methods for the generation of loads envelopes due to gust and turbulence were also reviewed; namely the tuned discrete gust, design envelope analysis and mission analysis. This is followed by a description of the Cranfield/Airbus AX-1 loads model and its FCS. This aeroelastic model together with the FCS and LAF provides the user with all the necessary features required for flight loads generation, such as the unsteady aerodynamics capable of capturing the effects of wing downwash on the horizontal tailplane. However, its application is limited to the linear region of the lift-curve slope and a lack of secondary control surfaces limits its application further to parts of the flight envelope where the aircraft is in a clean configuration. Moreover, the necessary superposition of GLA

demands on control surface deflections required for controlling rigid body dynamics also results in a loss of simulation fidelity.

The necessity to include the nonlinear FCS components such as GLA functions and actuator rate limits and saturations, meant that the internal loads envelope for the wings and empennage were obtained through time domain simulations at flight conditions within which the AX-1's aerodynamic model was valid. Manoeuvre loads envelope was obtained through a series of unchecked symmetric and asymmetric book-case manoeuvres specified in CS-25. The von Kármán turbulence model was used to derive the CT profiles needed to generate limit loads envelopes via design envelope analysis. Together with the manoeuvre envelope, this provides a scale for assessing the severity of loadings during turbulence/gust encounters or failure scenarios. Time domain simulations also allowed peak counting data to be collected and analysed to give an indication of the likelihood of certain acceleration peaks occurring during severe turbulence.

The discussion in this chapter aimed to inform the reader of two aspects needed for a critical interpretation of the results that will be presented in the following chapter. Firstly, it has discussed the capabilities and limitations of the flight loads model so that the scope of gust/turbulence encounter and failure case simulations can be defined and comments can be made with respect to their accuracy. Secondly, loads envelopes are provided to assess the severity of correlated loads obtained from these simulations. Description of envelope generation methods used here also allow engineers in industry to assess the implications of results in this thesis in the light of industry practice.

This page is intentionally left blank.

CHAPTER 7

Pilot-model-in-the-loop simulations

The inability to distinguish between rigid body dynamics and aeroelastic effects is an inherent limitation of the human sensory dynamics. As the modal frequencies of the aircraft structure encroach into the frequency ranges of the human senses, biodynamics and control, traditional assumptions in FCS design and handling qualities analysis no longer remain valid. Pilot's perception of aircraft states is corrupted just like the onboard IMU sensors. The angular rotations and linear accelerations perceived from the pilot's station are a function of rigid body as well as the structural dynamics. As shown in Figure 7.1, for longitudinal dynamics pitch attitude and normal acceleration at the pilot's station now include terms associated with fuselage flexibility:

$$\theta_p = \theta + \theta' \tag{7.0.1}$$

$$N_{zp} = (\dot{w} - L_1\dot{q})\cos\theta' + \dot{w}_p \tag{7.0.2}$$

Here, $\dot{w}_p$ represents accelerations due to fuselage bending obtained from the forward most node of the beam-element representation of the fuselage. Angular deflection at the pilot's station relative to the rigid body pitch attitude is given by θ'. As a result, pilot introduced gain and equalisation within the PVS may no longer be appropriate. Moreover, the rigid body dynamics are also affected by the flexibility of the empennage and wings upon which the primary control surfaces are placed. For example, given the span of an Airbus A380 HTP is approximately that of an A320 wing, the changes in spanwise effective angle-of-attack due to structural deformation and the consequent impact on the elevator's control effectiveness are very significantly.

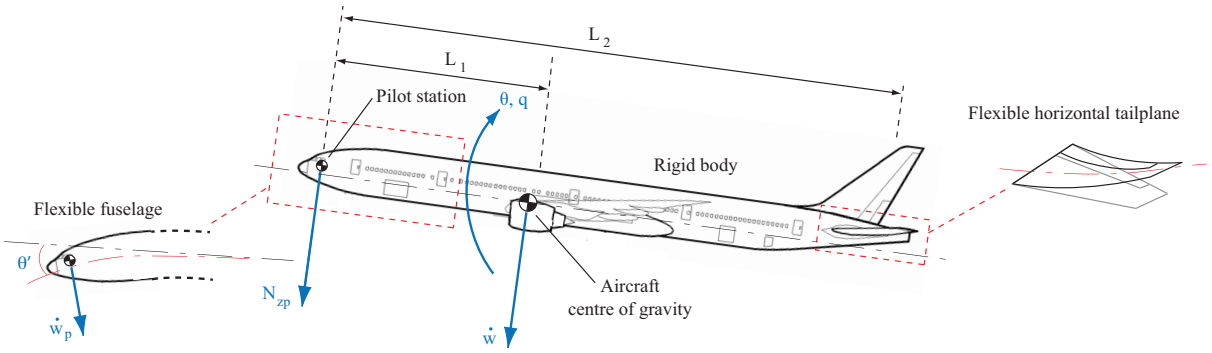

Figure 7.1: Aircraft longitudinal dynamics and effects of airframe flexibility.

This chapter brings together the work described so far and presents results from two case studies demonstrating the pilot-model-in-the-loop simulation environment developed as part of this study. The first case is an aileron failure simulation studying the effects of manual control and biodynamic feedthrough on airframe internal loads, whilst the second case is an attempt to reconstruct a gust encounter incident where manual control was found to be the cause of excessive loading. Preface to these studies is a brief discussion on the challenges in minimising flight incidents based on findings from when the author was granted limited access to the flight incidents database at Airbus UK.

7.1 Flight incidents

The recent series of accidents attributed to loss-of-control has meant that regardless of the aspect of pilot modelling one focuses on, it is very difficult to avoid the debate involving pilot training, cockpit automation and fly-by-wire flight control. The reader is not only referred to the large quantity of academic material but also to the regular supply of press articles that have appeared since the loss of Air France AF447. These have strongly influenced public opinion and thereby accelerated the aviation communities efforts to improve flight safety.

Mainly motivated to avoid fatal accidents like that of the American Airlines F587 that occurred in 2001, airframe manufacturers and airlines now have processes in place for a rapid assessment of airframe loads after a reported incident. These involve assessments at multiple levels ranging from interviewing the crew, inspecting peak accelerations to full nonlinear simulations attempting to recreate the exact scenario. The only source of raw information are the crew's description and the DFDR data that only records particular flight parameters at a mere 8 Hz. Here, the scope of the discussion is limited to cases of in-flight incidents that consist of severe turbulence or gust encounters and exceedences in airspeed. As already recognised by the aviation community, the problem of minimising flight incidents cannot be resolved through pilot training alone.

Figure 7.2 shows the initial flight conditions and relative weight of the aircraft immediately prior to an incident. The author was given access to a total of 47 incidents that have occurred since 2008. It must be emphasised that this is a subset that is primarily concerned with longitudinal dynamics and loads, and does not include ground incidents or fatal accidents.

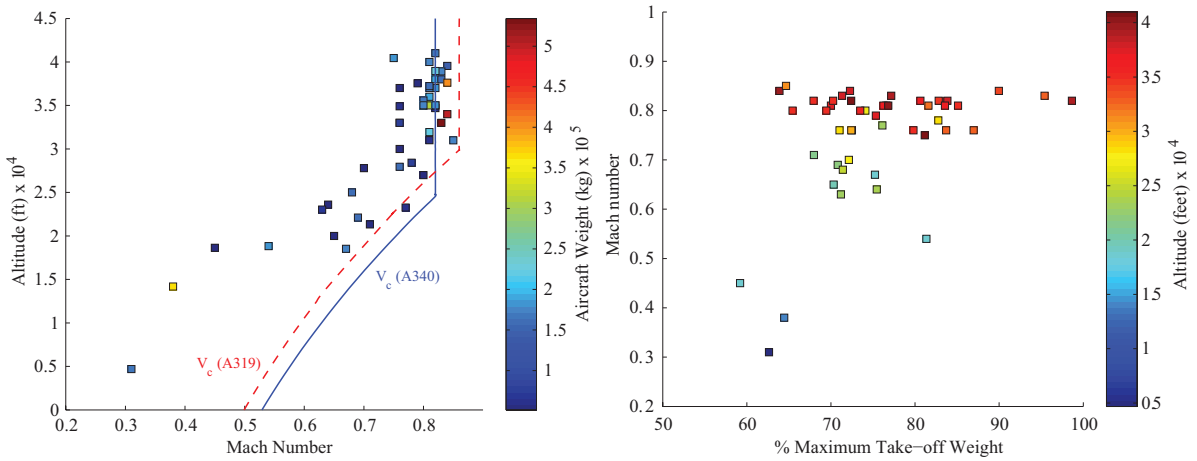

Figure 7.2: Flight conditions and aircraft weight immediately before incident.

It is evident from Figure 7.2(a) that majority of the incidents involve short-haul aircraft and this can be attributed to three factors. Firstly, there are far more short-haul aircraft in service than long-haul aircraft. Secondly, these fly the complete mission profiles far more frequently than long-haul types and are therefore, more exposed to turbulence at different altitudes due to the frequency of climbs and descents. Finally, long-haul crews tend to be far more experienced and are more familiar with aircraft dynamics (both under automatic and manual control) in response to gusts or turbulence patches.

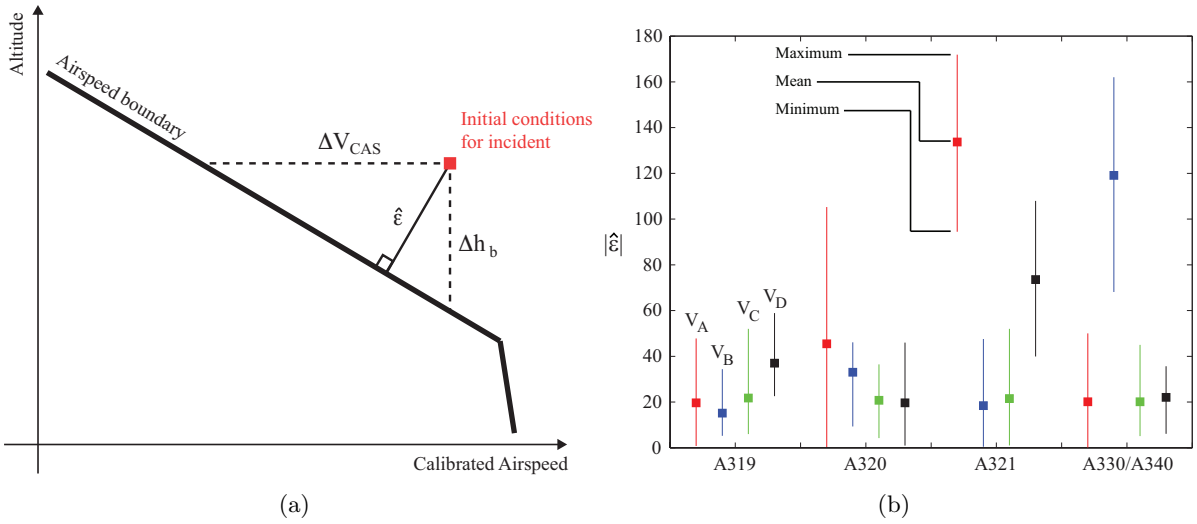

Figure 7.3: Graphical technique used to calculate proximity to an airspeed boundary and relative proximities for sample incidents.

The proximity of each incident to the aircraft's airspeed boundaries was calculated as shown in Figure 7.3(a) where:

$$\hat{\varepsilon} = \Delta V_{\text{CAS}} \sin\left(\tan^{-1}\left(\frac{\Delta h_b}{\Delta V_{\text{CAS}}}\right)\right) \tag{7.1.1}$$

Figure 7.3(b) shows $\hat{\varepsilon}$ calculated for all the incidents and categorised according to the airspeed boundaries and aircraft type. The figure confirms that most incidents occurred relatively close to the V_C boundary. However, the feature that stands out is the relative distance of the A330/A340 incidents from the V_B boundary.

Majority of the events occur near the V_C boundary above 30000ft. This susceptibility becomes evident if the aircraft's buffet onset envelope is studied with gust penetration margin in mind. Figure 7.4 shows three cases that highlight the role of altitude in determining the allowed load factor margin in cruise conditions. Case 1 shows that although the aircraft may be heavy with a forward centre of gravity, the permissible positive load factor at 31000ft is reduced from 2.5g to approximately 1.8g. As shown by Case 2, this is not significantly affected if the centre of gravity is moved aft and the altitude is increased by 4000ft. However, close to the altitude ceiling of 41000ft, even though the aircraft may be lighter the permissible load factor reduces by almost 0.5g.

Therefore, the incidents shown in Figure 7.2 indicate that cruise points are selected without sufficient concern for buffet margins. An encounter with high altitude turbulence in such flight conditions is bound to cause an airspeed fluctuation that can either result in the onset of low speed or high speed buffet. In the latter case, an overspeed alarm would be triggered and the pilot's corrective action (a pitch up command) can easily trigger a stall warning as the aircraft hits the low speed buffet boundary. Such a scenario along with the multitude of auditory and visual cues only increases the pilot's workload and creates levels of urgency the crew would have rarely, if ever, experienced before.

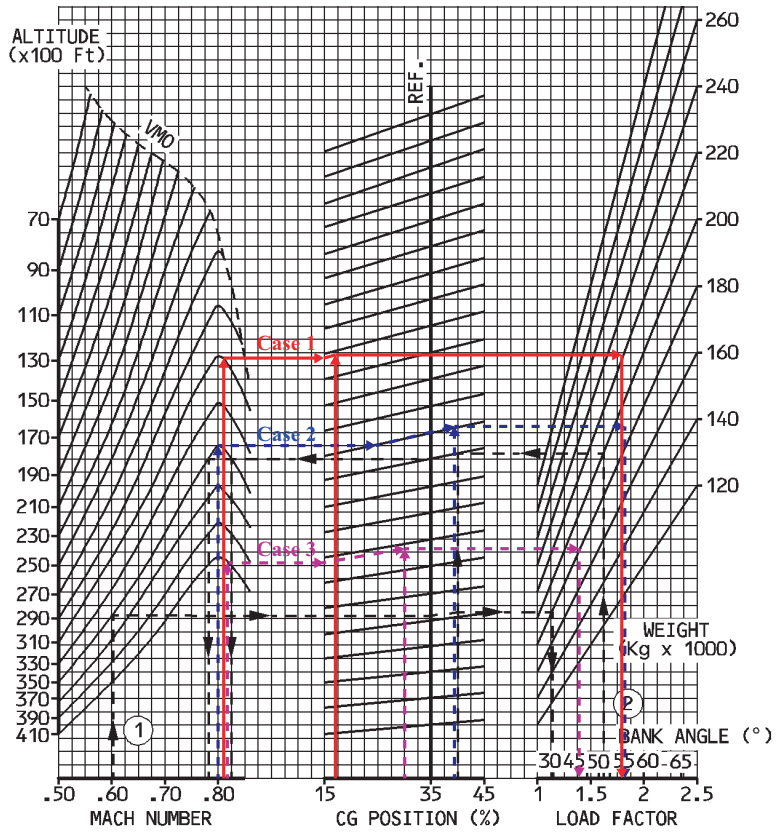

Figure 7.4: Airbus A340 buffet onset chart from the Airbus flight crew operating manual.

The need for experience and simulator training is further emphasised if failure scenarios are considered, especially where its detection by the onboard computer results in FCS mode switching. Airbus aircraft are known to revert from 'normal law' where the advanced flight envelope protection systems are active to modes with decreasing levels of sophistication, namely the 'alternate law' and 'direct law'. In alternate law the FCS may not provide flight envelope protection features but retains inner loop feedback control through a simplified CSAS, whilst in direct law the pilot is presented with the handling qualities of the bare airframe and he/she directly commands control surface deflections. In both cases the autopilots automatically disengage requiring the pilot to close the control loop and potentially exacerbate the situation. Therefore, although fly-by-wire has allowed designers to improve handling qualities, it does require the pilot to be familiar with aircraft dynamics corresponding to each FCS mode. Hence, simulator training of the initial stages of certain failure scenarios (where negative training is unlikely) where the pilots are exposed to the different FCS modes and switching dynamics is necessary to avoid APC and other undesirable effects of manual control.

Lack of sufficient pilot training, especially in the area of upset recovery was repeatedly emphasised in the author's meetings with flight instructors. Current and projected growth in air travel has led to an equal rise in the number of aircraft in service (mainly short-haul) that must be crewed. This has meant that less skilled pilots (who may log only 50 hr/year) are being recruited and training approaches that are highly intensive and simulation based are being adopted to meet this demand. Even a training route to the first officer level that requires no actual flight hours now exists; made possible by the simulation fidelity offered in Level D simulators and the advanced cockpits of modern transport aircraft. The need for upset training through the use of aerobatics aircraft is only in the process of being made a requirement at the time of writing this

document.[1] Reducing the frequency of flight incidents therefore, not only requires appropriate pilot training, but also the recognition of necessary airspeed margins at the mission planning stage.

7.2 Case 1: Aileron failure simulation

The motivation for this case study is demonstrating the capability to simulate failure cases such as that suffered by the Aer Lingus Airbus A330 (MSN59) on the 11th of May 2010.[169] MSN59 suffered from fatigue cracking and a consequent structural failure within the aileron servo attachment bracket. This resulted in a series of large uncommanded aileron deflections prior to a complete hard failure during which the aileron was stuck at roughly 15°.[170] Although the incident occurred in cruise conditions these simulations were done at a flight condition of Mach 0.6 (V_{TAS} = 200 m/s) and an altitude of 20000ft due to the limitations of the AX-1's aerodynamic model. The same mass case as that used for the derivation of the internal loads envelope was used here (see Appendix D). Furthermore, in case of MSN59, the pilots were kept out of the control loop by the satisfactory performance of the autopilots in maintaining aircraft attitude.

Here, the capability to investigate the effects of pilot control action, via the application of the MOCM and biodynamic models, on airframe internal loads in similar scenarios is demonstrated. A worst case soft starboard aileron failure scenario is first identified by the forced oscillation of the failed aileron at varying frequencies, which effectively localised the resonant frequency for such a failure. Worst case accelerations and loads are then obtained by simulating a forced aileron oscillation (FAO) at this frequency with the pilot model reproducing the manual control dynamics involved in maintaining aircraft attitude control.

7.2.1 Derivation of the MOCM

Upon linearisation the augmented aircraft model can be written in the state-space form of Equation 4.1.1, rewritten here for convenience:

$$\begin{aligned} \dot{\mathbf{x}} &= \mathbf{A}\mathbf{x} + \mathbf{B}\mathbf{u} + \mathbf{E}\mathbf{w} \\ \mathbf{y} &= \mathbf{C}\mathbf{x} + \mathbf{D}\mathbf{u} \end{aligned} \tag{7.2.1}$$

The internal model required by the MOCM algorithm is then based on a further reduced order model obtained through a balanced truncation[171]. This method prioritises system states according to their respective contribution to system dynamics and hence, allows removal of the least significant states. Thus, states associated with significant contributions to rigid body and aeroelastic modes can be retained. Simply truncating the model by removing all aeroelastic states would result in an unrealistic internal model that may lack aeroelastic modes considered by the pilot during manual control.

The following balanced realisation is then obtained by finding a state coordinate basis that ensures that the controllability and observability gramians are equal:

$$\begin{aligned} \dot{\mathbf{x}} &= \bar{\mathbf{A}}\mathbf{x} + \bar{\mathbf{B}}\mathbf{u} + \bar{\mathbf{E}}\mathbf{w} \\ \mathbf{y} &= \bar{\mathbf{C}}\mathbf{x} + \bar{\mathbf{D}}\mathbf{u} \end{aligned} \tag{7.2.2}$$

[1] Simulator based recovery training is typically minimal due to the likelihood of negative training because commercial training devices are unable to provide accurate sustained vestibular cues. Moreover, data regarding the aircraft's flight dynamics during the recovery may not be available or validated.

That is:

$$\mathbf{P} = \mathbf{Q} = \mathbb{H} \tag{7.2.3}$$

where $\mathbf{P}$ and $\mathbf{Q}$ are the controllability and observability gramians defined as follows[172]:

$$\mathbf{P} = \int_0^t e^{-\bar{\mathbf{A}}\iota}\bar{\mathbf{B}}\bar{\mathbf{B}}^T e^{-\bar{\mathbf{A}}^T\iota} d\iota \tag{7.2.4}$$

$$\mathbf{Q} = \int_0^t e^{\bar{\mathbf{A}}\iota}\bar{\mathbf{C}}^T\bar{\mathbf{C}} e^{\bar{\mathbf{A}}^T\iota} d\iota \tag{7.2.5}$$

$\mathbb{H}$ is the following diagonal matrix containing the system's Hankel singular values:

$$\mathbb{H} = \begin{bmatrix} \hat{\sigma}_1 & \dots & \dots & \dots \\ \dots & \hat{\sigma}_2 & \dots & \dots \\ \vdots & \vdots & \ddots & \vdots \\ \dots & \dots & \dots & \hat{\sigma}_n \end{bmatrix} \tag{7.2.6}$$

For brevity, the process of obtaining a balanced realisation is not included here and the reader is referred to standard textbooks on modern control theory, such as Whidborne et al[173] and Zhou et al[174]. The information contained within $\mathbb{H}$ is used to select a threshold value of $\hat{\sigma}_i$ for truncation. Glover[175] has shown that a frequency domain error between the original model and the reduced order model is bounded and can be estimated by the following norm:

$$||G(s) - G_r(s)||_\infty \leq \kappa \tag{7.2.7}$$

where $G(s)$ and $G_r(s)$ refer to the full and reduced order models respectively. κ can be found to be:

$$\kappa = 2\sum_{j=r+1}^{n} \hat{\sigma}_j \tag{7.2.8}$$

where n and r are the number of states in the full and reduced order models respectively. For the linearised aircraft model at the flight condition of interest, the effect of r on this error bound is shown in Figure 7.5. Reducing the model order to 21 was found to ensure errors lower than 1% ($\approx$ -40 dB). Models with $r \geq$15 were found necessary to capture magnitude and phase effects introduced by the low frequency aeroelastic modes.

In practice, the generation of the MOCM internal model is a three step process where the first step is to obtain a reduced order model of the bare airframe. This was achieved by linearising the aeroelastic model at the flight condition of interest and directly truncating the model such that the rigid body modes and low frequency structural modes were conserved. The second step is to augment it with the nonlinear inceptor, CSAS and actuator models. Finally, this composite model is linearised again to obtain a representation of the augmented aircraft. Here, a balanced realisation was implemented in the MOCM algorithm to ensure well conditioned matrices are used to solve the AREs within the algorithm. Figure 7.6 presents the model's stick force to pitch and roll attitude frequency responses. The internal model used for these simulations comprised of 21 states, resulting in a 29 state MOCM pilot model.

In this case, the following cost function was used for MOCM task definition:

$$\mathcal{J} = E\left\{ \lim_{\eta\to\infty} \frac{1}{\eta} \int_0^\eta \left(\begin{bmatrix} e_\theta & e_\phi \end{bmatrix} \begin{bmatrix} Q_\theta & 0 \\ 0 & Q_\phi \end{bmatrix} \begin{bmatrix} e_\theta \\ e_\phi \end{bmatrix} + \begin{bmatrix} \dot{F}_{s\theta} & \dot{F}_{s\phi} \end{bmatrix} \mathbf{S} \begin{bmatrix} \dot{F}_{s\theta} \\ \dot{F}_{s\phi} \end{bmatrix} \right) dt \right\} \tag{7.2.9}$$

The parameters shown previously in Table 4.4 were used for the generation of MOCM implemented here. Figure 7.7 presents the linearised open-loop frequency response of the PVS; that

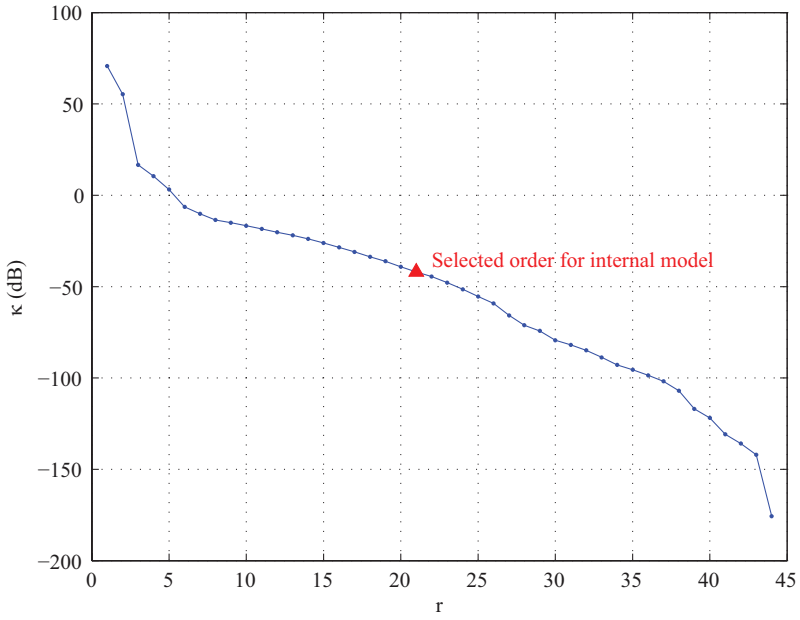

Figure 7.5: Variation of upper error bound with the order of reduced model.

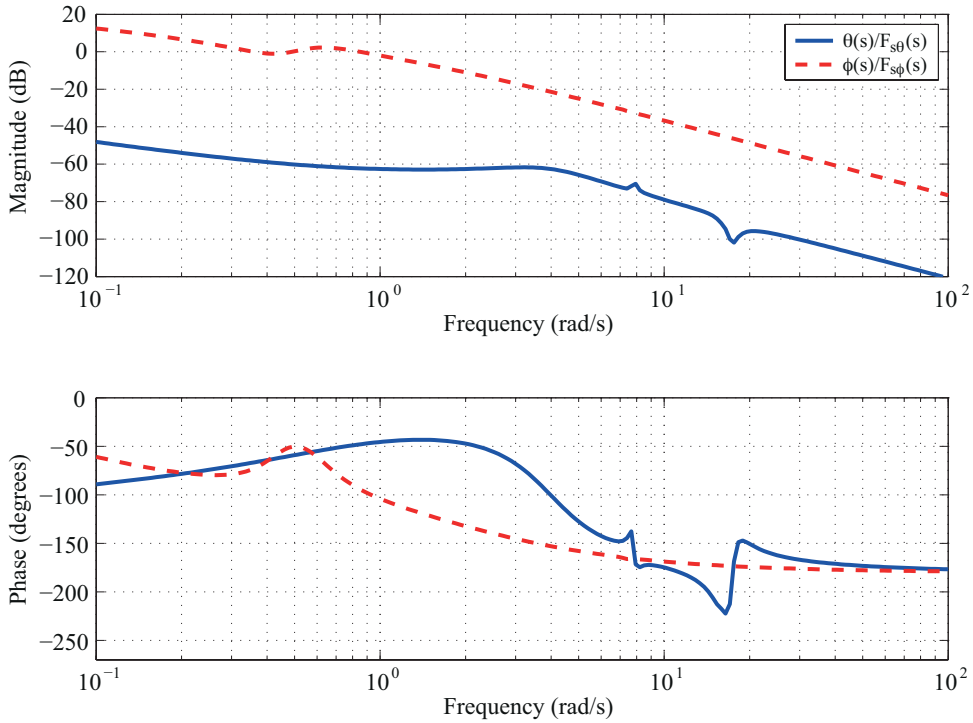

Figure 7.6: Frequency response of the linearised augmented aircraft.

is from the observed errors used as input to the MOCM to the controlled flight dynamic variables.[2] In this case, the latter were selected to be pitch and bank attitudes. Corresponding crossover frequencies together with the gain and phase margins are given in Table 7.1.

It should be noted that there is a sudden drop in phase around 8 rad/s along with a resonant peak around the same frequency. Such a phase loss, greater than 90°, in the middle of the manual control frequency range is often referred to as a handling qualities cliff and is a contributing

[2]All nonlinear features of the bank angle control law were removed prior to linearisation. These included the envelope protection features, automatic roll out and wing leveller.

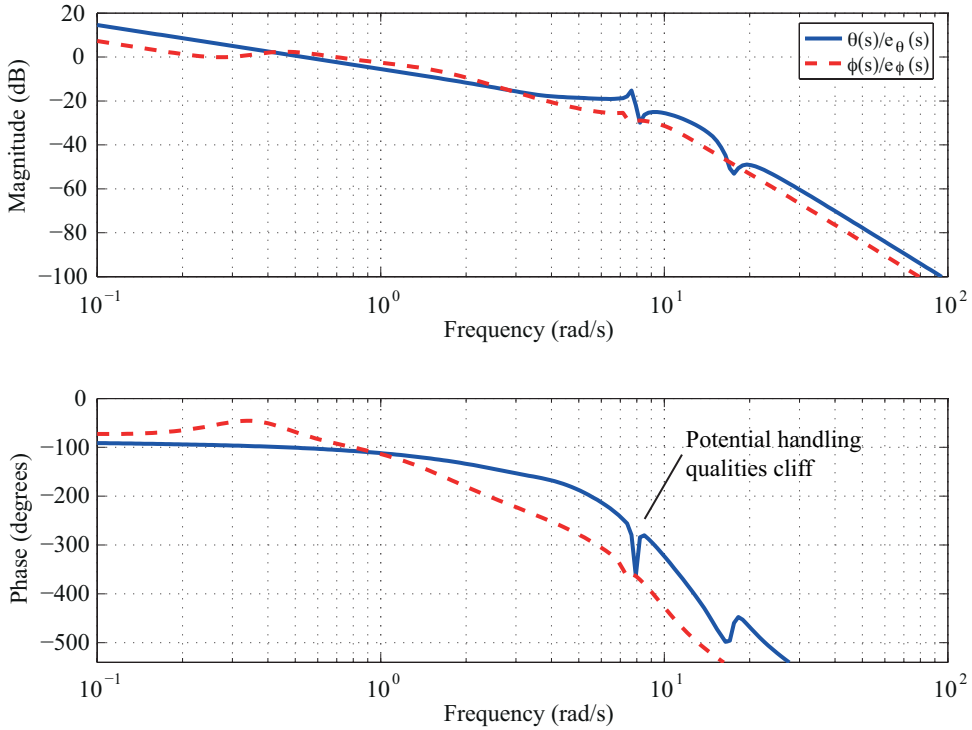

Figure 7.7: Open-loop PVS frequency response for pitch and bank attitude control.

	Pitch	Roll
Gain margin (dB)	18.44	9.72
Gain crossover frequency (rad/s)	0.62	0.25
Phase margin (degrees)	76.4	124.79
Phase crossover frequency (rad/s)	4.67	2.00

Table 7.1: Frequency domain PVS stability characteristics.

factor towards the susceptibility of an aircraft to APC.

7.2.2 Identification of resonance frequency

The worst case aileron oscillation frequency was obtained through a nonlinear time-domain simulation of the augmented aircraft (without the MOCM) during which the starboard aileron was forced to oscillate at frequencies that linearly rose from 0.1 Hz to 10 Hz over 150 seconds, as shown in Figure 7.8. The effects of actuator saturation and rate limits are clearly observable.

The resulting oscillations in pitch attitude were found to be relatively small whilst a maximum bank angle of 13° occurred during the large amplitude low frequency aileron deflections. However, as shown in Figure 7.9, more significant oscillations in normal acceleration that reached a maximum of $\pm 1g$ were found to occur around 20 seconds. Lateral accelerations were found to be negligible. The frequency content of the normal acceleration, presented in Figure 7.10(a), shows that this large amplitude oscillation corresponds to the peak occurring at 7.7 rad/s at the frequency of the first anti-symmetric wing bending mode; see Appendix D for mode shapes and modal frequencies for this mass case. The consequent impact on spanwise wing deformation is presented in Figure 7.11.

Oscillation of the starboard aileron was found to cause what seemed to be a whiplash effect on

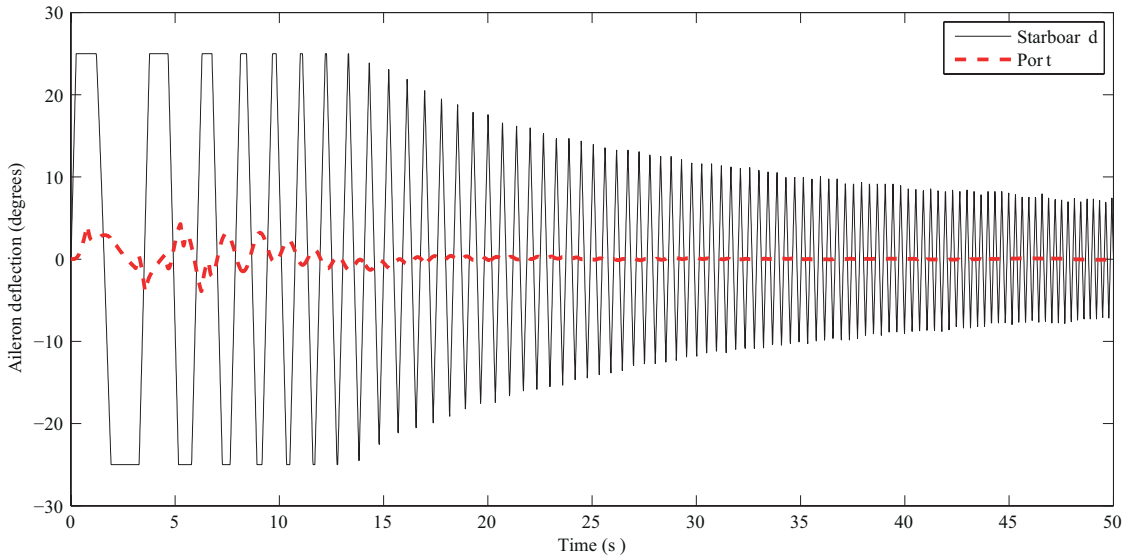

Figure 7.8: Forced starboard aileron deflection and corresponding port aileron deflection.

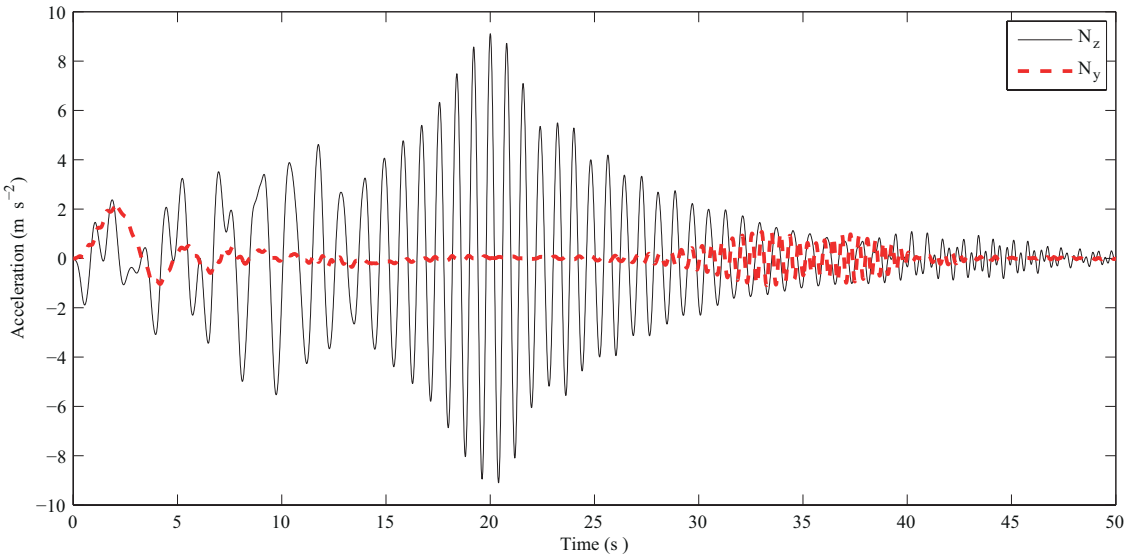

Figure 7.9: Accelerations due to forced starboard aileron frequency sweep.

the port wing resulting in wing tip deflections up to twice that undergone in steady trimmed flight. The source of this amplification is in fact the interaction of control demands from the CSAS, attempting to compensate for perturbations in pitch rate and normal acceleration, with the low frequency structural modes. This results in effectively a forced vibration of the port wing between frequencies covered by the aileron frequency sweep. Starboard wing deformations are damped by the changes in aerodynamic forces arising due to the FAO itself. Pilot-model-in-the-loop simulations were only found to amplify the effect as shown in Figure 7.10(a). Plotting the frequency response of the tip deflections due to starboard aileron, that is:

$$G_{\mu\xi}(j\omega) = \frac{|\mathbb{F}(\mu_{tip}(t))|}{|\mathbb{F}(\xi(t))|} \tag{7.2.10}$$

as presented in Figure 7.10(b), clearly shows the amplifications at the structural modal frequencies. Such amplification of the port wing deformation is seen to occur in three sets in Figure 7.11 around 20, 30 and 40 seconds in decreasing amplitudes; each corresponding to a modal frequency of the airframe structure.

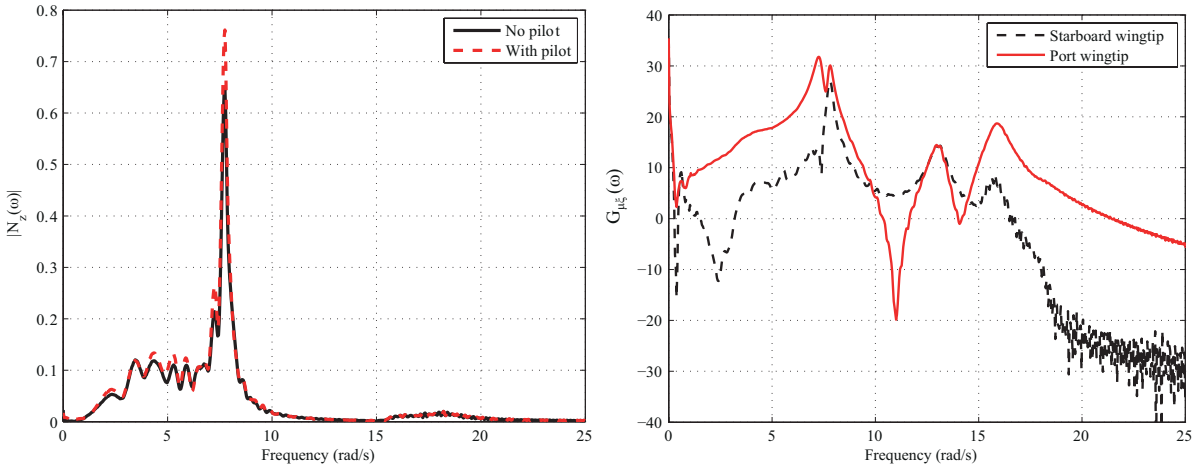

(a) (b)

Figure 7.10: Normal acceleration frequency content and frequency response of vertical wingtip deflections due to starboard aileron frequency sweep.

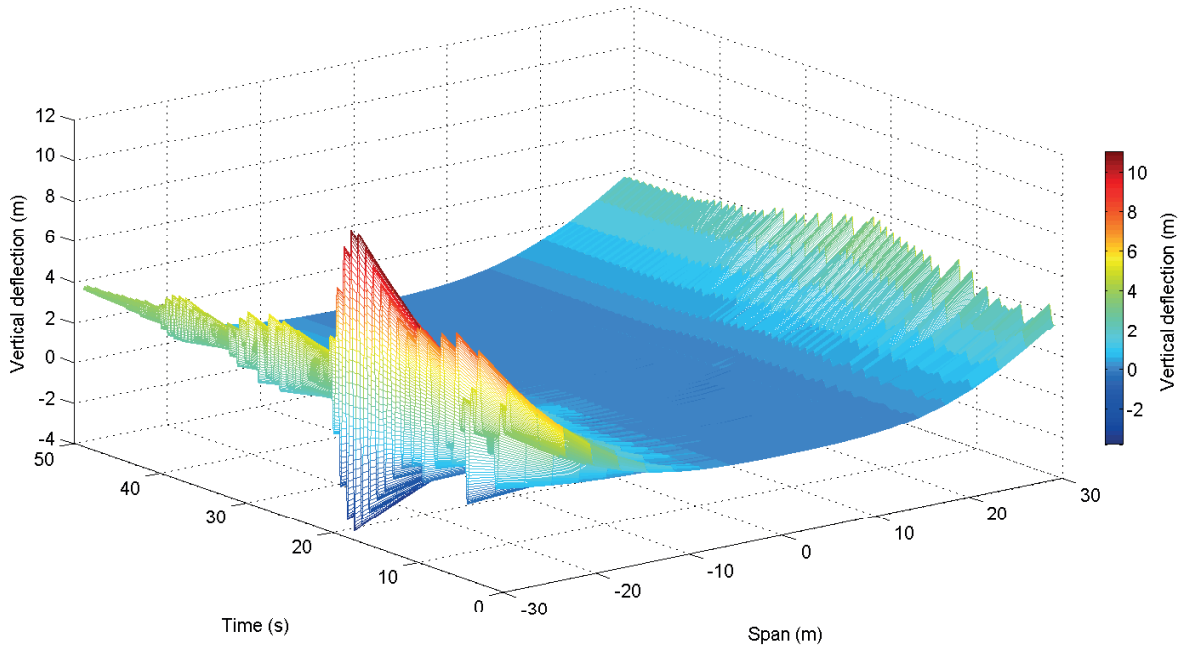

Figure 7.11: Spanwise vertical deflections due to forced starboard aileron frequency sweep.

Starboard WRBM was found to be relatively small compared to the port side. The large structural deformations undergone by the port wing together with the relatively small aileron deflections result in large changes in local angle of attack. This consequently affects aerodynamic loading resulting in large variations in internal loads. The initial effects of the forced aileron oscillation on WRBM is shown in Figure 7.12. Peak loadings occur around 9 seconds and correspond to an aileron deflection frequency of approximately 4 rad/s.

The starboard aileron frequency sweep has thus provided two critical frequencies for investigation: (1) 7.7 rad/s where the normal accelerations are greatest and, (2) 4.0 rad/s where the highest WRBM were observed.

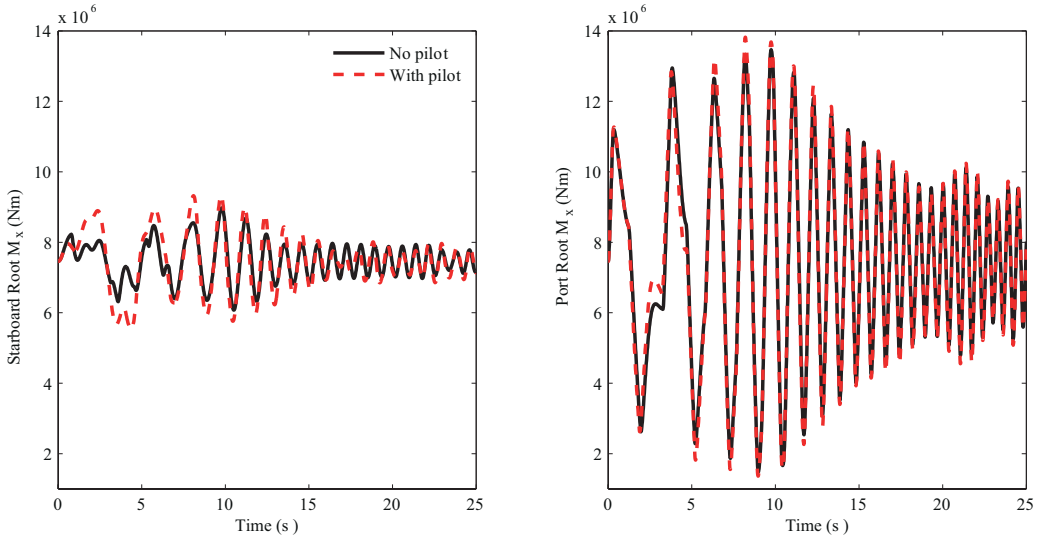

Figure 7.12: Initial development of starboard and port WRBM with aileron frequency sweep.

7.2.3 Aileron oscillation at 7 rad/s

Worst case accelerations can now be obtained by the forced oscillation of the starboard aileron at 7.7 rad/s with maximum allowable amplitude. The resultant deflection is effectively that of rate limited control surface oscillation as shown in Figure 7.13.

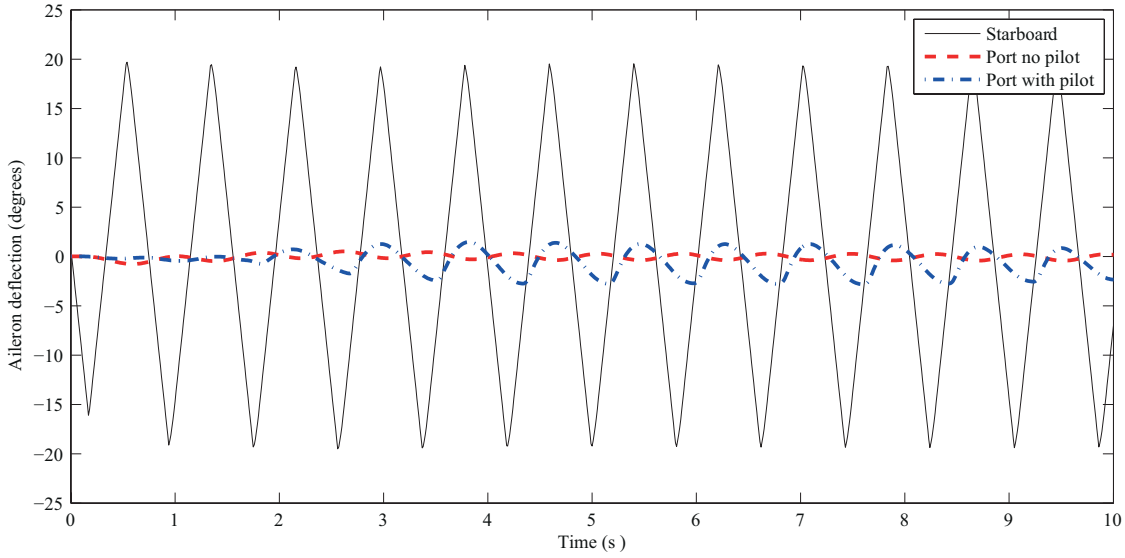

Figure 7.13: Starboard FAO at 7 rad/s and corresponding port aileron deflections.

Normal acceleration was found to rapidly exceed the $-1g$ lower load factor limit and the MOCM was found to only amplify the amplitude of these oscillations. Figure 7.14 shows the initial development of the normal acceleration and the fully developed steady-state oscillations. MOCM input was found to eventually amplify peak accelerations by 26%.

7.2.4 Aileron oscillation at 4 rad/s

In the last two cases, it has been evident that normal accelerations resulting from the pitch compensation have driven the oscillations in wing root bending bending moment. FAO at 7.7

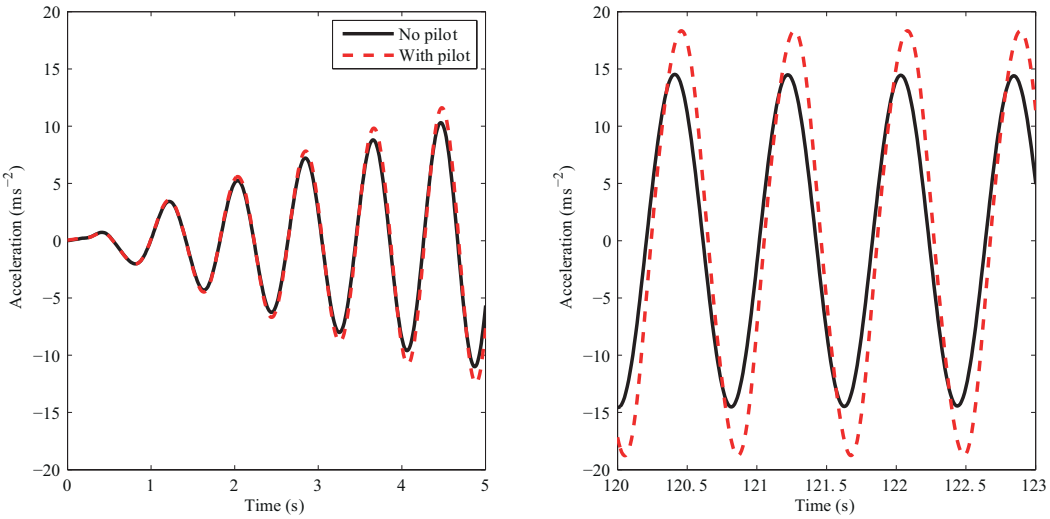

Figure 7.14: Normal accelerations with and without MOCM for 7 rad/s FAO.

rad/s effectively inserted energy at the first wing bending mode frequency. FAO at 4 rad/s now aims to not only excite the PVS at the frequency where the maximum WRBM was observed, but also close to the phase crossover frequency where the nonlinear PVS may be fully out of phase with the required attitude corrections.

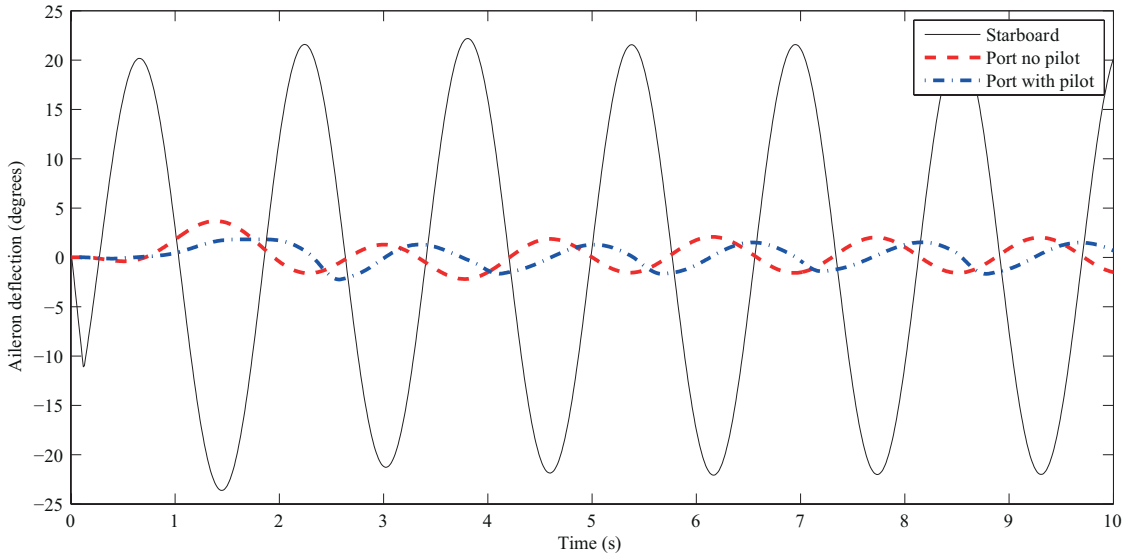

Figure 7.15: Starboard FAO at 4 rad/s and corresponding port aileron deflections.

The starboard FAO is shown in Figure 7.15 together with the port aileron deflections with and without MOCM input. The delay introduced by the MOCM is evident in the port aileron deflections. As shown in Figure 7.16, inclusion of the MOCM did not increase normal accelerations significantly.

Port and starboard WRBM with and without the MOCM are presented in Figures 7.17 and 7.18 respectively. Adverse effects of the MOCM compensation can be clearly seen for the starboard wing in the initial failure stages, but the oscillations are smaller than those undergone on the port side. Initial effects of the MOCM control action on port WRBM are negligible, but a 4.34% increase was found after transient features had subsided.

PIO features were assessed using the ROVER algorithm[176] detailed in Appendix G. It was

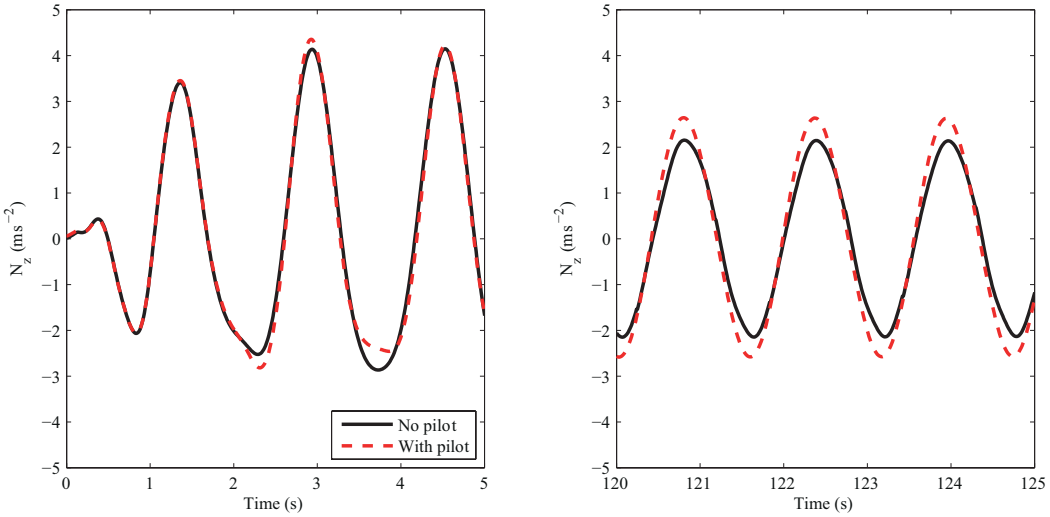

Figure 7.16: Normal acceleration with and without MOCM for 4 rad/s FAO.

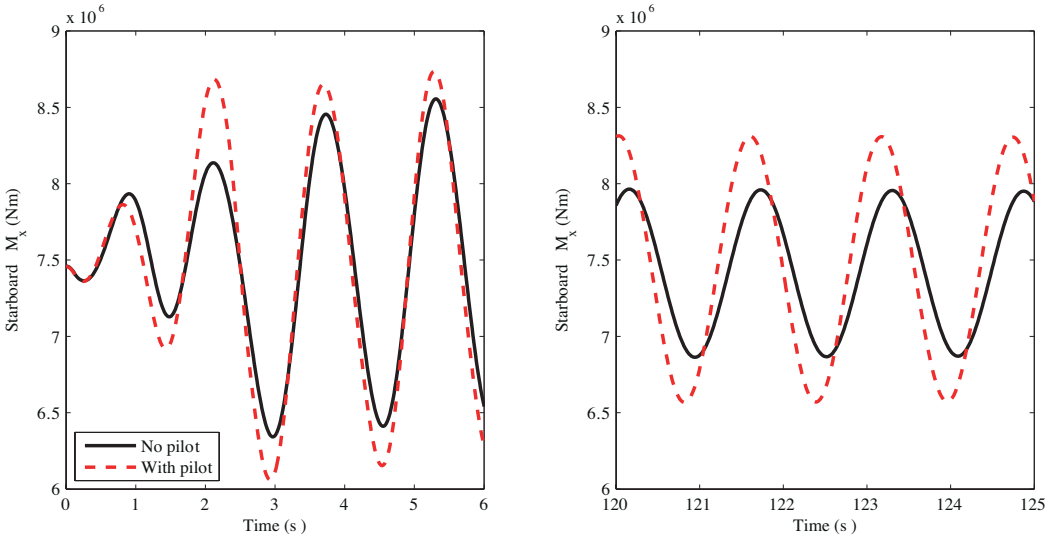

Figure 7.17: Starboard WRBM with and without MOCM for 4 rad/s FAO.

found that the observed oscillations were within the PIO frequency range and the aircraft response and MOCM inputs were sufficiently out of phase for the oscillations to be characteristic of a mild PIO. The magnitude of pitch and roll rates together with the stick deflections were found to be below the thresholds set for the observed dynamics to be classifieds as a PIO. ROVER output for this case can be found in Appendix G.

7.2.5 Biodynamics effects

Biodynamic feedthrough effects were studied by integrating the biomechanical model developed in Chapter 5 within the nonlinear PVS simulation environment and simulating the 4.0 rad/s FAO scenario again. The stick deflection output of the longitudinal model was converted to stick force by multiplying the deflections with the AMRL stick stiffness.[3]

[3]AMRL stick stiffness was determined by applying the final value theorem as follows: $\lim_{s\to 0}(\frac{164}{s^2+2(0.3)(23)s+23^2}) = 0.31$. Thus, the gain introduced by the AMRL stick in the command path is 0.31 m/N. Stick stiffness is simply the inverse of this gain.

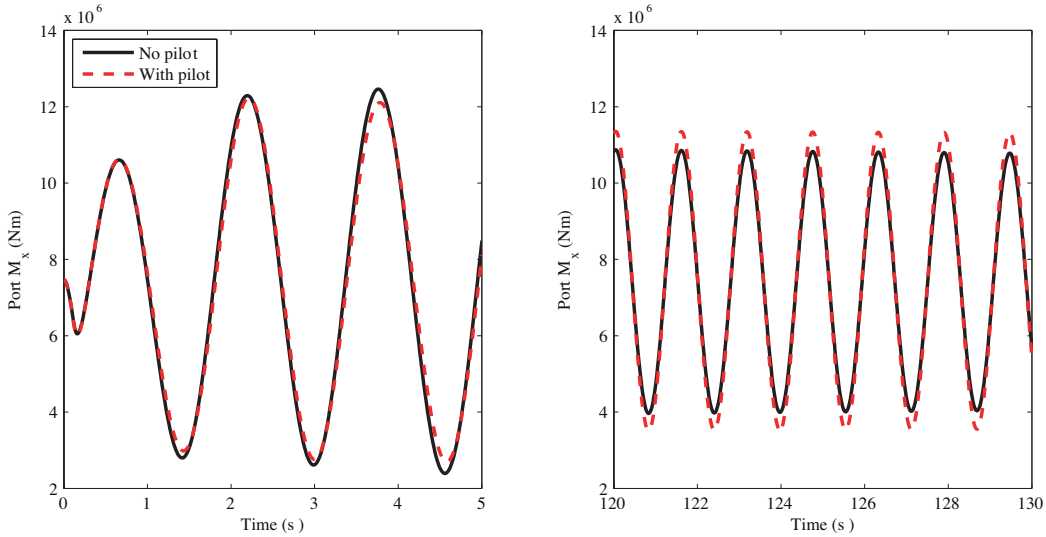

Figure 7.18: Port WRBM with and without MOCM for 4 rad/s FAO.

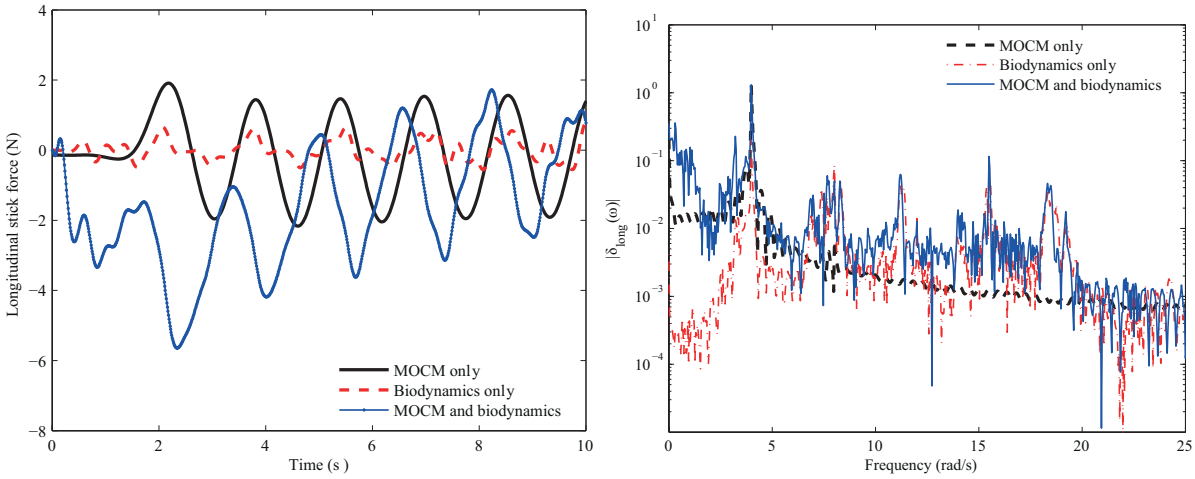

(a) (b)

Figure 7.19: Longitudinal stick characteristics with biodynamic effects for 4 rad/s FAO.

Longitudinal dynamics were found to be most significantly affected by the biodynamic feedthrough of normal acceleration, mainly due to the interaction between the MOCM and the involuntary stick deflections. This effect is clearly visible in the resultant stick forces and its frequency content as shown in Figure 7.19. From the frequency spectrum it can be deduced that stick forces between 5 rad/s to 20 rad/s are due to biodynamic feedthrough. Moreover, amplification of stick force below 2 rad/s can also be attributed to this effect.

Lateral stick forces, although small in magnitude, were found to be largely driven by the biodynamic response to lateral accelerations, as shown in Figure 7.20.

The combined effect of the MOCM and biomechanical model was found to be an 8.86% increase in peak port WRBM after the oscillations were fully developed, as shown in Figure 7.21. Simulations with the biodynamic model alone resulted in a 1.20% increase.

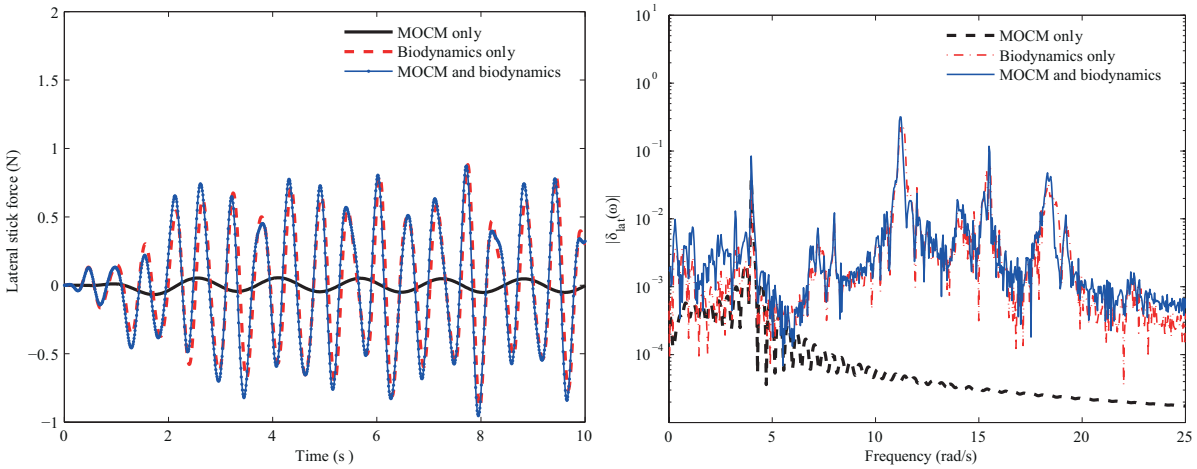

Figure 7.20: Lateral stick characteristics with biodynamic effects in response to 4 rad/s FAO.

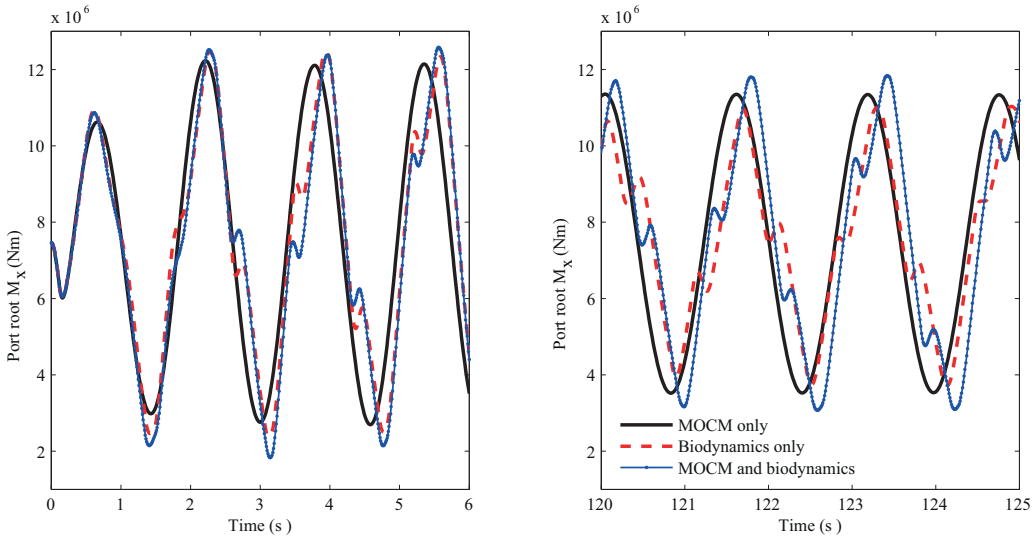

Figure 7.21: Effect of biodynamic feedthrough on port WRBM for 4 rad/s FAO.

7.2.6 Envelope comparison

Comparing the previous four sets of simulation results with the internal loads envelopes derived in Chapter 6 allows an assessment of the severity of internal loads and the identification of potential extreme loading scenarios.

Figures 7.27 and 7.28 compare the maximum and minimum uncorrelated loads due to FAO at 7.7 rad/s with the frequency sweep and 4 rad/s FAO cases. In this case, maximum loadings from the frequency sweep provide the upper and lower bounds for oscillatory failures for both wings with the MOCM input alone. However, as shown in Figure 7.28, the inclusion of biodynamic feedthrough effects results in greater loadings on the starboard wing.

The scenario for HTP loads on the other hand, is extreme. Internal loads undergone during both the frequency sweep and 7.7 rad/s FAO exceed the loads envelope. These are summarised in Table 7.2. Load factors undergone due to the coupling manual control and structural dynamics at these modal frequencies are a result of the commanded elevator deflections. These generate the desired pitching moments via changes in HTP aerodynamic loads. Therefore, HTP loads

	Frequency sweep		7rad/s FAO	
Envelope bound	Upper	Lower	Upper	Lower
Bending moment	-35.90	19.10	38.91	78.76
Shear force	16.13	-37.19	73.69	38.32
Torsion	0.63	15.43	55.51	128.89

Table 7.2: Percentage exceedence of HTP internal loads envelope.

are affected directly whereas, wing loads are driven indirectly by the resulting load factors.

Maximum loads from the 4.0 rad/s FAO case with and without biodynamic feedthrough were found to remain well within the envelope. VTP loads were also found to be within the envelope because the aircraft dynamics remained primarily in the longitudinal axis. Simple frequency sweep alone is therefore, not capable of exposing wing and empennage loads exceedences in the types of failure cases discussed in this section.

7.3 Case 2: Gust encounter simulation

This case demonstrates the capability to investigate gust and severe turbulence encounters with and without the effects of manual control and LAF. Together with the previous case, results are presented here from the simulation environment developed as part of this study. It consists of the AX-1 aeroelastic aircraft model, biomechanical and control-theoretic pilot model components and a LAF augmented FCS model. The motivation is to attempt to reconstruct the gust encounters similar to those discussed earlier in Section 7.1; especially where the load factor exceedences are thought to be driven by manual control action. A study investigating the effects of MOCM parameters and LAF is presented prior to the comparison of simulation results with DFDR data kindly provided by Airbus UK.[4]

7.3.1 Derivation of the MOCM

The MOCM models implemented here were derived via the same process detailed in Chapter 4 and discussed earlier in Section 7.2. The internal model was obtained by linearising the augmented aircraft model at the incident flight conditions and then generating a reduced order model that has a balanced and minimal state-space realisation. The MOCM parameter values used in this study are given in Table 7.3.

Inherent time delay, τ	0.3
Neuromuscular lag, τ_n	$0.08 \rightarrow 0.28$
Attention allocation, f_y	(1,1,1,1)
Disturbance intensity, $\mathbf{W}$	8.8
Disturbance filter	$1/(s+2)$
Noise-to-signal ratios (ρ_u, ρ_y) (dB)	(-50,-40)

Table 7.3: MOCM parameters for gust encounter simulations.

[4]The reader should note that large aircraft gust encounters reported as incidents are rare and those that are severe enough to require reconstruction are only a small subset. Moreover, given the skill and experience required to pilot large aircraft, incidents where loads are driven by manual control inputs rarely occur. Finding an incident that is suitable for validation purposes is therefore, very unlikely and made even more difficult when the limitations of the AX-1 model are considered.

Along with the assumptions made within the MOCM framework, it was further assumed that the pilot controlled longitudinal dynamics through monitoring the following cues:

- Pitch attitude and pitch rate at the IMU station, as displayed on the PFD.
- Normal acceleration felt at the pilot station.

Given the purely one dimensional vertical gust velocity profile (shown in Figure 7.22), only small perturbations in aircraft lateral dynamics, arising due to pitch-roll coupling, were expected. Therefore, the pilot's lateral stick deflections are assumed to be driven by roll attitude compensation, as opposed to roll rate. The task was defined via the following cost function:

$$\mathcal{J} = E\left\{ \lim_{\eta\to\infty} \frac{1}{\eta} \int_0^{\eta} \left(\mathbf{e}^T \mathbf{Q} \mathbf{e} + \dot{\mathbf{u}}^T \mathbf{S} \dot{\mathbf{u}} \right) dt \right\} \tag{7.3.1}$$

where

$$\mathbf{e} = \begin{bmatrix} e_\theta & e_q & e_{nzp} & e_\phi \end{bmatrix}^T \tag{7.3.2}$$

$$\mathbf{Q} = \begin{bmatrix} Q_\theta & 0 & 0 & 0 \\ 0 & Q_q & 0 & 0 \\ 0 & 0 & Q_{nzp} & 0 \\ 0 & 0 & 0 & Q_\phi \end{bmatrix} \tag{7.3.3}$$

$$\dot{\mathbf{u}} = \begin{bmatrix} \dot{F}_{s\theta} & \dot{F}_{s\phi} \end{bmatrix}^T \tag{7.3.4}$$

No weightings on stick forces have been included for simplicity and the diagonal weighting matrix $\mathbf{S}$ is tuned within the MOCM algorithm to set the neuromuscular lag parameter.

7.3.2 Effects of MOCM neuromuscular lag

Neuromuscular lags of 0.08 and 0.28 representing aggressive and passive pilots respectively were investigated. Figure 7.22 presents the response of the key flight dynamic parameters to the combined gust and MOCM control input. The LAF is active in both cases and aircraft response with no control surface deflections was simulated to highlight effects that can be attributed to the gust alone. Detailed time histories from the simulations can be found in Appendix F.

It can be seen that the aircraft's response to the disturbance is stable with load factors lying within the +2.5g and -1g limits. The response is characterised by two large normal acceleration deviations occurring around 15.5 and 18.0 seconds. Inclusion of the MOCM control input amplifies the small deviation around 17 seconds. In case of the more aggressive pilot model, this turns out to be greater than the initial gust driven deviation.

The relatively high gains introduced by the aggressive pilot model is also made evident by the large amplitude high frequency stick deflections, which eventually results in a fully developed Category II PIO driven by elevator rate limiting and saturation. This was confirmed using the ROVER algorithm, see Appendix G. The frequency of the stick deflection around 15 seconds was found to be 15.4 rad/s, indicating that the response is an attempt to compensate for accelerations driven by the fifth and sixth structural modes. These modes are defined by a combination of symmetric and asymmetric HTP bending along with lateral and longitudinal fuselage deformations. The amplification of these modes due to the MOCM can be seen in the singular values of the open loop PVS shown in Figure 7.23.

Biodynamic feedthrough effects were found to be negligible in this scenario, as shown in the stick force contributions presented in Figure F.3 in Appendix F.

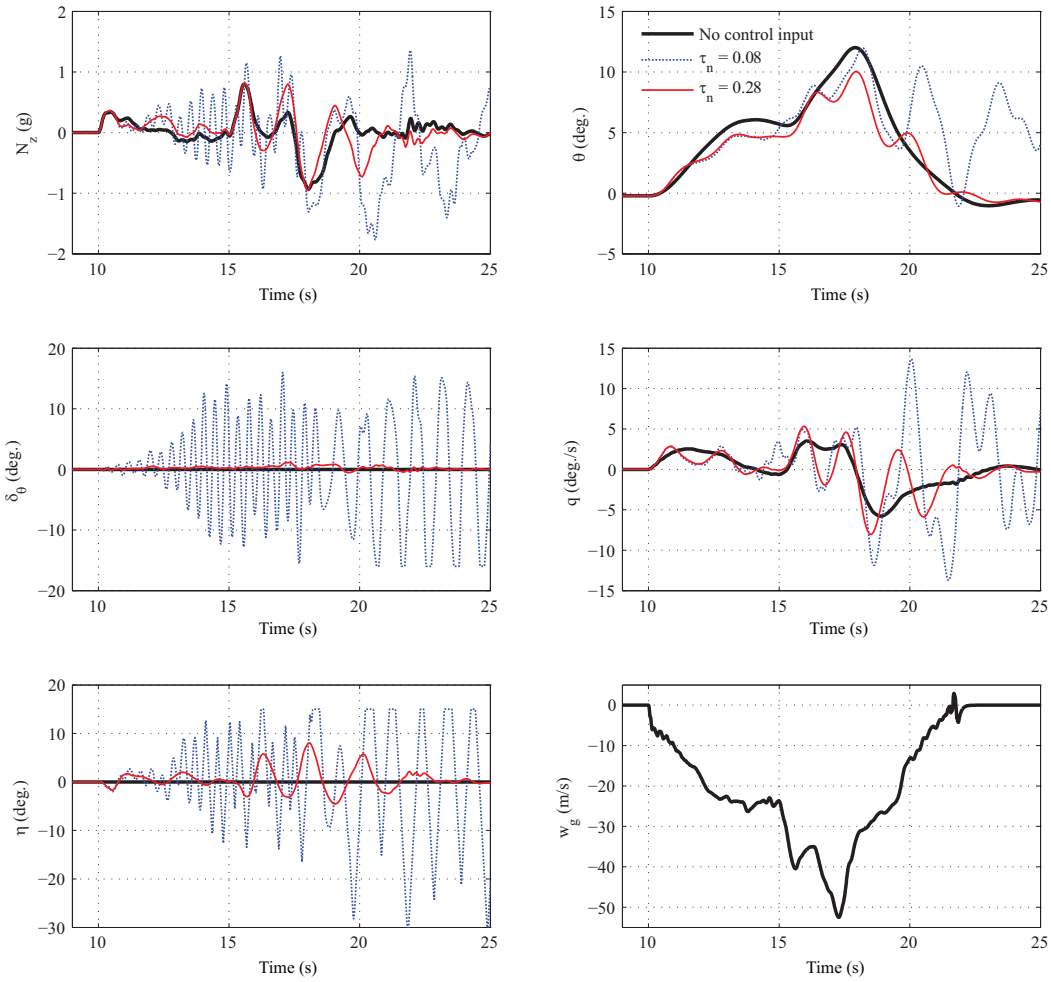

Figure 7.22: Effect of varying neuromuscular lag on aircraft gust response.

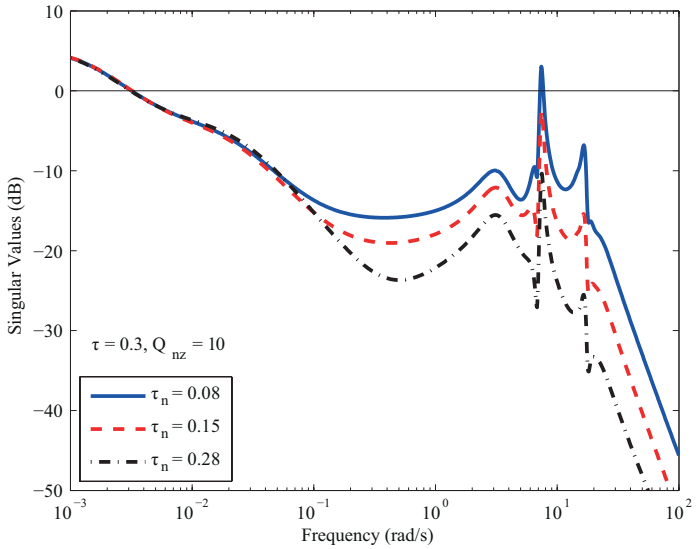

Figure 7.23: Effect of neuromuscular lag on open-loop PVS frequency response.

7.3.3 Combined effects of MOCM and LAF

Simulations with control surface deflections solely due to the MOCM and LAF were used to ascertain their respective effects for the scenario with the aggressive pilot model. Figure 7.24 presents the key flight dynamic parameters from these simulations.

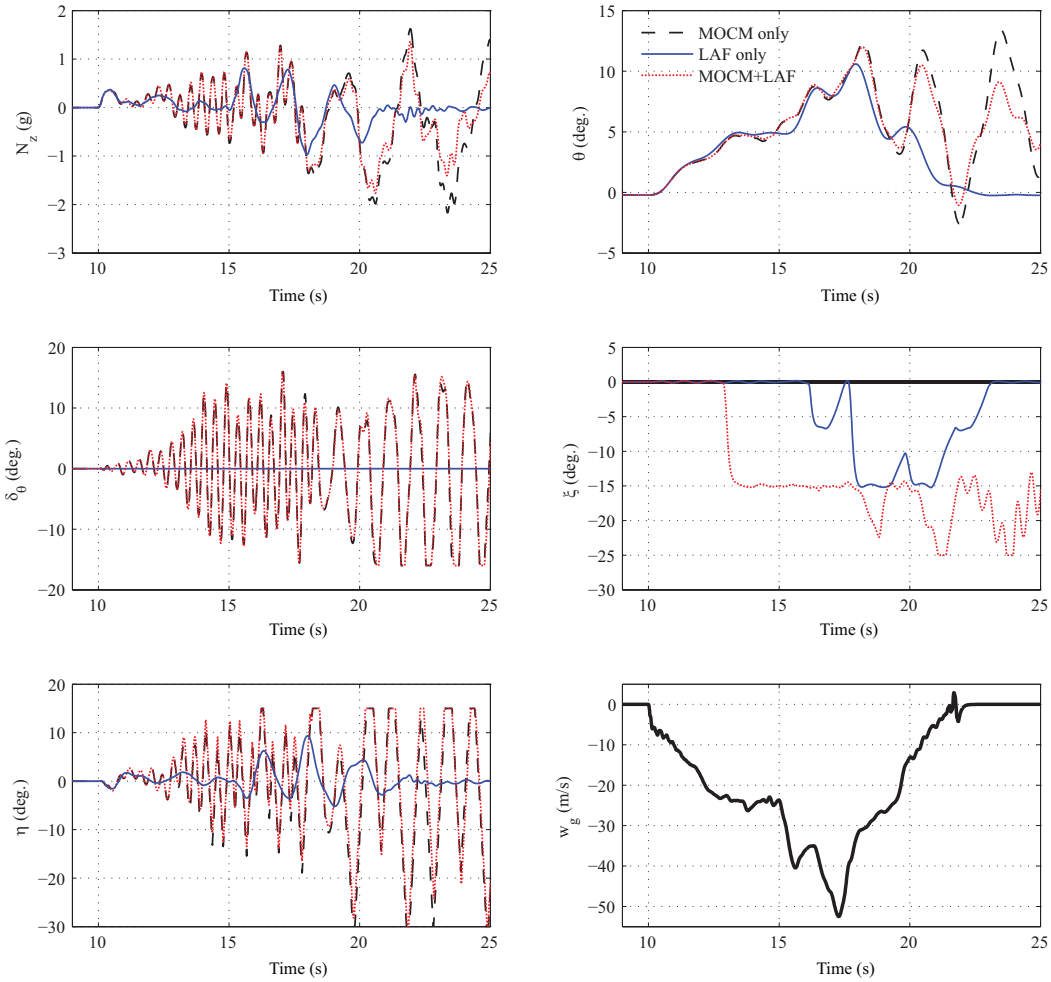

Figure 7.24: Effects of LAF and MOCM on aircraft gust response.

LAF only results demonstrate the operation of the AMC and GLA systems. The system only activates after the first normal acceleration peak passes the ±0.2g activation threshold. Overall, the effects of manual control dominate and the LAF is only capable of alleviating the acceleration peak occurring around 23 seconds. It is also evident that the normal accelerations resulting from aggressive manual control cause instances of aileron saturation (at 21 and 24 seconds), which could have drastically reduced roll authority if the gust profile had a lateral component and necessitated significant roll attitude compensation. In practice such a scenario is avoided by designing LAF that rely heavily on secondary control surfaces such as spoilers.

7.3.4 Comparison with DFDR data

This particular incident was selected because it was a rare gust encounter for which: (a) manual control was found to be the primary source of loads exceedence, (b) the complete uncorrupted DFDR dataset was available and, (c) Airbus in-house processes had extracted the gust profile. The incident and simulation mass case and flight conditions are given in Table 7.4.

	Incident	Simulation
Mass case (% MTOW)	72	75
Altitude (ft)	20400	20000
Mach	0.71	0.69
True airspeed (m/s)	223	220
Calibrated airspeed (kts)	324	322

Table 7.4: Initial flight conditions for incident and simulation.

Although significant differences exist between the actual aircraft involved in the incident and the model used in the simulations, such a comparison allows a rough assessment of the accuracy of the pilot model for loads analysis. Moreover, since structural flexibility effects were known to be small for the incident aircraft, the effects of fuselage flexibility on manual control can also be studied. Figure 7.25 allows the longitudinal dynamics and stick deflections to be compared. The data has been normalised using the maximum normal acceleration recorded by the DFDR.

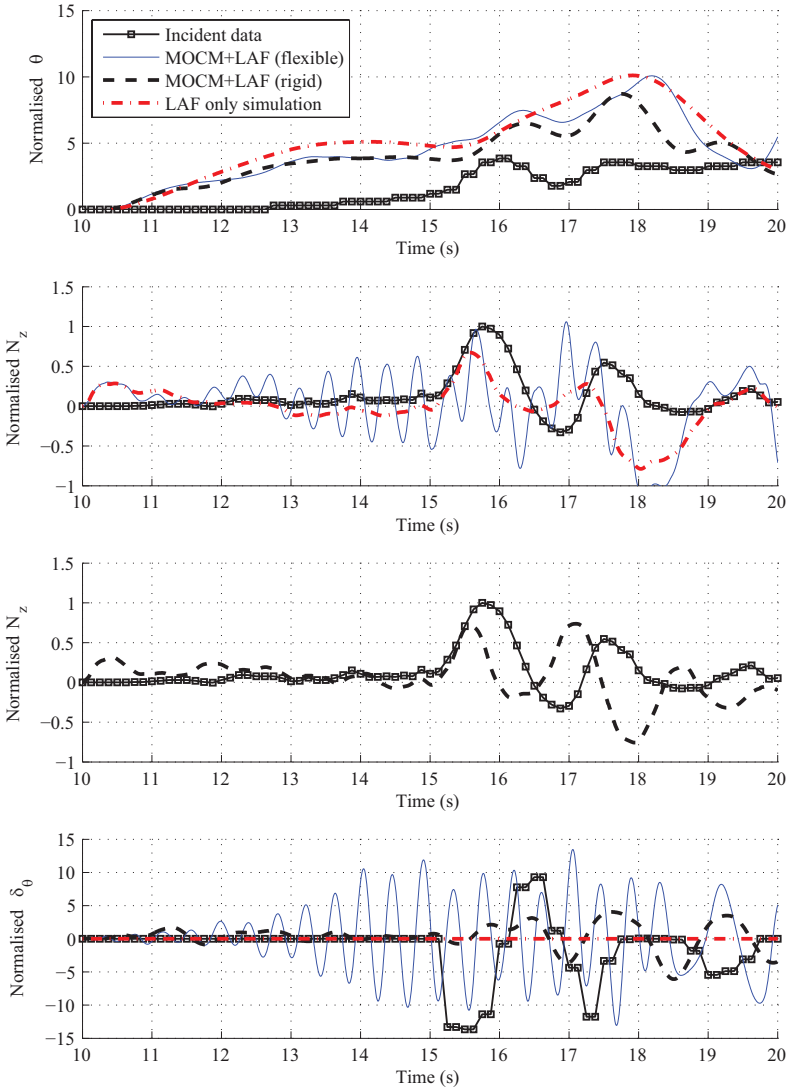

Figure 7.25: Comparison of pilot-model-in-the-loop simulation with normalised DFDR data.

The most significant limitations of the AX-1 model were discussed in Chapter 6. However, the following are the key differences between the incident aircraft and the AX-1 that must be kept

in mind during this comparison:

- The incident aircraft is in fact a much smaller twin-engine civil transport approximately three times lighter than the AX-1. This meant that the gust profile had to be scaled accordingly to generate representative dynamics during simulation.
- Information regarding certain nonlinear components of the FCS on board the incident aircraft was not available. So it can only be assumed that the FCS augmenting the AX-1 model yields similar flying and handling qualities.
- Centre of gravity information for the incident aircraft was also not known. Therefore, it has been assumed to be the same as that of the AX-1 and the resulting differences in static stability are assumed to be negligible.
- Although both aircraft have a conventional layout, the difference in the design point (that is the cruise Mach number and altitude) means that significant differences in aerodynamic coefficients can potentially exist.

However, given such drawbacks in simulation fidelity, the incident was reconstructed reasonably well for the LAF only case and the case where fuselage flexibility effects were omitted from the calculation of normal acceleration at the pilot station (by setting $\theta' = 0$).

The lack of high frequency stick deflections for the rigid fuselage case confirms the effect of the previously mentioned structural modes on manual control and brings the MOCM output closer to that of the pilot; at least in terms of the fundamental frequency. The pilot's input is approximately sinusoidal at 0.5 Hz and in comparison, the MOCM response for the rigid fuselage case is also characterised by a roughly 0.5 Hz oscillation. This is confirmed further by the frequency spectra shown in Figure 7.26. It is evident that the response with a rigid fuselage primarily consists of rigid body dynamics excited by the gust around 4.0 rad/s. Smaller secondary effects can be seen due to the first wing bending modes around 6.8 rad/s. In contrast, the effects of wing and fuselage flexibility on stick deflection are clearly represented by the distinct peaks in Figure 7.26(c) at around 6.5 rad/s and 14.8 rad/s respectively.[5]

Example gust profiles derived through the use of incident data and Airbus in-house codes are included in Appendix F.

7.3.5 Envelope comparison

From a flight loads perspective, the main concern is whether the incident has resulted in internal loads exceeding the estimated limit loads envelope. Here, the maximum and minimum non-correlated loads for each simulation case are plotted together with the envelopes derived in Chapter 6 in Figures 7.31 to F.9.

The effects of LAF and MOCM control on spanwise wing and HTP loads are presented in Figures 7.31 and 7.32. The upper and lower bounds on the wing bending moment set by the +2.5g unchecked pull up manoeuvre and continuous turbulence envelopes respectively are not exceeded in any of the cases. The beneficial effect of LAF can also be seen. It was found to reduce the maximum WRBM by 17.3% relative to the case where no control surface deflections were made. The inclusion of the MOCM control action effectively cancels this benefit and results in maximum and minimum WRBM that are only 26.0% and 18.1% away from the limits

[5]The DFDR's poor sampling rate together with the short duration of the incident means that frequency domain comparisons with the actual incident could not be made.

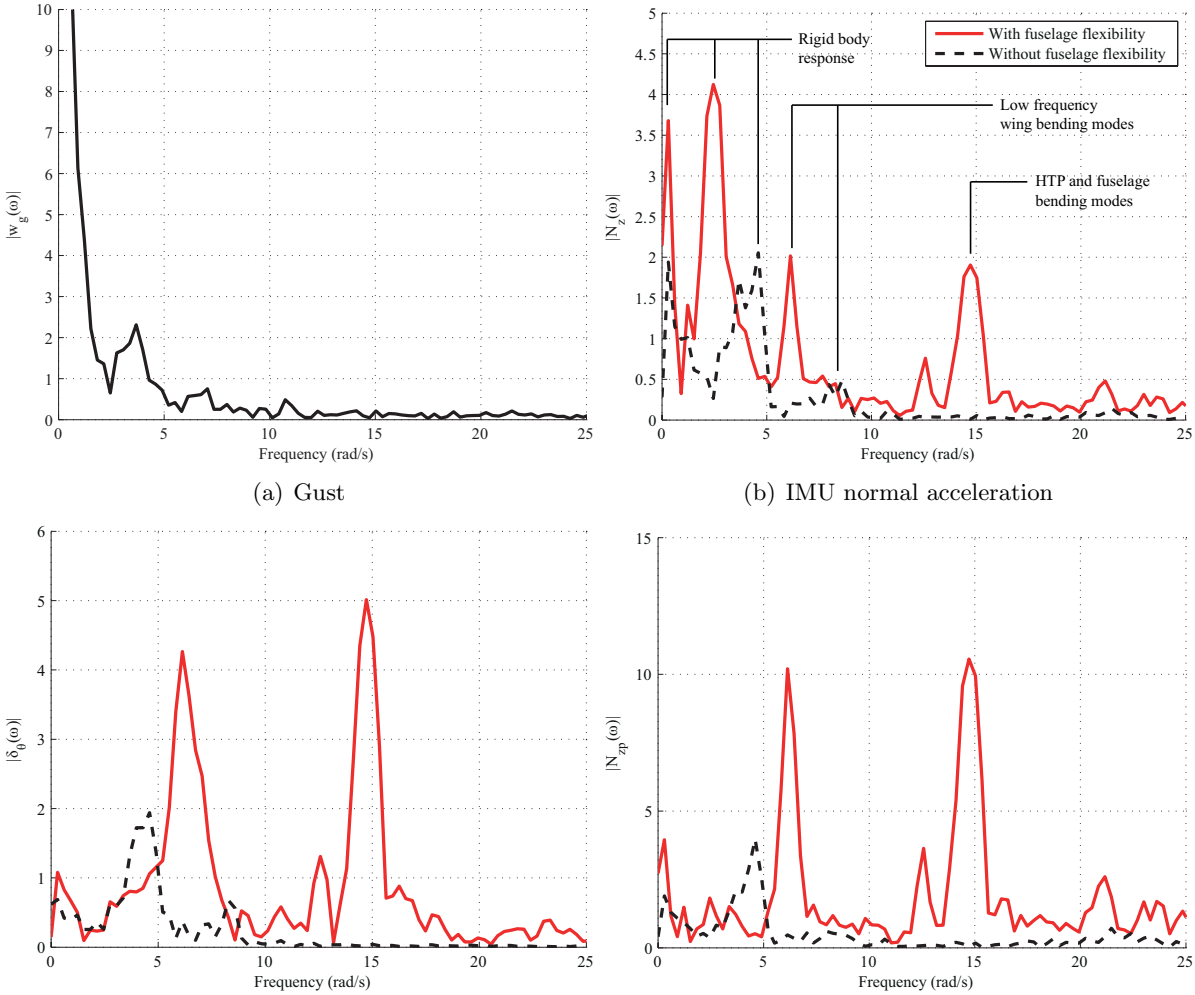

(a) Gust

(b) IMU normal acceleration

(c) Longitudinal stick deflection

(d) Cockpit normal acceleration

Figure 7.26: Frequency spectra for simulations with the aggressive MOCM ($\tau_n = 0.08$).

respectively. The proximity of the maximum wing root torsion to the upper limit load is also a cause for concern.

The impact of manual control action on HTP loads is far more severe due to the same reason mentioned in Section 7.2.6. In this case, the detrimental effects of LAF are also evident; implying that potential weight benefits that LAF offers for the wings must be able to offset the weight increase necessary to strengthen the HTP. However, although these exceedences show extreme adverse effects of manual control and LAF, on the HTP in particular, it should be noted that the envelope derivation process in Chapter 6 only considered a limited set of scenarios. It did not consider failure modes or other special circumstances considered in industrial practice.

The effect of changes in neuromuscular lag on the maximum and minimum internal loads can be deduced simply by comparing respective normal acceleration time histories. These are presented together with the envelope comparisons in Appendix F.

7.4 Conclusions

A brief discussion on the flight envelope points where 47 incidents occurred is presented as a preface to the pilot-model-in-the-loop simulations discussed later in the chapter. This chapter

has effectively brought together the pilot model components developed in Chapters 3 to 5, the Cranfield/Airbus AX-1 flight loads model and the LAF augmented FCS discussed in Chapter 6 within one unified simulation environment. This has in turn allowed the study of effects arising due to interactions between the airframe structural dynamics and manual control characteristics. A pilot's inability to distinguish between the contribution of fuselage flexibility and rigid body dynamics and the consequent adverse effects on airframe loads were investigated through the application of the MOCM and biomechanical models in two case studies: an aileron failure scenario and a gust encounter. Comparisons with DFDR data (courtesy of Airbus UK) were made for the latter case, which showed that the pilot model generated stick deflections are significantly affected by fuselage flexibility. Comparison of internal loads from these simulations with the loads envelopes highlighted that the HTP experiences far higher loads relative to the limit loads when compared to the wing. Even the LAF was found to have a detrimental effect on HTP loads. The reader is referred to Lone and Cooke[119] for a similar analysis investigating differences in manual and autopilot control in scenarios where the aircraft is subjected to continuous turbulence.

The analysis presented in this chapter has demonstrated the application of pilot models and the comparison with the DFDR data showed that the gust encounter was reconstructed reasonably well. More critically however, the need for validation and the difficulties in validating such results simply due to the rarety of such incidents have been highlighted.

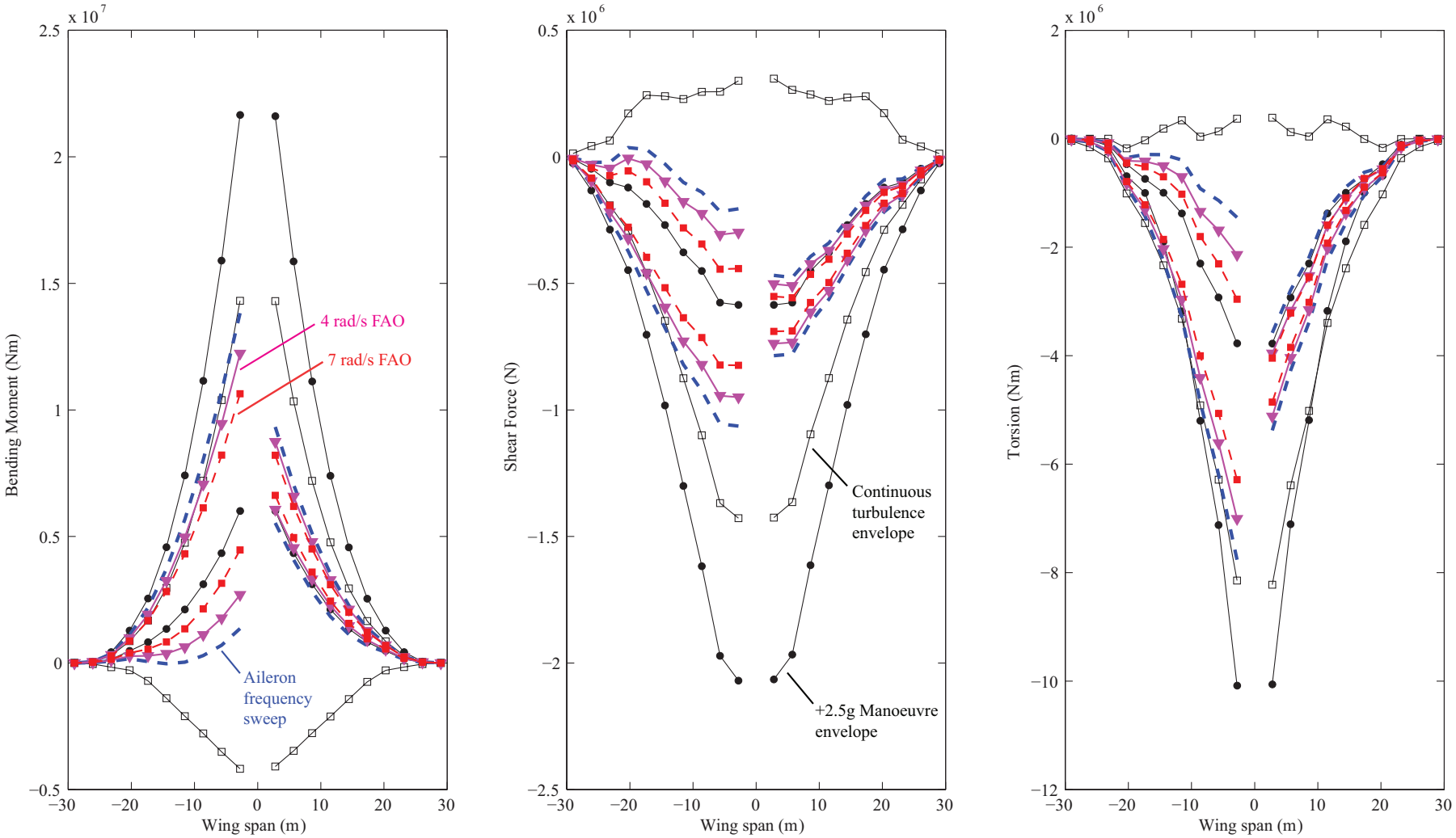

Figure 7.27: Comparison of aileron failure cases with MOCM input with wing loads envelope.

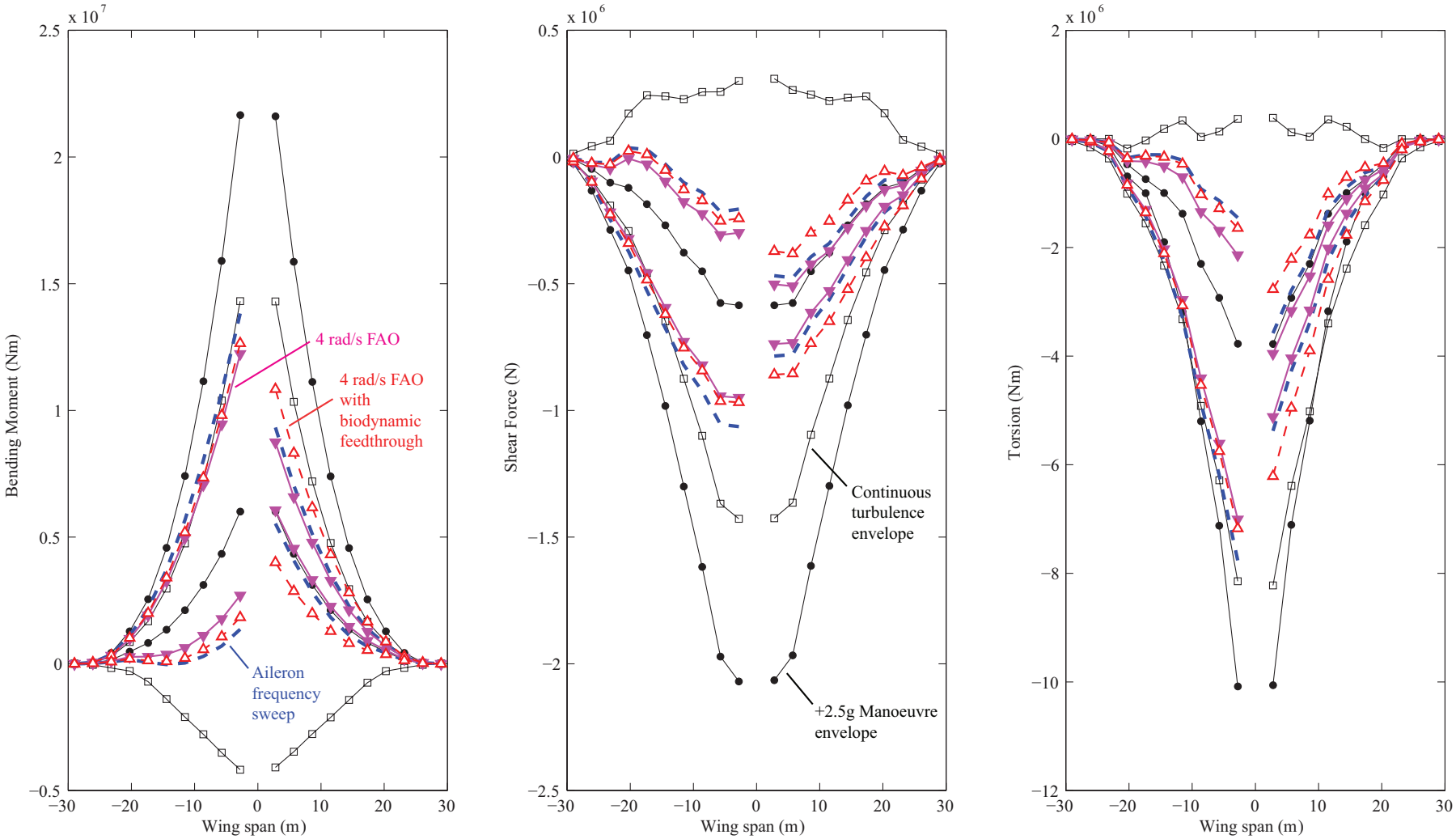

Figure 7.28: Comparison of aileron failure cases with MOCM and biodynamic feedthrough with wing loads envelope.

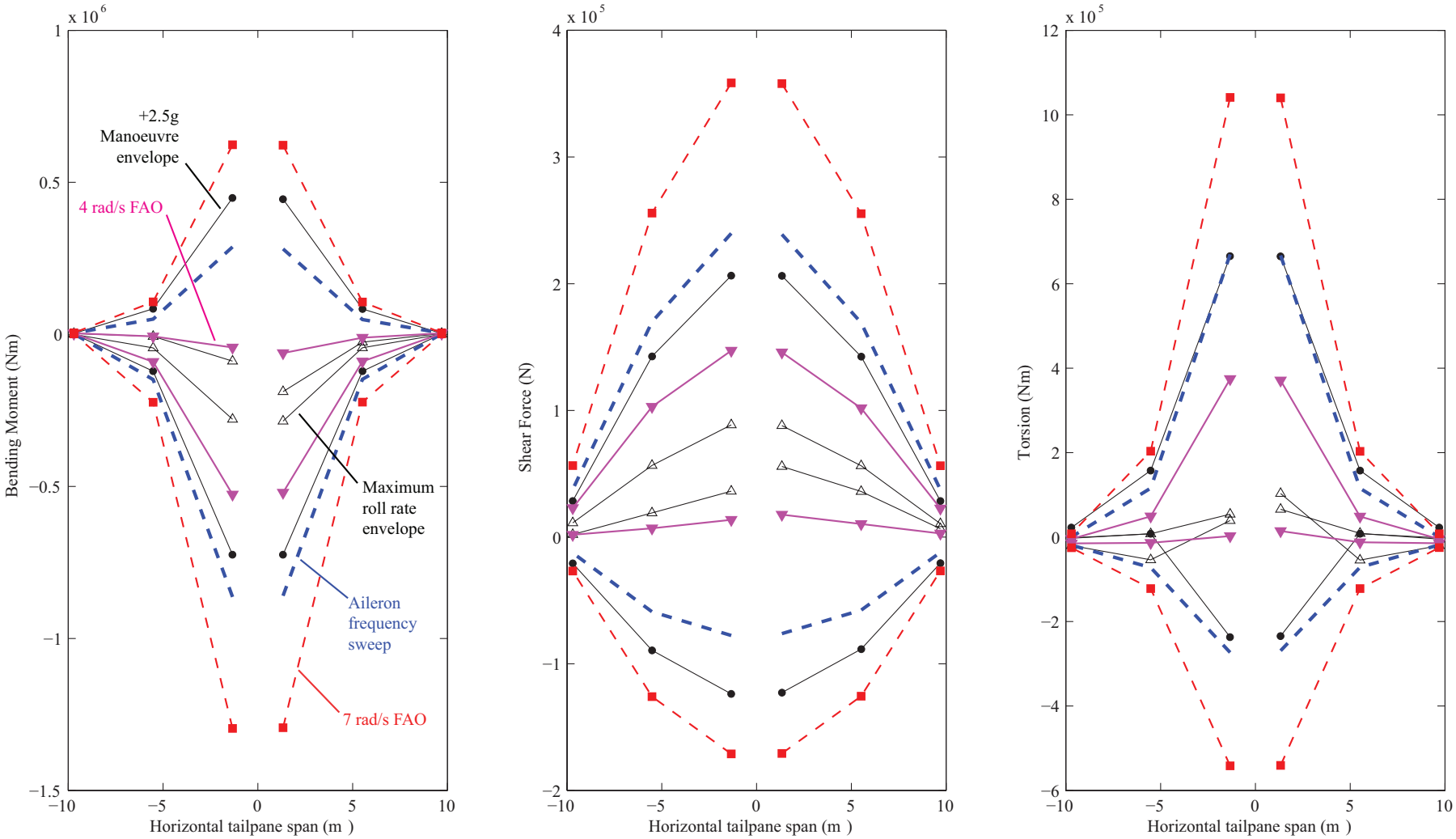

Figure 7.29: Comparison of aileron failure cases with MOCM input with HTP loads envelope.

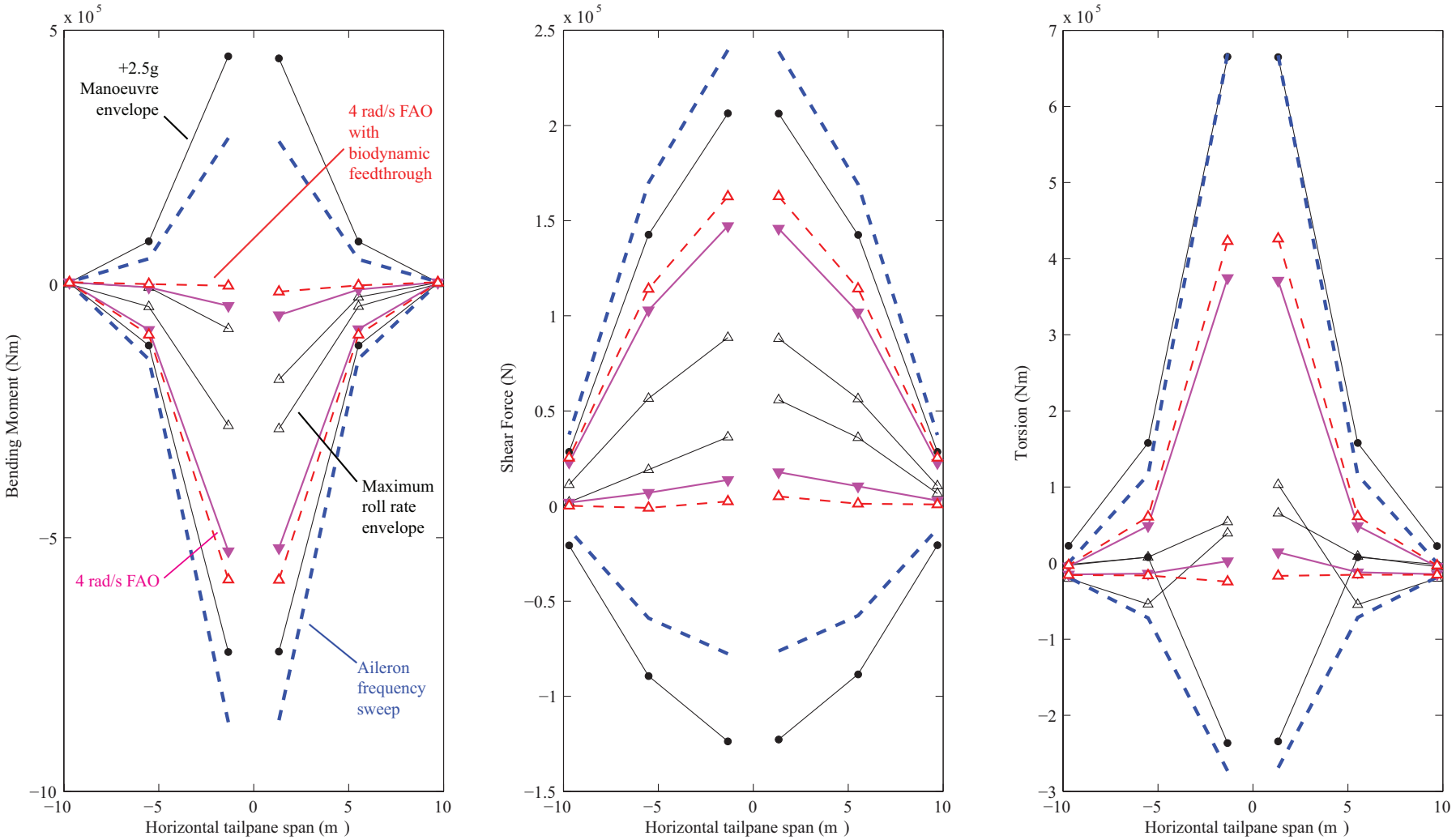

Figure 7.30: Comparison of aileron failure cases with MOCM and biodynamic feedthrough with HTP loads envelope.

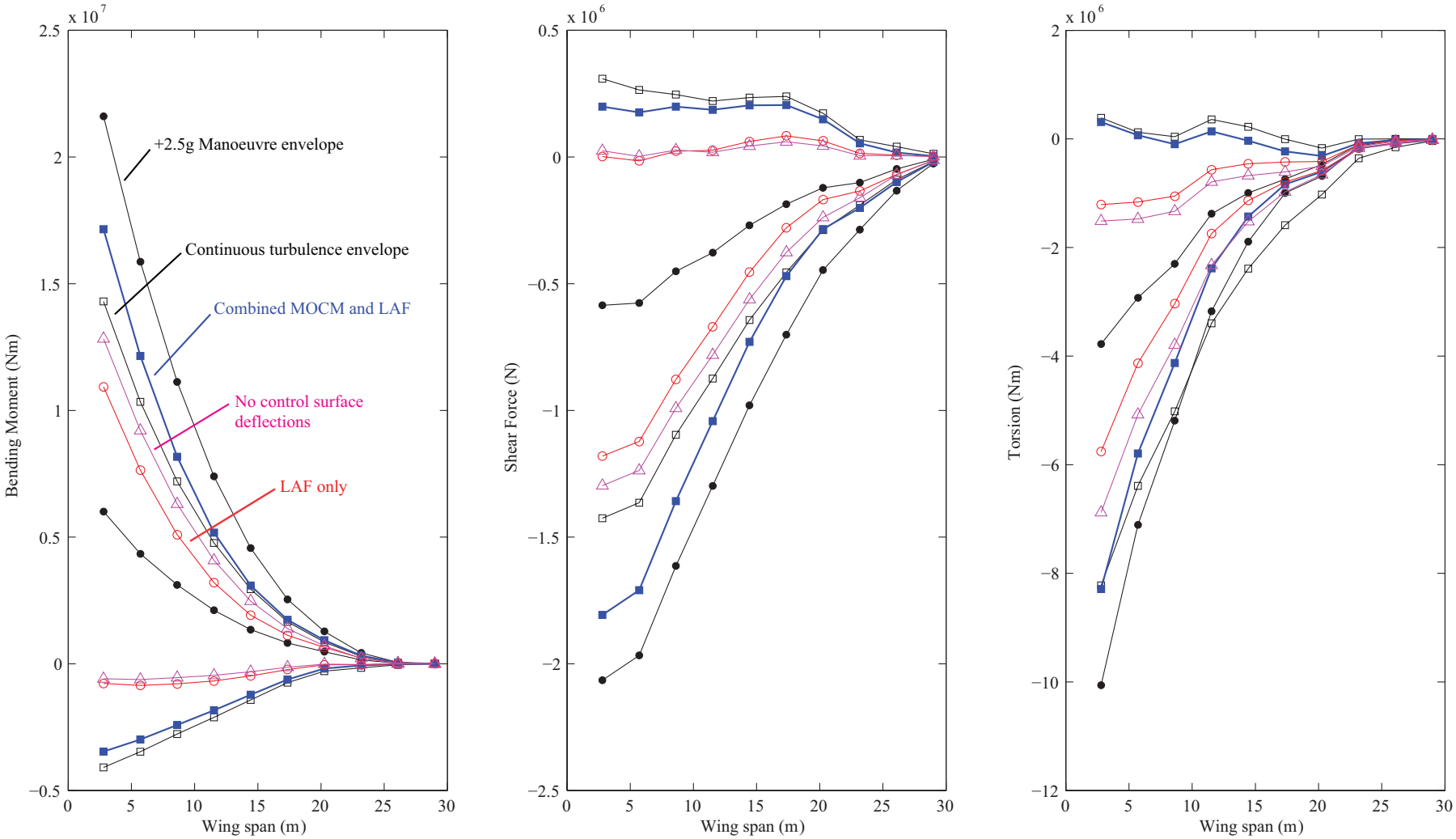

Figure 7.31: Wing loads envelope comparison of maximum and minimum internal loads from gust encounter simulations.

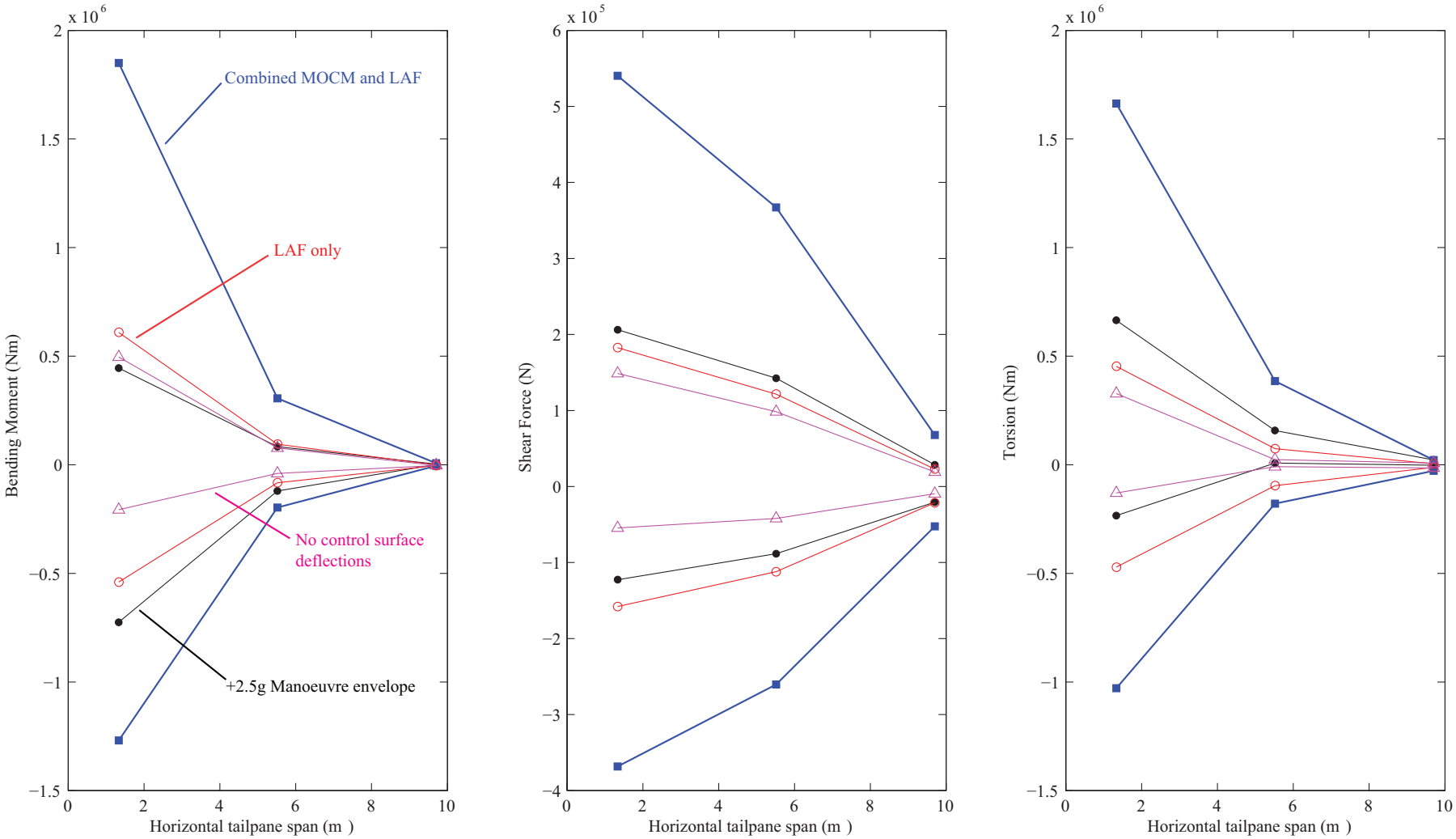

Figure 7.32: HTP loads envelope comparison of maximum and minimum internal loads from gust encounter simulations.

This page is intentionally left blank.

CHAPTER 8

Conclusions and future work

The effects of airframe flexibility on aircraft flight dynamic characteristics were acknowledged and investigated even before the advantages of large slender configurations were discovered. The progress made in the development of lightweight materials together with the adoption of aircraft design optimisation processes (that extract every possible ounce of efficiency) have allowed the realisation of ever larger and lighter airframes. The reduced structural stiffness and damping mean that aeroservoelastic effects have a far bigger impact on stability and control; which in turn affects handling qualities. Moreover, this encroachment of structural dynamics into the frequency range of the pilot's manual control actions can cause interactions that may be initiated by failures or atmospheric disturbances, but result in parts of the airframe exceeding the design limit loads. Therefore, the aim of the work presented in this thesis was to develop a pilot model suitable for the investigation of these interactions from the perspective of large aircraft flight loads.

So far, each chapter within this thesis came to a close by presenting specific conclusions regarding the work discussed within it. The purpose of this chapter is to firstly, remind the reader of some of the key conclusions and secondly, discuss their implications in the wider context of the aims of this research. Areas of future work and the key contributions to knowledge are also presented together with a list of how the results from this research effort were disseminated.

8.1 Summary of findings

A review of pilot modelling aspects thought to be necessary for modelling manual control dynamics of large civil aircraft pilots was presented in Chapter 2. It found that the most significant limitation of the state-of-the-art control-theoretic models is the reliance on experimental data for parameterisation. This limitation together with the fact that the data is typically obtained from a laboratory environment is the underlying cause for the limited application of pilot models for predictive purposes. It was also found that only models based on modern control theory have the potential for minimising the necessary engineering intuition and experience required for application to multi-axis tasks.

Based on the findings of the review, an experimental approach taking advantage of the negligible latencies achievable on current personal computer platforms was adopted. Manual control dynamics of pilots when performing compensatory and tracking tasks were studied. The SISO

pilot models that were proposed and parameterised showed variations of up to 14.6 dB (at the resonant frequency) could exist in the pilot's linear dynamics alone. Although inter-subject variations in the remnant PDFs only highlighted the difficulties in accurately modelling pilot dynamics, these provide best and worst case remnant models for future simulation work. The effects of nonlinear FCS components were found to affect demanding tasks during which subjects displayed nonlinear manual control dynamics, mainly crossover regression.

Given the advantages of pilot models based on modern control theory, the MOCM algorithm was explored. It was shown to provide the capability to treat manual control in a MIMO framework, whilst also allowing an explicit definition of flight dynamics expected by the pilot via an aircraft model. The model was found to provide reasonable agreement with experimental data obtained from a series of multi-axis manual control experiments. A parameter variation study found that the neuromuscular lag parameter effectively determined the gains introduced by the MOCM into the PVS and thus, could be used as a parameter to specify pilot aggression.

The verification of the adopted sensory model together with the development and parameterisation of a decoupled discrete biomechanical models was presented in Chapter 5. The sensory model coupled visual and vestibular perception of angular and translational self-motion and provided the capability to simulate SD scenarios such as spiral divergence. The discrete biomechanical modelling approach was selected to allow insight into potential sources of biodynamic feedthrough. Biodynamic response to longitudinal and lateral accelerations were decoupled. In both cases, the torso was represented by two dimensional planar models and coupled with a transfer function representation of the arm. The model is only capable of reproducing the transmissibilities observed in the experimental setups because of the the limited amount of suitable experimental data available for model parameterisation.

The pilot model components were integrated with the augmented Cranfield University/Airbus AX-1 model; for which internal loads envelopes were derived using book-case manoeuvres and CT analysis. The unified PVS simulation environment then allowed the study of interactions between manual control and airframe flexibility via the analysis of two case studies: a soft aileron failure scenario and a gust encounter. Comparison with DFDR data showed that the gust encounter was reconstructed reasonably well. However, the critical need for validation and difficulties in validating these results simply due to the rarity of such incidents, were highlighted. Comparison of internal loads from these simulations with the loads envelopes highlighted that the HTP experiences far higher loads relative to the limit loads when compared to the wing.

A motivation behind this research was to develop a capability to reconstruct incidents such as gust encounters where pilot control actions were found to exacerbate airframe loads. A brief discussion on the potential causes for such incidents was presented in the context of 47 incidents that the author was granted limited access to during his placement at Airbus UK. Majority of the incidents could not be analysed with the pilot model because of the limitations of the AX-1 model together with the lack of complete data sets available for the reconstruction of manual control driven incidents.

The methods used in this thesis show how preliminary studies with pilot models can provide insight not only into PVS performance but also into airframe loads under manual control. These provide fast and economical ways to evaluate flight control and active loads control strategies prior to piloted evaluations in flight simulators or flight tests.

8.2 Contributions to knowledge

The main contribution has been the demonstration of the applicability (and the involved difficulties) of pilot models to the simulation of complex scenarios involved highly augmented flexible

aircraft subjected to extreme atmospheric disturbances.[1]

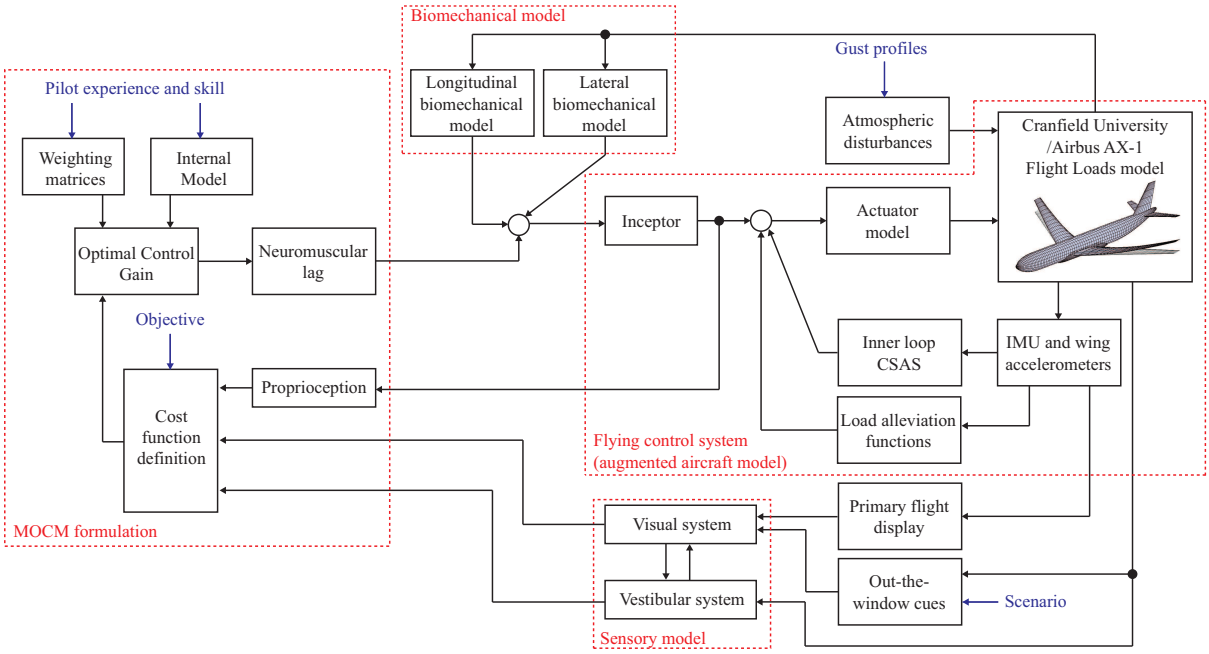

Figure 8.1: The PVS developed to study airframe flexibility effects on manual control.

Figure 8.1 is effectively a reproduction of the PVS shown in Figure 1.1 with additions and modifications to the key areas that were developed as part of this study. It also provides an overview of the pilot-model-in-the-loop simulations done in Chapter 7. The following lists the key areas of development:

1. Modelling of pilot control action and higher brain functions with the MOCM algorithm and the definition of the manual control task together with the pilot's skill and experience via the cost function and internal model respectively.

2. Treatment of the neuromuscular system and proprioception within the MOCM and the development of a decoupled biomechanics model.

3. Inclusion of a sensory model capable of reproducing interactions between the visual and vestibular sensory modalities.

4. Integration of a LAF augmented FCS with the Cranfield University/Airbus AX-1 flight loads aircraft model.

This research has also shown that desktop based manual control experiments are capable of giving valuable insight into manual control dynamics. Upper and lower bounds due to inter-subject variations for SISO pilot models were given; both for linear and remnant components.

A methodology for the implementation of the MOCM for pilot-model-in-the-loop simulation of large flexible aircraft is another contribution.[2] The process developed to generate the flight loads envelopes for the AX-1 model together with the loads envelopes themselves allow other researchers to focus on their area of interest and less on the loads envelope generation process.

[1]The gust profiles given in Appendix F also contribute towards more realistic simulations of extreme gust encounters in academia.

[2]This work has also highlighted the need for transparency between industry and academia if such applications of pilot models, especially for predictive purposes, are to be validated.

8.3 Recommendations for further work

The work done in this thesis has focused on a very small aspect of modern piloted flight and shown the complexities involved in modelling manual control of large flexible aircraft. Even within the limited scope, a number of assumptions were made and the main recommendation would be to improve the simulation fidelity by addressing these assumptions. The key areas of further work are as follows:

1. The pilot has been assumed to base his/her linear control strategy only on the perceived aircraft attitude, rates of change of attitude and normal acceleration. MOCM cost function that represent the importance given by the pilot to each of these cues require validation either via motion-based simulator trials or in-flight manual control experiments.

2. Inter-subject variations given by pilot model parameter bounds in Chapter 2 provide an indication of the level of uncertainty introduced by the pilot into the PVS dynamics. These can be adopted for a robust FCS design process that accounts for inter-subject variations and simulation of critical scenarios as shown by Lone et al[160].

3. Simulations in Chapter 7 assumed the aircraft to be in manual control prior to the incident, which is rarely the case in cruise conditions. Therefore, the cue (most likely to be the time derivative of normal acceleration, also known as jerk) used by the pilot to initiate manual control needs to be identified and investigated. This will also require the use of motion-based simulators or flight tests. Work in this area can then be linked to nonlinear manual control theory which has seen little development since the early 1990s.

4. Nonlinearities in human biodynamic response to vibrations and low frequency accelerations are only beginning to be understood and nonlinear biodynamic feedthrough models suitable for aerospace applications are yet to be proposed. The linear decoupled representation developed in this thesis is a starting point for the development of such models.

5. The pilot-model-in-the-loop simulations were limited by the flight envelope of the AX-1 model. Considering the fact that most incidents were found to occur in cruise conditions and resulted in the deployment of secondary controls surfaces, further development of this flight loads model is highly necessary.

6. Most critically however, a pilot model parameter identification process that identifies MOCM parameters for pilot action during actual incidents needs to be undertaken so that the simulations presented in Chapter 7 can be validated further and parameter ranges can be prescribed for future implementations. This will require sifting through the industry database of longitudinal and lateral incidents for relevant DFDR data.

Pilot modelling techniques will indeed improve along with with developments in manual control theory and aircraft handling qualities research. These models can play a more significant role in the processes used in aircraft design and optimisation. Also, as current and future aircraft designs demand higher levels of integration between the engineering disciplines to achieve efficiency and safety goals, tools for handling qualities studies that can be used at earlier design stages are needed.

8.4 Dissemination of results

8.4.1 Presentations at technical workshops, seminars and short courses

Pilot modelling in aerospace
Cranfield University Control Seminar
Cranfield University, Cranfield, December 2009

Modelling and simulation of large aircraft
Airbus-Stirling Dynamics DiPaRT Meeting
Advanced Simulation Research Centre, Bristol, November 2010

Simulation of large aircraft and applications of manual control theory
Foundation course in flight dynamics
Cranfield University, Cranfield, May 2011

Effects of airframe flexibility on manual control
Beijing University of Aeronautics and Astronautics, Beijing, July 2011

Pilot models to study impact of active load alleviation on handling qualities
Airbus-Stirling Dynamics DiPaRT Meeting
Advanced Simulation Research Centre, Bristol, December 2012

8.4.2 Technical reports

Effects of nonlinear flight control system elements on aircraft manual control
Cranfield College of Aeronautics Report No. CU/COA-2011/01
This report presents the experimental method and results from a series of desktop simulation tests designed to investigate manual control characteristics of young and relatively inexperienced civil pilots (24 years average age and 66 hours flight experience). Subjects were asked to perform tasks during which they had to establish longitudinal control through pitch attitude shown on a primary flight display. A linear aircraft model coupled with nonlinear flight control system was used to produce realistic vehicle dynamics. Increased encroachment into nonlinear command gearing was found to make aggressive subjects resort to high levels of crossover regression. The combined effects of rate-limiting and nonlinear command gearing was observed only for demanding tasks during which over-control was a typical feature. The classical precision and bimodal models were used for an in-depth study of pilot dynamics observed during compensatory tasks. Model parameters were found through the definition of a constrained nonlinear optimisation problem. A single feedforward equalisation element was used for tracking tasks. It was found that subjects developed similar low frequency feedforward equalisations, whilst large inter-subject variations exist for high frequency equalisations. The resulting models also provided some insight into the Neal-Smith and Bandwidth handling qualities criteria. Actuator rate-limiting could not be directly correlated to any of the pilot model parameters.

A MATLAB/Simulink suite for the real-time flight simulation of large aircraft
Cranfield College of Aeronautics Report No. CU/COA-2012/01
This report is an introduction to a quasi-linear parameter varying Boeing 747 model that has been used as a teaching and foundational level research tool within the Dynamics, Simulation and Control Group since 2010. The model is based on data provided by Heffley and Jewell in NASA-CR-2144 and has been developed in a MATLAB/Simulink environment. The equations of motion have been modified to include Mach number and altitude as scheduling parameters for the stability and control derivatives, and also to include a degree of nonlinearity and coupling

between the longitudinal and lateral-directional axes. A flight control system consisting of a command and stability augmentation system and an autopilot suite are also detailed. In addition a primary flight display module applicable to human-in-the-loop simulation has been implemented. Both these features are briefly described in this report.

8.4.3 Conference papers

Review of pilot modelling techniques
48th AIAA Aerospace Sciences Meeting, January 2010
As aircraft increase in size, unsteady aerodynamics and aeroelasticity pose new handling qualities challenges. These require a greater understanding of the pilot-vehicle system as a whole. The level of interaction between the flying control system and the pilot increases as structural mode frequencies enter into the manual control frequency range. Therefore, accurate physiological and control-theoretic models of the pilot are crucial. Interactions range from conscious changes in pilot gain and equalisation to unconscious biodynamic feedthrough of structural modes. So far, use of theoretical pilot models has been an effective way of gaining handling qualities insight. Pilot modelling can be split into three areas: human sensory modelling, biomechanical modelling and control-theoretic modelling. To date, a review that brings together these aspects and provides a holistic view of pilot modelling has not been presented. This paper aims to address this literature gap and presents a review of the state-of-the-art.

Development of a pilot model suitable for the simulation of large aircraft
27th International Congress of the Aeronautical Sciences 2010, September 2010
Effects of aeroservoelasticity on the manual control of large civil aircraft are investigated through a pilot modelling approach based on the modified optimal control model. A synopsis of modelling techniques is presented, followed by the description of the adopted technique. A simulation environment suitable for investigating pilot-vehicle dynamics in the longitudinal axis has been developed. The derivation of the pilot model was based on limiting the bandwidth. This approach showed that the pilot-vehicle system satisfied the crossover law between 3rad/s to 10rad/s for normal acceleration response. It was found that the pilot model and the low frequency tailplane bending mode introduced a resonant peak in the pilot-vehicle frequency response that may be a cause for concern in high gain scenarios. Gust response simulations highlighted the contribution of fuselage bending mode on pilot perceived normal acceleration.

Application of pilot models to study trajectory based manoeuvres
AIAA Modeling and Simulation Technologies Conference 2012, August 2012
A simulation environment that combines a trajectory generation scheme, an aeroelastic aircraft model and a pilot model is used to develop a methodology to study worst-case airframe loadings during trajectory-based avoidance manoeuvres. Such manoeuvres are defined as resolutions with specified three dimensional position and time characterised by simultaneous changes in altitude, heading and speed. These are obtained by imposing different dynamic constraints within a trajectory generation scheme. The expected contribution of this paper lies in the novel methodology and the airframe loading analysis, resulting from simulating the aeroelastic model coupled with the effect of pilots and wind disturbance. Loads during these manoeuvres are compared with a stochastically derived loads envelope. It is envisioned that such an analysis can be fed back to the design process of the trajectory generation scheme to assure and enhance the operational safety for trajectory-based avoidance manoeuvre.

8.4.4 Journal articles

Pilot-model-in-the-loop simulation environment to study large aircraft dynamics
Proceedings of the IMechE, Part G: Journal of Aerospace Engineering, March 2012
Effects of aeroservoelasticity on the manual control of large aircraft are investigated through a pilot modelling approach based on the modified optimal control model. A synopsis of modelling techniques is presented followed by the description of the adopted method. A simulation environment suitable for investigating pilot-vehicle dynamics in the longitudinal axis has been developed which couples an aeroelastic model of a large transport aircraft with the modified optimal control pilot model. The pilot model parameter selection was based on limiting the bandwidth. A comparison between a conventionally designed height hold autopilot and the pilot model control in continuous turbulence is made to demonstrate this simulation capability. It was found that a lack of vertical acceleration attenuation by the autopilot may be a reason behind the tendency of pilots to switch to manual control in severe turbulence.

Towards understanding effects of non-linear flight control system elements on inexperienced pilots
The Aeronautical Journal, November 2012
This note presents the experimental method and results from a series of desktop simulation tests designed to investigate the manual control characteristics of relatively inexperienced civil pilots; with an average age and experience of 24 years and 66 hours respectively. Increased encroachment into non-linear command gearing was found to make aggressive subjects resort to high levels of crossover regression. The combined effects of rate-limiting and non-linear command gearing was observed only for demanding tasks during which over-control was a typical feature.

This page is intentionally left blank.

References

[1] G. Weltz and K. Shweyk. Application of new and standard pilot-induced oscillation (PIO) analysis methods to flight test data of the C-17 transport aircraft. In *AIAA Atmospheric Flight Mechanics Conference and Exhibit, Hilton Head, South Carolina, Aug. 20-23, 2007*, number AIAA-2007-6387, 2007.

[2] W.J. Norton. Aeroelastic pilot-in-the-loop oscillations. In *Active Control Technology: Applications and Lessons Learned, AGARD, Turin, Italy, May 1994*, 1994.

[3] P. Grant and J. Schroeder. Modeling pilot control behaviorfor flight simulator design and assessment. In *AIAA Modeling and Simulation Technologies Conference, Toronto, Ontario, Aug. 2-5, 2010*, 2010.

[4] P.M.T. Zaal, D.M. Pool, and M.M. van Paassen. Multimodal pilot control behaviour in combined target-following and disturbance rejection tasks. *Journal of Guidance, Control and Dynamics*, 32:1418–1428, 2009.

[5] D.T. McRuer. Development of pilot-in-the-loop analysis. *Journal of Aircraft*, 10:515–524, 1973.

[6] National Research Council. *Aviation Safety and Pilot Control - Understanding and Preventing Unfavorable Pilot-Vehicle Interactions*. National Academy Press, 1997.

[7] B.P. Lee. Recent experience in flight testing for pilot induced oscillations (PIO) on transport aircraft. In *ICAS 2000 Congress*, pages 691.1 – 691.8. International Council of Aeronautical Sciences, 2000.

[8] A. Reinke. Evaluation of wake encounter flight tests in support of defining safe A380 separations. Presentation at the 4th Major Workshop of WakeNet3-Europe, February 2012.

[9] S.P. Andrews. *Modelling and simulation of flexible aircraft: Handling qualities with active loads control*. PhD thesis, Department of Aerospace Engineering, School of Engineering, Cranfield University, 2011.

[10] H. Markram. The human brain project. *Scientific American*, 306:50:56, 2012.

[11] Sebastian Seung. *Connectome: How the Brain's Wiring Makes Us Who We Are*. Houghton Mifflin Harcourt Trade, 2012.

[12] C. Bartlett. *Air Crashes and Miracle Landings Sixty Narratives (How, When...and Most Importanty Why)*. OpenHatch Books, 2010.

[13] P.S. Tsang and M.A. Vidulich. *Principles and practice in aviation psychology*. Lawrence Erlbaum Associtaes Inc. Publishers, 2003.

[14] F.H. Previc and W.R. Ercoline. *Spatial disorientation in aviation*. American Istitute of Aeronautics and Astronautics Inc., 2004.

[15] R.A. Hess. Obtaining multi-loop pursuit-control pilot models from computer simulation. In *45th AIAA Aerospace Sciences Meeting and Exhibit*, number AIAA-2007-247 in AIAA, Reno, Nevada, January 2007. AIAA.

[16] D.L. Kleinman, S. Baron, and W.H. Levison. An optimal control model of human response Part I: Theory and validation. *Automatica*, 6:357–369, 1970.

[17] R. Hess. Multi-axis pilot modeling: Models and methods for wake vortex encounter simulations. Presentation at Technical University of Berlin, June 2010.

[18] ADS-33E-PRF, Aeronautical design standard performance specification: Handling qualities requirements for military rotorcraft, 2000.

[19] J.M. Naish. Control information in visual flight. In *Seventh annual conference on manual control*, pages 167–176, 1971.

[20] D.K. Schmidt and A.B. Silk. Modeling human perception and estimation of kinematic responses during aicraft landing. In *AIAA Guidance, Navigation and Control Conference, Minneapolis, MN, Aug 15-17, 1988*, number AIAA-1988-4186, pages 1117–1126, 1988.

[21] David Allerton. *Principles of Flight Simulation*. John Wiley & Sons Inc., 2009.

[22] D.T. McRuer and E.S. Krendel. Mathematical models of human pilot behaviour. AGARDograph AGARD-AG-188, Advisory Group for Aerospace Research & Development, January 1974.

[23] H.M. Heerspink, W.R. Berkouwer, O. Stroosma, M.M. van Paassen, M. Mulder, and J.A. Mulder. Evaluation of vestibular thresholds for motion detection in the simona research simulator. In *AIAA Modelling and Simulation Technologies Conference and Exhibit,15-18 August 2005, San Francisco, California*, number AIAA 2005-6502, 2005.

[24] R.A. Hess. A unified theory for aircraft handling qualities and adverse aircraft-pilot coupling. Technical Report AIAA 97-0454, AIAA, Reno, Nevada, January 1997.

[25] R.J. Telban and F.M. Cardullo. An integrated model of human motion perception with visual-vestibular interaction. In *AIAA Modeling and Simulation Technologies Conference and Exhibit*, 2001.

[26] David L. Raney, E. Bruce Jackson, and Carey S. Buttrill. Simulation study of impact of aeroelastic characteristics on flying qualities of a high speed civil transport. Technical report, NASA, 2002.

[27] J. Serafini, M. Gennaretti, P. Masarati, G. Quaranta, and O. Dieterich. Aeroelastic and biodynamic modelling for stability analysis of rotorcraft-pilot coupling phenomena. In *34th European Rotorcraft Forum 2008*, 2008.

[28] R.D. Banks, J.W. Brinkley, R. Allnutt, and R.M. Harding. *Fundamentals of Aerospace Medicine*. Lippincott Williams and Wilkins, 2008.

[29] S. Kitazaki and M.J. Griffin. A modal analysis of whole-body vertical vibration, using a finite element model of the human body. *Journal of Sound and Vibration*, 200:83–103, 1997.

[30] N.J. Mansfield. *Human response to vibration*. CRC Press, 2005.

[31] Y. Matsumoto and M.J. Griffin. Modelling the dynamic mechanisms associated with the principal resonance of the seated human body. *Clinical Biomechanics*, 16:31–44, 2001.

[32] L.A. Wood, C.W. Suggs, and C.F. Abrams. Hand-arm vibration Part III: A distributed parameter dynamic model of the human hand-arm system. *Journal of Sound and Vibration*, 57:157–169, 1978.

[33] C.M. Harris and A.G. Piersol, editors. *Harris' Shock and Vibration Handbook*. McGraw-Hill, fifth edition, 2002.

[34] T.E. Coe, J.T. Xing, R.A. Shenoi, and D. Taunton. A simplified 3-D human body-seat interaction model and its applications to vibration isolation design of high-speed marine craft. *Ocean Engineering*, 2009.

[35] M.R. Sirouspour and S.E. Salcudean. Suppressing operator-induced oscillations in manual control systems with movable bases. *IEEE Transaction on Control Systems Technology*, 11:448–459, 2003.

[36] W.H. Levison and C.B. Harrah. Biomechanical and performance response of man in six different directional axis vibration environments. Technical Report AMRL-TR-77-71, Aerospace Medical Research Laboratory, 1977.

[37] M.J. Griffin. The validation of biodynamic models. *Clinical Biomechanics*, 16:81–92, 2001.

[38] G. Höhne. A biomechanical pilot model for prediction of roll ratcheting. In *AIAA Atmospheric Flight Mechanics Conference*, 1999.

[39] R. Koehler. A unified approach for roll ratcheting analysis. *Journal of Guidance, Control and Dynamics*, 22:718–720, 1999.

[40] G. Höhne. Computer aided development of biomechanical pilot models. *Aerospace Sciences Technology*, 4:57–69, 2000.

[41] G. Höhne. Evaluation of the LATHOS database using a biomechanical pilot model. Technical report, American Institute of Aeronautics and Astronautics, 2000.

[42] Martin Hanel. Discussion of some typical handling qualities issues encountered by industry during aircraft development : Roll ratchet & flight path display dynamics. Presentation to EADS Military Air Systems, November 2008.

[43] Joost Venrooij, Mark Mulder, Marinus M. van Paassen, Max Mulder, and David A. Abbink. Relating biodynamic feedthrough to neuromuscular admittance. In *Proceedings of the 2009 IEEE International Conference on Systems, Man, and Cybernetics San Antonio, TX, USA - October 2009*, 2009.

[44] S. Sovenyi and R.B. Gillespie. Cancellation of biodynamic feedthrough in vehicle control tasks. *IEEE Transactions on Control Systems Technology*, 15:1018–1029, 2007.

[45] R.B. Gillespie and Sövenyi. Model-based cancellation of biodynamic feedthrough using force-reflecting joystick. *Journal of Dynamic Systems, Measurement, and Control*, 128:94–103, 2006.

[46] Peter M. Thompson, David H.Klyde, and Martin J. Brenner. Wavelet-based time-varying human operator models. In *AIAA Atmospheric Flight Mechanics, Conference and Exhibit, 6-9 August 2001 Montreal, Canada*, number AIAA-2001-4009, 2001.

[47] E.N. Bachelder and D.H. Klyde. Wavelet-based analysis of roll ratchet using a flight test database. In *Atmospheric Flight Mechanics Conference, Austin, Texas,11-14 August 2003*, 2003.

[48] David L. Raney, E. Bruce Jackson, Carey S. Buttrill, and William M. Adams. The impact of structural vibration on flying qualities of a supersonic transport. In *AIAA Atmospheric Flight Mechanics Conference, 6-9 August 2001, Montreal, Canada*, 2001.

[49] M.R. Waszak and D.K. Schmidt. Flight dynamics of aeroelastic vehicles. *Journal of Aircraft*, 25:563:571, 1988.

[50] Anonymous. *Mechanical vibration and shock - Evaluation of human exposure to whole-body vibration.* British Standard, International Organization for Standardization.

[51] International Organization for Standardization. *Railway applications - Ride comfort for passengers - Measurement and evaluation.*

[52] N.J. Mansfield and M.J. Griffin. Non-linearities in apparent mass and transmissibility during exposure to whole-body vertical vibration. *Journal of Biomechanics*, 33:933–941, 2000.

[53] J. Yang, R.T. Marler, H. Kim, J.S. Arora, and K. Abdel-Malek. Multi-objective optimization for upper body posture prediction. In *10th AIAA/ISSMO Multidisciplinary Analysis and Optimization Conference, 30 August-1 September 2004, New York*, 2004.

[54] D. McRuer, R. Magdaleno, and G. Moor. A neuromuscular actuation system model. Technical report, NASA, 1967.

[55] D. McRuer, I. Ashkenas, and D. Graham. *Aircraft Dynamics and Automatic Control.* Princeton University Press, 1973.

[56] C. Schauf, D. Moffett, and S. Moffett. *Human Physiology.* Times Mirror/Mosby Publishing, 1990.

[57] R.E. Magdaleno and D.T. McRuer. Experimental validation and analytical elaboration for models of the pilot's neuromuscular subsystem in tracking tasks. Technical Report NASA CR 1757, National Aeronautics and Space Administrations, 1971.

[58] Younggun Cho and Yong-San Yoon. Biomechanical model of human on seat with backrest for evaluating ride quality. *International Journal of Industrial Ergonomics*, 27:331–345, 2001.

[59] D.T. McRuer, D. Graham, and E.S. Krendel. Human pilot dynamics in compensatory systems: Theory, models, and experiments with controlled element and forcing function variations. Technical Report AFFDL-TR-65-15, Air Force Flight Dynamics Laboratory, 1965.

[60] A. Tustin. An investigation of the operator's response in manual control of a power driven gun. C.S. Memorandum 169, Metropolitan-Vickers Electrical Co., August 1944.

[61] D.T. McRuer and H.R. Jex. A review of quasi-linear pilot models. *IEEE Transactions on Human Factors in Electronics*, HFE-8(3):231–249, September 1967.

[62] T.P. Neal and R.E. Smith. An in-flight investigation to develop system design criterea for fighter airplanes. Technical Report AFFDL-TR-70-74, Flight Dynamics Laboratory, Wright Patterson AFB, 1970.

[63] T. Neal and R. Smith. A flying qualities criterion for the design of fighter flight control system. *Journal of Aircraft*, 8(10):803–809, October 1971.

[64] R.E. Bailey and T.J. Bidlack. Unified pilot-induced oscillation theory Volume IV: Time-domain Neal-Smith criterion. Technical report, Wright Laboratory, Wright-Patterson Air Force Base, 1995.

[65] L.A. Foringer and D.B. Leggett. An analysis of the time-domain Neal-Smith criterion. In *AIAA Atmospheric Flight Mechanics Conference and Exhibit, Boston, MA, Aug. 10-12*, number AIAA-98-4250, 1998.

[66] F.M. Cardullo, K.B. Zaychik, and G. George. A conspectus on operator modeling: Past, present and future. In *AIAA Modeling and Simulation Conference and Exhibit*, number AIAA-2006-6625, Keystone, Colorado, August 2006. AIAA.

[67] R.K. Heffley. Use of a task-pilot-vehicle (TPV) model as a tool for flight simulator math model development. In *AIAA Guidance, Navigation, and Control Conference, 2 - 5 August 2010, Toronto, Ontario Canada*, 2010.

[68] O.H. Gerlach. Developments in mathematical models of human pilot behaviour. *Aeronautical Journal*, July:293:305, 1977.

[69] D.R. Towill. Man-machine interaction in aerospace control systems. *The Radio and Electronic Engineer*, 50:447:458, 1980.

[70] J.C. Gibson. *The Definition, Understanding and Design of Aircraft Handling Qualities*. Delft University Press, 1997.

[71] G. Padfield. The making of helicopter flying qualities: A requirements perspective. *Aeronautical Journal*, 102:409:437, 1998.

[72] P. van den Berg, P.M.T. Zaal, M. Mulder, and M.M. van Paassen. Conducting multimodal pilot model identification - results of a simulator experiment. In *AIAA Modeling and Simulation Technologies Conference and Exhibit, 20 - 23 August 2007, Hilton Head, South Carolina*, 2007.

[73] G.C. Beerens, H.J. Damveld, M. Mulder, and M.M. van Paassen. An investigation into crossover regression and pilot parameter adjustment. In *AIAA Modeling and Simulation Technologies Conference and Exhibit, 18 - 21 August 2008, Honolulu, Hawaii*, 2008.

[74] P.M.T. Zaal, D.M. Pool, J. de Bruin, M. Mulder, and M.M. van Paassen. Use of pitch and heave motion cues in a pitch control task. *Journal of Guidance, Control and Dynamics*, 32:366–377, 2009.

[75] P.M.T. Zaal, D.M. Pool, Q.P. Chu, M.M. Van Paaseen, M. Mulder, and J.A. Mulder. Modeling human multimodal perception and control using genetic maximum likelihood estimation. *Journal of Guidance, Control and Dynamics*, 32:1089:1099, 2009.

[76] R. Hosman. *Pilot's Perception & Control of Aircraft Motions*. Number 90-407-1384-7. Delft University Press, November 1996.

[77] R.D. Wierenga. An evaluation of a pilot model based on Kalman filtering and optimal control. *IEEE Transactions on Man-Machine Systems*, 10(4):108–117, December 1969.

[78] M. Innocenti. The optimal control pilot model and application. In *AGARD Lecture Series No. 157 Advances in Flying Qualities (AGARD-LS-157)*. North Atlantic Treaty Organisation, 1988.

[79] W.H. Levison. Alternative treatments of attention-sharing within the optimal control model. In *IEEE International Conference on Systems, Man and Cybernetics*, volume 2, pages 744 – 749, Cambridge, MA, November 1989. IEEE.

[80] P.M. Thompson and D.T. McRuer. Comparison of the human optimal control and crossover models. In *AIAA Guidance, Navigation and Control Conference*, number AIAA-88-4183-CP, Minneapolis, Minnesota, August 1988. AIAA.

[81] J.B. Davidson and D.K. Schmidt. Modified optimal control pilot model for computer-aided design and analysis. Technical Memorandum 4384, NASA, Langley Research Center, October 1992.

[82] M. Anderson and D. Doman. Fixed order optimal pilot models. In *AIAA Guidance, Navigation and Control Conference*, number AIAA-96-3871, July 1996.

[83] D.K. Schmidt. Pilot modeling and closed-loop analysis of flexible aircraft in the pitch tracking task. *Journal of Guidance, Control and Dynamics*, 8(1):56, Jan-Feb 1985.

[84] D.B. Doman. *Projection Methods for Order Reduction of Optimal Human Operator Models*. PhD thesis, Virginia Polytechnic Institute and State University, 1998.

[85] D.B. Doman. Optimal control pilot modeling for resolving Cooper-Harper rating discrepancies. In *AIAA Atmospheric Flight Mechanics Conference and Exhibit, Portland, OR, Aug. 9-11, 1999,*, number AIAA-1999-4091, pages 176–186, 1999.

[86] D.L. Kleinman and S. Baron. The human as an optimal controller and information processor. NASA Contractor Report CR-1151, NASA, September 1968.

[87] R.A. Hess. Prediction of pilot opinion ratings using an optimal pilot model. *Human Factors*, 19:459–475, October 1977.

[88] C.R. Edkins. *The Prediction of Pilot Opinion Ratings Using Optimal and Suboptimal Pilot Models*. PhD thesis, Air Force Institute of Technology, Wright-Patterson Air Force Base, Ohio, 1994. DTIC Report no. AD-278 679.

[89] N. Goto, K. Chatani, and S. Fujita. H-infinity-model of the human pilot controlling unstable aircraft. In *IEEE International Conference on Systems, Man and Cybernetics*, pages 50 – 57, 1995.

[90] R.G. Costello. The surge model of the well-trained human operator in simple manual control. *IEEE Transactions on Man-Machine Systems*, 9:2:9, 1968.

[91] R. Hess. A rationale for human operator pulsive control behavior. *Journal of Guidance and Control*, 2:221:227, 1979.

[92] R.H. Smith. A unifying theory for pilot opinion rating. In *Proceedings of the 12th Annual Conference on Manual Control*, number NASA TM X-73, pages 542–558. NASA, May 1976.

[93] Y. Zeyada and R. Hess. Modeling human pilot cue utilization with applications to simulator fidelity assessment. *Journal of Aircraft*, 37:588:597, 2000.

[94] Y. Zeyada and R.A. Hess. Modeling the human pilot in single-axis linear and nonlinear tracking tasks. In *Pilot-Induced Oscillation Research : Status at the End of the Century*, 2001.

[95] D. Andrisani and Gau Ching-Fu. A nonlinear pilot model for hover. *Journal of Guidance, Control and Dynamics*, 8(3):332, May-June 1985.

[96] M. Innocenti, A. Balluchi, and A. Balestrino. New results on human operator modelling during nonlinear behavior in the control loop. In *Proceedings of the American Control Conference, Albuquerque, New Mexico June 1997*, 1997.

[97] M. Innocenti, A. Petretti, and M. Vellutini. Human operator modelling during discontinuous performance. In *AIAA Atmospheric Flight Mechanics Conference and Exhibit*, number AIAA-98-4146, pages 31–38, 1998.

[98] M. Innocenti, A. Balluchi, and A. Balestrino. Modeling of nonlinear human operator in the control loop: Preliminary results. *Journal of Guidance, Control and Dynamics*, 4:736:739, 2000.

[99] M.R. Anderson, C. Clark, and G. Dungan. Flight test maneuver design using a skill- and rule-based pilot model. In *IEEE International Conference on Systems, Man and Cybernetics, 1995. Intelligent Systems for the 21st Century.*, 1995.

[100] M.R. Anderson and J. Phillips. A variable strategy pilot model. In *AIAA Atmospheric Flight Mechanics Conference*, number AIAA-2000-3983, pages 195–204, Denver, Colorado, August 2000. AIAA.

[101] A.A. Lambregts, G. Nesemeier, J.E. Wilborn, and R.L. Newman. Airplane upsets: Old problem, new issues. In *AIAA Modelling and simulation technologies conference and exhibit*, 2008.

[102] C. Fielding and P.K. Flux. Non-linearities in flight control systems. *The Aeronautical Journal*, 107:673–696, 2003.

[103] S. Andrews and A. Cooke. An aeroelastic flexible wing model for aircraft simulation. In *48th AIAA Aerospace Sciences Meeting Including the New Horizons Forum and Aerospace Exposition, Orlando, Florida, Jan. 4-7, 2010*, 2010.

[104] H.J. Damveld, G.C. Beerens, M.M. van Paassen, and M. Mulder. Design of forcing functions for the identification of human control behaviour. *Journal of Guidance, Control and Dynamics*, 33:1064–1081, 2010.

[105] M. Tischler and R. Remple. *Aircraft and Rotorcraft System Identification.* American Institute of Aeronautics and Astronautics Inc., 2006.

[106] D.G. Mitchell, B.A. Kish, and J.S. Seo. A flight investigation of PIO due to rate limiting. In *IEEE Aerospace Conference*, 1998.

[107] D.G. Mitchell and E.J. Field. Nonlinearities and PIO with advanced aircraft control systems. In *Active Control Technology for Enhanced Performance Operational Capabilities of Military Aircraft, Land Vehicles and Sea Vehicles*, 2000.

[108] M.M. Lone and A.K. Cooke. Review of pilot modelling techniques. In *48th AIAA Aerospace Sciences Meeting Including the New Horizons Forum and Aerospace Exposition*, number AIAA-2010-297, Orlando, Florida, January 2010.

[109] V. Klein and E.A. Morelli. *Aircraft System Identification: Theory And Practice.* American Institute of Aeronautics and Astronautics Inc., 2006.

[110] K.W. Iliff. Aircraft identification experience. Technical report, North Atlantic Treaty Organization, 1979.

[111] J.C. van der Vaart. *Modelling of perception and action in compensatory manual control tasks.* PhD thesis, Delft University, 1992.

[112] O.N.F. Mouton, M. Mulder, and M.M. van Paassen. Thresholds for visual perception of aircraft velocity changes. In *AIAA Modeling and Simulation Technologies Conference and Exhibit, 18 - 21 August 2008, Honolulu, Hawaii*, 2008.

[113] M. Duppen, P.M.T. Zaal, M. Mulder, and M.M. van Paassen. Effects of motion on pilot behaviour in target, disturbance and combined tracking tasks. In *AIAA Modelling and Simulation Technologies Conference and Exhibit*, 2007.

[114] F.D. Newell and H.J. Smith. Human transfer function characteristics in flight and ground simulation nfor a roll tracking task. NASA-TN-D-5007, National Aeronautics and Space Administration (NASA), February 1969.

[115] D.L. Kleinman. Optimal control of linear systems with time-delay and observation noise. *IEEE Transactions on Automatic Control*, 14:524–527, October 1969.

[116] S. Baron, D. Kleinman, and W. Levison. An optimal control model of human response Part II: Prediction of human performance in a complex task. *Automatica*, 6:371–383, 1970.

[117] P.M. Thompson. Minimum flying qualities Volume III: Program CC's implementation of the human optimal control model. Technical report, Systems Technology, Inc., 1989.

[118] D.B. Doman. Interactive flying qualities toolbox for MATLAB user's guide. Technical Report WL-TR95-3070, Wright Patterson AFB, August 1995.

[119] M.M. Lone and A.K. Cooke. Pilot-model-in-the-loop simulation environment to study large aircraft dynamics. *Proceedings of the Institution of Mechanical Engineers, Part G: Journal of Aerospace Engineering*, March 2012.

[120] J. Maciejowski and P. Austin. Non-linear and predictive control. Lectures given at Cambridge University Engineering Department, 2008.

[121] G. Vinnicombe and G.B. Stan. Optimal control and dynamic programming. Lectures given at Cambridge University Engineering Department, 2008.

[122] F.L. Lewis and V.L. Syrmos. *Optimal Control*. John Wiley & Sons Inc., second edition, 1995.

[123] T.B. Sheridan and W.R. Ferrell. *Man-Machine Systems: Information, Control and Decision Models of Human Performance*. The MIT Press, 1974.

[124] K. Dutton, S. Thompson, and B. Barraclough. *The art of control engineering*. Prentice Hall International Ltd., 1997.

[125] R.A. Hess. Theory for aircraft handling qualities based upon a structural pilot model. *Journal of Guidance, Control and Dynamics*, 12(6):792, November-December 1989.

[126] M.M. Lone, N. Ruseno, and A.K. Cooke. Towards understanding effects of nonlinear flight control system elements on inexperienced pilots. *The Aeronautical Journal*, 116(1185), 2012.

[127] Julie Bruzi. Robust control law design with manual control effects. Master's thesis, School of Engineering, Cranfield University, 2012.

[128] Shen Yingchun. Effect of flight control system mode switching on pilot dynamics. Master's thesis, School of Engineering, Cranfield University, 2011.

[129] D.G. Mitchell and D.H. Klyde. Testing for pilot-induced oscillations. In *AIAA Atmospheric Flight Mechanics Conference and Exhibit,15 - 18 August 2005, San Francisco, California*, 2005.

[130] R.K. Heffley and W.F.; Jewell. Aircraft handling qualities data. Technical Report NASA CR-2144, NASA, Hawthorne, California, 1972.

[131] Military standard: Flying qualities of piloted aircraft - MIL-F-8785C, November 1980.

[132] H.A. Mooij. *Criterea for low-speed longitudinal handling qualities of transport aircraft with closed-loop flight control systems*. Martinus Nijhoff Publishers, 1984.

[133] Military standard: Flying qualities of piloted aircraft. Technical Report MIL-STD-1797A, Department of Defence, United states of America, 1990.

[134] Captain Mohammed Aziz. Investigation Report on the Accident of Ethiopian 409 Boeing 737-800 Registration ET-ANB at Beirut - Lebanon on 25th January 2010. Technical report, Republic of Lebanon, Ministry of Public Works & Transport, 2012.

[135] Technical investigation into the accident of the B737-800 registration 5Y-KYA operated by Kenya Airways that occurred on the 5th of May 2007 in Douala. Technical report, Aviation Civile Au Cameroun, 2010.

[136] V.S. Ramachandran and Sandra Blakeslee. *Phantoms in the Brain: Human Nature and the Architecture of the Mind*. Fourth Estate, 1998.

[137] D. Purves and R.B. Lotto. *Why We See What We Do: a Wholly Empirical Theory of Vision*. Macmillan Press, 2003.

[138] R.A. Hess. Structural model of the adaptive human pilot. *Journal of Guidance, Control and Dynamics*, 3(5):416–423, September-October 1980.

[139] R.A. Hess. Model for human use of motion cues in vehicular control. *Journal of Guidance, Control and Dynamics*, 13(3):476, May-June 1990.

[140] A. Berthoz, B. Pavard, and L.R. Young. Perception of linear horizontal self-motion induced by peripheral vision (linear-vection). *Experimental Brain Research*, 23:471–489, 1975.

[141] C. Fernandez and J.M. Goldberg. Physiology of peripheral neurons innervating semicircular canals of the squirrel monkey II: Response to sinusoidal stimulation and dynamics of peripheral vestibular system. *Journal of Neurophysiology*, 34:661–675, 1971.

[142] R.J. Telban, F.M. Cardullo, and L. Guo. Investigation of mathematical models of otolith organs for human centered motion cueing algorithms. In *AIAA Modeling and Simulation Technologies Conference and Exhibit*, 2000.

[143] R.W. Allen, H.R. Jex, and R.E. Magdaleno. Manual control performance and dynamic response during sinusoidal vibration. Technical Report AMRL-TR-73-78, Aerospace Medical Research Laboratory, October 1973.

[144] Y. Matsumoto and M.J. Griffin. Movement of the upper-body of seated subjects exposed to vertical whole-body vibration at the principal resonance frequency. *Journal of Sound and Vibration*, 215:743–762, 1998.

[145] D. Howe. *Aircraft Loading and Structural Layout*. American Institute of Aeronautics and Astronautics Inc., 2004.

[146] J.R. Wright and J.E. Cooper. *Introduction to aircraft aeroelasticity and loads*. John Wiley & Sons Inc., 2007.

[147] *EASA Certification Specifications for Large Aeroplanes CS-25, Book 2, Acceptable Means of Compliance*, September 2007.

[148] *EASA Certification Specifications for Large Aeroplanes CS-25, Book 1, Airworthiness Code*, September 2007.

[149] R.P. Chen. Statistical-discrete-gust/power-spectral-density methods overlap - A holistic proof and beyond. Technical report, NASA Langley Research Center, Hampton, USA, 1963.

[150] J.G. Jones. Statistical discrete gust theory for aircraft loads : A progress report. Technical Report RAE TR 73167, Royal Aeronautical Establishment, 1973.

[151] J.G. Jones. Documentation of the linear statistical discrete gust method. Technical report, U.S. Department of Transportation, Federal Aviation Administration, 2004.

[152] B. Etkin. *Dynamics of atmospheric flight*. John Wiley & Sons Inc., 1972.

[153] F.M. Hoblit. *Gust loads on aircraft: Concepts and applications*. American Institute of Aeronautics and Astronautics Inc., 1988.

[154] D. McLean. *Automatic Flight Control Systems*. Prentice Hall International Ltd., 1990.

[155] J.W. Rustenburg, D.A. Skinn, and D.O. Tipps. A method to derive continuous turbulence field parameters based on aircraft acceleration measurements. Technical report, Structural integrity division, University of Dayton Research Institute, 2008.

[156] J.W. Rustenburg, D.A. Skinn, and D.O. Tipps. Statistical loads data for the Airbus A320 aircraft in commercial operations. Technical report, U.S. Department of Transportation, Federal Aviation Administration, 2002.

[157] D.O. Tipps, D.A. Skinn, J.W. Rustenburg, T. Jones, and D.A. Harris. Statistical loads data for the Boeing 777-200ER aircraft in commercial operations. Technical report, U.S. Department of Transportation, Federal Aviation Administration, 2006.

[158] F.M. Hoblit, N. Paul, J.D. Shelton, and F.E. Ashford. Development of a power-spectral gust design procedure for civil aircraft. Technical report, Federal Aviation Agency, 1966.

[159] M.M. Lone and A.K. Cooke. Modelling and simulation of large aircraft. Presented at the Annual Airbus Flight Physics Distributed R&T Partnership (DiPaRT) Workshop, November 2010.

[160] M.M. Lone, C.K. Lai, A.K. Cooke, and J. Whidborne. Application of pilot models to study trajectory based manoeuvres. In *AIAA Modelling Simulation Technologies Conference*, 2012.

[161] N.X. Li, P.R. Grant, and H. Abbasi. A comparison of the fixed-axes and the mean-axes modeling methods for flexible aircraft simulation. In *AIAA Modeling and Simulation Technologies Conference, 2-5 August 2010, Toronto, Ontario Canada*, 2010.

[162] M.R. Waszak and J.B. Davidson. A simulation study of the flight dynamics of elastic aircraft : Volume 1 - Experiment, results and analysis. Technical report, National Aeronautics and Space Administration, 1987.

[163] M.R. Waszak and J.B. Davidson. A simulation study of the flight dynamics of elastic aircraft : Volume 2 - Data. Technical report, National Aeronautics and Space Administration, 1987.

[164] R. Palacios and C.E.S. Cesnik. Structural models for flight dynamic analysis of very flexible aircraft. In *50th AIAA/ASME/ASCE/AHS/ASC Structures, Structural Dynamics and Materials Conference, Palm Springs, California*, 2009.

[165] R. Palacios, J. Murua, and R. Cook. Structural and aerodynamic models in nonlinear flight dynamics of very flexible aircraft. *AIAA Journal*, 48:2648–2659, 2010.

[166] J.G. Leishman. *Principles of Helicopter Aerodynamics*. Cambridge University Press, 2006.

[167] M.M. Lone, M.N. Rouyan, and A.K. Cooke. A MATLAB/Simulink suite for the real-time flight simulation of large aircraft. Technical report, Cranfield College of Aeronautics, 2012.

[168] Airbus. *Airbus A340 Flight Crew Operating Manual (Rev 24)*.

[169] D. Learmont. A330 laboured after aileron's failure. Flight International, October 2012.

[170] Anonymous. Serious Incident Report, Airbus A330-301, EI-ORD Over Iceland, 11 May 2010. Technical Report 2012-015, Air Accident Investigation Unit Ireland, Department of Transport, Tourism and Sport, September 2012.

[171] G. Obinata and D.O. Anderson. *Model reduction for control system design*. Springer, 2001.

[172] J.L. Junkins and Y. Kim. *Introduction to dynamics and control of flexible structures*. American Istitute of Aeronautics and Astronautics Inc., 1993.

[173] J.F. Whidborne and Guoping Liu. *Critical Control Systems Theory, Design and Applications*. John Wiley & Sons Inc., 1993.

[174] K. Zhou, C.D. Doyle, and K. Glover. *Robust and Optimal Control*. Prentice Hall International Ltd., 1996.

[175] K. Glover. All optimal Hankel-norm approximations of linear multivariable systems and their L(infinity)-error bounds. *International Journal of Control*, 39:1115:1193, 1984.

[176] D.G. Mitchell, A.J. Arencibia, and S. Munoz. Real-time detection of pilot-induced-oscillations. In *AIAA Atmospheric Flight Mechanics Conference and Exhibit, 16-19 August 2004, Providence, Rhode Island*, number AIAA-2004-4700, 2004.

[177] F.M. Dekking, C. Kraaikamp, H.P. Lopuhaa, and L.E. Meester. *A Modern Introduction to Probability and Statistics: Understanding Why and How*. Springer, 2005.

[178] A. Rutherford. *ANOVA and ANCOVA: A GLM Approach*. Wiley-Blackwell, Second edition, 2011.

[179] R.W. Pratt. *Flight Control Systems: Practical Issues in Design and Implementation*. Institution of Engineering and Technology, 2000.

[180] S.P. Andrews. Handling qualities of large aircraft with active load control. Periodic Review Report 2, Cranfield University, Department of Aerospace Sciences, School of Engineering, June 2008.

[181] M.K. Cook. Lectures in automatic flight control systems. 2009 Lecture notes given at Cranfield University, 2009.

[182] S.P. Andrews. Handling qualities of large aircraft with active load control. Periodic Review Report 1, Cranfield University, Department of Aerospace Sciences, School of Engineering, October 2007.

[183] S.P. Andrews. Handling qualities of large aircraft with active load control. Periodic Review Report 3, Cranfield University, Department of Aerospace Sciences, School of Engineering, November 2007.

[184] S.P. Andrews. Handling qualities of large aircraft with active load control. Periodic Review Report 4, Cranfield University, Department of Aerospace Sciences, School of Engineering, July 2009.

[185] S.P. Andrews. Handling qualities of large aircraft with active load control. Periodic Review Report 5, Cranfield University, Department of Aerospace Sciences, School of Engineering, January 2010.

[186] D.A. Johnson. *Suppression of pilot-induced-oscillations (PIO).* PhD thesis, Air Force Institute of Technology, 2002.

[187] Q. Liu. Pilot-induced-oscillation detection and mitigation. Master's thesis, Department of Aerospace Engineering, Cranfield University, 2013.

[188] Q. Liu, M.M. Lone, and X.S. Tan. Towards the design of a pilot-induced-oscillation detection and mitigation scheme. *Chinese Journal of Aeronautics.* Under review.

APPENDIX A

Manual control experiments and modelling details

A.1 Summary of Analysis of Variance (ANOVA) testing

For the reader's convenience, a brief description of ANOVA testing and its assumptions is given here. A detailed discussion and theoretical treatment can be found in many statistics books[177][178]. Only one-way ANOVA tests were used in this study to test the statistical significance of the differences observed between the groups of parameter estimates. The null (H_0) and alternative (H_1) hypotheses are as follows:

H_0 : All parameter estimates are drawn from the same population.

H_1 : Parameter estimates are drawn from different populations with different means.

Note that the alternative hypothesis is very general, implying that the test cannot give information regarding the source of the difference. A one-way ANOVA test uses the F-distribution to compare the sample means. The following assumptions are made regarding the collected data:

1. Sample populations have a normal distribution and equal variance.
2. Observations are mutually independent.

The analysis involves calculating an F-statistic that can be interpreted as an indicator for relative difference between and within groups. A large value implies a large difference between the groups. A p-value is then calculated using the cumulative distribution function of the F-statistic (that is the F-distribution). If the resulting p-value is small, the null hypothesis should be rejected and it can be said that at least one sample mean is significantly different. A 10% significance level was used here.

A.2 Control-theoretic modelling details and results

Using Equation 3.1.3 the PVS crossover frequencies were calculated for each of the training runs. These are shown in Figure A.1. The observed differences in inter-subject crossover frequencies was an indication of the variation to be expected from the final series of tests.

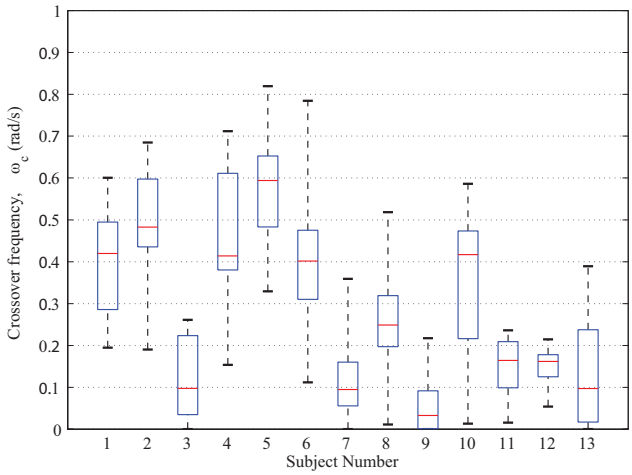

Figure A.1: Inter-subject variations in crossover frequencies during training.

The parameter identification process was also applied to the training data using the bimodal pilot model. Figure A.2 shows the variation in the variance of the remnant signal; effectively an indication of the subject's adherence to linear control behaviour.

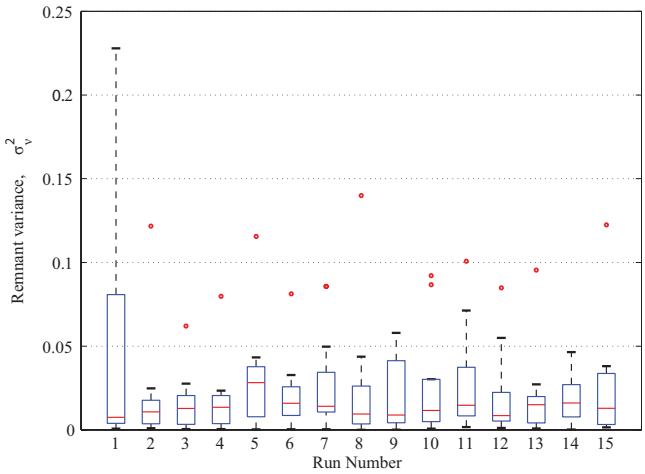

Figure A.2: Variation of remnant variance with run number during training.

Details of the individual subjects who conducted the manual control experiments in Chapter 3 are given in Table A.1. The Piper PA28 and Diamond DA40 are single propeller engine trainers and the PA28 and DA40 models are similar configuration twin engine aircraft. Figure A.3 shows the experimental setup and subject posture when conducting manual control tasks.

Subject	Gender	Age (years)	Flight experience (hours)	Aircraft type
A	M	25	25	PA28, DA40
B	M	21	10	DA28
C	M	25	250	PA28, PA44; DA40, DA42
D	M	25	30	DA40
E	M	18	15	DA40
Average	-	23.8	66	-

Table A.1: Subject details (PA = Piper, DA = Diamond).

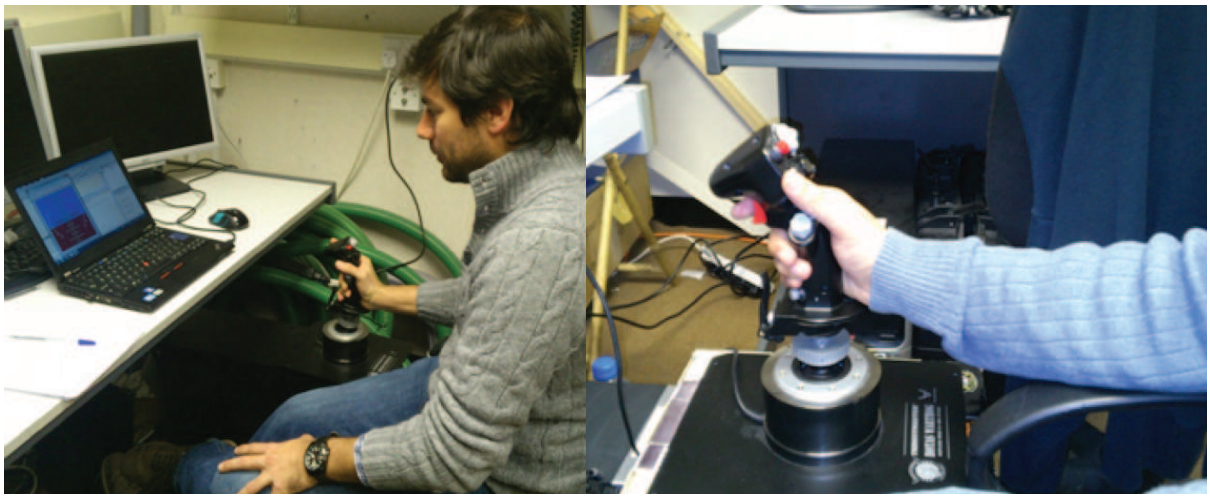

Figure A.3: Subject posture and sidestick position used in manual control experiments.

Side-stick	
Spring constant, K_s	0.16°/N
Break-out force	±4N
Saturation limit	±16° (22.5lbf)
C* CSAS	
Pitch rate gain, K_{qc}	12.4
Command gain, K_c	0.1
Integral gain, K_i	12
Inner-loop pitch rate gain, K_q	-0.4

Table A.2: Flight control system parameter values.

Joystick dynamics were investigated with the assumption that they can be modelled as a second order system with fixed stiffness and damping originating from the mechanical springs and dampers. The transient peak ratio method was used for parameter identification. The transient response required for this process was obtained by simply deflecting the stick fully aft and releasing it. The time history immediately after the release was then used for the process. Therefore, the following second-order transfer function was used to model longitudinal joystick dynamics:

$$G_{s\theta}(s) = \frac{86^2}{s^2 + 2(0.14)(86)s + 86^2} \tag{A.2.1}$$

Results for parameters in the compensatory component of the bimodal and precision pilot models obtained for tracking tasks are presented in Figures A.4 and A.5 respectively.

A.3 MOCM parameter variation study results

Another parameter of interest is the attention allocation vector that models the fraction of attention allocated by the pilot to each observed variable. Figure A.6 presents the changes in frequency response due to variations in this parameter. Inspecting the frequency response shows that assuming an improvement in performance (error minimisation) due to higher visibility of error is incorrect. Although the objective is to minimise error, the phase bandwidth is minimum when 90% of the attention is placed on error and maximum when 90% of the attention is placed

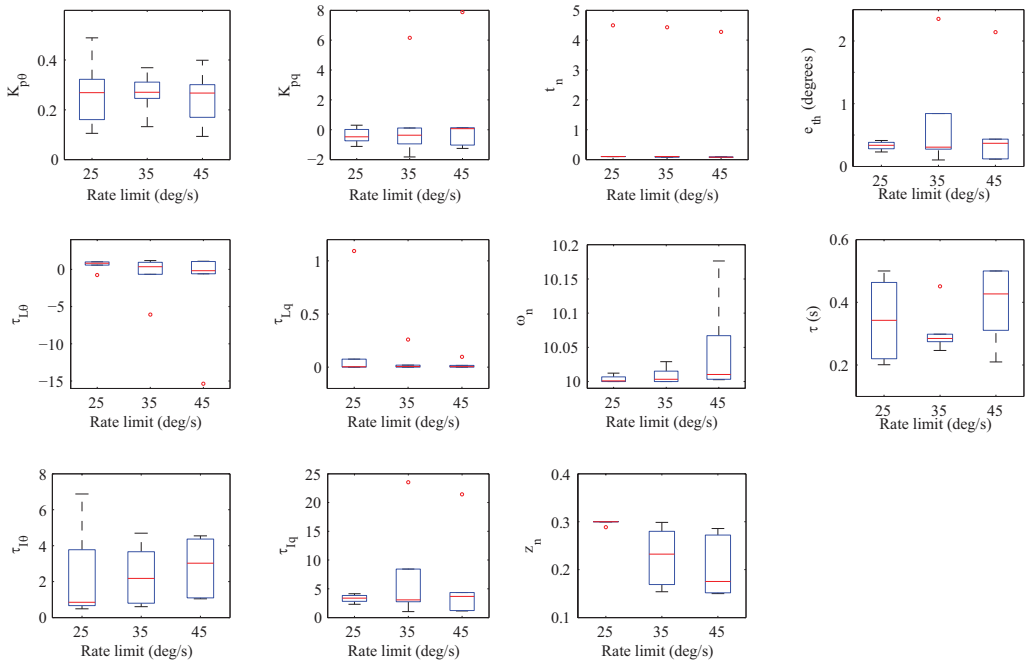

Figure A.4: Bimodal model compensatory parameter values for tracking tasks.

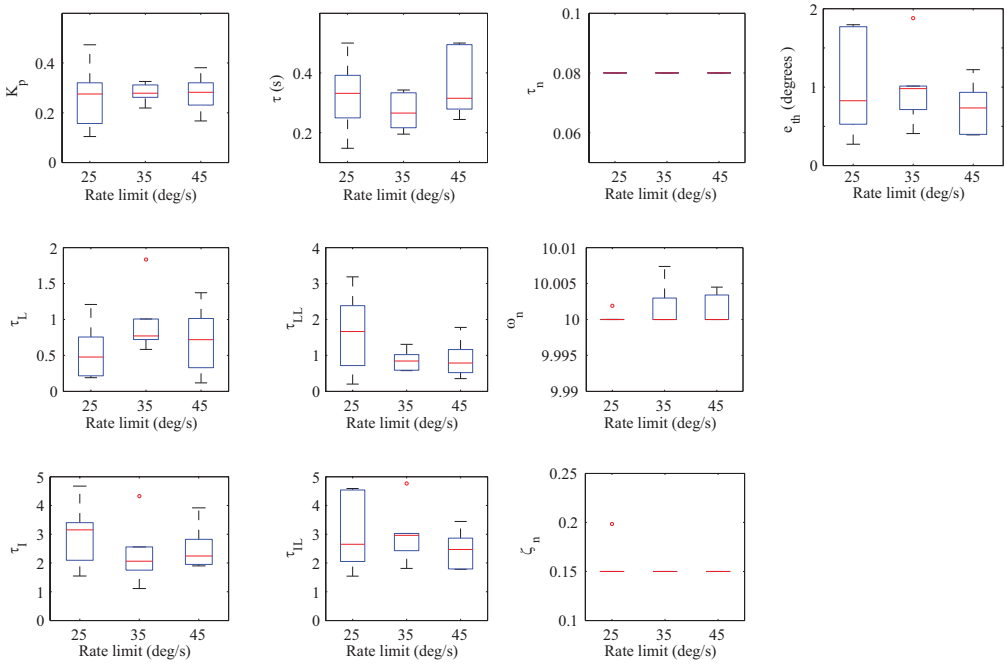

Figure A.5: Precision model compensatory parameter values for tracking tasks.

on rate of change of error. This further confirms the fact that human control performance is superior when an inner error rate loop is allowed to be closed; analogous to the improvements observed when inner rate loops are implemented in flight control systems.

The movement of the MOCM poles and zeros as the inherent time delay and neuromuscular lag parameters are varied are shown in Figures A.7 and A.8 respectively.

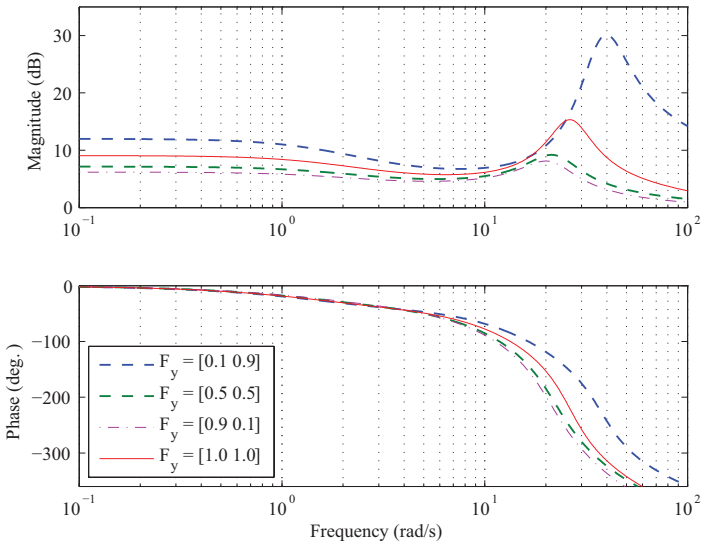

Figure A.6: Effect of varying attention allocation on MOCM frequency response.

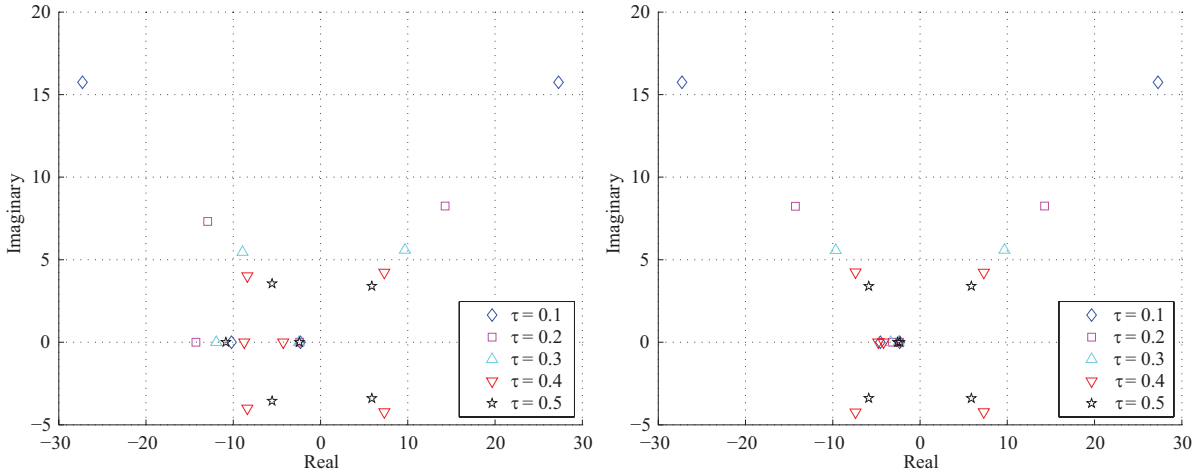

(a) Error to stick deflection

(b) Error rate to stick deflection

Figure A.7: Effects of varying inherent time delay on MOCM transfer function zeros.

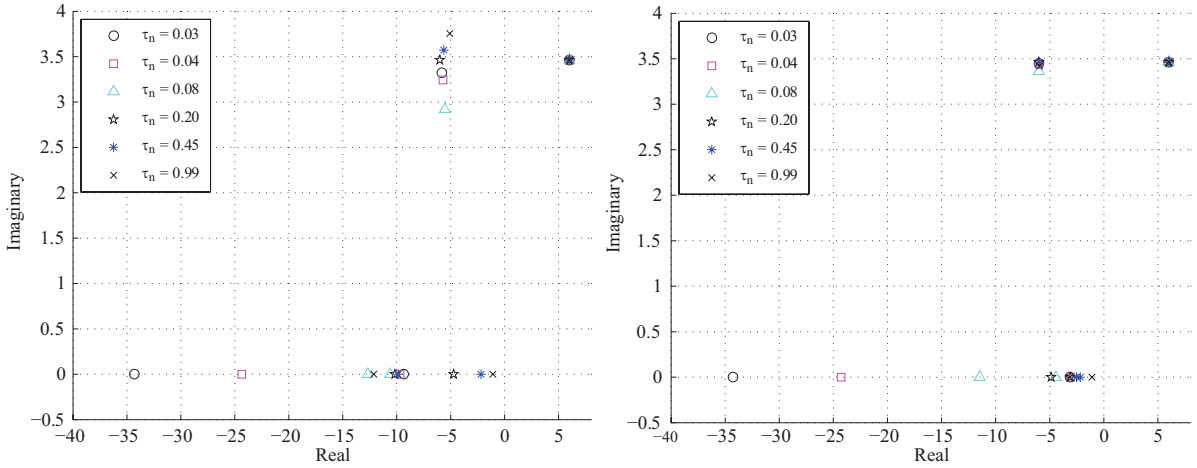

(a) Error to stick deflection

(b) Error rate to stick deflection

Figure A.8: Effects of varying neuromuscular lag on MOCM transfer function zeros.

A.4 Pilot and aircraft model block diagram

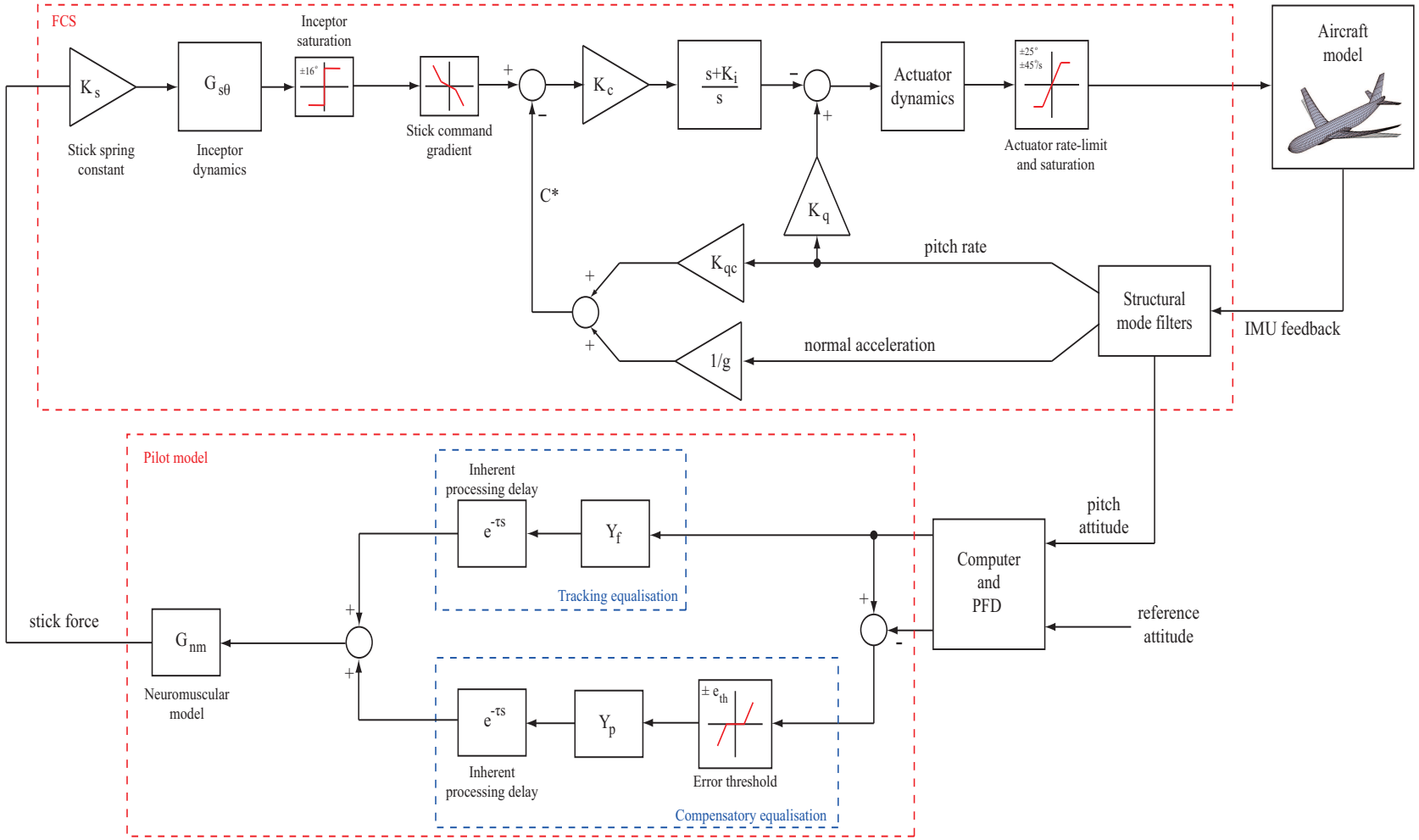

Figure A.9: PVS block diagram used to study the effects of nonlinear FCS components.

APPENDIX B

A note on handling qualities criteria

To date, only the Neal-Smith (both time[65] and frequency domain[62][63]) and the approach introduced by Zeyada et al[94] (which uses the *handling qualities sensitivity function*) are the criteria that explicitly use a pilot model. On the other hand, the Bandwidth criterion includes pilot dynamics implicitly through the assumption used to define the phase bandwidth shown in Figure G.3. It is defined as the frequency for which the open loop PVS phase is -135°, i.e. it assumes the pilot introduces an additional 45° of phase lag. Inspection of the PVS frequency response, shown in Figure B.1, allows some discussion on the effects of subject dynamics on open-loop dynamics and also the basis of the existing frequency domain Neal-Smith and Bandwidth criteria. It can be seen that the effects due to pilot introduced dynamics are quite dramatic: (a) the crossover frequency is shifted back from 8.4 rad/s to around 0.2 rad/s and, (b) almost 40% of the phase improvement due to the CSAS is lost.

The Neal-Smith pilot model is based on McRuer's classical pilot modelling approach from the early 1960's, whilst Zeyada's method relies on the structural model developed by Hess later in the 1990's. The following observations can be made when considering the closed-loop PVS frequency response in the context of the Neal-Smith requirements:

1. The system bandwidth for both pilot models are between 2.74 rad/s and 3.23 rad/s. So it can be said that the requirement to fix the closed-loop bandwidth at 3.5 rad/s is for a more aggressive pilot, resulting in a more conservative criterion.

2. The maximum low frequency droop with the precision and bimodal pilot models were found to be -8.52 dB and -12.99 dB respectively. Therefore, the requirement to fix the maximum low frequency droop at -3 dB is non-conservative. The pilots involved in the experiments took much longer to settle aircraft nose onto the desired attitude.

3. The requirement to minimise the resonant peak was also found to be non-conservative, especially from the perspective of PIO susceptibility for such a configuration. This is highlighted by the insufficient gain attenuation and the resulting small gain margin.[1]

[1]The large inter-subject variations evident in the magnitude plots of Figure 3.18 and the small sample size of pilots predict that this configuration is even more PIO prone. Figure B.1 also highlights the potential for aeroelastic APC due to low wing stiffness that can further reduce the frequency of the first wing bending mode. Moreover a 10% global structural damping used in this study is more than twice that used by large aircraft manufacturers; increasing the likelihood of large amplitude APC.

Application of the Bandwidth criterion to the open-loop dynamics was found to only confirm the current popularity of this criterion[6]. Gain and phase bandwidths were found to be 4.94 rad/s and 4.59 rad/s. The open-loop PVS bandwidth (frequency at -180° phase) was found to equal the phase bandwidth because 44.30° of phase delay was introduced by the pilot; confirming the criterion's assumption that the pilot adds 45° phase lag.

Observations made regarding PIO susceptibility and the Neal-Smith criterion can be studied further by introducing uncertainty into the estimates for the pilot model parameters. This provides insight into parameter combinations required for the worst case scenario. Here, the effects of injecting parametric uncertainty into the bimodal model parameters are presented. The level of uncertainty used for each parameter can be found in Table B.1.

Parameter	Uncertainty (%)	Parameter	Uncertainty (%)
$K_{p\theta}$, K_{pq}	25	τ	20
$\tau_{\mathrm{L}\theta}$, $\tau_{\mathrm{I}\theta}$, $\tau_{\mathrm{L}q}$, $\tau_{\mathrm{I}q}$	25	τ_n, ω_n, ζ_n	10

Table B.1: Bimodal model parametric uncertainty.

The nominal parameter values are the mean values obtained from Figure 3.17 in Chapter 4. In this study, a sample set of 2000 models were randomly generated along with the corresponding closed-loop PVS. Parameters were sampled assuming each varied according to a uniform distribution bound by the selected degree of uncertainty. Figure B.1 also presents the open and closed-loop frequency response with the observed upper and lower bounds. It can be seen that inter-subject variations can cause a large resonant peak and nonminimum phase dynamics around the short period mode frequency; that is the pilot introduces a right-half-plane zero. Thus, there exists a combination of pilot model parameters where given a particular command, the PVS responds initially in the opposite sense. There is also a sharp phase drop due to this nonminimum phase behaviour that may lead to what is often referred to as a *handling qualities cliff*.

Table B.2 presents the upper and lower stability margins for the open-loop system. It shows that a 25% variation in model parameters can lead to a 12.2 dB and 56° difference in gain and phase margins respectively. This highlights the need to adopt a robust approach towards the design of CSAS that explicitly considers variations in pilot dynamics.

	Upper bound	Nominal	Lower bound
Gain margin (dB)	7.1	12.1	19.4
Phase margin (deg.)	119.8	87.1	63.8

Table B.2: Stability margins for open-loop pilot vehicle system.

Although no uncertainty was introduced to the aircraft model, its inclusion may highlight unwanted dynamics in the high frequency regions where the traditional CSAS can interact with structural modes.

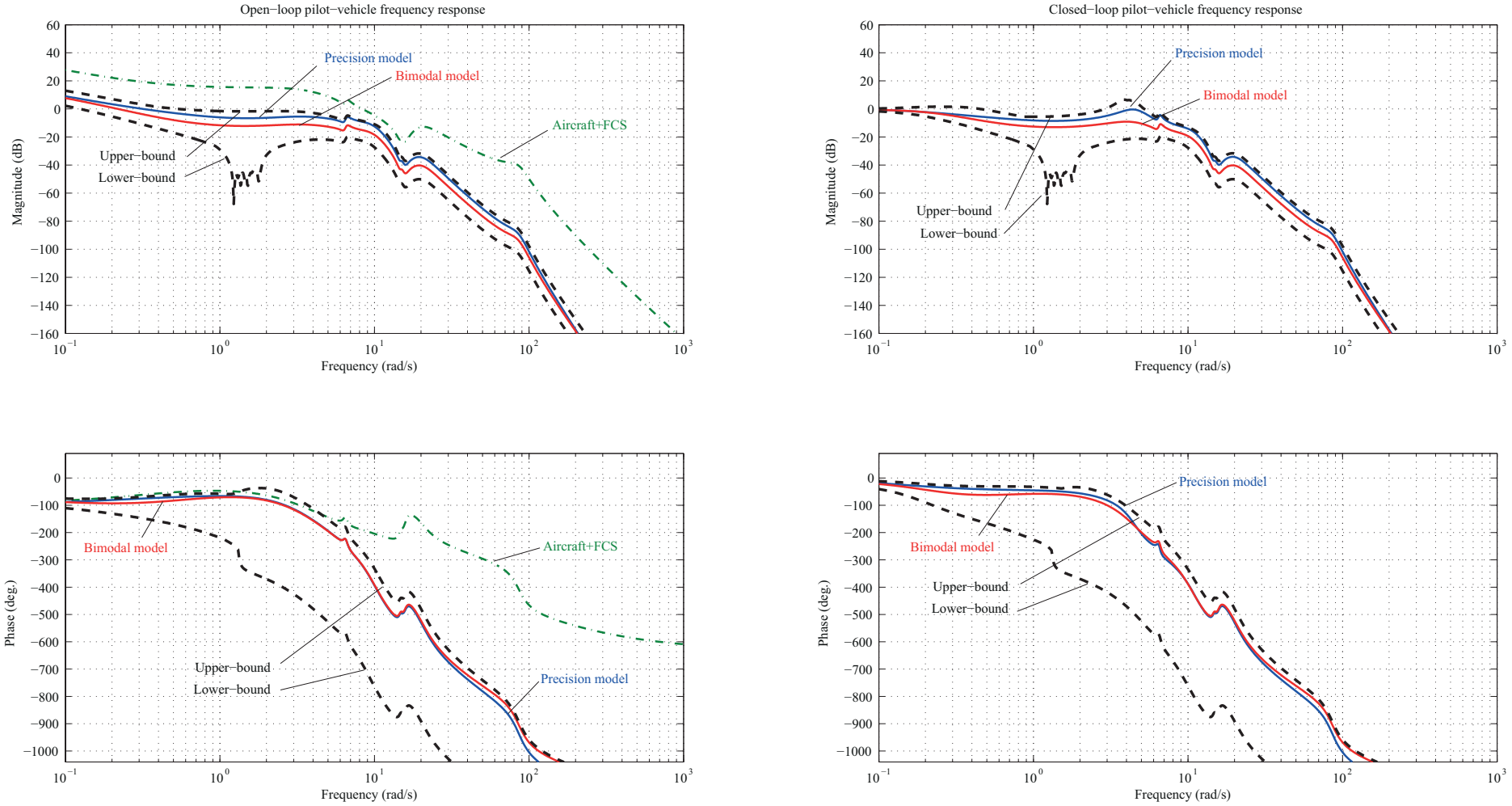

Figure B.1: Pilot-vehicle system frequency responses.

This page is intentionally left blank.

APPENDIX C

Flight control system details

The FCS augmenting the AX-1 aircraft model used extensively in this study originates from work done by Lone et al[167] using an LPV flight dynamic model of the Boeing 747. The system was designed using the classical root locus technique. When the FCS was adopted for the AX-1, it was initially tested and the gains were tuned to provide adequate handling qualities. However, preliminary simulations showed the coupling of FCS and low frequency structural modes, which was resolved through the design of structural mode filters. A longitudinal handling qualities assessment of the fully augmented aircraft was done using the time-domain Gibson Dropback criterion. This appendix begins by describing the design process for the structural mode filters followed by the results of the handling qualities assessment.

C.1 Structural mode filters

Accelerometers that are part of the IMU detect composite accelerations that consist of those due to rigid body motion as well as aeroelastic modes. In the past, accelerations due to structural modes could be ignored because they occurred at sufficiently high frequencies. For smaller more rigid aircraft, the aeroelastic modes are at frequencies well beyond the manual control range; naturally eliminating interactions with the pilot[179]. Therefore, designers have been mainly concerned with minimising interactions with the FCS. However, since modern large aircraft have lightly damped aeroelastic modes at much lower frequencies, these can potentially pass through the IMU and couple with the FCS and rigid body modes to produce unwanted dynamics. Such interactions are very difficult to eliminate because of the proximity of these aeroelastic modes to rigid body modes in the frequency domain. Problems such as handling qualities degradation, passenger ride discomfort, airframe fatigue issues and aeroelastic instability can occur if these modes, or at least modes at higher frequencies, are not attenuated appropriately.

On combat aircraft, filters are employed to mitigate the effects of aeroelastic modes on feedback signals used by FCS, as shown in Figure C.1. These filters are employed as a means of passive structural mode control that prevent the measured structural oscillations from being transmitted through the FCS to the actuation system, reducing the effects of structural modes on rigid body motion.[1] Figure C.2 shows the position of these filters onboard large transport aircraft. Placing

[1] Complex multi-mode FCS allow designers to use notch filters to target modes at specific frequencies. However, these filters are only effective when employed to mitigate modes that remain stationary at a particular frequency.

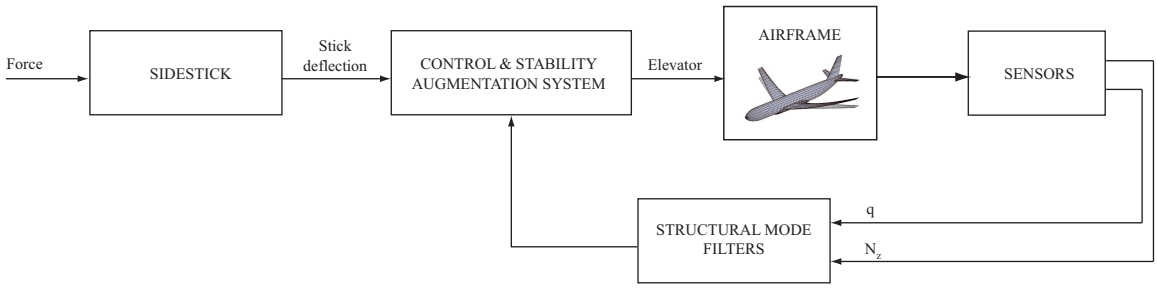

Figure C.1: Filtering scheme as employed for small rigid aircraft (scheme A).

the filters just before the actuation system implies that both the pilot and FCS cannot drive the control surfaces at frequencies that may excite aeroelastic modes. These filters also cause the actuation systems to operate at lower frequencies, therefore minimising the overall power requirements and improving aircraft efficiency.

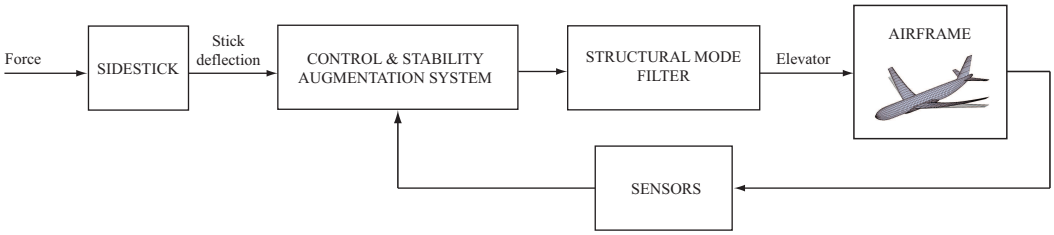

Figure C.2: Filtering scheme as employed for large flexible aircraft (scheme B).

This section describes the process used to select filter properties and the consequent effect on longitudinal aircraft dynamics. Due to the scope of this project, this study was limited to investigating Butterworth and Type I Chebyshev filters to attenuate high frequency structural modes. Frequency domain filter characteristics, as shown in Figure C.3, were considered along with time domain filter characteristics. Both schemes (shown in Figures C.1 and C.2) have also been compared.

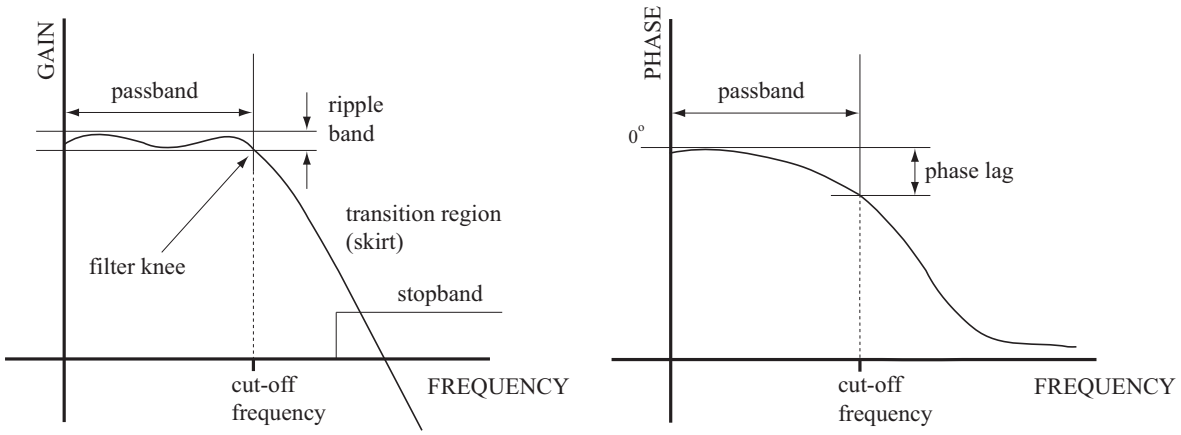

Figure C.3: Filter frequency domain characteristics.

C.1.1 Butterworth filters

The Butterworth filter trades off the sharpness of the the filter knee and the degree of attenuation in the transition region to produce the flattest possible passband response. The generalised

amplitude response of the filter is as follows:

$$\frac{y}{u} = \frac{1}{\sqrt{1 + (f/f_c)^{2n}}} \tag{C.1.1}$$

where u and y are the filter input and output signals respectively. f, f_c and n stand for frequency, the filter's cut-off frequency and order respectively.

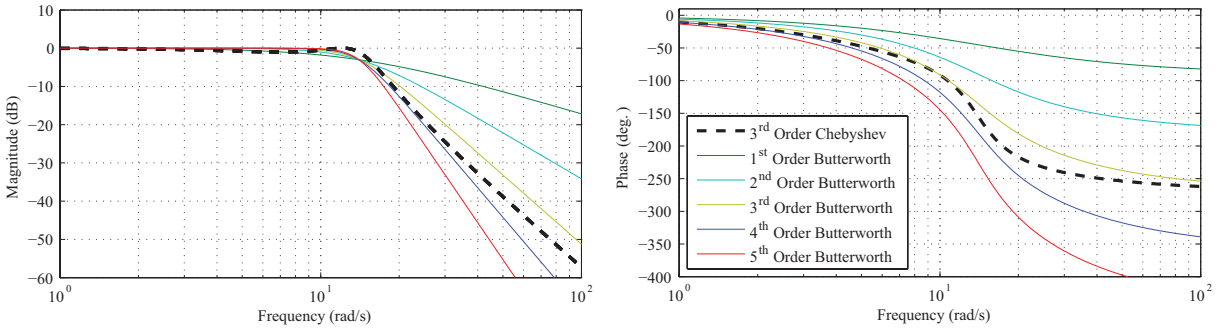

Figure C.4: Frequency response of the Butterworth filter.

The effect of varying the order of the filter can be seen in Figure C.4. It is clear that higher order filters provide much steeper attenuation in the transition region. This is at the cost of increased phase lag within the passband frequency range.

Comparison with a Type I Chebyshev filter shows that the Butterworth filter also lacks sharpness at the filter knee. Figure C.4 also shows that a 3rd order Chebyshev filter provides greater attenuation than a 3rd order Butterworth filter whilst maintaining similar phase characteristics within the passband region.

C.1.2 Type I Chebyshev filters

The Chebyshev filter allows a limited degree of gain variation within the passband to improve the sharpness of the filter knee and to increase attenuation in the transition region. This approach is more practical because in reality, a sharp filter knee followed by a steep transition region are the desired features for isolating unwanted signal contents. The following is the generalised amplitude response of a Chebyshev filter:

$$\frac{y}{u} = \frac{1}{\sqrt{1 + \epsilon^2 C_n^2(f/f_c)}} \tag{C.1.2}$$

The effects of varying filter order can be seen in Figure C.5. It is clear that the high order filters will provide a sharper knee followed by a steeper transition region. However, this is accompanied by dramatic increases in phase lags.

Another feature that defines Chebyshev filters is the ripple band. The effects of varying the ripple band magnitude for a third order filter are presented in Figure C.6. It is evident that a larger ripple band has a more detrimental effect on performance; it results in a more pronounced resonant peak and increased low frequency phase lag.

Therefore, with regards to frequency domain performance, the selection of a Chebyshev filter involves achieving a desired magnitude response whilst minimising the phase lags introduced by the filter into the closed loop system.

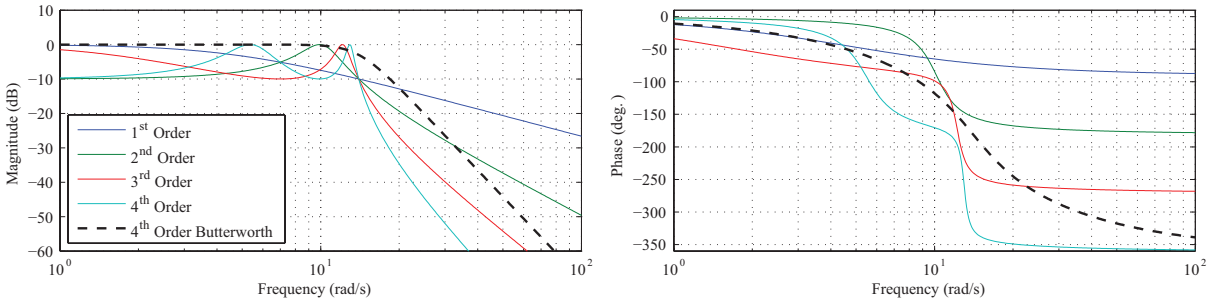

Figure C.5: Effect of increasing order of Chebyshev filter.

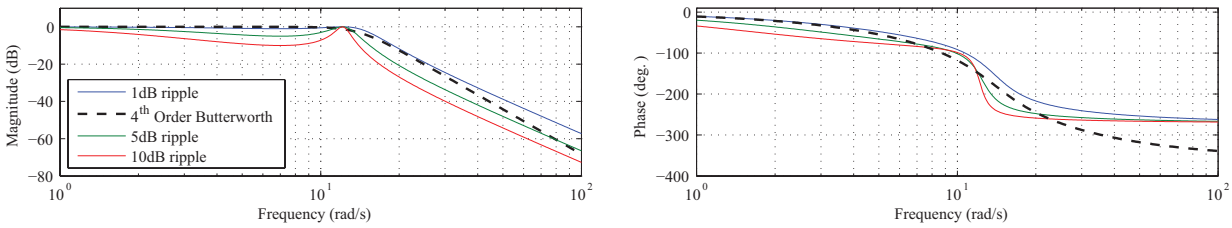

Figure C.6: Effect of varying the magnitude of ripple band (third order Chebyshev filter).

Comparing time-domain performance can also help select the appropriate filter. In this case, features of the step response can be used. In Figure C.7, step responses of first and fourth order Butterworth filters are compared with a first and third order Chebyshev filters (1 dB ripple band) respectively. Comparing the first order response clearly demonstrates the superiority of the Chebyshev filter in the time domain. With regards to the higher order filters, the Chebyshev filter has a smaller delay and overshoot but the response does not settle as quickly as the Butterworth filter. This is a consequence of allowing the existence of a ripple band in the passband frequency range.

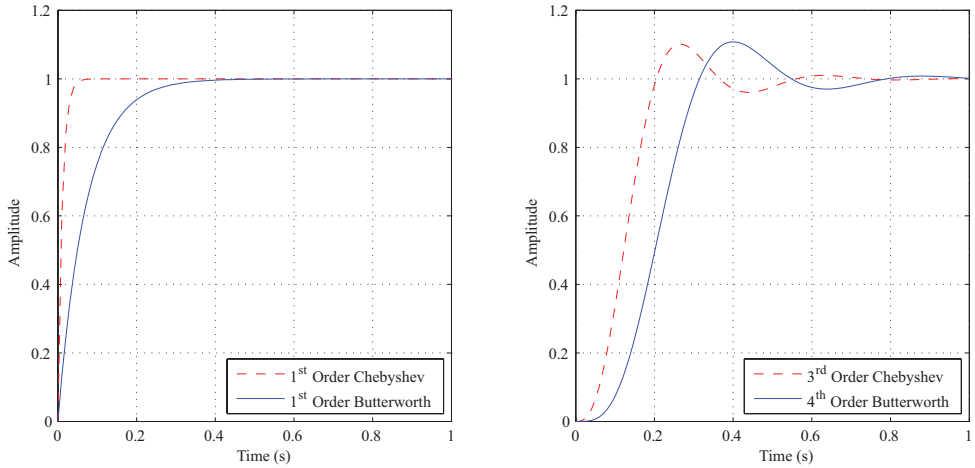

Figure C.7: Comparison of filter step responses.

C.1.3 Effect on aircraft dynamics

Effects due to changes in filter properties on aircraft dynamics were investigated using the AX-1 flexible aircraft model[180]. The aircraft is equipped with a C* longitudinal CSAS with the

following control law:

$$C^* = N_{zp}/g + K_{q_1} q \tag{C.1.3}$$

$$\eta = K_{CS}\delta_\theta - (K_C + K_i/s)\, C^* - K_{q_2} q \tag{C.1.4}$$

The twelve airframe structural modes included for this study are summarised in Table D.2. All modes lie below 30 rad/s, which is the upper limit of manual control frequency range. The filtering schemes shown in Figures C.1 and C.2 will be referred to as schemes A and B respectively. The following sections allow the comparison of the design process and the eventual performance assessment.

C.1.4 Filtering scheme A

The performance of Butterworth and Chebyshev filters were investigated in Sections C.1.1 and C.1.2. For this scheme a third order Chebyshev filter with 0.1dB ripple band was selected because it features a sharper knee and introduces smaller phase lags compared to the fourth order Butterworth filter. It also introduces fewer states but provides performance equivalent to a Butterworth filter of a higher order. The selected filter transfer function is as follows:

$$G_f(s) = \frac{9553.1}{(s + 17.5)(s^2 + 17.5s + 547.5)} \tag{C.1.5}$$

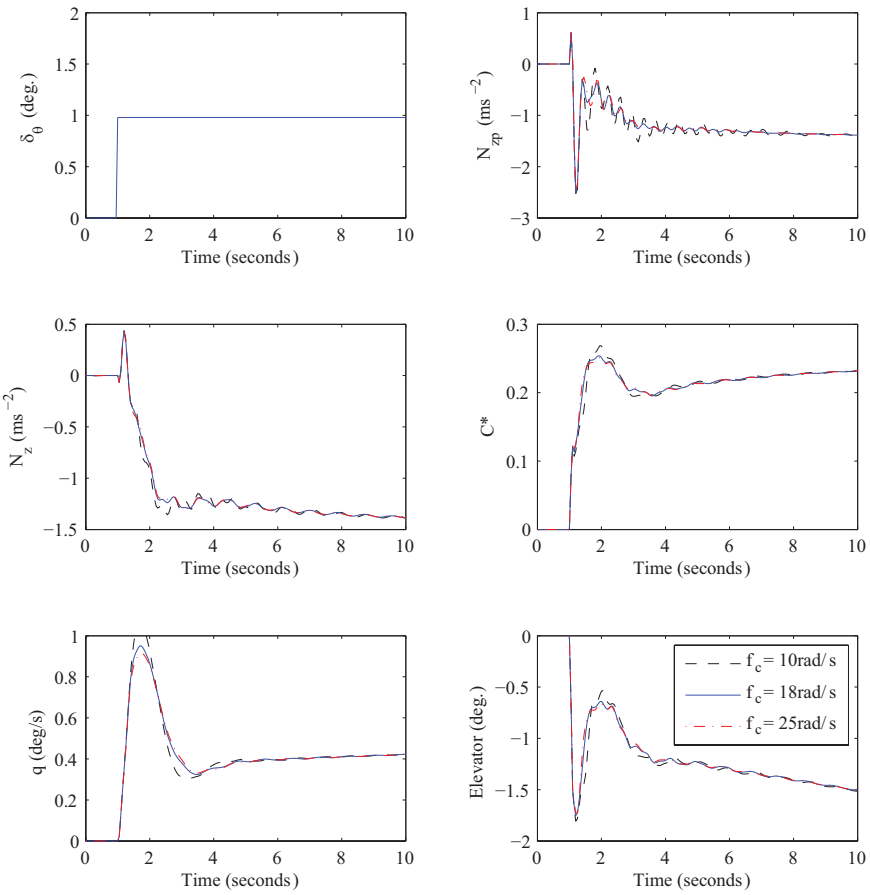

Figure C.8: Effect of varying filter cut-off frequency.

The filter cut-off frequency was selected by considering the aircraft response to a step stick deflection as shown in Figure C.8. This frequency should be selected such that the FCS is not impaired when controlling rigid body dynamics. Therefore, a lower bound for this frequency would be 10 rad/s; well above the aircraft's short period pitch oscillation frequency of approximately 3 rad/s. The key parameter when selecting this frequency was N_{zp} because it is a cue used by the pilot during manual control and is also an indication of ride comfort. A cut-off frequency of 18 rad/s was selected after comparing aircraft step response with different frequencies.

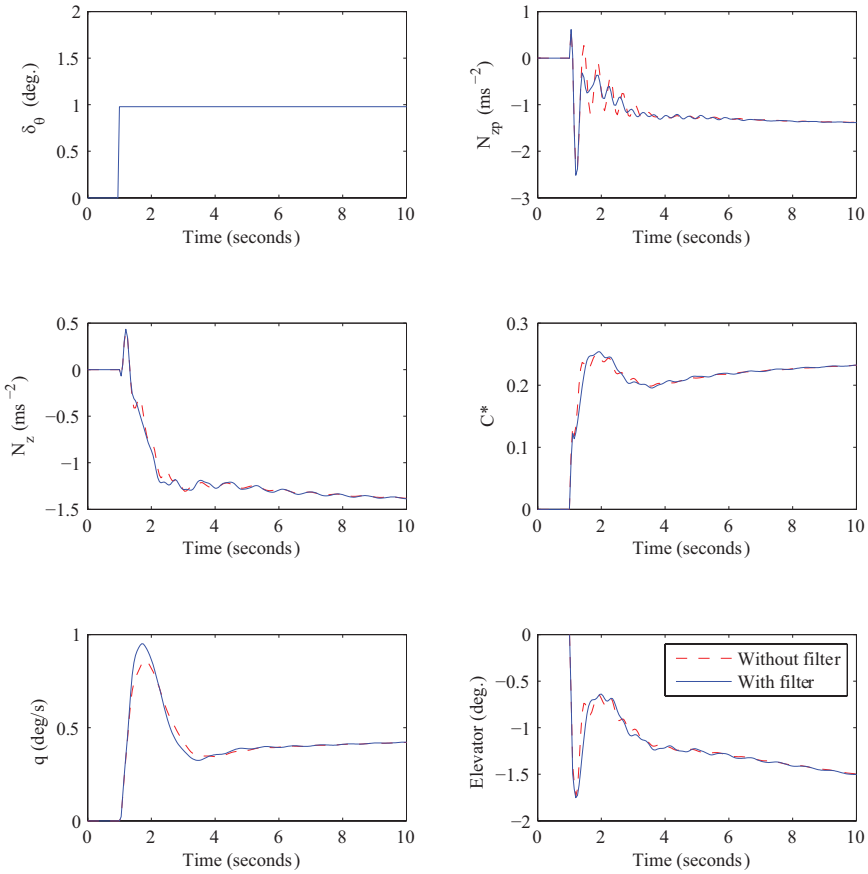

Figure C.9: Effect of filtering on aircraft step response.

The improvement can be seen in Figure C.9 where aircraft step response with and without the filter is presented. Again, inspecting N_{zp}, it can be seen that the response after the initial sharp overshoot remains below zero. Therefore, for greater stick deflections the pilot will no longer feel an opposite acceleration cue.

Figure C.10 shows the effects of filtering on aircraft stick to N_{zp} frequency response, which has been affected in three major areas:

1. Response between 1 rad/s and 10 rad/s has been amplified; aircraft is more responsive within this frequency range.

2. The resonant peak around 11 rad/s has been attenuated by 5 dB such that majority of the peak lies below 0dB. This affect is evident in the less oscillatory step response.

3. A phase lag of approximately 25° has been introduced around 10 rad/s; which lies within the manual control frequency range.

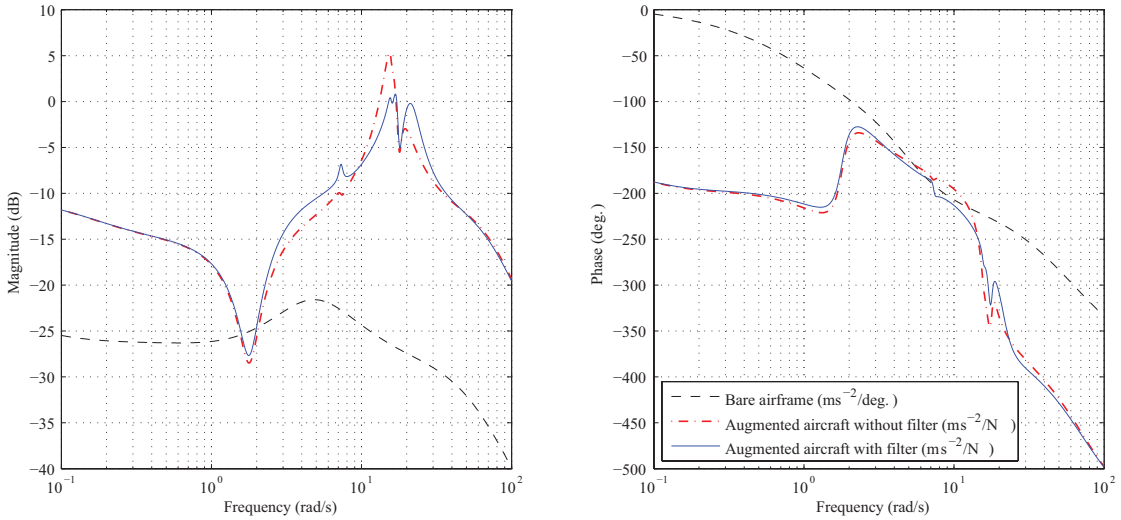

Figure C.10: Effect of structural mode filter on stick force to N_{zp} frequency response.

C.1.5 Filtering scheme B

Unlike scheme A that only limited the bandwidth of FCS demands to the actuation system, scheme B also puts an upper limit on the frequency at which the pilot can drive the system. In this case, Chebyshev filters were found to be either ineffective or inferior to Butterworth filters. It was found that even with ripple bands as small as 0.1 dB, Chebyshev filters introduced unwanted oscillations into aircraft response.

Figures C.11 and C.12 show the effects of varying the order and cut-off frequencies of Butterworth filters. A first order filter with a cut-off frequency of 10rad/s was selected on the basis of faster response time and a less oscillatory response shape. The filter transfer function is as follows:

$$G_f(s) = \frac{10}{s+10} \tag{C.1.6}$$

Figure C.13 allows the comparison of aircraft response with no filtering and with first order Chebyshev and Butterworth filters. The Chebyshev filter has almost no affect on aircraft response whilst the effect of the Butterworth filter is similar to Scheme A.

However, the penalty of improving time domain response and attempting to limit the effects of both pilot and FCS demands on aeroelastic modes becomes evident when inspecting the resulting frequency response shown in Figure C.14. The placement of the filter in series results in dramatic high frequency attenuation and phase lag. The resonant peak around 11rad/s now lies entirely below 0dB and the phase lag of 46 at the filter cut-off frequency is almost twice that of Scheme A. Such contrast in frequency domain response highlight the different method of manual control required for small combat aircraft when compared to large flexible aircraft. Thus, scheme A is most often implemented for small combat aircraft that are primarily flown in the frequency domain. On the other hand, time domain characteristics are far more important for large aircraft handling qualities. Therefore, scheme B was selected for implementation because it prevents interaction between both pilot and FCS and results in similar time domain performance.

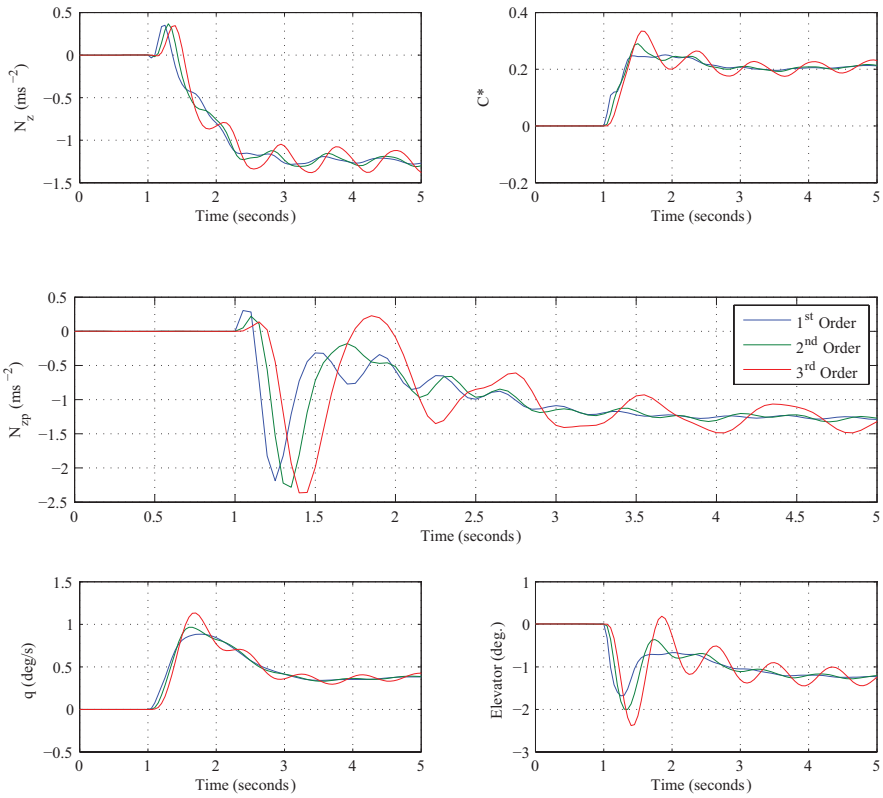

Figure C.11: Effect of varying filter order.

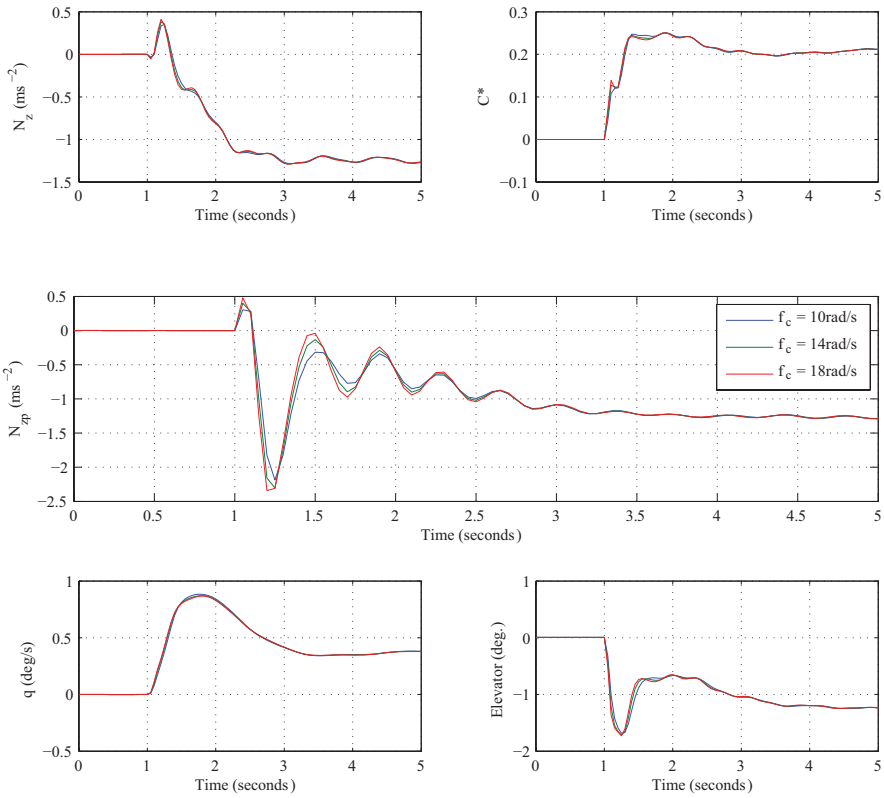

Figure C.12: Effect of varying filter cut-off frequency.

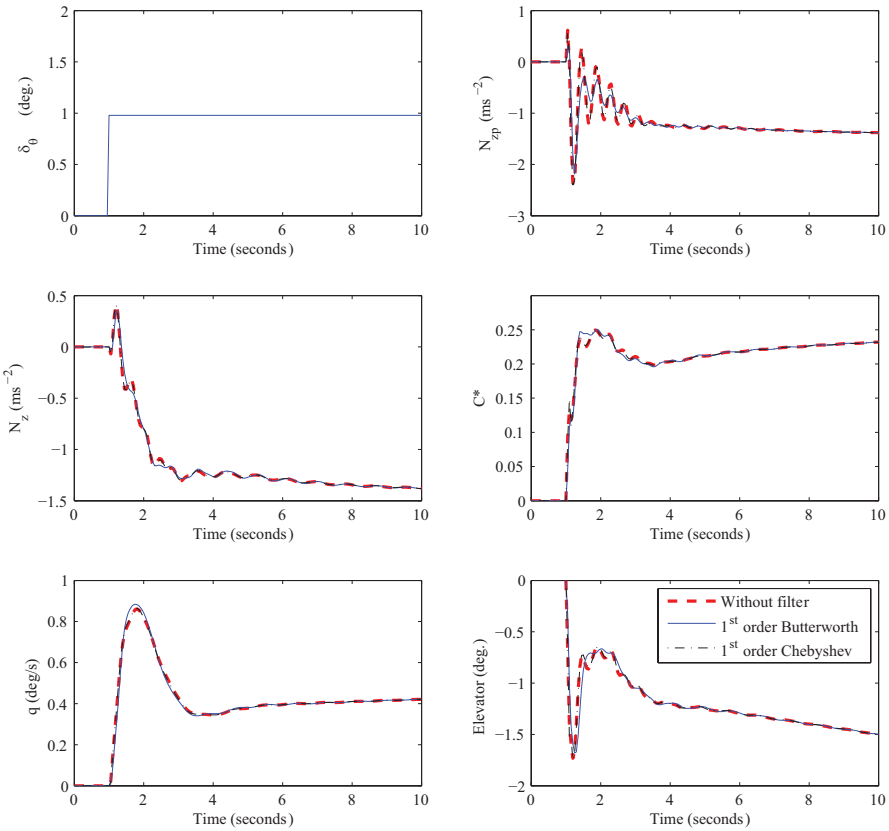

Figure C.13: Effect of filtering on aircraft step response.

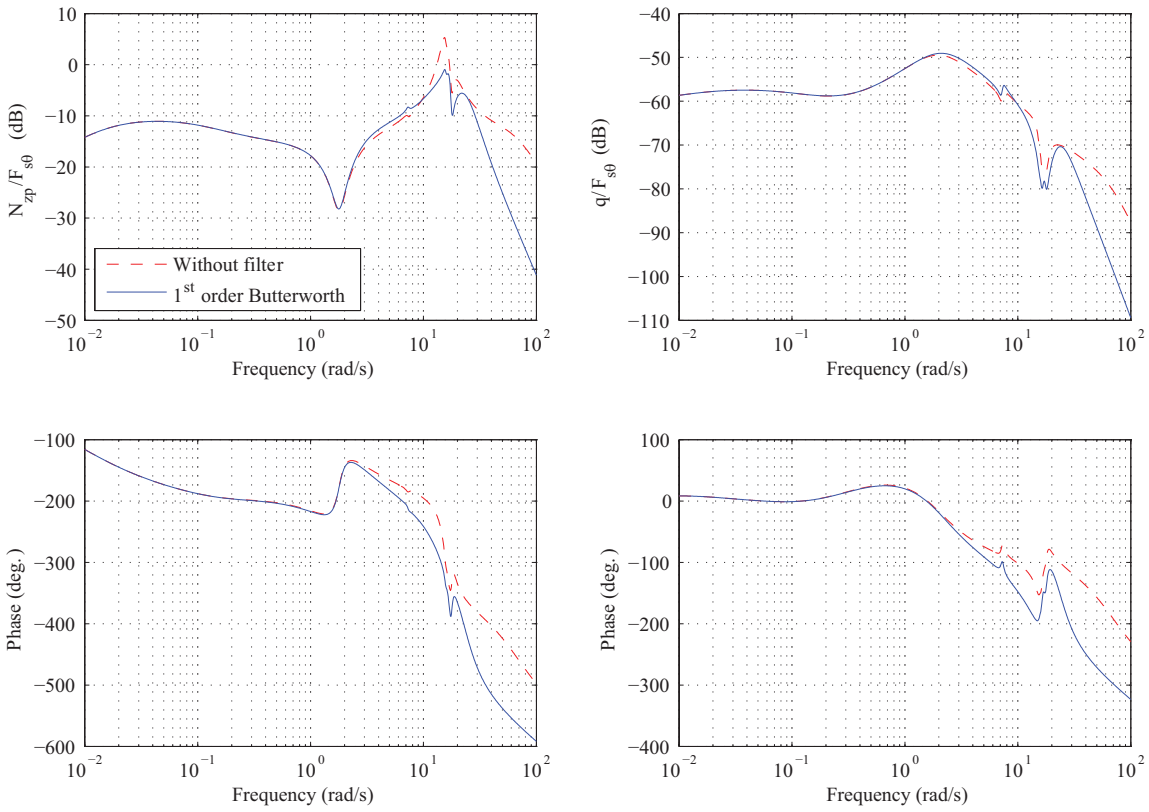

Figure C.14: Effect of structural mode filter on aircraft frequency response.

C.1.6 Conclusions

This study was limited to investigating Butterworth and Type I Chebyshev filters within two schemes. A brief study of filter types found that filter selection is a compromise between attenuation characteristics within the transition region and filter introduced phase lag. Scheme A placed the filters in the FCS feedback path and so limited the bandwidth of FCS demands. Scheme B placed the filters just before the actuation system and so prevented both the pilot and FCS from interacting with the aeroelastic modes. Scheme B was selected for implementation because it prevents interaction between both pilot and FCS and also, because time domain characteristics are more important for manual control of large aircraft.

C.2 Handling qualities assessment

A longitudinal handling qualities assessment was done following the inclusion of the structural mode filters within the FCS. The time-domain Gibson Dropback criterion[70][181] was used here because it was desired that the criterion account for the nonlinear effects introduced by the control surface actuators (rate limiting and saturation), active loads control systems (MLA, GLA and AMC) and unsteady aerodynamics. Therefore, only time domain criteria were suitable. It was also desired that the concept upon which the criterion is based be relatable to manual control experiments. The Dropback criterion's reliance on effectively a tracking task together with features easily observable by a subject when performing a pitch control task made it the most suitable criterion. The parameters used in this criterion are presented in Figure C.15.

Figure C.16 shows the effect of airspeed on handling qualities at 5000ft and 30000ft. Figure C.17 and Table C.1 show results from all the flight conditions at which the criterion was evaluated. Improvements due to the FCS are clear if the positions of the unaugmented and augmented cases are compared. Satisfactory handling qualities were predicted for the augmented aircraft at all flight conditions

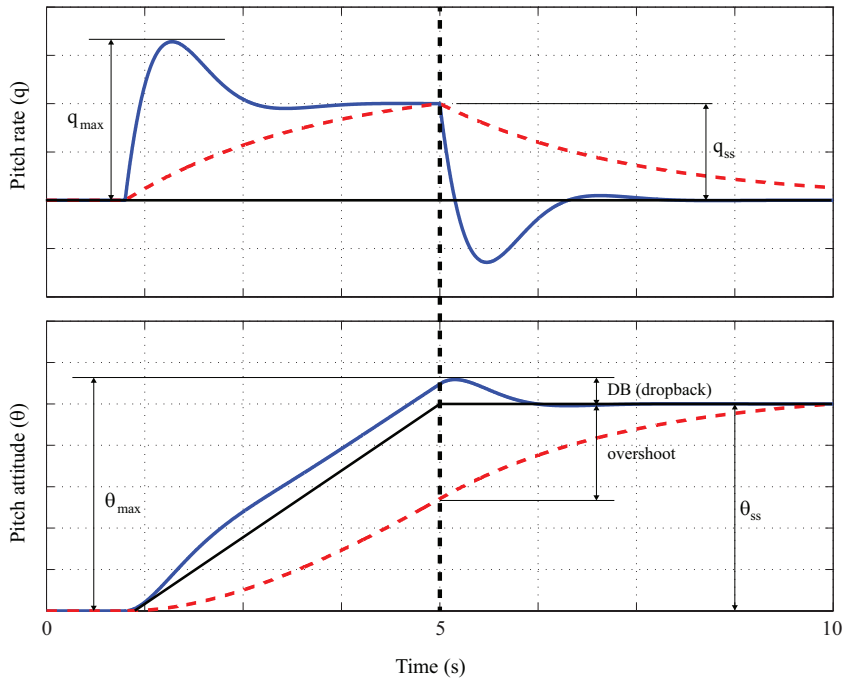

Figure C.15: Response characteristics used for evaluating the Gibson Dropback criterion.

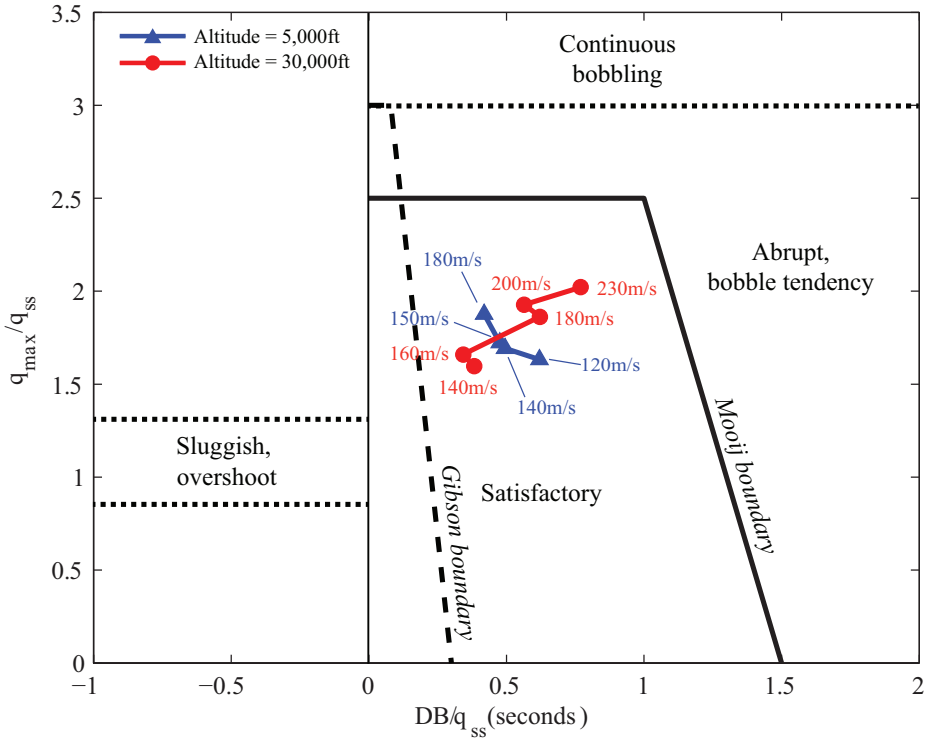

Figure C.16: Effect of airspeed on longitudinal handling qualities of the augmented AX-1 model.

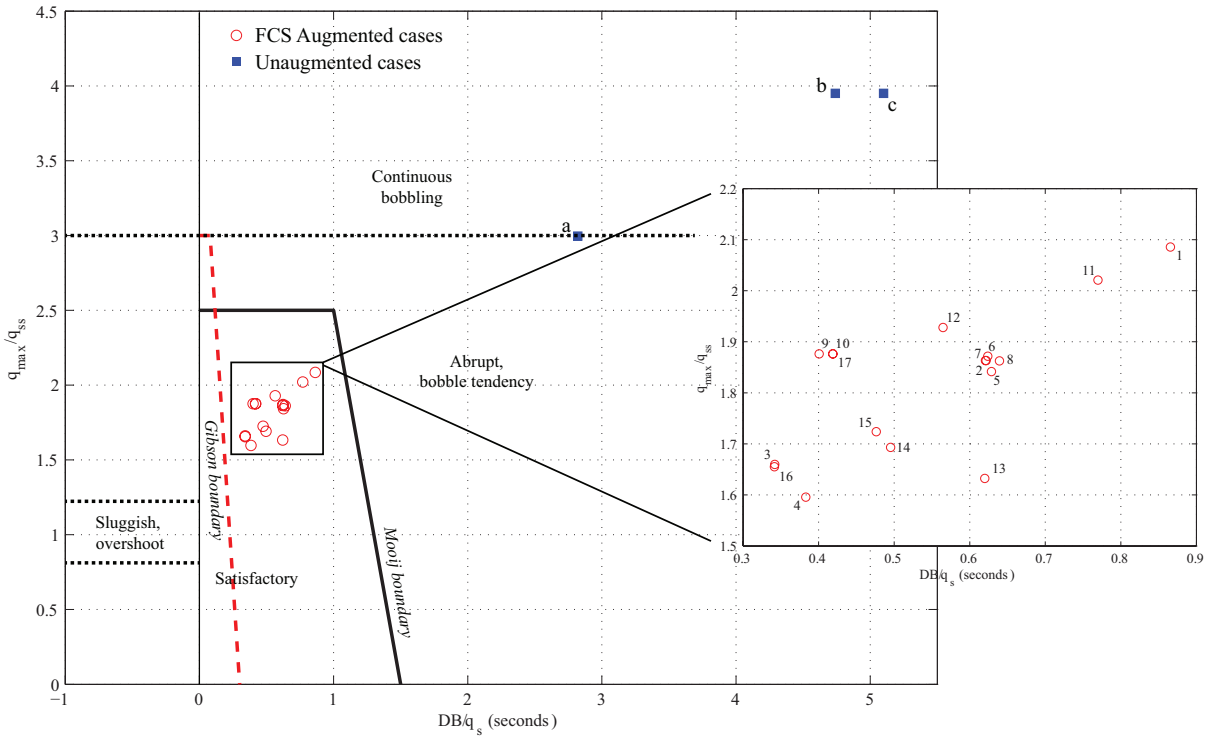

Figure C.17: Handling qualities performance of the FCS at various flight conditions.

Future work should consider using the time-domain Neal-Smith for this assessment. Although the criterion is more involved and requires an optimisation process, the explicit use of pilot models may allow the predicted handling qualities to be related to the pilot model parameters found in Chapter 3.

Run	Mach	V_{TAS} (m/s)	α_{trim} (rad)	q_{max} (rad/s)	q_{ss} (rad/s)	q_{max}/q_{ss}	θ_{max} (rad)	θ_{ss} (rad)	DB	DB/q_{ss} (s)	Altitude (ft)
FCS augmented cases											
1	0.688	210	0.05	0.011	0.005	2.085	0.084	0.08	0.004	0.866	28848.6
2	0.594	180	0.05	0.01	0.005	1.863	0.09	0.086	0.003	0.622	30175.2
3	0.528	160	0.05	0.01	0.006	1.66	0.065	0.063	0.002	0.342	30175.2
4	0.462	140	0.05	0.01	0.006	1.596	0.096	0.094	0.002	0.383	30175.2
5	0.665	210	0.05	0.008	0.004	1.841	0.048	0.046	0.003	0.629	27036.9
6	0.607	180	0.05	0.01	0.005	1.872	0.089	0.085	0.003	0.624	35204.4
7	0.581	180	0.05	0.01	0.005	1.863	0.091	0.087	0.003	0.621	25146
8	0.57	180	0.05	0.01	0.005	1.863	0.092	0.088	0.004	0.639	20116.8
9	0.548	180	0.05	0.01	0.005	1.876	0.054	0.052	0.002	0.401	10058.4
10	0.538	180	0.05	0.01	0.005	1.876	0.054	0.052	0.002	0.419	5029.2
11	0.759	230	0.05	0.002	0.001	2.021	0.017	0.016	0.001	0.77	30175.2
12	0.66	200	0.05	0.01	0.005	1.928	0.063	0.06	0.003	0.565	30175.2
13	0.359	120	0.05	0.011	0.007	1.632	0.162	0.157	0.004	0.62	5029.2
14	0.419	140	0.05	0.011	0.006	1.693	0.113	0.11	0.003	0.495	5029.2
15	0.449	150	0.05	0.011	0.006	1.724	0.094	0.092	0.003	0.476	5029.2
16	0.474	160	0.05	0.01	0.006	1.656	0.068	0.066	0.002	0.341	20116.8
17	0.538	180	0.05	0.01	0.005	1.876	0.054	0.052	0.002	0.419	5029.2
Unaugmented cases											
a	0.688	210	0.05	0.034	0.009	3.946	-	-	0.04	4.736	28667.1
b	0.665	210	0.05	0.037	0.012	2.996	-	-	0.035	2.817	20116.8
c	0.678	210	0.05	0.034	0.009	3.95	-	-	0.043	5.1	25146

Table C.1: Evaluation data for Gibson Dropback criteria.

APPENDIX D

Mass case for loads envelope generation

Table D.1 presents the weight breakdown for this case and the resulting centre of gravity. Equation D.0.1 presents the corresponding inertia matrix (in kgm^2). The mode shapes and frequencies are presented in Figure D.1 and Table D.2 respectively.

		Centre of Gravity (Model Axis)		
Component	Mass (kg)	x (m)	y (m)	z (m)
Operational empty weight	131218.402	-5.207	0	-0.896
Fuel	24269.500	-6.355	0	-0.641
Passengers	18870.000	-5.341	0	-1.268
Cargo	19855.671	+2.111	0	+0.335
Total	194213.573	-4.616	0	-0.774
Maximum Take-Off Weight	257000.000			

Table D.1: Weight breakdown for mass case used to derive flight loads envelope.

$$\begin{bmatrix} I_{XX} & I_{XY} & I_{XZ} \\ I_{YX} & I_{YY} & I_{YZ} \\ I_{ZX} & I_{ZY} & I_{ZZ} \end{bmatrix} = \begin{bmatrix} +1.282E+07 & -5.901E-11 & -1.082E+06 \\ -5.901E-11 & +2.617E+07 & +5.556E-12 \\ -1.082E+06 & +5.556E-12 & +3.860E+07 \end{bmatrix} \quad \text{(D.0.1)}$$

Sample time histories from continuous turbulence simulations at Mach 0.6 and 20000ft is shown in Figure D.2. This has been included to demonstrate the functioning of the GLA and AMC active loads control systems.

Details of the modelling approach adopted to develop the Cranfield University/Airbus AX-1 flight loads model together with its implementation in MATLAB/Simulink® are thoroughly discussed by Andrews in his thesis[9], Airbus update reports[182][180][183][184][185] and publications[103][9].

Mode no.	Mode type	Frequency (rad/s)
1	Wing (Asymmetric)	6.9
2	Wing (Symmetric)	6.9
3	Wing+Fuselage (Symmetric)	7.5
4	Wing+HTP+Fuselage (Asymmetric)	12.8
5	Wing+Fuselage (Asymmetric)	14.7
6	Wing+HTP+Fuselage (Asymmetric)	16.0
7	Wing (Asymmetric)	16.2
8	Wing (Symmetric)	16.2
9	Wing+HTP+Fuselage (Symmetric)	16.9
10	Wing+HTP (Asymmetric)	17.2
11	Wing (Asymmetric)	18.4
12	Wing (Symmetric)	18.4

Table D.2: Aircraft structural mode types and frequencies.

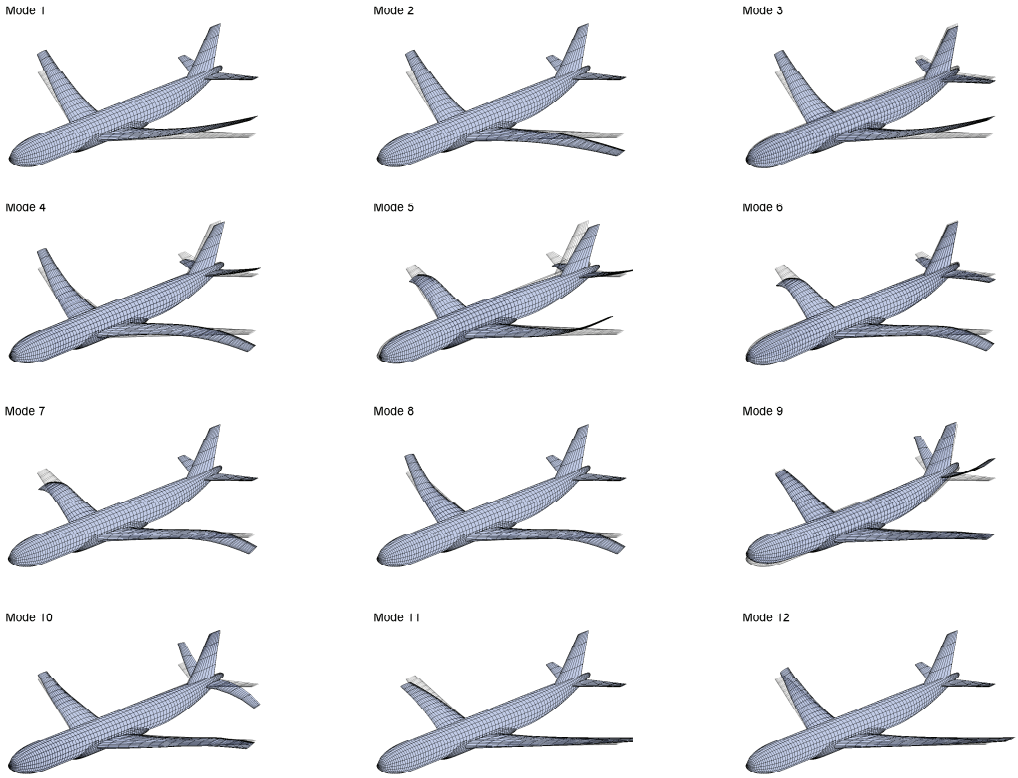

Figure D.1: Airframe flexible mode shapes.

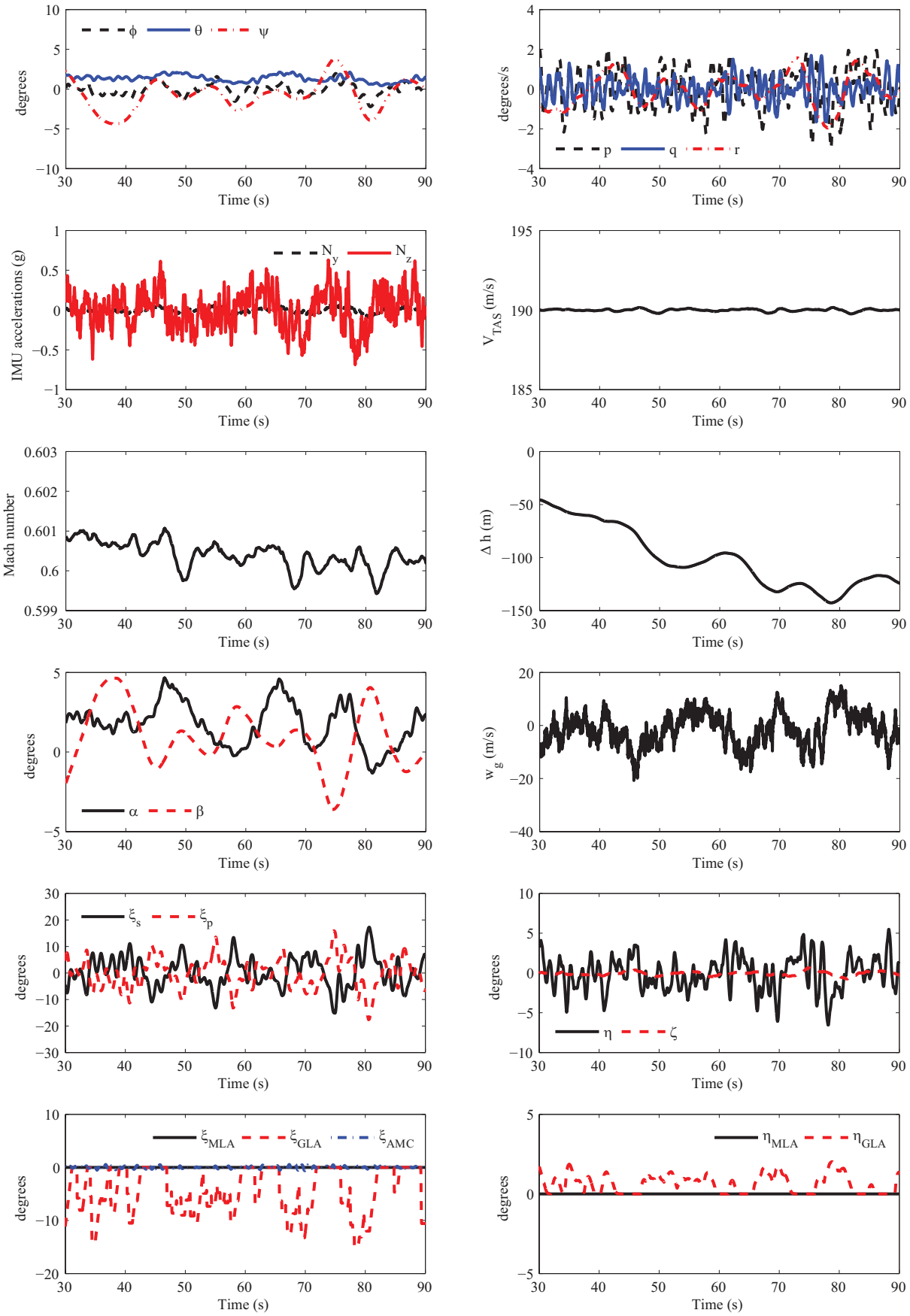

Figure D.2: Example simulation time history with LAF on.

This page is intentionally left blank.

APPENDIX E

Derivation of lateral biomechanical model

The discrete biomechanical model shown in Figure E.1, reproduced below for convenience, will be used to model lateral biodynamics.

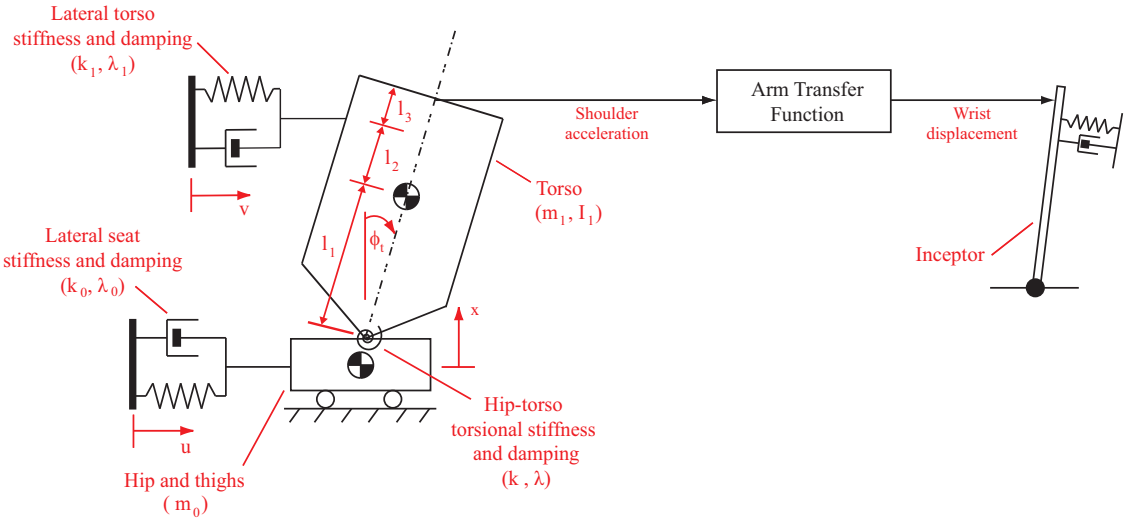

Figure E.1: Lateral biomechanical model.

Equations of motion for the torso may be derived via the extended Euler-Lagrange equation:

$$\frac{d}{dt}\left(\frac{\partial \mathcal{K}}{\partial \dot{q}_i}\right) - \frac{\partial \mathcal{K}}{\partial q_i} + \frac{\partial \mathcal{V}}{\partial q_i} + \frac{\partial \mathcal{D}}{\partial \dot{q}_i} = \mathcal{Q}_i \tag{E.0.1}$$

where K, V and D refer to system kinetic, potential and dissipative energy components respectively. These can be found to be:

$$\mathcal{K} = \frac{1}{2}(m_0 + m_1)\dot{x}^2 + \frac{1}{2}\dot{\phi}_t^2(I_1 + m_1 l_1^2) \tag{E.0.2}$$

$$\mathcal{V} = \frac{1}{2}k_0(x-u)^2 + \frac{1}{2}k_1\phi_t^2 + \frac{1}{2}k_2(l_1\sin\phi_t - u)^2 + m_1 g l_1(1-\cos\phi_t) \tag{E.0.3}$$

$$\mathcal{D} = \frac{1}{2}\lambda_0(\dot{x}-\dot{u})^2 + \frac{1}{2}\lambda_1\dot{\phi}_t^2 + \frac{1}{2}\lambda_2(\dot{\phi}_t l_1\cos\phi_t - \dot{u})^2 \tag{E.0.4}$$

$\mathcal{Q}_i$ refers to the generalised force associated with generalised coordinate q_i. Assuming both the upper and lower torso parts are excited by the same input, that is $u(t) = v(t)$, Equation E.0.1 yields the following nonlinear equations of motion for the torso:

$$(m_0 + m_1)\ddot{x} + \lambda_0\dot{x} + k_0 x = \lambda_0\dot{u} + k_0 u + m_0 g\cos\phi \tag{E.0.5}$$

$$(m_1 l_1^2 + I_1)\ddot{\phi_t} + (\lambda + \lambda_1 l_1^2\cos^2\phi_t)\dot{\phi_t} + k\phi_t + 0.5k_1 l_1^2\sin 2\phi_t = m_1 l_1 g\cos(\phi + \phi_t) + \dot{u}\lambda_1 l_1\cos\phi_t + uk_1 l_1\cos\phi_t \tag{E.0.6}$$

Gravity has been treated as a roll attitude dependant force input. The above equations fit into the following general form after linearisation about a seating posture:

$$\mathbf{M}\ddot{\varrho} + \mathbf{\Lambda}\dot{\varrho} + \mathbf{K}\varrho = \mathbf{\Lambda}_\varphi\dot{\varphi} + \mathbf{K}_\varphi\varphi \tag{E.0.7}$$

where $\mathbf{M}$, $[\mathbf{\Lambda}, \mathbf{\Lambda}_\varphi]$ and $[\mathbf{K}, \mathbf{K}_\varphi]$ are the system mass, damping and stiffness matrices respectively and vectors

$$\varrho = \begin{bmatrix} \delta x & \delta\phi_t \end{bmatrix} \tag{E.0.8}$$

$$\varphi = \begin{bmatrix} \delta u \end{bmatrix} \tag{E.0.9}$$

contain the generalised coordinate variables and system inputs respectively. Linearisation about a torso inclination angle (ϕ_{t0}) and a roll attitude, ϕ_0 yields the following:

$$\mathbf{M} = \begin{bmatrix} m_0 + m_1 & 0 \\ 0 & m_1 l_1^2 + I_1 \end{bmatrix} \tag{E.0.10}$$

$$\mathbf{\Lambda} = \begin{bmatrix} \lambda_0 & 0 \\ 0 & \lambda + \lambda_1 l_1^2\cos^2\phi_{t0} \end{bmatrix} \tag{E.0.11}$$

$$\mathbf{K} = \begin{bmatrix} k_0 & 0 \\ 0 & k + k_1 l_1^2\cos 2\phi_{t0} + m_1 l_1 g\cos\phi_{t0} \end{bmatrix} \tag{E.0.12}$$

$$\mathbf{\Lambda}_\mu = \begin{bmatrix} \lambda_0 & 0 \\ 0 & \lambda_1 l_1\cos\phi_{t0} \end{bmatrix} \tag{E.0.13}$$

$$\mathbf{K}_\mu = \begin{bmatrix} k_0 & 0 \\ 0 & k_1 l_1\cos\phi_{t0} \end{bmatrix} \tag{E.0.14}$$

Therefore, the torso model takes the following state-space form:

$$\begin{bmatrix} 1 & 0 & 0 & 0 \\ 0 & m_0 + m_1 & 0 & 0 \\ 0 & 0 & 1 & 0 \\ 0 & 0 & 0 & m_1 l_1^2 + I_1 \end{bmatrix} \begin{bmatrix} \delta\dot{x} \\ \delta\ddot{x} \\ \delta\dot{\phi_t} \\ \delta\ddot{\phi_t} \end{bmatrix} = \begin{bmatrix} 0 & 1 & 0 & 0 \\ -k_0 & -\lambda_0 & 0 & 0 \\ 0 & 0 & 0 & 1 \\ 0 & 0 & -\check{h} & -\lambda - \lambda_1 l_1^2\cos^2\phi_{t0} \end{bmatrix} \begin{bmatrix} \delta x \\ \delta\dot{x} \\ \delta\phi \\ \delta\dot{\phi} \end{bmatrix} + \begin{bmatrix} 0 & 0 & 0 \\ k_0 & \lambda_0 & -m_0 g\sin\phi_0 \\ 0 & 0 & 0 \\ k_1 l_1\cos\phi_{t0} & \lambda_1 l_1\cos\phi_{t0} & -m_1 l_1 g\sin(\phi_0 + \phi_{t0}) \end{bmatrix} \begin{bmatrix} \delta u \\ \delta\dot{u} \\ \delta\phi_g \end{bmatrix} \tag{E.0.15}$$

where,

$$\check{h} = k + k_1 l_1^2\cos 2\phi_{t0} + m_1 l_1 g\cos\phi_{t0} \tag{E.0.16}$$

The following state-space system, which is effectively a double integrator then allows lateral acceleration (δN_{yp}) to be an input to the torso model:

$$\begin{bmatrix} \dot{a}_1 \\ \dot{a}_2 \\ \dot{a}_3 \end{bmatrix} = \begin{bmatrix} 0 & 1 & 0 \\ 0 & 0 & 0 \\ 0 & 0 & 0 \end{bmatrix} \begin{bmatrix} a_1 \\ a_2 \\ a_3 \end{bmatrix} + \begin{bmatrix} 0 & 0 \\ 1 & 0 \\ 0 & 0 \end{bmatrix} \begin{bmatrix} \delta N_{yp} \\ \delta\phi \end{bmatrix} \tag{E.0.17}$$

$$\begin{bmatrix} \delta u \\ \delta \dot{u} \\ \delta\phi \end{bmatrix} = \begin{bmatrix} 1 & 0 & 0 \\ 0 & 1 & 0 \\ 0 & 0 & 0 \end{bmatrix} \begin{bmatrix} a_1 \\ a_2 \\ a_3 \end{bmatrix} + \begin{bmatrix} 0 & 0 \\ 0 & 0 \\ 0 & 1 \end{bmatrix} \begin{bmatrix} \delta N_{yp} \\ \delta\phi \end{bmatrix} \tag{E.0.18}$$

This page is intentionally left blank.

APPENDIX F

Example gust profiles and pilot-model-in-the-loop simulation results

The gust profiles shown in Figures F.1 to F.2 are obtained as part of the process to reconstruct flight incidents for the estimation of airframe internal loads. The process begins with the extraction of equations of motion from the certification model. This is used to generate impulse response functions describing the effects of control surface deflections and gusts on flight dynamic and loads interesting quantities. These functions are then used to determine the aircraft's response to the recorded control surface deflections. This response is subtracted from the DFDR response to obtain normal acceleration solely due to the gust. Deconvolution then allows the estimation of the vertical gust profile experienced during the incident. Response to this gust profile is then linearly summed with that due to control surface deflections to allow the reconstruction of the incident. The estimated loads are then compared to the certification limit loads envelope to identify areas of the airframe that may be overloaded.

An incident's reconstruction is done by considering only the longitudinal parameters and the aircraft's mass and mass distribution are assumed to be time invariant. Immediately prior to the gust encounter, the aircraft is assumed be in steady trimmed level flight. Moreover, due to the DFDR sampling rate of 8 Hz, the data is filtered to account for potential peaks or troughs missed between two samples. Note that the gust profiles presented in Figures F.1 to F.2 do not adhere to a North-East-Down axes system. Here, the z-axis is assumed to be positive upwards. Therefore, a positive w_g refers to an up-gust.

Figures F.3 to F.7 present the time histories of the flight dynamic parameters, control surface deflections due to CSAS and LAF and the stick forces observed from the pilot-model-in-the-loop simulations discussed in Case 2 of Chapter 7. The wing and HTP loads envelope comparisons of the maximum and minimum non-correlated loads for simulations with different MOCM parameters are shown in Figures F.8 and F.9.

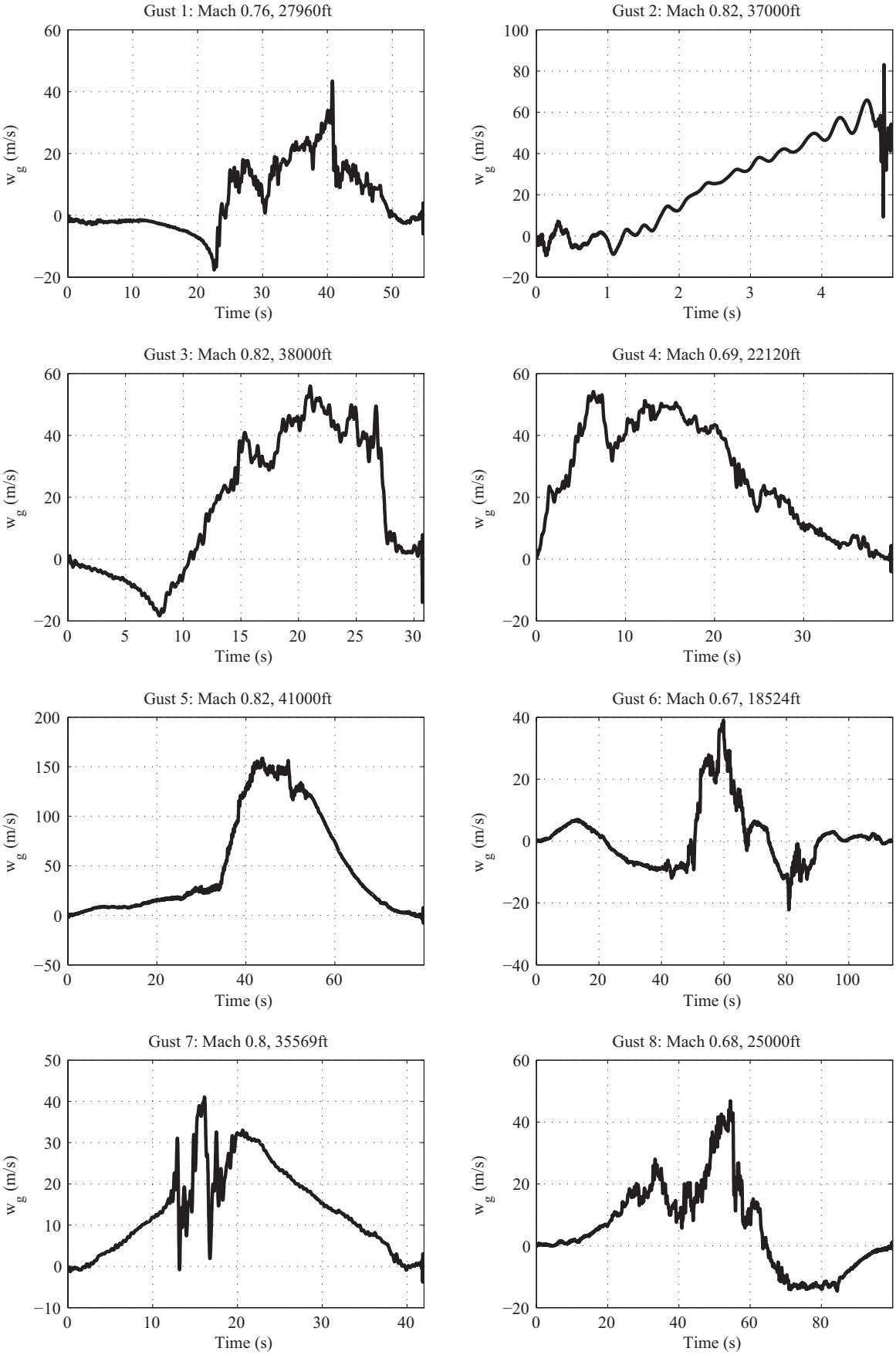

Figure F.1: Gust profiles 1 to 8.

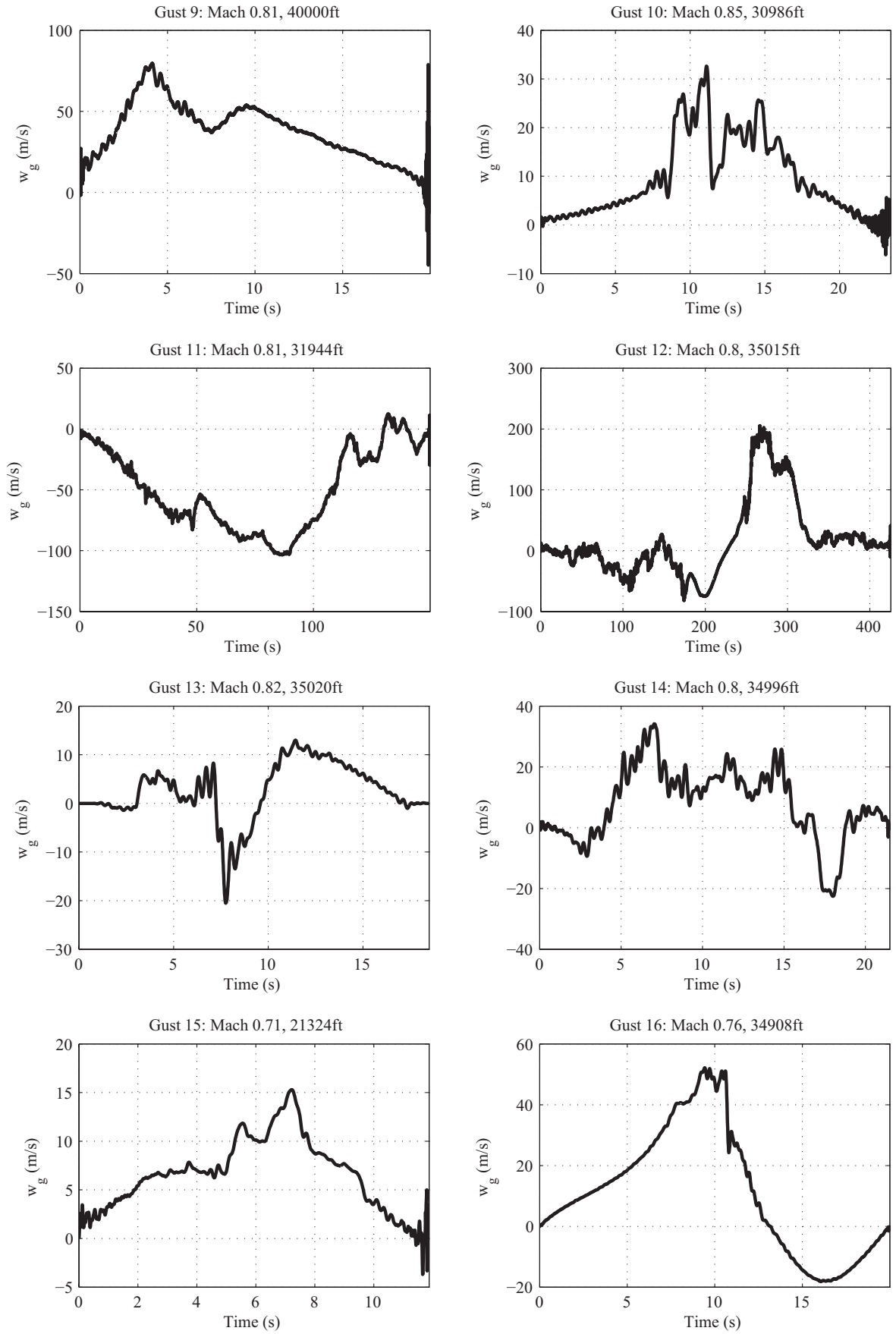

Figure F.2: Gust profiles 9 to 16.

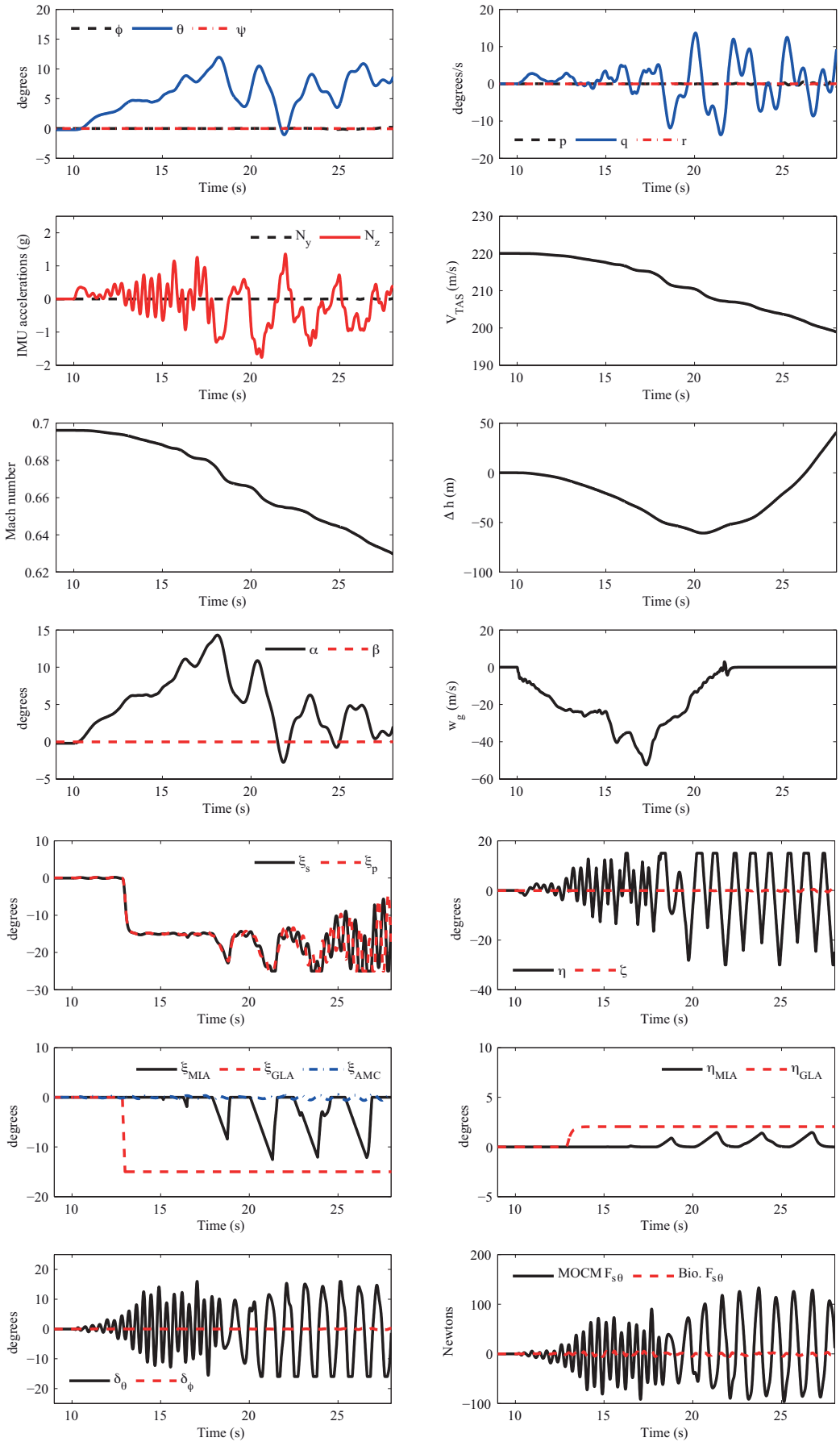

Figure F.3: Gust encounter simulation with aggressive MOCM ($\tau_n = 0.08$) and LAF.

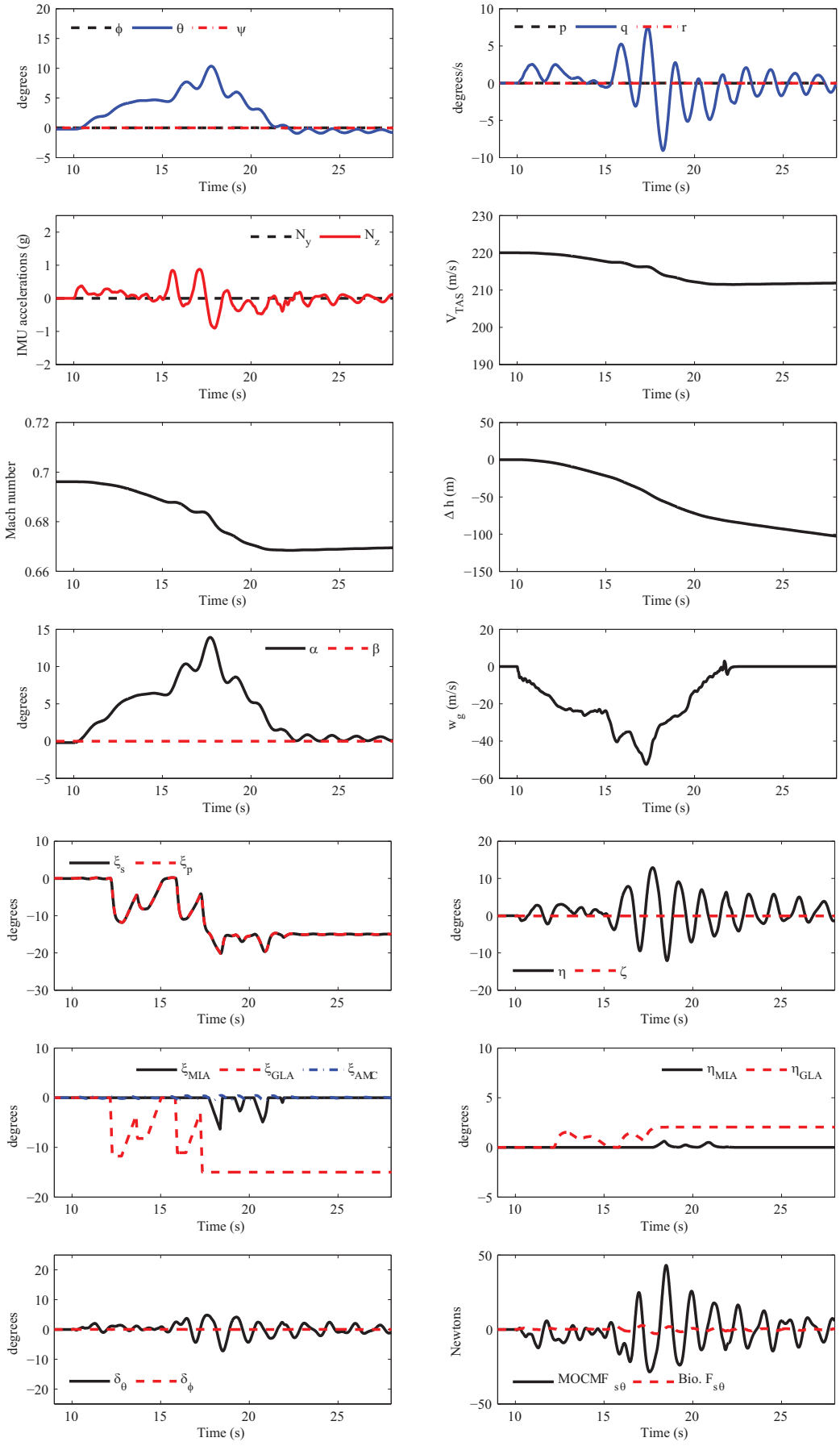

Figure F.4: Gust encounter simulation with aggressive MOCM ($\tau_n = 0.08$), LAF and no fuselage flexibility effects.

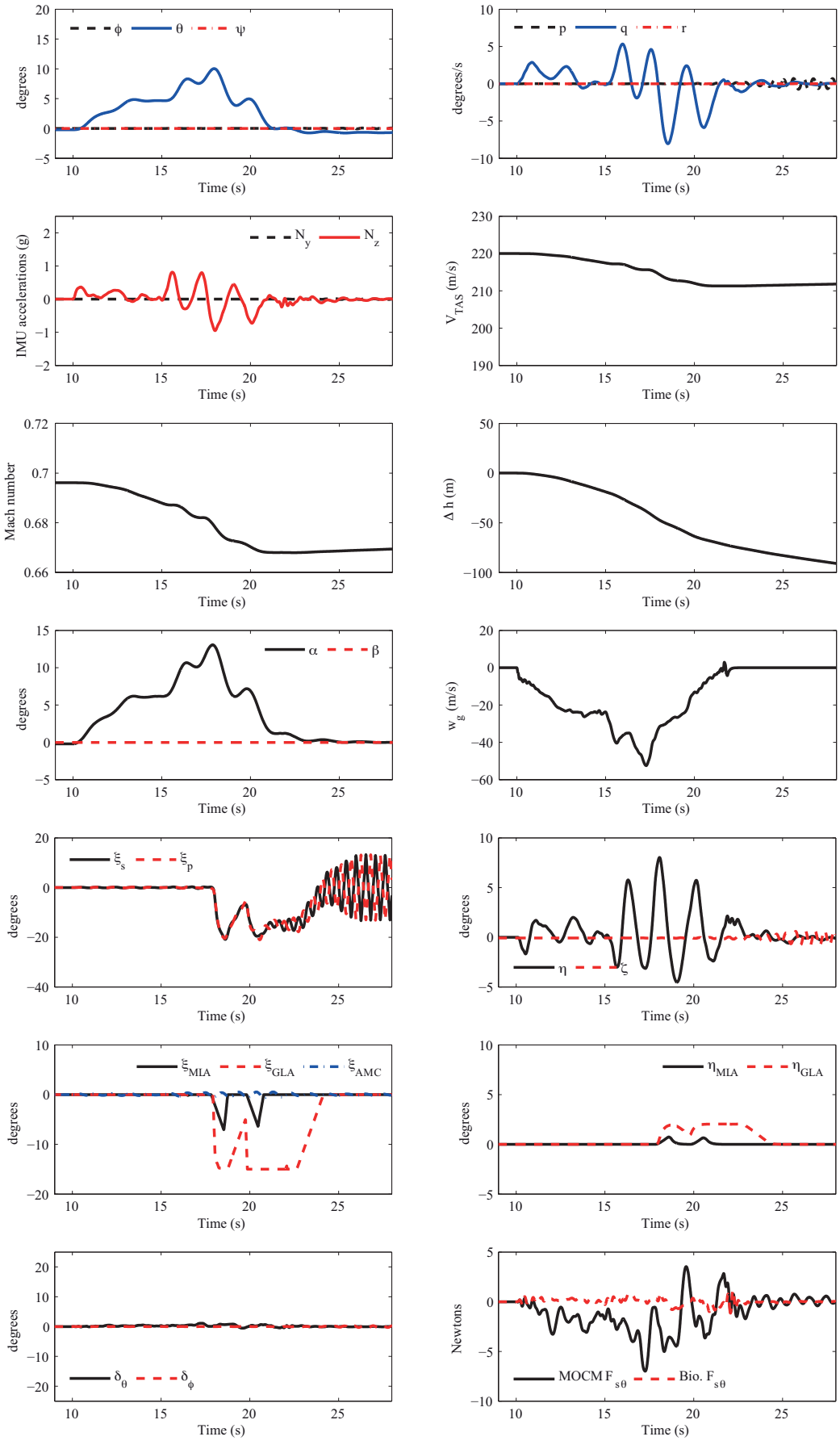

Figure F.5: Gust encounter simulation with passive MOCM ($\tau_n = 0.28$) and LAF.

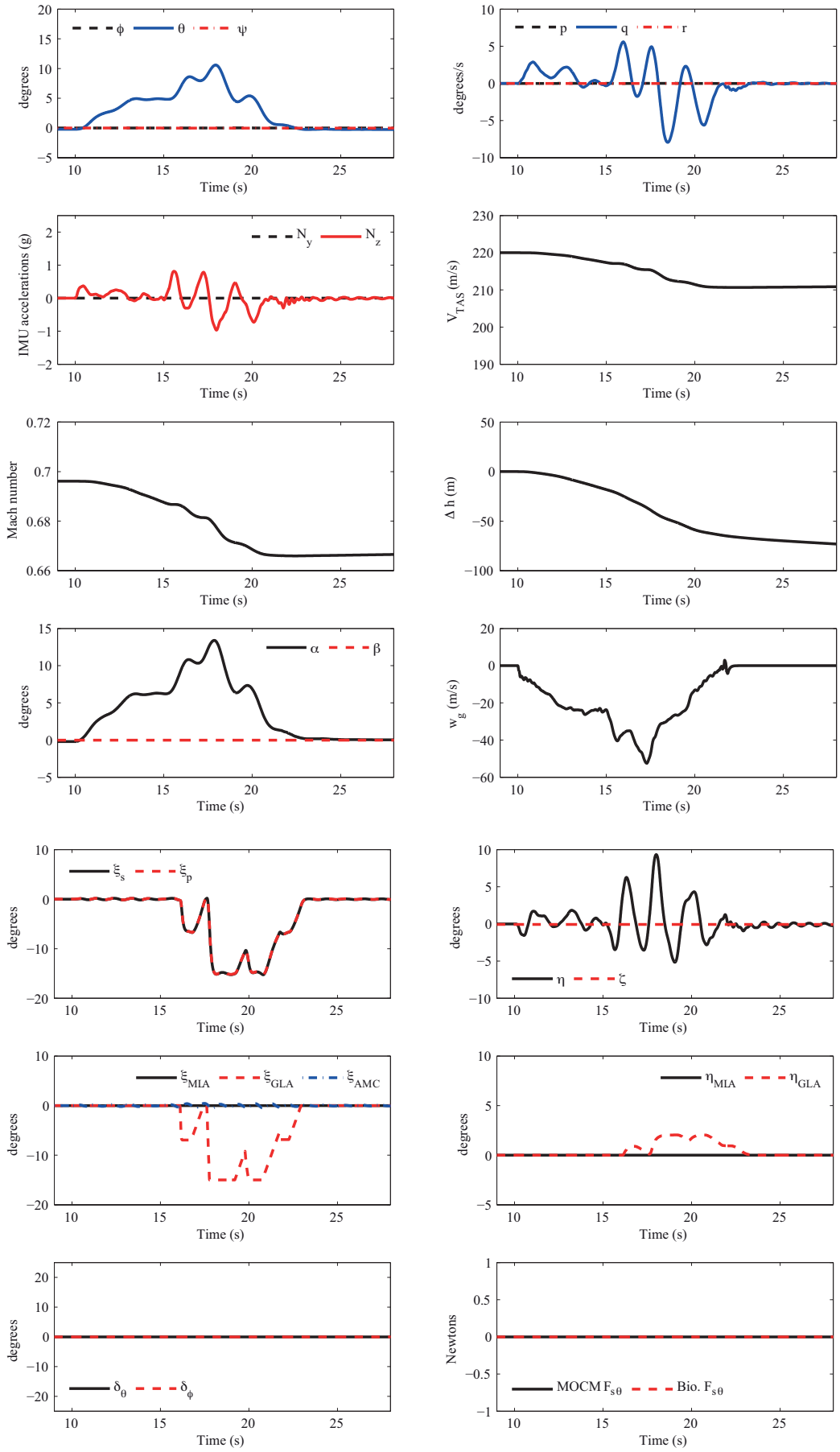

Figure F.6: Gust encounter simulation with LAF only.

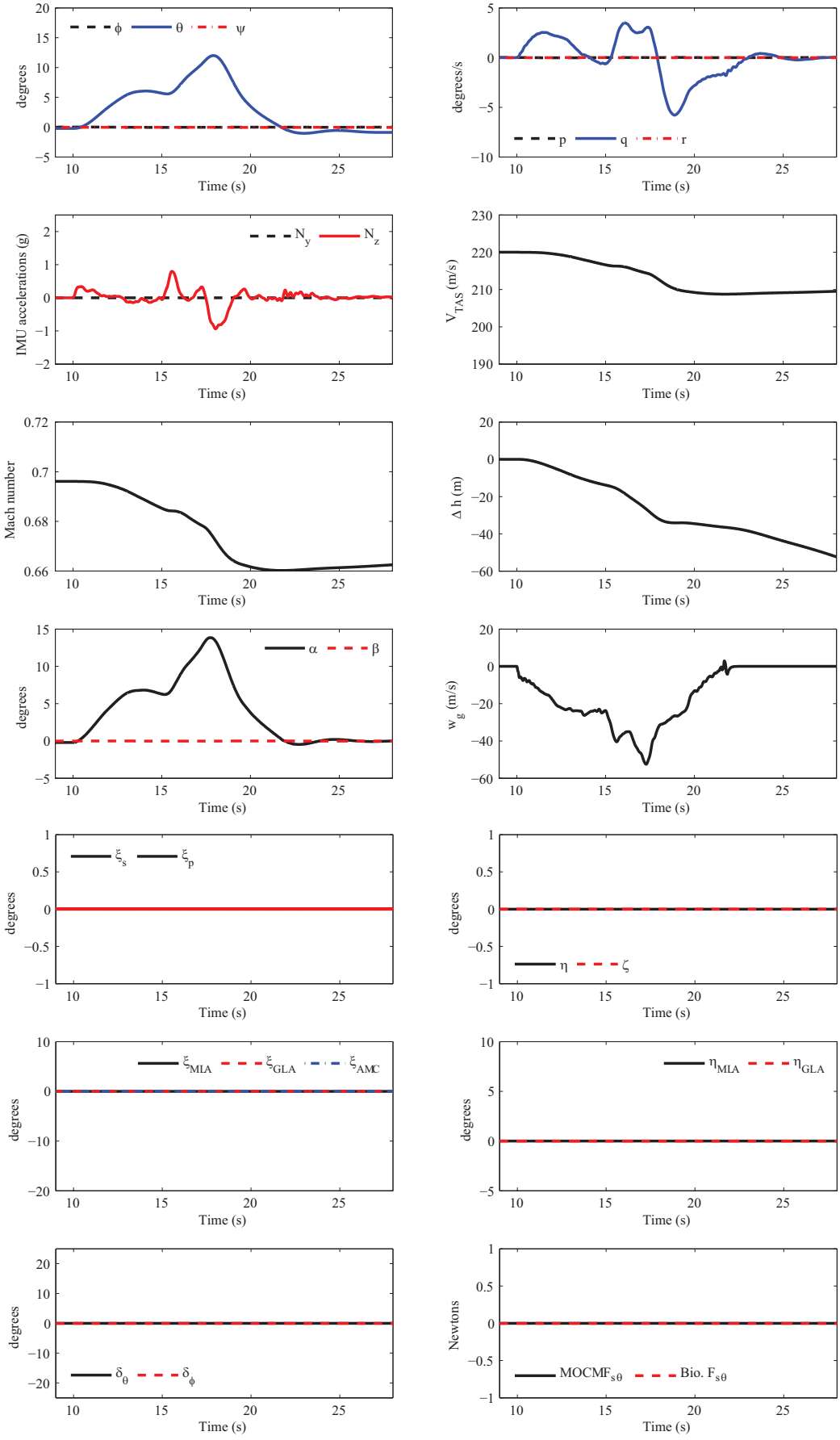

Figure F.7: Gust encounter simulation without control surface deflections.

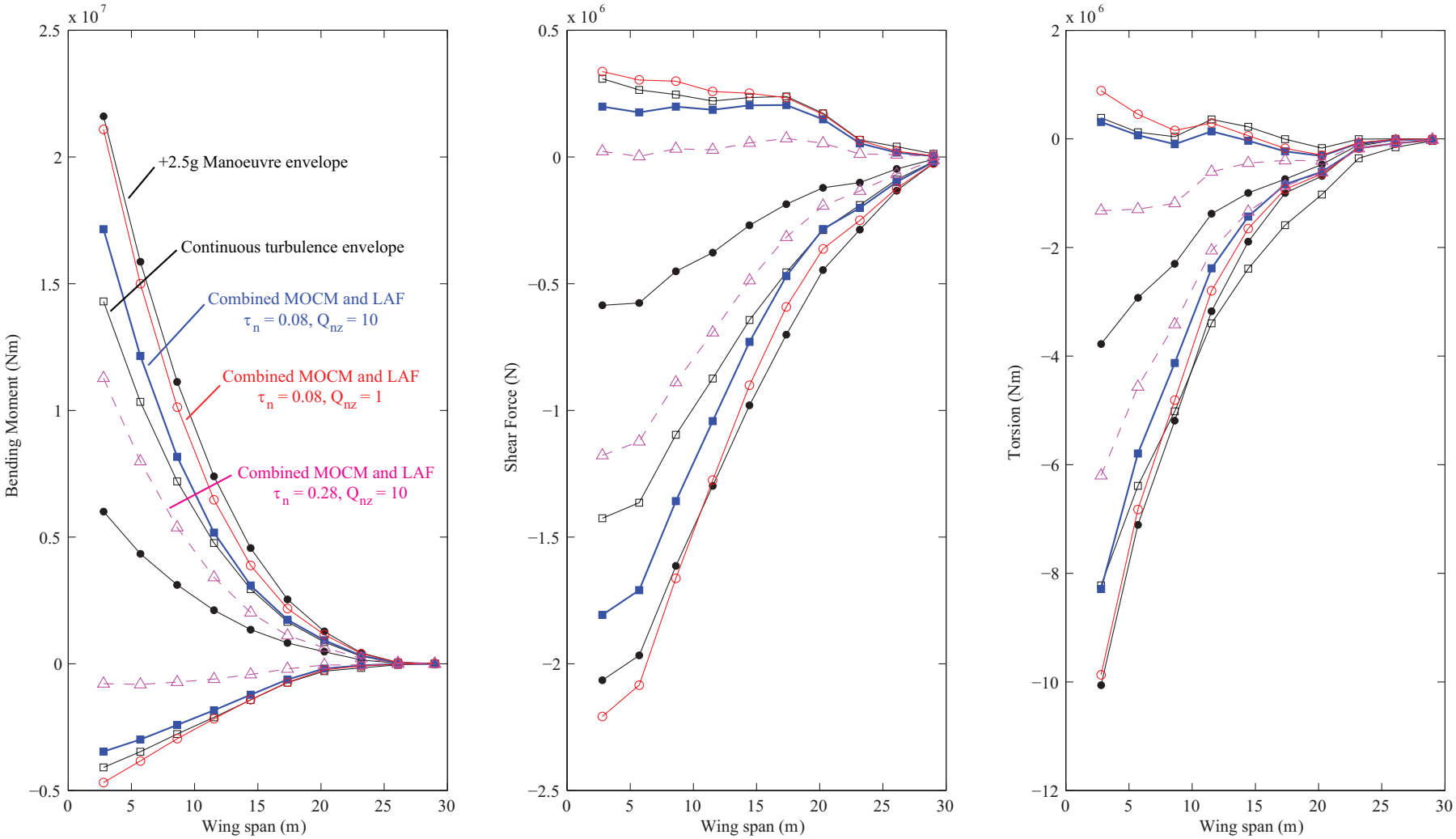

Figure F.8: Wing loads envelope comparison of maximum and minimum internal loads from gust encounter simulations with different levels of MOCM aggression.

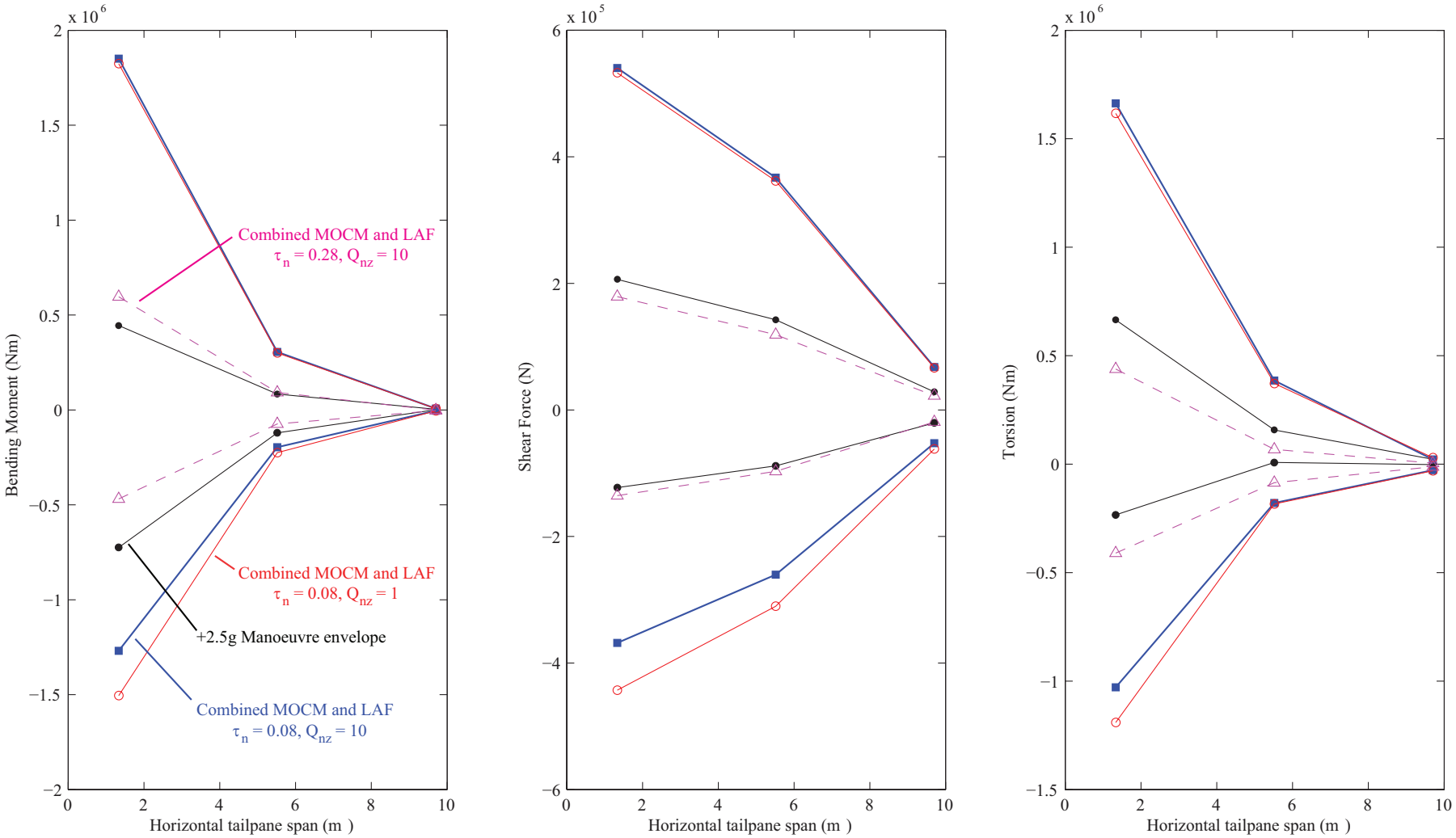

Figure F.9: HTP loads envelope comparison of maximum and minimum internal loads from gust encounter simulations with different levels of MOCM aggression.

APPENDIX G

Off-line detection of pilot-induced-oscillations

Unwanted oscillations resulting from coupling between manual control and aircraft dynamics, also known as APC (of which PIOs are a subset), and their causes have been investigated and scrutinised over 50 years. However, all attempts at either studying the causes or developing cures and methods of prevention have been only partially successful; not due to lack of effort, but due to the nature of the problem. Many studies have found that there is no reliable pre-PIO condition and that positive identification requires much less effort than proving the non-existence of PIO. A fully developed PIO has the following four features[176]:

1. The pilot-aircraft system must demonstrate oscillatory behaviour.
2. The vehicle must be out of phase with the pilot's input. A phase difference of 180 is usually assumed when relating pilot input to aircraft attitude.
3. The frequency of the oscillation must be within the manual control range. The most severe events have been found between 1 rad/s and 8 rad/s.[1]
4. The amplitudes of the pilot input and aircraft response must be large enough to be of concern.

During the 1990's, the US Air Force led a concerted effort to develop techniques aimed towards reducing the risk of PIO. A product of this effort was the Realtime Oscillation Verifier (ROVER) developed as a realtime PIO detection tool. Although it was only used for post-processing flight data, a later heavily modified version was flight tested at the USAF Test Pilot School in real-time[186]. The ROVER project was also aimed to provide a 'scientific' means of PIO detection, as opposed to engineers visually inspecting time histories and deciding upon the existence of PIO when noticing some oscillations[129]. This section presents a technique based on ROVER and implemented within MATLAB for post-processing simulation data and PIO identification.

The implementation assumes that every aircraft response is an oscillation and that PIO is limited to the manual control frequency range. The general procedure used within this approach is as follows:

1. Aircraft response is focused upon prior to conducting a backward search on pilot input.

[1] If considering roll ratcheting or yaw chatter, the upper bound would be around 25 rad/s.

2. Phase difference between aircraft response and pilot input is then checked.[2]

3. Amplitudes of peak aircraft response and pilot inputs are then checked.

The implementation associates flags to the earlier mentioned PIO features and so provides an indication of its presence. Assume $y(t)$ and $u(t)$ represents aircraft response and pilot input respectively. Flag 1 (F_1) checks whether the aircraft response magnitude criteria is met via the following:

$$F_1 = 1 \quad \text{if} \quad \Delta y = |y_{max} - y_{min}| > \Delta y_T \tag{G.0.1}$$

where y_{max} and y_{min} are the response maxima and minima respectively, and Δy_T is a pre-defined oscillation magnitude threshold. Flag 2 (F_2) checks the magnitude criteria for pilot input:

$$F_2 = 1 \quad \text{if} \quad \Delta u = |u_{max} - u_{min}| > \Delta u_T \tag{G.0.2}$$

where u_{max} and u_{min} are the input maxima and minima respectively, and Δu_T is a pre-defined control input magnitude threshold.[3] Similarly, if control surface deflection (δ) data is available, Flag 3 (F_3) may be implemented as follows:

$$F_3 = 1 \quad \text{if} \quad \Delta \delta = |\delta_{max} - \delta_{min}| > \Delta \delta_T \tag{G.0.3}$$

The calculation of signal maxima and minima requires noise filtering. A low pass Butterworth filter is used here for both signals. The filter does distort the signal and introduce a time delay, but since both signals are filtered by the same filter and most calculations involve differences it has a small effect on results. The following Butterworth filter has been used:

$$H(s) = \frac{20^4}{(s+20)^4} \tag{G.0.4}$$

The flag for phase difference is set by considering the times when $y(t)$ and $u(t)$ reach their corresponding maxima and minima. A time lag is defined as follows:

$$\Delta t = t|_{y=y_{max}} - t|_{u=u_{min}} \tag{G.0.5}$$

Phase difference is then defined as follows:

$$\Delta \hat{\phi} = \frac{\Delta t}{P} \tag{G.0.6}$$

where P is the aircraft response period, defined as follows:

$$P = 2(t|_{y=y_{max}} - t|_{y=y_{min}}) \tag{G.0.7}$$

Then Flag 5 (F_5) is set as follows:

$$F_5 = 1 \quad \text{if} \quad \Delta \hat{\phi} > 75^\circ \tag{G.0.8}$$

Flag (F_4) is concerned with aircraft response frequency and is set as follows:

$$F_4 = 1 \quad \text{if} \quad 1\text{rad/s} \leq \frac{2\pi}{P} \leq 8\text{rad/s} \tag{G.0.9}$$

[2]Easily monitorable aircraft states such as pitch rate or roll rate should be used noting that PIO will now be characterised by 90° phase difference.

[3]The minima and maxima detectors are effectively gradient calculators. To detect a maxima the current gradient is stored if the previous gradient was positive and the current gradient is either zero or negative; vice versa for the minima. In case of stick saturation this basically identifies the leading edge of the signal plateau.

The algorithm developed here was used to post-process the Lockheed YF-22 PIO event for verification and the results are presented in Figure G.1. Inspecting the flag status shows that PIO has been detected around 5 seconds. Detection time in this case was limited by the flag corresponding to pitch rate oscillation magnitude, which was deemed small in magnitude till 5 seconds. The threshold values for Δy_T, Δu_T and $\Delta \delta_T$ were set as 0.26 rad/s (15 deg/s), 14 N (3.2 lbs) and 0.07 rad (4°) respectively[176].

The author has also been involved in extending the ROVER concept to include a means of detection that takes advantage of real-time identification of ARX based pilot models.[187][188] It effectively monitors the rate of change of open-loop PVS crossover frequency to assess urgency and an adaptive gain for mitigation purposes.

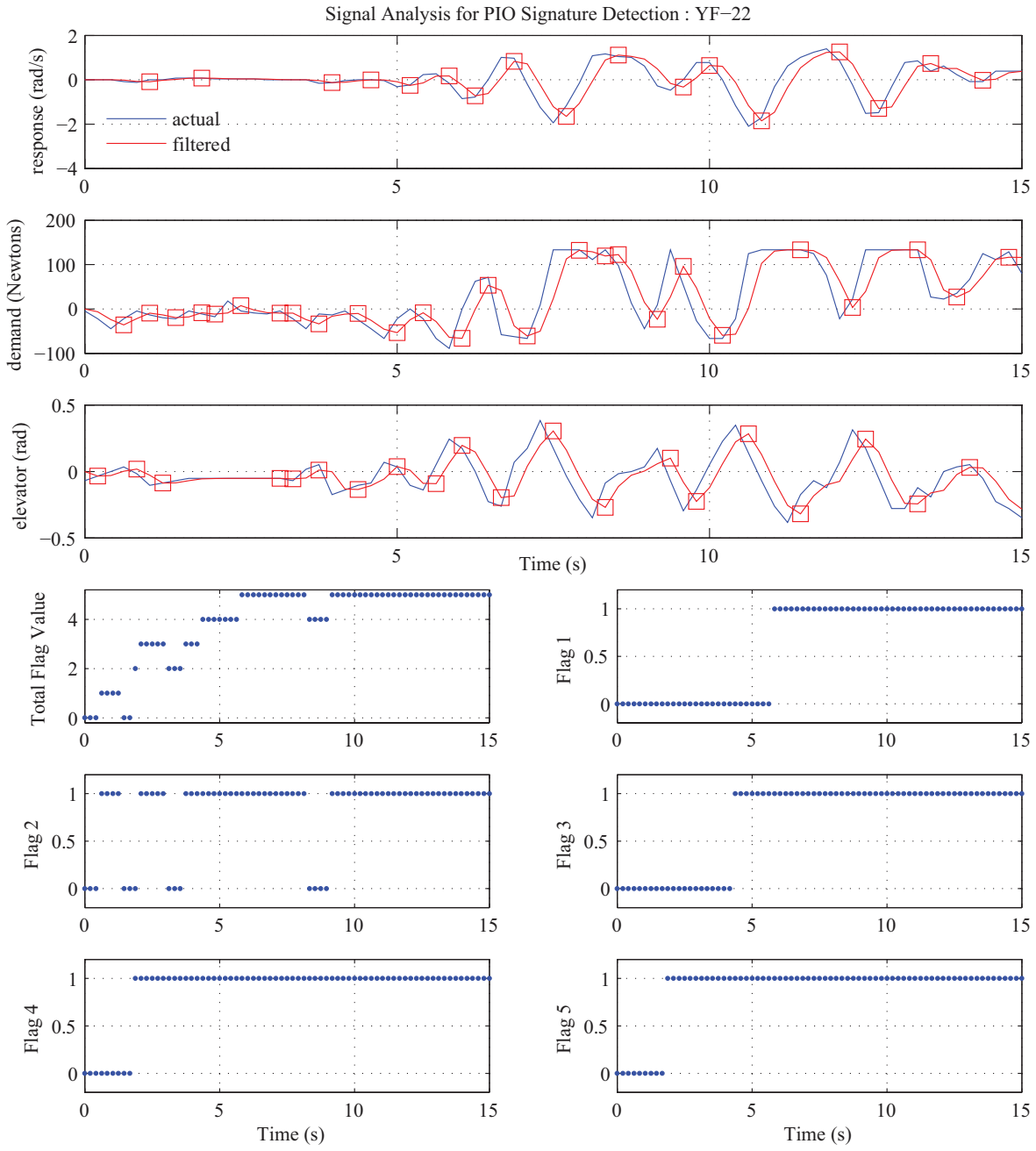

Figure G.1: Performance of detection scheme for Lockheed YF-22 PIO case.

Although the ROVER algorithm and flag threshold settings were verified via the available Lockheed YF-22 data, its application to large aircraft meant that these thresholds had to be changed according to the differences in flight dynamics and stick forces. For example, in contrast to a civil transport a pitch rate of 10 deg/s may not be very significant for a small combat aircraft. Therefore, the 15 deg/s threshold on pitch rate must be changed. This threshold was set to 10 deg/s. The thresholds set for stick force and elevator deflection were not changed. Figures G.2 to G.4 present ROVER output charts for pilot-model-in-the-loop simulations described in Chapter 7.

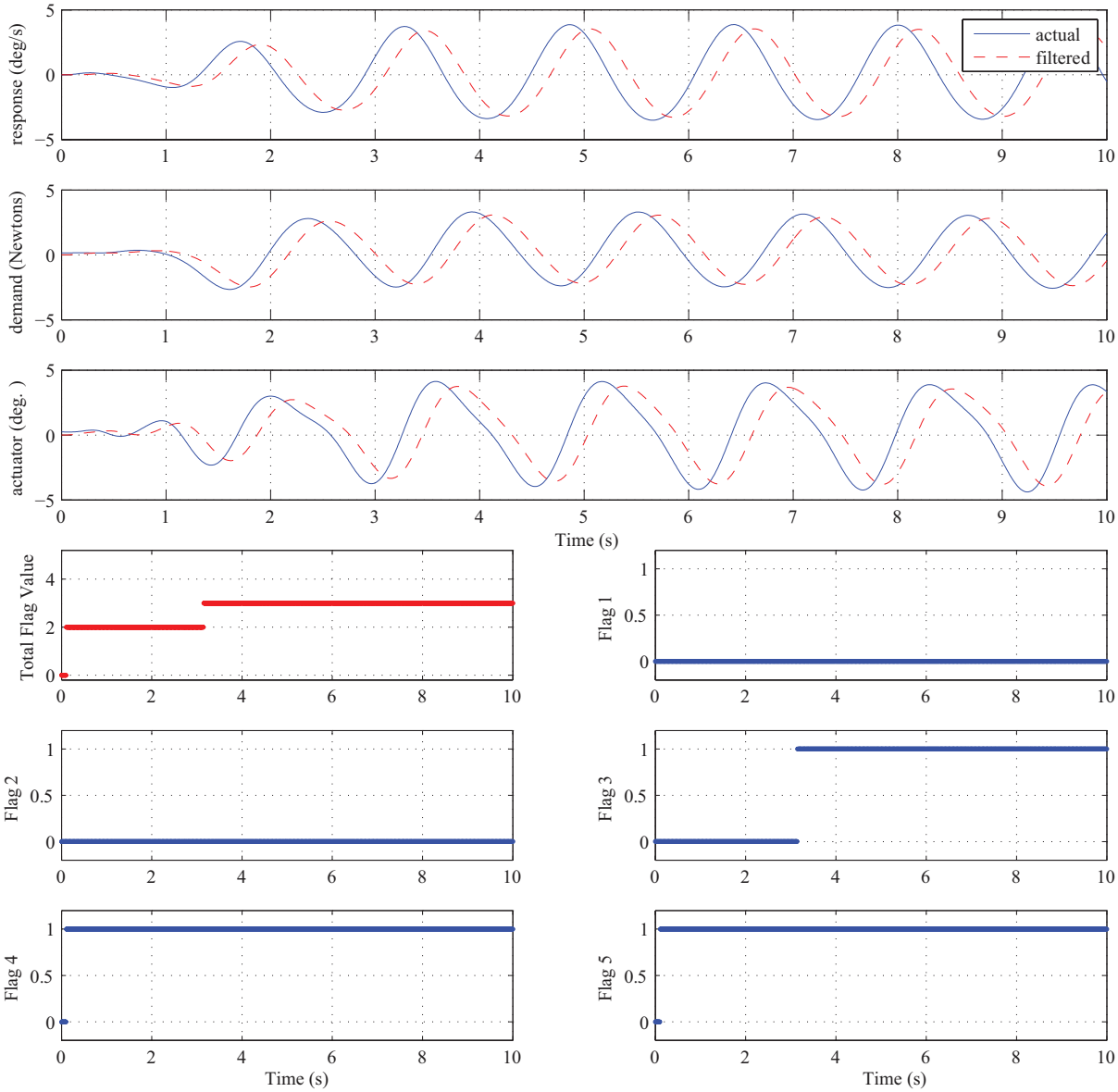

Figure G.2: ROVER output chart for 4 rad/s FAO: pitch dynamics.

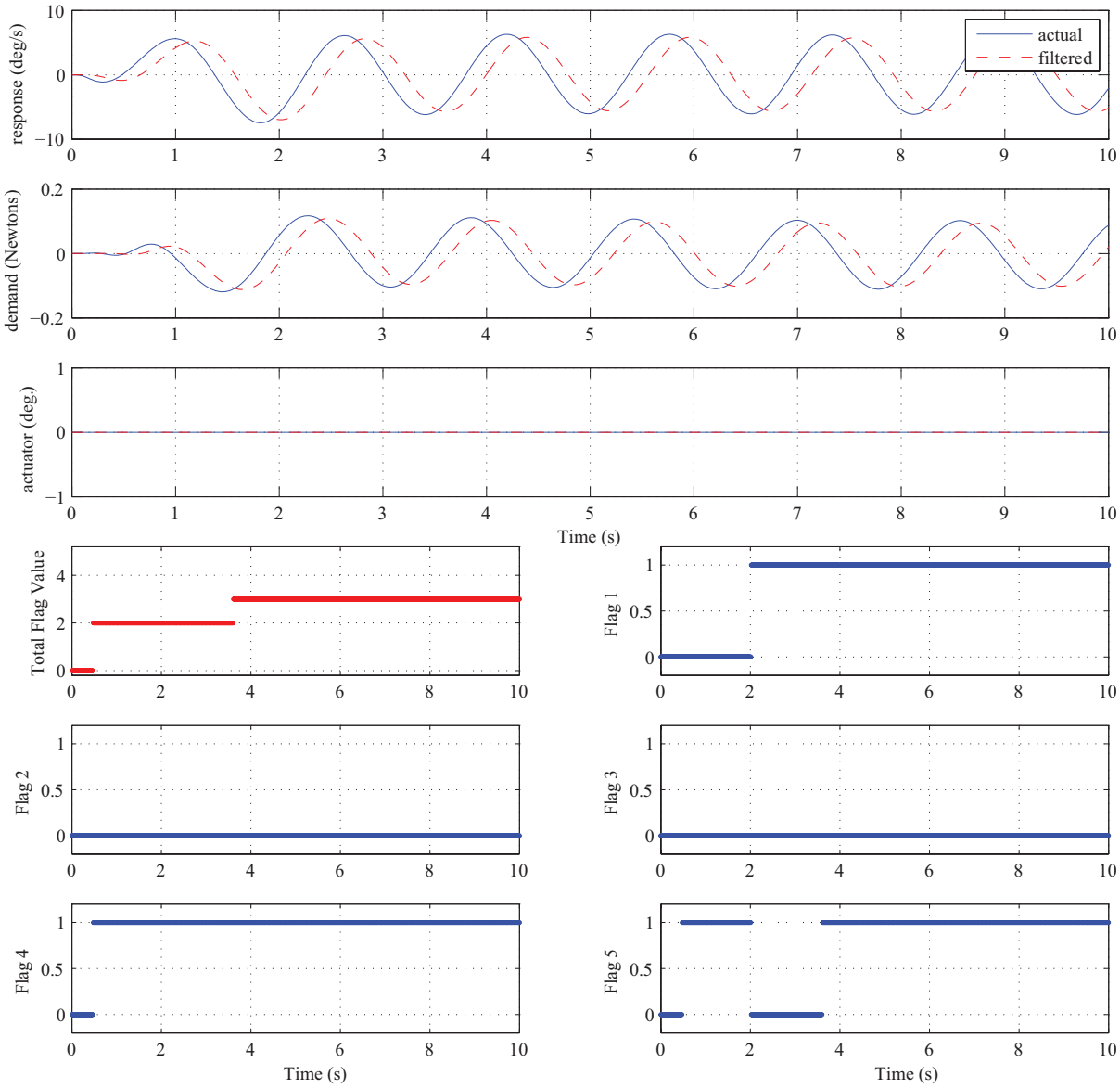

Figure G.3: ROVER output chart for 4 rad/s FAO: roll dynamics.

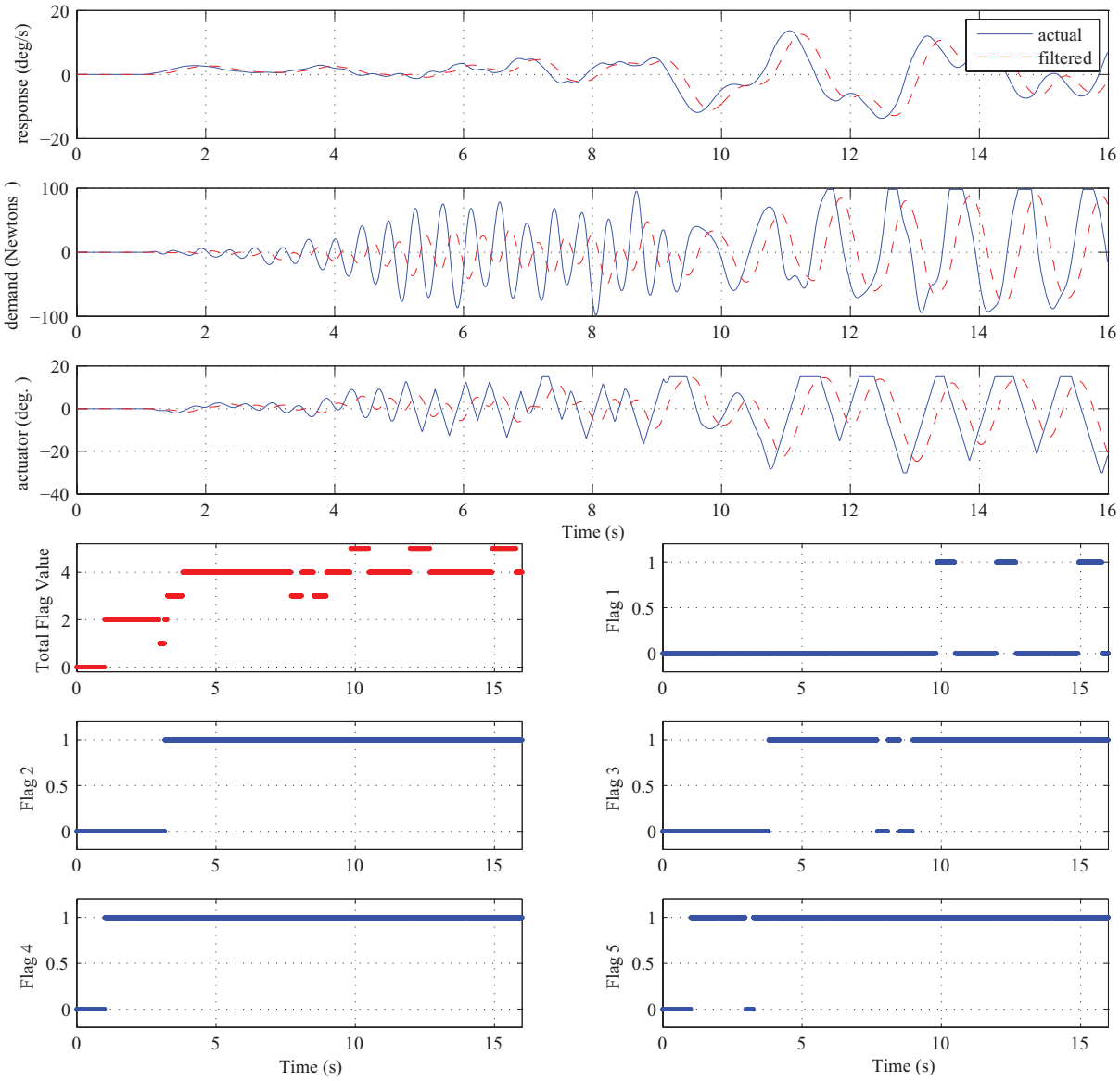

Figure G.4: ROVER output chart for gust encounter simulation ($\tau_n = 0.08$): pitch dynamics.